

Study and characterization of insulating material using partial discharge measurements for power electronics application in HVDC and MVDC

Somya Anand

▶ To cite this version:

Somya Anand. Study and characterization of insulating material using partial discharge measurements for power electronics application in HVDC and MVDC. Electronics. Université de Lyon, 2022. English. NNT: 2022 LYSEI001. tel-03772408

HAL Id: tel-03772408 https://theses.hal.science/tel-03772408v1

Submitted on 8 Sep 2022

HAL is a multi-disciplinary open access archive for the deposit and dissemination of scientific research documents, whether they are published or not. The documents may come from teaching and research institutions in France or abroad, or from public or private research centers.

L'archive ouverte pluridisciplinaire **HAL**, est destinée au dépôt et à la diffusion de documents scientifiques de niveau recherche, publiés ou non, émanant des établissements d'enseignement et de recherche français ou étrangers, des laboratoires publics ou privés.



N°d'ordre NNT: 2022LYSEI001

THESE de DOCTORAT DE L'UNIVERSITE DE LYON

opérée au sein de **INSA de Lyon**

Ecole Doctorale N° ED160 Electronique, Electrotechnique, automatique (EEA)

Spécialité / discipline de doctorat : Génie électrique

Soutenue publiquement le 13/01/2022, par :

Somya ANAND

Study and characterization of insulating materials using partial discharge measurements for power electronic applications in HVDC and MVDC

Devant le jury composé de :

M. CAVALLINI Andrea	Professor, Universita Di Bologna, Italy	Rapporteur
M. LESAINT Olivier	Directeur de recherche CNRS, G2ELAB, Grenoble, France	Rapporteur
M. PECASTAING Laurent	Professeur, Université de Pau et des Pays de l'Adour, France	Président
Mme LOCATELLI Marie-Laure	Chargée de recherche CNRS, Université Paul Sabatier, France	Examinatrice
Mme AIT AMAR Sonia	Maître de conférences, Université d'Artois, France	Examinatrice
M. JOUBERT Charles	Professeur, Université Claude Bernard Lyon, Ampère, France	Examinateur
M. BUTTAY Cyril	Directeur de recherche CNRS, INSA de Lyon, Ampère, France	Directeur de thèse
M. VAGNON Eric	Maître de conférences, Ecole Centrale de Lyon, Ampère, France	Co-Directeur de thèse
M. ZOUAGHI Ayyoub	Maître de conférences, Ecole Centrale de Lyon, Ampère, France	Invité
M. GUILLET Martin	Team Leader, Medium Frequency Transformer, SuperGrid Institute, France	Invité
M. LEBEY Thierry	High voltage Team Leader, Safran Tech, France	Invité

Abstract

For future smart grid infrastructures, the medium voltage direct current (MVDC) grid will play a crucial role in enabling new features at distribution and sub-transmission levels by integrating distributed energy sources, connecting remote loads, and in the interconnection of existing AC substations. Utilizing the capabilities of recently introduced wide band-gap (WBG) devices can significantly reduce the weight, volume, and maturation cost of power applications. However, the presence of these devices in the power network will introduce a new electrical constraint in the form of repetitive fast -rising voltage waveforms (10-100 kV/µs) characterized by a high repetition rate (> 100 kHz). These waveforms can influence the discharge mechanism of the insulation system of power equipment in a different way than AC.

Under such circumstances, it is necessary to investigate the reliability of power conversion equipment for the future transmission network such as medium frequency transformer (MFT). For high power applications the insulation system of MFT is expected to incorporate dielectric liquid as its primary insulation medium. However, the discharge mechanism of dielectric liquid under fast repetitive square voltages is not very clear today.

Therefore, this thesis aims to investigate the partial discharge (PD) mechanism under square voltage waveform to address power electronic applications like MFT. For this, the specifications of a test bench are defined and developed during this thesis to reproduce the electrical stresses in the form of fast-rising unipolar square voltages (USV) with repetition rates higher than 50 Hz. As the PD measurement under fast-rising square voltage is difficult due to electromagnetic interferences generated by the high-speed switching of semiconductor devices, the PD detections are performed by optical method, which detects the photons emitted during discharge events.

In the first step, the optical detection technique is validated under AC 50 Hz by comparing it to the standard electrical measurement as defined by IEC 60270 in oil/barrier insulation system. Then, using the same technique, the PD measurements are performed under USV, and the results are compared to those obtained under AC excitations. As a result, the inception voltage in USV is found to be lower as compared to AC 50 Hz which points towards the arrival of PD activity at a lower voltage under USV than in bipolar AC. Further, PD measurements are performed by varying the square voltage parameters such as repetition rate, duty cycle and rise times.

The major outcome from this thesis is the development of a test bench generating USV with dV/dt in the range of 10-100 kV/ μ s. The test campaign has demonstrated the capability of the optical method as a decent PD detector under USV. Also, it allows the PD assessment under varying rise times, repletion rates, and duty cycles. Hence, the test bench can be further used for PD studies in transparent media as well as to validate other detection techniques.

Keywords: Partial discharge, dielectric liquid, optical detection, square voltage, fast rise time, high repetition rate, MFT

Acknowledgement

With several ups and downs including the pandemic and system breakdowns, this PhD journey has been quite incredible; but it would not have been possible without the support of those involved in it. I would begin by thanking SuperGrid Institute and Ampère Laboratory for selecting my candidature for this work. I take this moment to express my gratitude to my supervisors: starting with my co-thesis director Mr. Eric VAGNON, who have always been patient and pushed me for learning by doing. My industrial supervisor Mr. Martin GUILLET has been quite encouraging throughout this journey, and I must thank him for providing me certain degree of freedom. My thesis director Mr. Cyril BUTTAY has always overwhelmed me with his thoughtful advice and pitched in at important times. I hope to have delivered a small fraction of their expectation through this work.

I am grateful to the esteemed Jury members for evaluating my thesis work. I would like to begin by thanking Mr. Olivier LESAINT and Mr. Andrea CAVALLINI for reviewing my thesis. I would also like to thank Mr. Laurent PECASTAING (President), Mme Marie-Laure LOCATELLI, Mme Sonia AIT-AMAR, Mr. Charles JOUBERT, and Mr. Thierry LEBEY for examining my thesis. I am very thankful to all of you for your insightful comments and thought-provoking questions during the defense session.

I would also like to thank Mr. Christophe PERRIER from GE Villeurbanne, Mr. Ayyoub ZOUAGHI from ECL, Mr. Thanh VU and Mrs. Servane HALLER from SuperGrid Institute for their assistance and not to forgot Mr. Bruno LEFEBVRE with whom I started this journey initially. Also, I cherish to have known Aris Sid-AHMED who improved the models during his internship, making its implementation easier at a later stage. Furthermore, I recognize the effort of administrative staffs in SuperGrid Institute for providing me required resources.

During this thesis, as I worked at three different locations, the experience has been enlightening, be it velo ride to La Doua with SuperGrid colleagues, in-depth discussion on various topics, light moments during lunchtime, morning pick-ups to Ecully and off course not to forget the afterwork reunions. I am thankful to each one of you in program-3 and many of you in program-1 from SuperGrid for your support on technical, professional as well as joyful conversations. I even made some friends at laboratory Ampère who always boosted me up and have been exceptional in opening laboratory doors for me during the pandemic when access was limited. Special thanks to my colleagues from Ampère and SuperGrid who contributed to experimental set-up fabrication. I am also grateful to my Indian and International friends who are always there for cheerful talks.

Finally, I would like to thank my family who always supported me to accomplish my dreams. My grandfather and grandmother have always been my source of inspiration. My mom has been

a pillar of strength in my life. My brother and sister-in-law have always been encouraging me in all steps I have taken. My playful cute niece, just remembering you brings a smile to my face! Not to forget my caring wife who has been very positive ever since and always calmed me down from stress. I am also thankful to all my relatives who have always bestowed their blessings on me.

Résumé détaillé en français

Table des matières

I.	Contexte	3
I.1	Contrainte électrique sur le transformateur du convertisseur HVDC	4
I.2	Contrainte électrique sur le transformateur moyenne fréquence (TMF)	6
I.3	Problème de mesure de la décharge partielle sous forme d'onde carrée	7
II.	Définition de l'objet sous test (OST)	9
III.	Mesures de décharges partielles en courant alternatif	10
III.	1 Mise en place de la détection de la DP sous signal AC 50 Hz	10
III.	2 Corrélation entre les mesures électrique et optique	12
IV.	Méthodologie de détection des décharges partielles sous forme d'onde de tension carrée	15
IV	1 Impact de la commutation rapide d'un interrupteur HT	17
IV	2 Essais de DP avec configuration pointe-barrière-plan dans l'air	18
	3 Essais de DP avec configuration pointe-barrière-plan dans un liquide lectrique	19
	•	
V.	Etude du phénomène de décharge partielle sous tensions carrées unipolaires (TCU)	21
V.	1 Comparaison PDIV entre AC et TCU	21
V.:	2 Comparaison PDIV entre deux liquides diélectriques en tension carrée	23
uni	ipolaire	
	3 Résultats des essais en faisant varier le temps de montée, la fréquence et le	24
•	oport cyclique	2.5
V.4	4 Conclusion et perspective	25

I. Contexte

L'électronique de puissance est amenée à jouer un rôle important dans la transition énergétique permettant de diminuer la part des combustibles fossiles et dans l'augmentation de l'efficacité du système électrique des futurs réseaux. Le composant fondamental de l'électronique de puissance est l'interrupteur semi-conducteur. Un grand nombre d'entre eux sont assemblés dans des configurations spécifiques pour convertir le courant alternatif en courant continu et vice versa [3] [4]. Au fil des ans, les dispositifs d'électronique de puissance ont connu des avancées technologiques, des valves à arc de mercure utilisée auparavant aux dispositifs à large bande interdite (LBI) mis en œuvre aujourd'hui. Ces dispositifs LBI avancés comme le carbure de silicium (SiC) offrent une tension de blocage élevée, une fréquence de commutation très élevée (centaine de kHz), peuvent fonctionner à des températures plus élevées et présentent des vitesses de commutation importantes avec des pertes en commutation réduites [5][6] par rapport à leurs homologues antérieurs.

En raison de leur vitesse de commutation élevée et de leur fonctionnement à haute fréquence, les formes d'onde de tension générées par ces dispositifs semi-conducteurs sont des carrés répétitifs. Les convertisseurs du réseau de transmission en courant continu à haute tension (CCHT) sont généralement équipés de thyristors. D'autre part, le transformateur moyenne fréquence (MFT) du futur réseau à courant continu à moyenne tension (CCMT) devrait intégrer des dispositifs SiC. Le transformateur du réseau électrique, tant dans la liaison CCHT que dans le futur réseau CCMT, sera continuellement soumis à ce type de forme d'onde, dont les caractéristiques (temps de montée, fréquence, rapport cyclique) sont différentes de celles du courant alternatif sinusoïdal classique.

Le système d'isolation du transformateur CCHT est composé de cellulose et d'huile minérale. On s'attend à ce que la même combinaison soit utilisée dans le TMF pour les applications à haute puissance. Cependant, le mécanisme de décharge partielle (DP) sous forme d'onde de tension carrée n'est pas clairement compris aujourd'hui, notamment dans le cas du fluide diélectrique.

Par conséquent, pour maitriser la fiabilité du système d'isolation du transformateur, il devient nécessaire d'étudier le mécanisme de décharge partielle dans une liquide diélectrique sous une forme d'onde carrée à montée rapide. Le travail effectué dans cette thèse est une étape de cette étude.

Le système d'isolation des transformateurs dans le schéma CCHT existant et le schéma CCMT à venir ont été choisis comme cas d'application. Dans la première étape, les formes d'onde de tension aux bornes de l'enroulement côté valve d'un transformateur dans un lien CCHT conventionnel et dans le futur CCHT seront discutées. Ensuite, les problèmes rencontrés avec les

techniques de détection de DP conventionnelles sous des formes d'ondes de tension à montée rapide seront présentés.

Puis, l'objet sous test (un système d'isolation composite) pour effectuer les mesures de DP sera présenté.

Dans la section suivante, la mesure de DP à l'aide d'un tube photomultiplicateur (l'élément principal de la détection optique) en courant alternatif pour l'objet sous test sélectionné sera introduite.

Ensuite, la description de la configuration de test pour générer des formes d'onde carrées sera présentée. Les résultats préliminaires des tests utilisant différentes techniques de détection de DP seront également présentés.

Enfin, une comparaison de la tension de début de décharge partielle (PDIV) entre l'excitation carrée et AC sera fournie. L'impact du temps de montée, de la fréquence de commutation et du cycle d'utilisation seront étudiés.

Cette thèse rassemble les travaux réalisés en trois ans dans le cadre d'une collaboration entre le programme Electronique de puissance et convertisseur de SuperGrid Institute, Villeurbanne, France et le Laboratoire Ampère, Ecully, France. Le dispositif expérimental a été développé au sein du laboratoire Ampère.

I.1 Contrainte électrique sur le transformateur du convertisseur CCHT

La figure 1 montre le schéma d'un pont à 12 impulsions pour un schéma monopôle connecté à une liaison CCHT. Comme on peut le voir sur la figure, le transformateur qui relie le réseau AC à la station de conversion est un transformateur triphasé à trois enroulements, souvent appelé transformateur CCHT. L'enroulement primaire de ce transformateur triphasé a généralement un enroulement en étoile et est mis à la terre. Du côté de la valve (ou du convertisseur), les enroulements sont respectivement en étoile et en triangle avec des masses flottantes. Les deux enroulements côté valve du transformateur triphasé sont connectés à deux ponts triphasés à 6 impulsions. Ces deux ponts à 6 impulsions sont connectés en série, ce qui en fait un pont redresseur à 12 impulsions. Idéalement, la tension de sortie totale sur la liaison CCHT est divisée de manière égale entre les deux ponts. L'enroulement en étoile et en triangle offre un déphasage de 30° entre les deux ponts, ce qui permet un fonctionnement efficace à 12 impulsions [10][13].

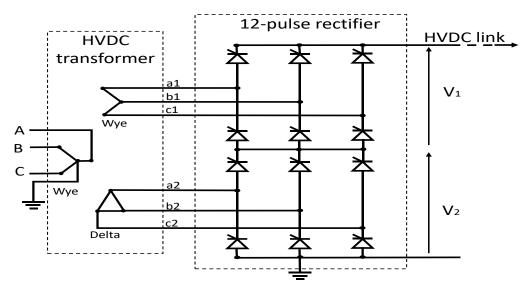


Figure 1 : Connexion d'un transformateur triphasé avec des convertisseurs en pont à 12 impulsions dans une transmission CCHT

La figure 2 donne la tension aux bornes du transformateur CCHT en régime permanent pour le modèle simulé dans la Simulink (référence du modèle en Simscape: power_hvdc12pulse). La tension mesurée entre la phase et la terre du côté primaire du transformateur CCHT (V_{pAG}) dans la figure 2 est une forme d'onde sinusoïdale non déformée qui est due à la présence d'un filtre passif entre l'enroulement primaire du transformateur et la source CA.

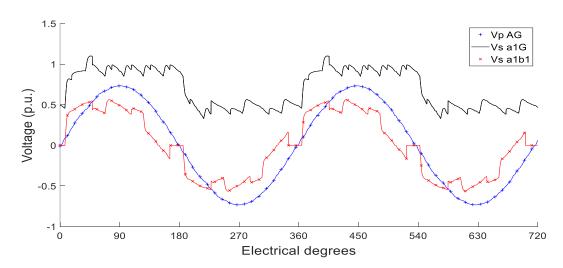


Figure 2 : Forme d'onde de la tension à travers l'enroulement côté ligne et côté vanne du transformateur CCHT

En revanche, les tensions mesurées entre la phase et la terre et V_{sa1G} et les deux phases V_{sa1b1} de la topologie sont déformées, ce qui a également été discuté dans [13] et [15]. Ceci est dû au chevauchement de commutation pendant la commutation successive des valves. Les chutes de

tension à travers la réactance du circuit pendant la commutation successive des valves conduisent à la distorsion comme on le voit dans V_{sa1b1} et V_{sa1G} [10][11].

De plus, la tension entre la phase et la terre dans le pont supérieur V_{sa1G} est caractérisée par un grand décalage en courant continu. Pendant le fonctionnement normal de la liaison CC, le décalage CC pour le pont supérieur avec un enroulement en étoile est de 75% tandis que celui connecté au pont inférieur est de 25% environ de la tension dans la liaison CC [16]. La présence d'un contenu harmonique élevé superposé à la tension continue sollicite continuellement les enroulements côté valve et, par conséquent, l'isolation du transformateur CCHT.

I.2 Contrainte électrique sur le transformateur moyenne fréquence (TMF)

De nombreuses études ont été réalisées pour analyser les formes d'onde d'entrée et de sortie de la topologie DC/DC, mais la contrainte électrique au niveau des enroulements du TMF en raison de la mise en série des convertisseurs dual active bridge (DAB) est plutôt peu représentée dans la littérature. Par conséquent, pour mener une étude de simulation à cet égard, la spécification d'une topologie DC/DC isolée avec quatre convertisseurs DAB, fournie dans [4] a été considérée. La tension côté basse tension dans l'étude était de 5 kV pour générer une tension de sortie de 20 kV après mise en série des convertisseurs DAB.

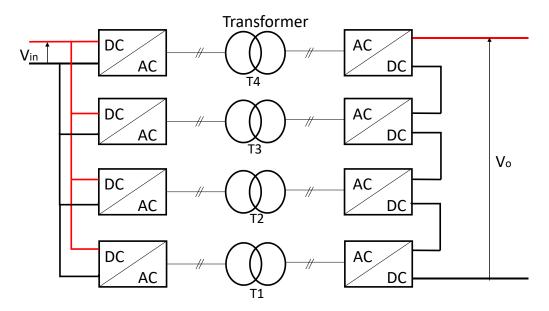


Figure 3 : Mise en série des convertisseurs DAB dans une topologie DC-DC isolée pour atteindre une tension de sortie élevée (Vo)

Pour reproduire cette situation en simulation, on a d'abord généré un convertisseur DAB avec un rapport de transformation de 1:1 pour le TMF. Les blocs de commutation mosfet ont été utilisés pour concevoir les ponts inverseur et redresseur et la fréquence de commutation a été fixée à 10 kHz. On a ensuite créé la structure illustrée à la figure 3, qui comprend quatre étages de

convertisseurs DAB. Les convertisseurs DAB ont été connectés en parallèle du côté de l'entrée (Vin) tandis que l'autre extrémité était connectée en série pour obtenir une sortie de 20 kV (Vo).

La figure 4 montre la tension aux bornes des TMF à différents stades (T1 à T4 comme indiqué sur la figure 3) pour la tension de sortie (Vo) par rapport à la terre. Au fur et à mesure que les niveaux du transformateur augmentent de bas en haut dans la topologie (T1 à T4), on constate que l'enroulement secondaire est soumis à une tension de décalage continue en plus de la forme d'onde carrée à montée rapide. La contrainte d'isolation maximale a été observée pour l'enroulement secondaire du transformateur le plus haut (T4) dans l'architecture. Dans ce scénario, la distribution du champ électrique dans l'isolation de l'enroulement des transformateurs positionnés au sommet de la topologie (adjacents à la ligne MT de 20 kV), serait la somme du champ électrique dû à la tension continue constante et de celui dû aux impulsions de tension répétitives rapides.

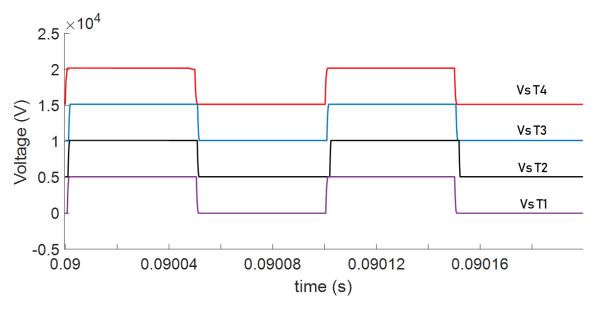


Figure 4 : Résultat de la simulation de la tension aux bornes de l'enroulement secondaire (côté de la tension Vo comme indiqué sur la figure 11) avec Vs T1, Vs T2, Vs T3 et Vs T4 représentant les tensions à chaque étage du transformateur pour la topologie DC-DC en régime permanent

13. Problème de mesure de la décharge partielle sous forme d'onde carrée

Les essais de DP sont généralement réalisés sous excitation AC. La norme IEC60270 décrit la méthode et la procédure pour réaliser des essais de DP sous des tensions alternatives jusqu'à 400 Hz. Une impulsion de DP est caractérisée par une amplitude qui augmente rapidement dans un laps de temps très court (la dizaine de nanosecondes ou ns). Elle a une amplitude typique de quelques picocoulomb (pC) à quelques centaines de picocoulomb. La configuration de mesure de l'essai de DP sous excitation AC comprend une alimentation haute tension, un filtre haute tension (pour supprimer le bruit de l'alimentation), un objet sous test (OST), un condensateur de

couplage (Ck), une impédance de mesure (Zmi) et un instrument de mesure MI comme présenté dans la Figure 5.

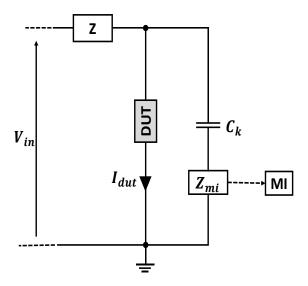


Figure 5: Circuit de mesure de la DP en courant alternatif utilisant l'impédance de mesure Zmi en série avec le condensateur de couplage Ck avec l'objet sous test en parallèle

La détection des DP est difficile avec le circuit ci-dessus sous une forme d'onde de tension carrée à montée rapide. Cela est dû à la perturbation causée par les courants de déplacement générés pendant les actions de commutation rapides [54][56], comme le montre la figure ci-dessous.

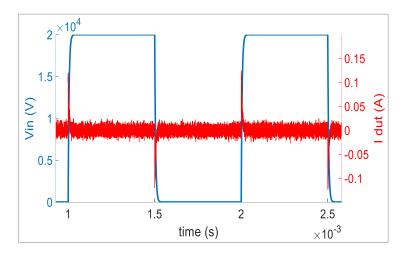


Figure 6: Représentation de la forme d'onde de tension carrée et du courant de déplacement dû à la commutation rapide lorsqu'ils sont alimentés au circuit de mesure de base de la mesure de la DP

Dans ces conditions, il est nécessaire d'explorer d'autres méthodes pour détecter les DP sous une tension qui augmente rapidement. Différentes études ont présenté la mise en œuvre de techniques de mesure non intrusives telles que le transformateur de courant haute fréquence [57] et l'antenne

ultra-haute fréquence (UHF) [58]. Cependant, ces techniques peuvent également être affectées par de fortes interférences électromagnétiques (EMI) produites par le courant de déplacement. D'autres articles ont proposé des méthodes de post-traitement comme la transformation en ondelettes et des approches stochastiques [59] [60] pour discriminer les DP sous une forme d'onde carrée avec un temps de montée court. Une autre technique est la détection optique qui offre une sensibilité raisonnable et une immunité contre les EMI [55][62]. Des études comme [62] ont démontré la mise en œuvre d'un tube photomultiplicateur (PMT) pour la détection des DP sur un circuit imprimé noyé dans un liquide isolant. Mais sa principale limite est que seule la détection des DP dans les milieux transparents est possible.

II. Définition de l'objet sous test (OST)

Les essais de décharge partielle ont été réalisés dans une configuration pointe-plan avec une barrière diélectrique solide reposant contre l'électrode de mise à la terre, l'ensemble étant complètement immergé dans un liquide diélectrique, comme le montre la figure 7. L'objet sous test avec une pointe d'aiguille de 1 µm de rayon et un espace de 0,7 mm a été choisi pour créer un champ électrique suffisamment élevé pour la génération de DP. Un plan circulaire de 20 mm de diamètre a été fabriqué en acier inoxydable. La pointe de l'aiguille a été connectée à l'alimentation haute tension et le plan à la terre.

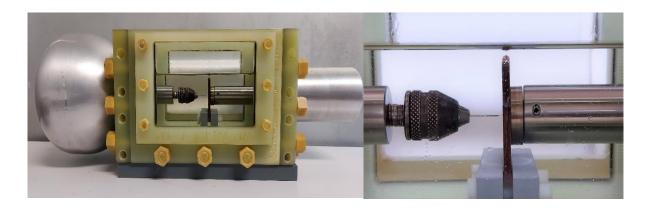


Figure 7: (a) Objet testé avec la configuration pointe-barrière-plan complètement immergé dans le liquide diélectrique, utilisée pour toutes les mesures de décharge partielle (b) vue agrandie du petit espace entre la pointe de l'aiguille et la barrière

Dans le cadre de ce travail, différentes combinaisons d'isolants liquides/solides susceptibles d'être utilisés dans des équipements haute tension ont été envisagées. La Nytro4000X (huile minérale) et la Midel7131 (ester synthétique) ont été considérées pour les mesures de décharge partielle. Du carton comprimé imprégné, du chlorure de polyvinyle (PVC) et du nitrure d'aluminium AlN ont été choisis comme barrières. L'épaisseur, la dimension, la permittivité

relative typique et le nombre d'échantillons de barrières sélectionnés pour les tests avec chaque type de liquide diélectrique sont indiqués dans le tableau 1.

Barrier Thickness Samples tested Samples tested with Sample size $(mm \times mm)$ **MIDEL 7131** samples (mm) with Nytro 4000X 1 40×40 **PVC** 2 5 5 40×40 0.63 40×40 3 3 AlN 40×40 3 3 **Impregnated** 2 36×36 5 NA Pressboard

Tableau 1 : Spécification des barrières solides testées

Avant les mesures de DP, les liquides diélectriques et les échantillons de barrière ont été traités. Les échantillons traités de liquides diélectriques ont été contrôlés pour obtenir les même conditions tout au long des tests.

III. Mesures de décharges partielles en courant alternatif

III.1. Mise en place de la détection de DP sous AC 50 Hz

Conformément aux directives de la norme IEC60270, le banc d'essai en courant alternatif a été développé pour la mesure de la DP avec l'aide d'autres chercheurs du laboratoire Ampère. Le banc d'essai expérimental (Figure 8) sous excitation AC était composé de deux parties principales : un circuit haute tension et un circuit de mesure de DP.

La haute tension était générée à l'aide d'un transformateur sans DP (230 V/ 25 kV) à l'intérieur de la cage de Faraday. La tension appliquée à l'objet sous test et son profil (rampe, échelon, taux de montée de la tension) étaient contrôlés depuis l'extérieur de la cage.

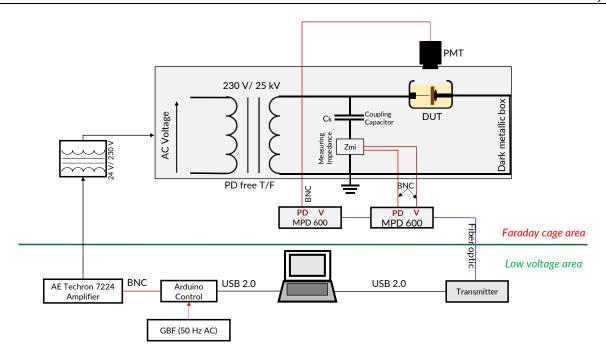


Figure 8: Schémas du banc d'essai PD en AC 50 Hz

Le circuit de mesure de la DP comprend un détecteur de DP Omicron (MPD600) pour la mesure électrique et un tube photomultiplicateur (PMT R943-02 de Hamamatsu) qui détecte les photons émis pendant les processus de décharge. L'objet sous test a été placé à l'intérieur d'une petite boîte métallique sombre (dans une grande cage de Faraday) qui a amélioré la capacité de capture du PMT. Deux unités MPD 600 ont été utilisées pour acquérir les DP simultanément à partir des techniques de détection électrique et optique.

Le bruit de fond du banc d'essai s'est avéré être inférieur à 0,3 pC jusqu'à 16 kVrms pour la détection électrique des DP. Comme le PMT compte les photons émis par le processus de décharge, les paramètres de DP mesurés par le PMT sont rapportés ici en utilisant une unité arbitraire (a.u.). La détection optique n'a pas été affectée par le niveau de tension appliquée et son bruit de fond est toujours resté inférieur à 0,2 pa.u (pico unité arbitraire). Le PMT a été alimenté par une source négative de courant continu. La tension continue appliquée au PMT a été optimisée et maintenue à -1,3 kV pour toutes les mesures de DP.

Pour les essais de DP, la tension appliquée aux bornes de l'objet sous test a été augmentée par paliers de 1 kV avec un taux de montée de 1 kV/s. Cette augmentation était suivie d'un temps d'attente de 30 s au niveau de tension élevé avant de le diminuer jusqu'à zéro avec un taux de diminution de 1 kV/s. Un intervalle de 30 s a été prévu à tension nulle avant d'augmenter à nouveau la tension aux bornes de l'objet sous test, comme le montre la figure 9. La tension a été augmentée à nouveau jusqu'à ce que la tension de début de décharge partielle (PDIV) soit atteinte.

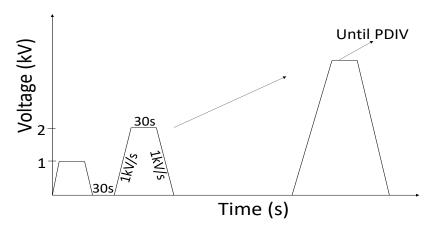


Figure 9: Profil d'application de la tension aux bornes de l'objet sous tes

L'objet à tester comprend un liquide diélectrique traité, une aiguille neuve et un échantillon de barrière traité. Pour vérifier la reproductibilité des essais de DP, six essais ont été effectués avec chaque spécimen d'objet sous test. Après six essais de DP, l'aiguille, le liquide diélectrique et l'échantillon de barrière solide ont été remplacés par des échantillons vierges. Cette opération s'est poursuivie jusqu'à ce que tous les échantillons de barrière aient été testés pour chaque type de barrière, conformément au tableau 1

III.2. Corrélation entre les mesures électriques et optiques

Le couplage des techniques de détection optique et électrique a permis la visualisation et l'enregistrement des décharges partielles au même moment. Le système Omicron affiche l'intégration du signal de DP sous la forme d'un motif PRPD, où chaque point correspond à un événement de DP. La figure 10 montre les motifs PRPD (sous la forme d'un amas de DP) obtenus par les techniques de détection électrique et optique au même instant pour un carton de 2 mm d'épaisseur dans de l'huile minérale à 12 kV (rms). On peut observer sur la figure que la PMT a détecté l'apparition d'événements de DP pendant la même phase (entre 0°-90° et 180°-270°) que la technique de détection électrique.

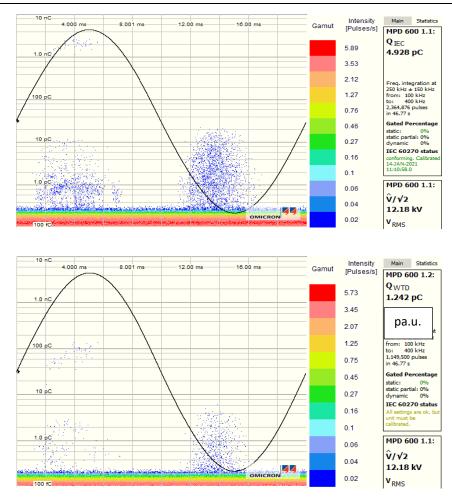


Figure 10: Image PRPD d'un carton comprimé de 2 mm d'épaisseur dans Nytro 4000X prise au même instant à partir d'une détection électrique (en haut) et optique (en bas) à 12 kV (supérieure à la PDIV)

La moyenne des valeurs de PDIV ainsi obtenues pour chaque type de barrière testée avec de l'huile minérale a été tracée dans la Figure 11 en considérant 2 pC comme seuil de PDIV avec la mesure électrique et 0,25 pa.u. (ou 0,25 pC dans le système Omicron) avec la mesure optique. On peut observer que les valeurs moyennes de PDIV acquises électriquement et optiquement sont presque dans la même gamme pour chaque type de barrière.

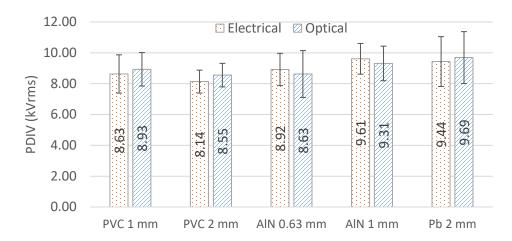


Figure 11: Corrélation entre la PDIV observée à partir de la détection électrique avec un seuil de 2 pC et la détection optique dans l'huile minérale (Nytro 4000X) pour différentes barrières

Une corrélation similaire a été trouvée entre les PDIV obtenus à partir de la mesure électrique et optique avec l'ester synthétique (Midel 7131), cependant en choisissant le seuil de PDIV de 10 pC avec la mesure électrique et de 0,25 pa.u. pour la mesure optique.

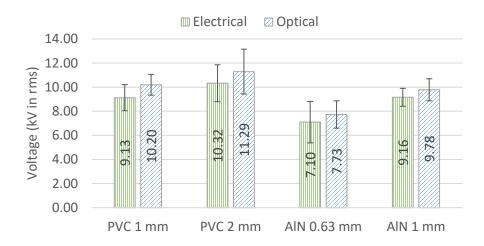


Figure 12: Corrélation entre la PDIV observée à partir de la détection électrique avec un seuil de 10 pC et la détection optique dans le MIDEL7131 pour différentes barrières

À partir des corrélations ci-dessus, on peut déduire que l'amplitude de 0,25 pa.u. obtenue par détection optique correspond à 2 pC avec l'huile minérale alors qu'elle est correspond à 10 pC avec l'ester synthétique. De plus, deux conclusions majeures peuvent être tirées :

pour la configuration d'électrode avec des barrières dans un liquide diélectrique, le PMT a détecté les PDIV au même angle de phase que la mesure électrique

- Les PDIV obtenus optiquement correspondent aux valeurs de PDIV électriques, à condition que le seuil de détection approprié soit fixé pour les deux types de liquides diélectriques testés ici.

Ainsi, la détection optique à l'aide du PMT peut être considérée comme un indicateur de qualité raisonnable pour confirmer l'occurrence de l'activité de DP pour le système d'isolation composite également. La technique de détection électrique a un niveau de bruit de 0,3 pC jusqu'à 16 kV. Au-dessus de cette tension, elle montre quelques décharges générées par les connexions HT dans le montage. Alors que le PMT montre un niveau de bruit de moins de 0,2 pa.u. à toutes les tensions. Le PMT est sensé être immunisé contre le courant de déplacement généré par l'action de commutation rapide des commutateurs HV, par conséquent, il peut être une technique appropriée pour détecter les DP sous des formes d'onde non sinusoïdales complexes.

IV. Méthodologie de détection des décharges partielles sous forme d'onde de tension carrée

Cette section traite des étapes suivies pour générer une tension carrée et expérimenter les mesures de DP sous cette tension. Les mesures de DP ont été réalisées avec un tube photomultiplicateur, un shunt résistif et un transformateur de courant à haute fréquence (HFCT). Au début, les formes d'ondes de tension carrées ont été fournies par le générateur d'impulsions de Nanogen comme indiqué dans le tableau 2. Mais il s'est avéré fragile et n'a pas duré longtemps.

Parameters	Solution 1 (Nanogen)	Solution 2 (HV switch)	
	Micro	Fig. 1 Pump & reservoir Large Large	
Configuration	Half-bridge	Single switch	
HV switch reference	HTS 301-10-GSM (Behlke)	HTS 1401-10-LC2 (Behlke)	
Output voltage	30 kV	140 kV	
Output current	50 A (at 1 kHz and 1 % duty cycle)	100 A	
Remote control	Integrated inside the Nanogen	Developed in laboratory	
circuitry	(Plug and play)		
Pulse frequency	Up to 100 kHz	Up to 500 Hz	

Tableau 2: Caractéristiques du générateur d'impulsions (Nanogen) et de l'interrupteur HT

Après la défaillance de Nanogen, un montage avec un seul interrupteur HV a été réalisé dans le cadre de cette thèse. Pour cela, le schéma électrique correspondant a d'abord été étudié et les composants ont été choisis en fonction de leur disponibilité. Ensuite, le dimensionnement des composants a été validé par une simulation électrique. Après cela, le banc de test a été réalisé avec les composants disponibles comme le montre la figure 13.

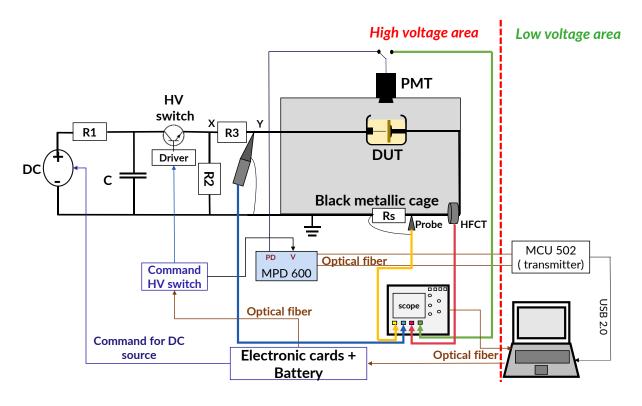


Figure 13: Schéma d'un banc d'essai HT pour générer une forme d'onde de tension carrée en utilisant un seul commutateur HTavec un tube photomultiplicateur (PMT), un transformateur de courant à haute fréquence (HFCT) et un shunt résistif (Rs) pour la détection des DP

Dans l'étape suivante, les formes d'onde générées par le banc d'essai ont été vérifiées. Les tensions de sortie ont été mesurées après l'interrupteur HT et aux bornes de l'objet sous test, en plaçant la sonde HT aux nœuds 'X' et 'Y' respectivement, comme indiqué dans les schémas (Figure 13). Le temps de montée au niveau de l'interrupteur HT a été mesuré à environ 28 ns alors qu'il était de 256 ns au niveau de l'objet sous test, comme le montre la figure 14.

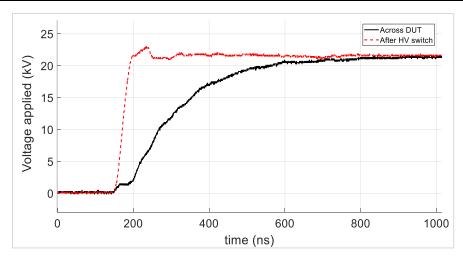


Figure 14: Front montant de la tension mesurée aux bornes de l'objet sous test et après le commutateur HV dans le montage

De plus, dans la Figure 14, une certaine distorsion de la forme d'onde après l'interrupteur HT peut être observée. Cela pourrait être dû à la résonance qui se produit entre de la capacité de la sonde et l'inductance du câble de terre sous des signaux transitoires rapides [106].

IV.1 Impact de la commutation rapide d'un interrupteur HT

Comme on peut le voir sur la Figure 15, à 20 kV, le PMT, le HFCT et la résistance shunt ont tous été affectés par les perturbations électromagnétiques pendant la commutation à grande vitesse de l'interrupteur HT. Le shunt résistif a été le plus affecté alors que le PMT s'est montré le plus robuste.

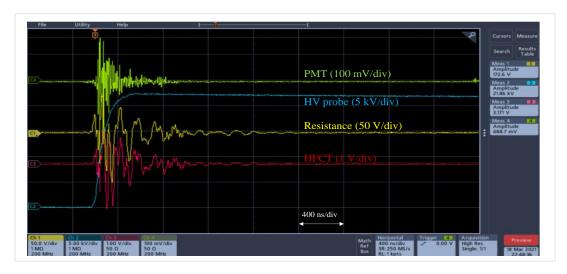


Figure 15: Impact de la commutation rapide de l'interrupteur HT sur toutes les techniques de détection à 20 kV

IV. 2 Essais de DP avec configuration pointe-barrière-plan dans l'air

Le renforcement de champ créé par la pointe dans l'air a été considéré pour les tests préliminaires de DP. Les paramètres ainsi utilisés lors de ces mesures sont résumés dans le tableau 3.

Tableau 3: Paramètres de la configuration pointe-barrière-plan dans l'air utilisée pour les essais préliminaires de
DP

Electrode configuration	Needle- FR4-plane
Needle tip radius	1 μm (new)
Barrier	FR4 sample (0.7 mm thick)
Plane diameter (grounded)	20 mm
Medium	Air
Gap (needle tip to barrier)	2 mm
Detection technique	PMT (DC supply at -1.3 kV), HFCT and resistive shunt
Voltage waveform	Unipolar square/50 Hz/ 10 % duty cycle

Pendant cette acquisition, un déclenchement non répétitif a été utilisé, c'est pourquoi la figure montre un seul événement de DP. D'après les observations ci-dessus, on peut conclure que le PMT a été affecté par une petite perturbation et a pu détecter les DP, juste après la montée de tension et à la tension maximale de la forme d'onde carrée (Figure 16).

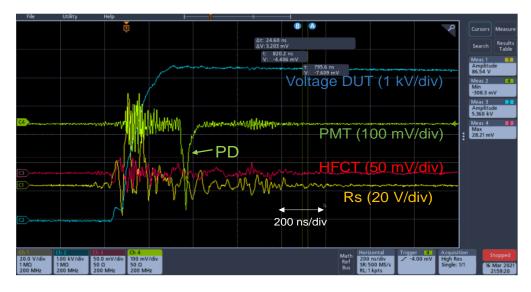


Figure 16: Image de l'acquisition des événements de DP à 5,4 kV à l'aide de PMT, HFCT et Rs près du front montant de la tension carrée pour la configuration pointe-barrière-plan dans l'air

Alors qu'avec le HFCT et le Rs, la détection des DP n'était possible que pendant le plateau de tension. Le courant de commutation dû au condensateur dans le circuit a largement influencé l'acquisition des DP avec le HFCT et le Rs, même juste après la montée de la tension (Figure 17).

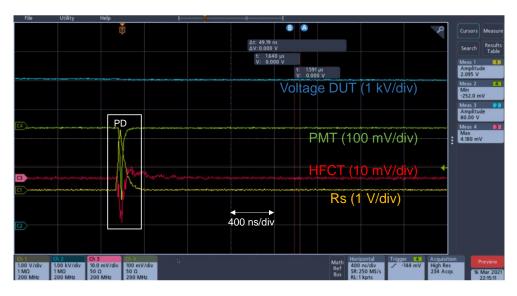


Figure 17: Image de l'acquisition des événements de DP pour la configuration plane aiguille-FR4 dans l'air à 5,4 kV à l'aide de PMT, HFCT et Rs au plateau de la tension maximale pour la configuration choisie

La génération d'un événement de DP a été confirmée comme indiqué dans la section suivante.

IV. 3 Essais de DP avec configuration pointe-barrière-plan dans un liquide diélectrique

Dans l'étape suivante, des mesures de DP ont été effectuées avec une configuration pointebarrière FR4-plan dans un liquide diélectrique. Pour ces tests, l'écart de 0,7 mm a été maintenu.

Comme dans le cas de l'air, les premières DP qui se produisent juste après le front montant de la tension n'ont pas été détectés par le HFCT et le shunt résistif, mais la PMT a été capable de les détecter. L'apparition des événements de DP a été confirmée en coupant l'alimentation en courant continu du PMT et en retirant l'aiguille de l'objet sous test tout en maintenant la tension appliquée au même niveau. Les formes d'onde ainsi sauvegardées de l'oscilloscope, ont été tracées ensemble comme le montre la Figure 18.

Sur la figure 18 on peut observer que les pics négatifs (PD1, PD2, PD3, PD4, PD5, PD6) ne sont visibles que lorsque l'alimentation en courant continu du PMT est à -2 kV avec l'aiguille dans l'objet sous test. Les pics négatifs détectés par le PMT se sont produits principalement juste après le front montant de la forme d'onde carrée. Dans les autres conditions, c'est-à-dire lorsque l'alimentation en courant continu du PMT était coupée et que l'aiguille était retirée de l'objet sous test, avec la même tension appliquée à l'objet sous test, aucun événement PD n'a été détecté.

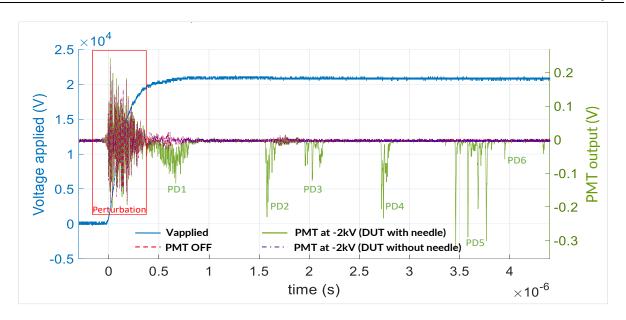


Figure 18: Vérification de l'acquisition des DP en maintenant l'alimentation en courant continu du PMT à -2 kV avec le DUT, en coupant la polarisation en courant continu du PMT avec le même DUT et en retirant l'aiguille du DUT à 20 kV

Les tests ont été poursuivis en connectant le PMT avec l'Omicron pour le même objet sous test.

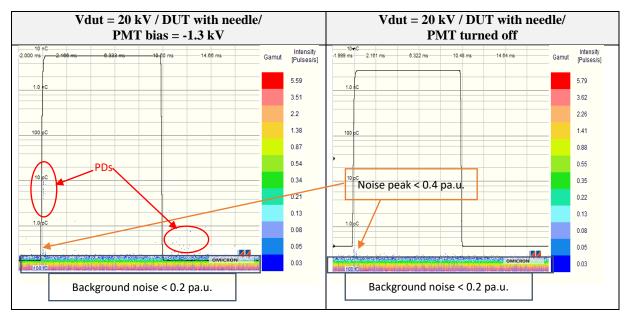


Figure 19: Acquisition d'événements de DP à 20 kV pour une configuration pointe-barrière FR4-plan dans un ester synthétique avec un PMT connecté à l'Omicron (à gauche) avec une tension d'alimentation du PMT à -1,3 kV et (à droite) avec une tension d'alimentation du PMT désactivée

Comme on peut l'observer sur la figure 19, les DP ont pu être détectés même à une tension d'alimentation continue de -1,3 kV pour le PMT. Le bruit de fond était inférieur à 0,2 pa.u. et le pic de bruit dû à la commutation était inférieur à 0,4 pa.u. à 20 kV. Le test était reproductible et

pendant de nombreux instants, les DP ont été détectés même autour de 17 kV pour le même objet sous tension continue du PMT à -1,3 kV.

D'après les résultats ci-dessus, on peut observer que l'acquisition des DP avec le système Omicron peut se faire à une tension inférieure au niveau de l'objet sous test en maintenant une valeur optimale d'alimentation en courant continu du PMT (c'est-à-dire -1,3 kV). En outre, la tension PDIV et le modèle PRPD ainsi obtenus en utilisant la PMT avec Omicron peuvent être directement comparés aux résultats obtenus en AC 50 Hz pour le même objet. Même si l'oscilloscope fournit des formes d'onde (pic négatif) des DP avec le PMT, la localisation des DP initiaux à la tension d'amorçage semble plus facile avec le système Omicron. De plus, l'Omicron peut enregistrer plusieurs périodes électriques qui peuvent être utilisées pour l'analyse même après avoir terminé les tests.

Parmi les techniques de détection, la détection optique semble avoir une meilleure résistance aux EMI et détecte les DP même juste après le temps de montée. Compte tenu des avantages susmentionnés de l'utilisation du système Omicron, il a été décidé de réaliser les études de PDIV avec une forme d'onde de tension carrée en reliant le PMT au système Omicron pour des tests ultérieurs.

V. Etude du phénomène de décharge partielle dans les tensions carrées unipolaires (TCU)

V.1 Comparaison PDIV entre AC et TCU

Le premier objectif ici était de faire la comparaison PDIV entre AC et TCU d'étudier le comportement de l'activité de DP sous forme d'onde carrée par rapport à la tension AC. Les liquides diélectriques étudiés étaient l'huile minérale (Nytro 4000X) et l'ester synthétique (Midel7131). Les mêmes procédures de filtration, de mesure de la tension de claquage et de mesure de la teneur en eau ont été appliquées pour le conditionnement et le contrôle des liquides diélectriques, comme indiqué dans l'annexe D.

Le tableau 4 présente la liste des barrières utilisées pour la comparaison des PDIV. Les essais ont été réalisés avec cinq spécimens DUT pour chaque combinaison d'isolation solide/liquide, sauf pour les barrières AlN où seuls trois spécimens DUT ont été testés, en fonction de leur disponibilité. D'après l'expérience acquise lors des essais préliminaires, il a été établi que dix mesures de DP peuvent être effectuées avec le même objet sous test. Par conséquent, pour vérifier la reproductibilité, dix mesures de DP ont été effectuées avec chaque spécimen de l'objet à tester, cinq sous forme de courant alternatif et cinq sous forme d'onde carrée. La forme d'onde

de tension carrée utilisée pendant cette étude a été maintenue à un rapport cyclique de 50 % avec une fréquence de commutation de 50 Hz pour la comparaison avec le courant alternatif de 50 Hz.

Tableau 4: Barrières solides utilisées pour la comparaison PDIV entre le courant alternatif et la forme d'onde	
carrée	

Barrier samples	Thickness (mm)	Sample size (mm × mm)	Samples tested with Nytro 4000X	Samples tested with MIDEL 7131
PVC	1	40 × 40	5	5
rvc	2	40 × 40	5	5
FR4	0.7	40 × 40	5	5
	1.3	40 × 40	5	5
AlN	0.63	40 × 40	3	3
	1	40 × 40	3	3
Impregnated	2	36 × 36	5	NA
Pressboard	3	40 × 40	5	NA

Les résultats de PDIV ainsi obtenus ont été comparés entre le CA et la forme d'onde carrée unipolaire (TCU) comme le montre la Figure 20.

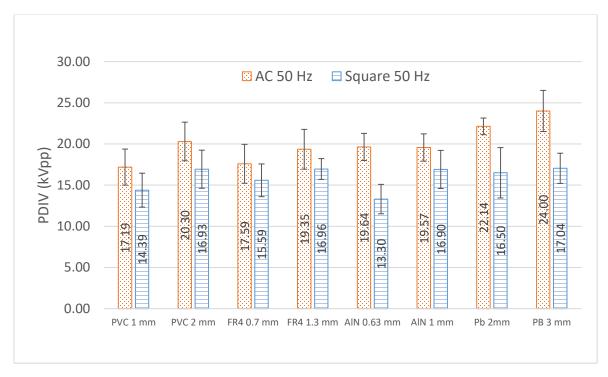
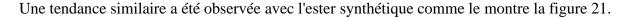


Figure 20: Comparaison de la PDIV entre le courant alternatif et la forme d'onde carrée unipolaire pour différentes combinaisons de systèmes d'isolation liquide/solide dans de l'huile minérale (Nytro4000X)

D'après le graphique de la Figure 20, le premier point que l'on peut remarquer est les faibles valeurs de PDIV avec TCU par rapport à l'AC. Cela s'est avéré vrai pour toutes les combinaisons d'isolation liquide/solide.



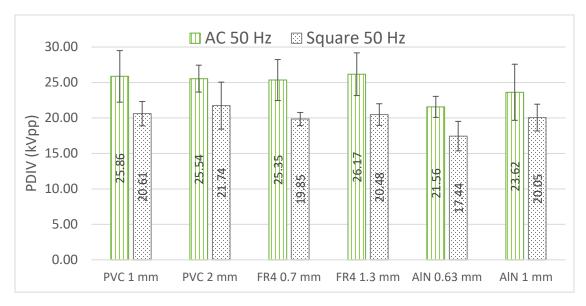


Figure 21: Comparaison PDIV entre le courant alternatif et la forme d'onde carrée unipolaire réalisée pour différentes combinaisons de systèmes d'isolation liquide/solide en ester synthétique (Midel713)

V.2. Comparaison PDIV entre deux liquides diélectriques en tension carrée unipolaire

Dans l'étape suivante, les PDIV obtenus à partir de deux liquides diélectriques sous TCU ont été comparés. Comme on peut l'observer sur la figure 22, le PDIV de l'huile minérale est faible par rapport à celui de l'ester synthétique pour la même barrière. Dans les esters, une magnitude plus élevée de PD (10 pC) est détectée par le PMT que dans l'huile minérale (2 pC). Cela aurait éventuellement élevé la PDIV de l'ester avec la détection optique.

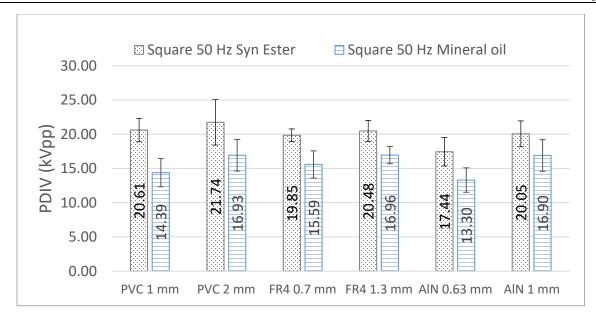


Figure 22: Comparaison PDIV entre l'ester synthétique et l'huile minérale avec une tension carrée unipolaire à 50 Hz de fréquence de commutation

V.3 Résultats des essais en faisant varier le temps de montée, la fréquence et le rapport cyclique

D'autres tests ont également été effectués en faisant varier la fréquence de commutation, le rapport cyclique et le temps de montée sur l'objet sous test. Un résumé des résultats a été fourni dans ce tableau.

Figure 8: Résumé des recherches effectuées avec une forme d'onde de tension carrée unipolaire

Parameter tested	DUT used	Statistical difference in PDIV (using t-test)
Switching frequency (at 50 Hz and 460 Hz)		No significant difference observed
Duty cycle (at 5 % and 50 %)	Needle-Pb-plane in mineral oil	Found lower at 5 % duty cycle
Same duration at voltage maximum (with 5 % at 50 Hz and 50 % at 460 Hz)		No significant difference observed
Rise time (160 ns, 256 ns and 560 ns)	Needle-AlN-plane in mineral oil	No significant difference observed

V.4 Conclusion et perspective

Pour toutes les combinaisons d'isolants liquides/solides, la PDIV obtenue sous TCU est inférieure à celle obtenue en AC. Avec la forme d'onde TCU, on a constaté que les DP se produisaient principalement juste après la montée de la tension à la PDIV.

L'ester synthétique a montré un PDIV plus élevé sous la forme d'onde USV. Dans les esters, une magnitude plus élevée de PD (10 pC) est détectée par le PMT que dans l'huile minérale (2 pC). Cela aurait éventuellement élevé la PDIV de l'ester avec la détection optique. Afin d'assurer l'utilisabilité de l'ester pour les applications d'électronique de puissance, des investigations supplémentaires telles que des tests de vieillissement et de rupture sous tension carrée répétitive seront nécessaires.

Aucune différence significative de PDIV n'est constatée entre 50 Hz et 460 Hz. Pour détecter un éventuel effet de la fréquence de commutation sur la PDIV, il faudrait donc adopter une gamme de fréquences plus élevée (comme 1 kHz ou plus). En revanche, on constate que le rapport cyclique entraîne une différence significative de PDIV. Un résultat intéressant est trouvé pour les USV avec la même durée d'impulsion mais des fréquences différentes (5 % de service à 50 Hz et 50 % de service à 460 Hz) : les deux conditions donnent le même PDIV.

En changeant la résistance en série avec l'objet sous test, on obtient des temps de montée différents d'environ 160 ns, 256 ns et 560 ns. Si l'on considère les PDIV moyennes obtenues aux trois temps de montée, l'objet sous test a subi des dV/dt d'environ 110 kV/µs, 73 kV/µs et 34 kV/µs respectivement. Encore une fois, aucune différence significative n'est observée dans les PDIVs pour les dV/dt testés.

Les résultats obtenus ici ont fourni des indications significatives sur le comportement de la DP dans un système d'isolation composite sous dV/dt entre 10 et 100 kV/µs. Ils considèrent l'impact de facteurs tels que le temps de montée, la fréquence de commutation et le rapport cyclique pour l'objet sous test sélectionné. Ainsi, il s'agit d'un pas vers une meilleure compréhension du processus de dégradation dû aux DP dans des applications d'électronique de puissance, qui pourrait être utile aux concepteurs d'isolation.

A partir de là, plusieurs perspectives peuvent être envisagées. Tout d'abord, il faut tirer parti du banc d'essai de tension carrée unipolaire existant. Il peut être utilisé pour améliorer les connaissances sur le mécanisme de décharge dans différents liquides diélectriques sous des tensions carrées répétitives. La ségrégation des paramètres de DP pendant le front montant, la tension maximale et le front descendant pourrait donner un meilleur aperçu du mécanisme de DP pour les objets testés.

D'autres améliorations seraient nécessaires pour surmonter le problème des interférences électromagnétiques qui ont un impact sur la détection optique. Cela peut ensuite être utilisé pour valider des techniques de détection électrique avancées telles que le HFCT avec des techniques de traitement numérique efficaces. Ceci est nécessaire pour permettre des mesures de DP pour les systèmes d'isolation opaques et pour des mesures en ligne pour des équipements comme le MFT.

Si l'on considère la configuration en pont complet des convertisseurs de puissance, l'isolation du TMF sera exposée à une forme d'onde de tension bipolaire carrée. Les mesures de DP sous bipolaire carrée pour le même objet sous test permettraient d'avoir une analyse comparative entre TCU et bipolaire carrée. De même, une comparaison directe avec le courant alternatif 50 Hz à la même fréquence sera possible avec la tension bipolaire carrée.

Table of Contents

List of fig	gures	vi
List of tab	oles	XV
1 Doolse	and and and antique	1
_	ground and context	
	VDC transmission	
1.1.1.	Electrical stress on HVDC converter transformer	
1.1.2.	Need for alternative solution	
	VDC transmission	
1.2.1.	Electrical stress on medium frequency transformer	
	onitoring methods of the insulation systems	
	otivation and objective	
1.5. Ou	utline of thesis	21
23 2.1. Pa	artial discharge	23
2.1. Pa 2.1.1.	rtial dischargeQuantities derived from PD activity	
2.1.1.	PD activity in dielectric liquids	
2.1.2.	PD activity in oil/pressboard	
	actors impacting PDs under repetitive square voltages	
2.2. Ta	Voltage amplitude	
2.2.2.	Rise time	
2.2.3.	Effect of frequency	
2.2.4.	Duty cycle	
2.2.5.	Summary	
2.3. Me	easurement techniques under square waveform	
2.3.1.	Optical detection	35
2.3.2.	High frequency current transformer (HFCT)	
2.3.3.	Antenna	38
2.3.4.	Other PD detection techniques	38
235	Summary	42

2.4.	Simulation approach for PD detection	43
2.4.1	. ABC model	43
2.4.2	. ABCD model	45
2.4.3	. Modeling of HFCT	47
2.4.4	. Circuit for generating square waveform	51
2.5.	Assessment of electrical methods of PD detection	52
2.5.1	. HFCT	52
2.5.2	Other methods of PD detection	56
2.5.3	. Discussion on electrical detection of PDs	62
2.6.	Statistical analysis of measurement results	62
2.6.1	. Steps to perform t-test	63
2.6.2	. Types of t-test	63
2.7.	Summary	65
3. Dev	ice under test for partial discharge detection	67
3.1.	DUT design methodology	68
3.1.1		
3.1.2	. Selection of DUT configuration	69
3.1.3	. Analysis of DUT with finite element method (FEM)	70
3.2.	Additional investigation with selected DUT configuration	
3.2.1	. Selection of barrier dimension	75
3.2.2	. Impact of tip radius	76
3.2.3	. Impact of permittivity of barriers	78
3.2.4	. Impact of barrier thickness	81
3.2.5	. Impact of varying gap between tip and barrier	81
3.2.6	. Observations from FEM analysis	82
3.3.	DUT for PD measurements	83
3.4.	DUT preparation	85
3.5.	Summary	88
4. Part	ial discharge measurements in AC 50 Hz	90
	Experimental set-up for PD detection under AC 50 Hz	
	Determination of background noise	
	Corona discharge in air	
	Partial discharge in dielectric liquid	
	PD test with needle-barrier plane configuration	

4.5.1.	Correlation between electrical and optical measurements	97
4.5.2.	PRPD patterns	
4.5.3.	Comparison of PDIV and PRPD patterns in two dielectric liquids	105
4.5.4.	Impact of varying tip radius	110
4.5.5.	Impact of gap variation	111
4.6. Su	mmary	113
5. Metho	odology for partial discharge detection under square voltage way	eform
5.1. Sc	hematics for generating square waveform	117
5.1.1.	Proposed schematics of the test bench	117
5.1.2.	Component selection	118
5.1.3.	Simulation and validation of proposed schematic	118
5.2. De	evelopment of square waveform test bench	121
5.2.1.	Components of high voltage circuit	121
5.2.2.	EMI management in design phase of test bench	124
5.2.3.	Output waveforms from test bench	124
5.3. Pro	eliminary tests with unipolar square waveform	126
5.3.1.	Impact due to fast switching action of HV switch	127
5.3.2.	Varying rise times	128
5.3.3.	Synchronization between control signal and voltage output	130
5.3.4.	PD tests with needle-barrier plane configuration in air	132
5.3.5.	PD tests with needle-barrier plane configuration in dielectric liquid	135
5.3.6.	Conclusions from preliminary tests	142
5.4. Su	mmary	143
6. Study	of partial discharges in unipolar square voltages	144
•	ocedure of PD comparison between AC and unipolar square voltages (USV)	
6.1.1.	Test method for PDIV comparison	
6.1.2.	Device under test for PDIV comparison	
6.1.3.	Results and discussion	
6.1.4.	Outcomes from consistency tests	
	O comparison between AC and unipolar square waveform	
6.2.1.	Estimation of charge magnitude from optical detection	
6.2.2.	PD comparison between AC and USV waveforms	
6.2.3.	PD comparison between dielectric liquids under USV	

6.2.4.	Influence of barrier thickness, permittivity and tip radius on PDIV in USV	160
6.2.5.	Summary of PD comparison	164
6.3. Asset	ssment of PD under varying parameters of USV	165
6.3.1.	Impact of switching frequency	166
6.3.2.	Impact of duty cycle	168
6.3.3.	Same pulse duration	170
6.3.4.	Impact of rise time	173
	ral discussion	
6.5. Conc	·lusion	177
	sion and perspective	
References.		182
Appendix A	a: Partial discharge model under AC 50 Hz and square waveform.	194
Appendix B	: Modeling of DUT in FEMM	196
Appendix C	: Tip radius under microscope	197
Appendix D	2: Conditioning and monitoring of dielectric liquid	199
Appendix E	: Components of HV test set-up and EMC management	204
Appendix F	: Behavior of photomultiplier tube	208
Appendix G	S: S-parameters used for modeling of HFCT	211
Abbreviatio	ns	216
Units and sy	ymbols	217

List of figures

Figure 1-1: Cost comparison between HVAC and HVDC for long transmission line
Figure 1-2: Basic Schematics of a monopolar HVDC transmission
Figure 1-3: Connection of 3-phase transformer with 12 pulse bridge converters in an HVDC transmission
Figure 1-4: Voltage waveform across the line side and valve side winding of HVDC transformer5
Figure 1-5: Voltage application in an HVDC transmission link during (1) turn on, (2) steady state, (3 during voltage polarity reversal and (4) steady state after polarity reversal (source: [19])
Figure 1-6: Comparison of resistivity of oil and paper as function of temperature. Note: Different oil and pressboard/paper can show different characteristics (source: [14])
Figure 1-7: Electric field distribution on the insulation system of a converter transformer at 500 kV AC (peak), at 500 kV DC during steady state and during DC polarity (from +500 kV to -500 kV) ([21])
Figure 1-8: Example of interconnection of renewable source of energy (wind and solar farms), AC load electric vehicle (EV) infrastructure, energy storage systems (ESS) and HVDC link to MVDC line
Figure 1-9: Radial collection configuration at windfarm and its connection to offshore AC substation (source :[35])
Figure 1-10: A proposed scheme for offshore wind power plant with step-up DC/DC for each wind turbine feeder which then connects to another DC/DC converter at offshore platforms (image source:[35])
Figure 1-11: Schematics of a dual active bridge (DAB) converter implementing medium frequency transformer (MFT)
Figure 1-12: Fast rising front of output voltage waveform across a 30 pF capacitive load using a model of a commercially available high voltage SiC-Mosfet switch (G2R1000MT33J from GeneSiC)
Figure 1-13: Serialization of DAB converters in isolated DC-DC topology to attain high voltage outpu (Vout)
Figure 1-14: Simulation result of voltage stress across secondary winding of transformer with respect to ground at each stage of in DC-DC topology (see Figure 1-13) in steady state
Figure 1-15: Partial discharges in dielectric liquid [53]
Figure 1-16: (a) PD measurement circuit as per IEC60270 (b) PD current and voltage measured across DUT
Figure 1-17: (Left) Square voltage waveform fed to PD measurement circuit as per IEC60270; (right) 1 kV square voltage with rise time of 3 µs and displacement current obtained across DUT; a 50 pC PD generated during rise time is not visually identified.

Figure 1-18: FFT spectrum of displacement current without PD (black), displacement current overlapped with PD of 250 pC (red) and PD of 250 pC generated at voltage plateau (blue) for a 20 kV square voltage waveform with rise time of 250 ns across a DUT of 30 pF
Figure 2-1: Representation of breakdown triggered by a partial discharge before the expected lifetime due to continuous degradation of insulation medium under voltage stress
Figure 2-2: Increasing average velocity of positive streamers from 2 km/s to 100 km/s in mineral oil with increasing voltage across the needle for an inter electrode gap of 10 mm [image source: [69]]
Figure 2-3: Model of positive discharge growth with a positive extended filament tip (image source:[72])
Figure 2-4: PRPD patterns of mineral oil (left) and synthetic ester (right) at 25 kV in needle-plane configuration [image source: [67]]
Figure 2-5: (Left) Orientation of needle along the pressboard to study surface discharges [74] and (right) needle perpendicular to pressboard to study complete breakdown of insulation system [75]
Figure 2-6: PRPD pattern of needle-plane with pressboard in mineral oil at 25 kV [75]
Figure 2-7: Space charge distribution under needle-plane electrode configuration (image: [77])29
Figure 2-8: PDs measured for needle in air under increasing square voltage level with same rise time [54]
Figure 2-9: Effect of fast rising impulse voltage on PDIV (adapted from [78])
Figure 2-10: (a) PD magnitude as function of rise time and (b) PDIV as function of rise time for crossed pair of wires [58]
Figure 2-11: PDIV as a function of rise time for Kraft paper impregnated in mineral oil (Shell Diala B) [50]
Figure 2-12: PDIV with increasing frequency of sinusoidal waveform [80]
Figure 2-13: PDIV as a function of frequency for Kraft paper impregnated in mineral oil (Shell Diala B) [43]
Figure 2-14: (a) PD magnitude as a function of voltage duration in crossed pair of cables during (a) rising flank and (b) falling flank of square voltage [114]
Figure 2-15: Circuits with optical detection of PDs under square voltage (left) using photomultiplier tubes in a test cell containing dielectric liquid and; (right) optically obtained PD using PM tubes ([62])
Figure 2-16: Representation of an HFCT with a single turn primary with current Ip and multi-turn secondary across a resistive load and its equivalent circuit ([86])
Figure 2-17: PDs detected only during fall time under impulse voltage using HFCT for cable joints [57]37

Figure 2-18: (Left) Representation of set-up for PD detection using SiPM and HFCT sensor for metal-air insulation defect model; (right) successful detection of PDs by SiPM and HFCT under unipolar square voltage at $8.2~kV$, $2~kHz$ with $5~\mu s$ as rise time [55]
Figure 2-19: (Left) Detection of one PD pulse by antenna for a rise time of 16 µs; (Right) the antenna output impacted by switching current for a rise time of 200 ns [58]
Figure 2-20: (Left) Signal traces measured by antenna at 2.8 kV which was higher than PDIV, shows overlapping of commutation noise and PDs; (right) signal traces processed with standard deviation provided evidence of PDs (source:[55])
Figure 2-21: PD decoupling device proposed in [60]which can suppress high frequency component of up to 20 MHz in measured signal and the values assigned to the components of PD decoupling device 40
Figure 2-22: (a) Signal treated with moving average and a latest PD trace; (b) PDs recovered after subtraction of moving average waveform from latest PD trace ([60])
Figure 2-23: (Left) Measuring set up to detect partial discharges using balanced bridge circuit; (right) Square wave voltage and output of differential amplifier without PD events ([89])
Figure 2-24: PD pulses obtained using balanced bridge circuit under square waveform at 5 kV (source: [89])
Figure 2-25: (a) Illustration of a cavity inside an insulation medium and (b) its representation as three capacitor model
Figure 2-26: Equivalent circuit of partial discharge mechanism using three capacitor model
Figure 2-27: (Left) Circuit of ABCD model and values assigned to its components; (right) IDP of 10 pC generated in ABCD model using gaussian function
Figure 2-28: Comparison of switching current flowing through the DUT (IDUT) with and without PD using ABCD model; dV/dt across DUT $\approx 2~kV/\mu s$
Figure 2-29: Block diagram of the set-up for measuring S-parameters of the HFCT probe
Figure 2-30: Magnitude and phase of S-parameters as a function of frequency
Figure 2-31: Magnitude and phase of Z-parameters as a function of frequency
Figure 2-32: Comparison of estimated transfer functions of different orders
Figure 2-33: Set up for performance evaluation of the Simulink model with the HFCT50
Figure 2-34: Comparison of HFCT model and real HFCT response for two pulses from calibrator51
Figure 2-35: Schematics for PD detection under square waveform with ABCD model
Figure 2-36: HFCT signals with a PD of 10 pC and without PD during voltage rise time53
Figure 2-37: PD signal recovered using standard deviation

Figure 2-38: Standard deviation of two HFCT traces at two different switching instant without PD54
Figure 2-39: Traces of HFCT signal without PDs, recorded during rise time at 1 kV and 990 V keeping all other parameters constant
Figure 2-40: Standard deviation of two HFCT traces (without PD) obtained at two different voltage level
Figure 2-41: Circuit simulated in Simscape with PD decoupler circuit
Figure 2-42: Signal traces with PD (Vpd) and without PD (Vnpd) recorded using PD decoupler circuit .57
Figure 2-43: PD signal recovered by subtracting the previous signal trace (Vnpd) from the current trace (Vpd)
Figure 2-44: Signal recovered when Vnpd101 (signal without PD at 101 ns) is deducted from Vnpd100 (signal without PD at 100 ns)
Figure 2-45: Signal recovered when Vnpd101 (signal without PD generated at instant 101 ns)is deducted from Vpd (signal with 10 pC PD generated at 100 ns)
Figure 2-46: Signal traces (without PD) obtained at two different voltage level
Figure 2-47: Signal traces (without PD) obtained at two different voltage level and recovered signal after deduction
Figure 2-48: Balanced bridge circuit used in simulation
Figure 2-49: Voltage measured across Rsh1 and Rsh2 during switching in balanced bridge circuit 60
Figure 2-50: PD signal recovered using balanced bridge technique by cancellation of voltages across Rsh1 and Rsh2 due to commutation
Figure 2-51: Output voltage waveform (Vo) obtained after subtraction of voltages across Rsh1 and Rsh2 when Rsh1 was changed to $1.05~\Omega$, considering 5 % tolerance in resistor value
Figure 3-1: DUT models with pressboard in oil in plane-plane configuration from [14] and [18] used for investigating insulation performance under HVDC
Figure 3-2: Design of axis-symmetric model of selected needle-barrier plane DUT (note: not to scale) 70
Figure 3-3: Representation of axis-symmetric model of needle-plane DUT adapted from study [67](not to scale)
Figure 3-4: (Left) 3 µm tip built in FEMM from study [67] produced a tip field of 1724 kV/mm at 20 kV; (right) 1 µm tip built in FEMM for selected DUT configuration produced a tip field of 2476 kV/mm at 10 kV
Figure 3-5: Comparison of electric fields at needle tip between selected DUT with 1 µm tip radius at 10 kV and the DUT from study [67] with tip radius of 3 µm at 20 kV73

Figure 3-6: Full view of the DUT configuration with electric field and meshing around the tip in FEMM with a magnified view of needle tip
Figure 3-7: Tangential electric field along the barrier surface for different lengths of barrier76
Figure 3-8: Impact of tip radius on the electrical field near the tip
Figure 3-9: Impact of tip radius on the electrical field at the liquid/solid interface
Figure 3-10: Electric field as a function of distance from needle tip, with a magnified view near the tip for barriers of different permittivity in mineral oil (MO) and synthetic ester (SE)
Figure 3-11:Electric field at the interface of liquid/solid insulation, for barriers of different permittivity in mineral oil (MO) and synthetic ester (SE) as dielectric medium
Figure 3-12: (left) Device under test with needle-barrier plane configuration completely immersed in mineral oil used for all partial discharge measurements (right) magnified view of the small gap between needle tip and barrier
Figure 3-13: Dielectric liquid in Baur cell with sphere-sphere electrodes maintained at 2.5 mm gap 86
Figure 3-14: Average and standard deviation of breakdown tests of treated mineral oil (Nytro 4000X) fo ten different batches
Figure 3-15: Average and standard deviation of breakdown tests of treated synthetic ester (Midel 7131 for ten different batches
Figure 4-1: Schematics of PD test bench in AC 50 Hz
Figure 4-2: Background noise check for electrical measurement with DUT filled with oil and pressboard without needle
Figure 4-3: Background noise estimation with the gain of PMT set at DC bias of -1.3 kV using a DUT without needle
Figure 4-4: PRPD pattern for corona discharge in air using needle-plane electrode configuration for 10 mm gap in AC 50 Hz from (left) electrical detection and (right) optical detection
Figure 4-5: Correlation in PD detection using electrical, optical and HFCT at 1.5 kV (rms) for DUT with needle-plane in air. Horizontal scale: 100 ns/div (1 µs total)94
Figure 4-6: Needle-plane configuration in dielectric liquid used for PD tests
Figure 4-7: PRPD pattern for PDs in mineral oil using needle-plane electrode configuration for 10 mm gap in AC 50 Hz from (left) electrical detection and (right) optical detection
Figure 4-8: Correlation in PD detection using electrical, optical and HFCT at 11 kV (rms) for DUT with needle-plane in mineral oil. Horizontal scale: 100 ns/div (1 µs total)95
Figure 4-9: Voltage application profile across DUT for PD test in AC 50 Hz97

Figure 4-10: PRPD pattern of 2 mm thick pressboard in Nytro 4000X taken at same instant from electrical (top) and optical (bottom) detection at 12 kV (higher than PDIV)
Figure 4-11: Comparison of number of PDs for pressboard in Nytro 4000X from both electrical and optical measurements by increasing the voltage in steps above PDIV
Figure 4-12: Correlation in PD detection among electrical measurement, optical measurement and HFCT at 9 kV (rms) for DUT with pressboard in mineral oil: horizontal time scale at 100 ns/div; total 1 μ s99
Figure 4-13: Correlation in PD events for 2 mm thick pressboard barrier in mineral oil at 10 kVrms. (top) PDs observed with threshold set at 2 pC with electrical measurement and (bottom) PDs observed with threshold at 0.25 pa.u. with optical detection
Figure 4-14: Correlation between PDIV observed from electrical with threshold of 2 pC and optical detection in mineral oil (Nytro 4000X) for different barriers
Figure 4-15: Correlation between PDIV observed from electrical with threshold of 10 pC and optical detection in MIDEL7131 for different barriers
Figure 4-16: Correlation in PD events occurring for 1 mm thick AlN barrier in synthetic ester. (top) PDs acquired electrically with threshold set at 10 pC and (bottom) PDs obtained optically with threshold set at 0.25 pa.u. at 10 kVrms
Figure 4-17: PRPD pattern of 1 mm thick PVC in synthetic ester at PDIV from electrical detection 103
Figure 4-18: Evolution of PRPD pattern with increasing voltage above PDIV for pressboard (1 mm thick) in Nytro 4000X (mineral oil) in needle-barrier plane configuration for same DUT specimen
Figure 4-19: (a) PRPD pattern of AlN (0.63 mm thick) in mineral oil (Nytro 4000X) and synthetic ester (Midel 7131) at 10 kV from electrical detection
Figure 4-20: Comparison of PDIV values for different barriers in Nytro 4000X and MIDEL7131 from electrical detection with threshold at 0.5 pC
Figure 4-21: Electric field for different barriers in mineral oil and synthetic ester for corresponding average PDIV found experimentally, obtained from FE simulation
Figure 4-22: Comparison of PDIV values for different tip radius from electrical measurement
Figure 4-23: Tip fields obtained from FE simulation at average PDIVs for three tip radii tested
Figure 4-24: Comparison of PDIV values at different gaps from electrical measurement
Figure 4-25: Comparison of PDIF values at different gaps for corresponding average PDIVs113
Figure 5-1: (Top) Output voltage waveform from pulse generator across a DUT without needle and (bottom) magnified view of same waveform with a rise time of 71 ns
Figure 5-2: Simplified schematics proposed to generate square voltage waveform
Figure 5-3: Image of the circuit simulated in Simscape electrical for generation of unipolar square voltage waveform using HV switch from Behlke

Figure 5-4: Rising front of square voltage after high voltage switch (across 2 $M\Omega$ resistor) and across DUT of 30 pF from simulation
Figure 5-5:Output voltage across DUT at switching frequency of 500 Hz with R2 as 2 M Ω from simulations
Figure 5-6: Schematics of HV test bench to generate USV waveform using a single HV switch with photomultiplier tube (PMT), high frequency current transformer (HFCT) and resistive shunt (Rs) for PD detection
Figure 5-7: Photo of GUI software to communicate with DC source and HV switch with the help of PCBs placed inside the Faraday cage
Figure 5-8: Photograph of the square voltage test bench developed in Ampère laboratory, Ecully, France
Figure 5-9: Unipolar square voltage waveform (VR2) measured at 20 kV with a switching frequency of 50 Hz at a duty cycle of 10 %
Figure 5-10: Rising front of voltage measured across the DUT (V_DUT) and after HV switch (VR2)125
Figure 5-11: Voltage measured across DUT at 460 Hz at 20 kV using HV probe with scope
Figure 5-12: Impact of fast switching action of HV switch on all detection techniques at 20 kV
Figure 5-13: Disturbance peak due to fast switching action of HV switch observed with PMT when connected to Omicron system at 20 kV besides the background noise
Figure 5-14: Rising voltage across the same DUT comprising of needle-barrier plane with dielectric liquid, for R3 resistor values of 2.7, 5 and $10~\text{k}\Omega$
Figure 5-15: Rising front measured across DUT with R3 = 100Ω
Figure 5-16: Voltage across DUT obtained from simulation for $100~\Omega$ and $5~k\Omega$ resistors as R3 with series inductance and capacitance of $250~\mu H$ and $250~nF$ respectively for both cases
Figure 5-17: Synchronization between PWM signal (of 3 V) sent to driver control unit of HV switch and the output voltage waveform (of 13.2 kV) generated across the DUT
Figure 5-18: Transients observed with control signal being fed to driver unit during switching operation of HV switch
Figure 5-19: Rise time of about 200 µs observed for control signal on Omicron due to low bandwidth of MPD600 (timescale on top)
Figure 5-20: PD acquisition at 5.4 kV tried with PMT, HFCT and Rs near the rising front of square voltage for needle-FR4 plane configuration in air
Figure 5-21:Image of the acquisition of PD events for needle-FR4 plane configuration in air at 5.4 kV using PMT, HFCT and Rs at maximum voltage for the chosen configuration

Figure 5-22: Detection of PD events by using the PMT with Omicron system acquired after 30 seconds of recording at 4.4 kV
Figure 5-23: Image of the acquisition of PD events at 20 kV for needle-FR4 plane configuration in synthetic ester using PMT, HFCT and Rs during rising voltage across the DUT
Figure 5-24: Image of the acquisition of PD events at 20 kV for needle-FR4 plane configuration in synthetic ester using PMT, HFCT and Rs at maximum voltage across the DUT
Figure 5-25: Verification of the acquisition of PDs by keeping DC supply of PMT at -2 kV with DUT, turning off DC bias of PMT with same DUT and removing the needle from the DUT at 20 kV
Figure 5-26: Acquisition of PD events at 20 kV for needle-FR4 plane configuration in synthetic ester with PMT coupled to MPD600 from Omicron shows (a) noise band with -2 kV DC supply of PMT and (b) noise band suppressed by adjusting threshold to 5 pa.u. in Omicron for same DC supply of PMT139
Figure 5-27: Acquisition of PD events at 20 kV for needle-FR4 plane configuration in synthetic ester with PMT connected to Omicron (left) with DC supply voltage of PMT at -1.3 kV and (right) with supply voltage of PMT turned off
Figure 5-28: PD detection with PMT at 23 kV (a) with supply voltage of PMT at -1.5 kV and (b) PMT turned off
Figure 6-1: Voltage profile chosen for PDIV comparison between square and AC voltages146
Figure 6-2: PDIV results for DUT n°1 under USV and AC at 50 Hz
Figure 6-3: PDIV results for DUT n°2 under square waveform and AC 50 Hz
Figure 6-4: (Left) A new 1 µm needle tip and (right) tip after 10 PDIV tests viewed under microscope 149
Figure 6-5: Average PDIV (in peak to peak) for different barriers tested in mineral oil; using electrical detection only in AC and optical detection in both AC and USV; the threshold set in electrical detection is 2 pC while for optical detection is 0.5pa.u
Figure 6-6: Average PDIV (in peak to peak) for different barriers tested in synthetic ester; using electrical detection only in AC and optical detection in both AC and USV; the threshold set in electrical detection is 10 pC while for optical detection is 0.5pa.u
Figure 6-7: Optically acquired PRPD pattern in AC and USV for 2 mm thick pressboard in mineral oil at inception voltage; after a recording time of 30 seconds
Figure 6-8: Comparison of number of PDs (NPDs) for needle-pressboard plane in mineral oil under AC and USV
Figure 6-9: Comparison of average charge magnitude (Qavg) for needle-pressboard plane in mineral oil under AC and USV
Figure 6-10: PDIV comparison between synthetic ester and mineral oil in unipolar square voltage at 50 Hz and 50 % duty cycle

Figure 6-11: Optically acquired PRPD pattern obtained at PDIV (20 kV) for 1 mm thick AlN barrier in mineral oil and synthetic ester
Figure 6-12: Comparison of number of PDs (NPDs) between mineral oil (MO) and synthetic ester (SE) for needle-AlN plane under USV
Figure 6-13: Comparison of average charge magnitude (Qavg) between mineral oil (MO) and synthetic ester (SE) for needle-AlN plane under USV
Figure 6-14: Electric field obtained in FEM at experimentally obtained PDIV values for AlN barriers of different thicknesses in USV
Figure 6-15: Comparison of PDIVs obtained for varying tip radius under USV and AC waveform 164
Figure 6-16: PDIV comparison performed with needle-pressboard plane configuration in mineral oil with varying switching frequency
Figure 6-17: Number of PDs (NPDs) at 50 Hz and 460 Hz for needle-pressboard plane configuration in mineral oil under USV
Figure 6-18: Average PD magnitude (Qavg) at 50 Hz and 460 Hz for needle-pressboard plane configuration in mineral oil under USV
Figure 6-19: PDIV measurements at 5 % and 50 % as duty cycles with 50 Hz as switching frequency 168
Figure 6-20: Number of PDs (NPDs) measured at 5 % and 50 % as duty cycles with 50 Hz as switching frequency
Figure 6-21: Average PD magnitude (Qavg) measured at 5 % and 50 % as duty cycles with 50 Hz as switching frequency
Figure 6-22: PRPD patterns taken at PDIV with 5% (top) and 50 % (bottom) duty cycles at 50 Hz for needle-pressboard plane in mineral oil after 30 s
Figure 6-23: PDIV measurements for same voltage duration at maximum voltage plateau for different switching frequencies and duty cycles
Figure 6-24: Number of PDs measured with same voltage duration at maximum voltage plateau for different switching frequency and duty cycle
Figure 6-25: Average PD magnitude with same voltage duration at maximum voltage plateau for different switching frequency and duty cycle
Figure 6-26: PRPD pattern taken at PDIV after 30 s, with 50 % duty cycle at 460 Hz for needle-pressboard plane in mineral oil
Figure 6-27: PDIV measurements at different rise time across the DUT
Figure 6-28: Number of PDs measured at different rise time across the DUT
Figure 6-29: Average PD magnitude measured at different rise time across the DUT

List of tables

Table 1-1: Some key properties of mineral oil (Nytro 4000X), synthetic ester (Midel 7131) and natural ester (FR3) taken from [27]–[29]
Table 2-1: Values assigned to different parameters in the schematics with single HV switch
Table 3-1: Permittivity of the chosen barrier materials
Table 3-2: Values used for constructing axis symmetric models of a DUT from study and selected mode of DUT in FEMM
Table 3-3: Calculation of ratio of permittivity in barrier and oil and comparison with ratios of electric fields obtained from simulations in oil and barrier at the interface
Table 3-4: Electric fields at the tip (Etip) obtained from simulations for varying thickness of barrier; and the approximate percentage decrease in tip field with respect to increase in barrier thickness
Table 3-5: Electric fields at the tip (Etip) obtained from simulations by varying gap spacing
Table 3-6: Specification of tested solid barriers
Table 3-7: Measured water content of dielectric liquids for different batches
Table 4-1: Analysis of difference in average value of PDIVs between mineral oil and synthetic ester in AC 50 Hz using t-test
Table 4-2: Analysis of difference in average value of PDIVs between barrier thickness in AC 50 Hz using t-test
Table 4-3: Analysis of difference in average value of PDIVs for changing permittivity of barriers in AC 50 Hz using t-test
Table 5-1: Characteristics of pulse generator (Nanogen) and HV single switch
Table 5-2: Values assigned to different parameters for unipolar square waveform circuit
Table 5-3: Time constant of RC present in schematics of test bench of partial discharge
Table 5-4: Input impedance chosen in the oscilloscope while connecting the different detection techniques
Table 5-5: R3 values and corresponding measured rise times across the DUT
Table 5-6: Parameters of the needle-barrier plane configuration in air used for preliminary PD tests 133
Table 5-7: Parameters of the needle-barrier plane configuration in synthetic ester used for preliminary PD tests

Table 5-8: Comparison of voltage across DUT and supply voltage of PMT used for PD investigation using oscilloscope and Omicron system
Table 6-1: Parameters of the DUT used for PDIV consistency checks between AC and USV146
Table 6-2: Solid barriers used for PDIV comparison between AC and USV waveform
Table 6-3: Estimation of difference in average value of PDIVs between AC and USV for mineral oil using T-test
Table 6-4: Estimation of difference in average value of PDIVs between AC and USV for synthetic ester using T-test
Table 6-5: Decrease in PDIV observed in unipolar square waveform for different barriers tested 154
Table 6-6: Estimation of difference in average value of PDIVs between mineral oil and synthetic ester in USV using T-test
Table 6-7: Estimation of difference in average value of optically obtained PDIVs between mineral oil and synthetic ester in AC using T-test
Table 6-8: Estimation of difference in average value of PDIVs for changing barrier thickness in mineral oil under USV using T-test
Table 6-9: Estimation of difference in average value of PDIVs for changing barrier thickness in synthetic ester under USV using T-test
Table 6-10: Comparison of tip field obtained at PDIV and PDIV for increasing thickness of AlN barrier in mineral oil and synthetic ester under USV
Table 6-11: Estimation of difference in average value of PDIVs for different barrier permittivities in both mineral oil and synthetic ester under USV waveform using T-test
Table 6-12: Parameters of the DUT used for PD tests with varying switching frequencies and duty cycle
Table 6-13: Estimation of difference in average value of PDIVs for varying frequencies under USV waveform using T-test
Table 6-14: Estimation of difference in average value of PDIVs at 5 % and 50 % as duty cycles with 50 Hz as switching frequency using T-test
Table 6-15: Estimation of difference in average value of PDIVs for almost same voltage duration at maximum voltage plateau with different switching frequencies and duty cycles using T-test171
Table 6-16: Parameters of the DUT specimen used and USV waveform for investigating varying rise times
Table 6-17: Estimation of difference in PDIVs for varying rise times across DUT using T-test

1. Background and context

The alternating current (AC) gained dominance in the electricity generation, transmission and distribution in early 20th century, mainly due to its ability to transform the voltage level using electric transformers. Since then, large networks with high voltage AC (HVAC) systems have been deployed all around the world to transport electricity. But over the time, new challenges have emerged out of long transmission lines in HVAC due to voltage regulations caused by reactive power flow, transmission losses and stability.

To overcome the problem of bulk power transmission over long distances, high voltage direct current (HVDC) systems are being looked upon as an alternative solution. In HVDC system, capital cost of DC station is higher than AC, but transmission line cost predominates in AC system. For a case study considered in [1], it has been found that for same transmission capacity over long distances (over 500 km), the HVDC is more economical than HVAC after break-even point as shown in Figure 1-1. The break-even point can range from 500-800 km for overhead lines depending upon factors like terrain, cost of labour and environmental regulations [1], [2].

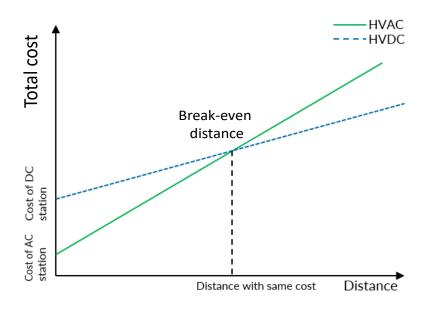


Figure 1-1: Cost comparison between HVAC and HVDC for long transmission line

Moreover, the easier controllability of active power, interconnection between non-synchronized isolated systems and limited environmental impacts such as reduced corona effects, limited electric field hazards, make direct current (DC) system more practical and efficient [1].

As reported in [3], the gross electricity production in the world has increased from 6928 TWh to 26730 TWh between 1974 and 2018 with an average yearly growth rate of 3.3 %. Because of environmental concerns, it has been decided by many European countries to incorporate more renewable sources of energy such as wind and solar farms into existing grids [4]. In order to facilitate the energy transition away from fossil fuels and increase the efficiency of the power system for future smart grids, power electronics is playing an important role [5]. The fundamental component of power electronics is the switching device (or valve). Many of them are assembled together in specific configurations to convert AC to DC and vice versa [2]. Over the years the power electronics devices have undergone technological advancements from mercury arc valves used earlier to recently introduced wide band gap (WBG) devices. These advanced WBG devices like Silicon Carbide (SiC) offer high blocking voltage, very high switching frequency, high operating temperature and show fast switching speeds with reduced commutation losses [5][6] as compared to their earlier counterparts.

The growing interest in DC systems and availability of new power electronics devices have led to the introduction of novel power conversion techniques to integrate loads, traction and renewables. These power converters are expected to mainly operate in medium voltage (MV) range (tens of kV) in medium frequencies (MF), which may range up to few hundreds of kHz, thanks to the fast-switching WBG devices.

The medium frequency transformers (MFT) will form the core of such power conversion topology, for providing galvanic isolation with improved efficiency [7]. On one hand, these new power conversion techniques will offer high power density, along with weight and volume reduction of transformer. But on the other hand, the fast, repetitive square voltage waveforms experienced by the MFT may have an adverse effect on its insulation reliability. This makes it important to evaluate the reliability of the insulation system of MFTs under repetitive fast rising voltage waveforms [6][7][8].

In the context of reliability study, the insulation system of transformers in existing HVDC scheme and upcoming MV/MF scheme have been chosen as application cases. Hence, this chapter discusses the complex voltage waveforms across the valve-side winding of a transformer in a classical HVDC link and its impact on insulation performance. Then, due to the advent of new converter topologies, the multi-level complex voltage waveforms experienced by MFTs are discussed. After this, the constraints associated with partial discharge measurements under fast rising square waveform is reviewed. The objectives of this thesis have been addressed towards the end of this chapter, which has been derived from the context discussed hereafter.

1.1. HVDC transmission

The first HVDC scheme was commercialized in the year 1954 between the island of Gotland and the Swedish mainland, without mechanical conversion. Even before this, there were several DC transmission projects in Europe, many of which were based on motor-generator system designed by Swiss pioneer Réne Thury. One of the most notable schemes was Lyon-Moutier transmission line which rated 20 MW, 125 kV and connected hydroelectric plant more than 200 km away from Lyon. It operated for 30 years before being dismantled in 1936 due to high maintenance and energy losses [9].

Over the years, the technological aspect of HVDC lines has evolved [2]. The basic monopolar scheme of a classical HVDC link connecting two AC grids with rectification and inversion stages has been presented in Figure 1-2. The rectifier transforms the AC into DC power which is then transmitted through HVDC link. The inverter on other side converts the DC power back to AC before feeding it into the AC network. An another scheme called the bipolar scheme is a combination of two monopolar schemes [10][11]. In the bipolar scheme, the connections are made in such a way that one DC link conductor is at positive polarity while the other is at the same magnitude but at negative polarity with respect to the ground. The monopolar and bipolar schemes rely on line commutated converters (LCC) technology, which is quite mature and mainly incorporates thyristor as switching devices [10][12].

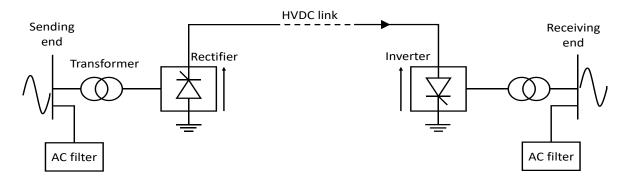


Figure 1-2: Basic Schematics of a monopolar HVDC transmission

With the development of insulated gate bipolar transistor (IGBT) devices known for fast switching speed and high efficiency [2], the voltage source converter (VSC) technology gained popularity in late 1990s. Owing to the greater number of LCC units worldwide [12], [13], here the discussion will be limited to HVDC-LCC technology.

Figure 1-3 shows the 12-pulse bridge schematic for monopole scheme connected to HVDC link. As can be seen in the figure, the transformer connecting AC grid to the converter station is a 3-phase, 3 winding transformers, quite often termed as HVDC transformer. The primary side winding of this 3-phase transformer generally has wye winding and is grounded. On the valve (or

converter) side, the windings consist of wye and delta winding respectively with floating grounds. Both valve-side windings of the 3-phase transformer are connected to two 3-phase, 6-pulse converter bridges. These two 6-pulse bridges are connected in series making it a 12-pulse bridge rectifier. Ideally, the total output voltage at HVDC link is equally divided between two bridges. The wye and delta winding offers a phase shift of 30° between the two bridges, thereby providing an effective 12-pulse operation [10][14].

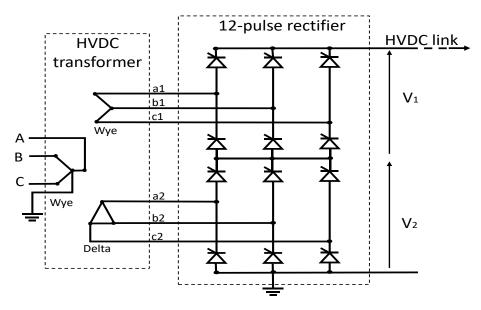


Figure 1-3: Connection of 3-phase transformer with 12 pulse bridge converters in an HVDC transmission

In the 12-pulse bridge converter, many thyristor valves are coupled in series/parallel to achieve the required voltage and current ratings. A thyristor is a semi-controlled switch (unlike IGBTs and power MOSFETs): the control signal can turn the thyristor on, but circuit conditions are required to turn it off. In terms of power capabilities, thyristors with voltage ratings of at least 8 kV are available today [13]. Taking an example of a phase control thyristor (Infineon part number T1081N) with maximum blocking voltage of 6 kV, the critical turn-on current slope is 300 A/µs, while the critical turn-off voltage slope is 2 kV/µs as per its datasheet. These relatively fast current and voltage switching transients of the thyristors can cause voltage distortion in the power network, by inducing harmonics. To suppress these harmonics and prevent them from entering the AC system, filters are deployed on the AC side of the monopolar HVDC scheme which offers a low impedance bypass path as shown in Figure 1-2 [10].

1.1.1. Electrical stress on HVDC converter transformer

In order to analyze the electrical constraints across the HVDC transformer, a model was developed in Simulink whose parameters were adapted from a thyristor based HVDC link model available in Simscape power system library (reference: power_hvdc12pulse). The model thus

developed had 12-pulse converters, 1000 MW (500 kV-2kA) DC link from 500 kV, 5000 MVA, 60 Hz AC system to a 345 kV, 10000 MVA, 50 Hz system.

The voltage stresses across the HVDC transformer were thus analyzed during steady state operation in the simulated model (Figure 1-4). The voltage measured across phase to ground on the primary side of the HVDC transformer V_{pAG} in Figure 1-4 is a non-distorted sinusoidal waveform which is due to the presence of passive filter between the primary winding of the transformer and AC side (see Figure 1-2).

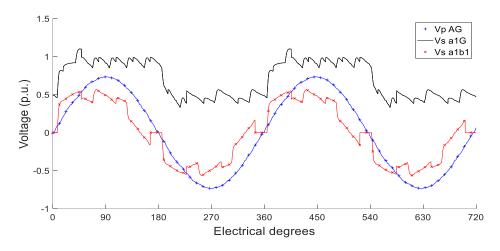


Figure 1-4: Voltage waveform across the line side and valve side winding of HVDC transformer

While the voltages measured across phase to ground (V_{sa1G}) and two phases (V_{sa1b1}) in the topology, are distorted, which has also been discussed in [14] and [15]. This is due to commutation overlap during successive switching of valves as explained further. During converter operation, the transfer of current from one switch to next takes a finite interval of time, which is slowed down by reactance (line and transformer leakage reactance) in the circuit. As a result of this, the current does not fall to zero instantly in one valve and while it starts rising due to switching of next valve. This leads to the overlapping of current in two phases. The voltage drops across the circuit reactance during successive switching of valves lead to the distortion as seen in V_{sa1b1} and V_{sa1c} [10], [11].

Moreover, the voltage between phase and ground in upper bridge V_{sa1G} is characterized by a large DC offset. During normal operation of DC link, the DC offset for upper bridge with wye winding is 75% while the one connected to lower bridge is 25% approximately of the voltage in DC link [16]. The presence of high harmonic content superimposed over DC voltage continuously stresses the valve-side windings and thereby the insulation of the HVDC transformer.

Insulation system in HVDC transformer

In HVDC transformers, the insulation system is composite in nature, as it incorporates both solid and liquid dielectrics. It mainly comprises of mineral oil and cellulose (pressboard) due to their proven performance, reasonable service lifetime and low cost in AC transformers. The dielectric liquid serves the dual purpose of insulation by providing high dielectric strength against voltage stress and act as excellent coolant by heat dissipation. One of the major advantages of dielectric liquid is its self-healing property unlike solid. Temporary failures inside the liquid are reinsulated after breakdown by the virtue of its flow to the affected area. Also, like gases, liquids can fill the entire volume to be insulated and dissipate heat by convection [17]. But, the dielectric strength of liquid can be affected by fine droplets of water suspended in oil and presence of solid impurities.

The cellulose possesses good oil impregnation characteristics due to its porous nature, which provides excellent performance in electric fields under different voltage conditions. In transformer, the liquid is used in conjunction with solid barriers against high voltage stress. The barrier subdivides the oil channels into narrow gaps inside the transformer and prevents the line-up of impurities. This type of configuration brings good mechanical stability under surges and short circuit conditions [18].

Electric field distribution during different stages of HVDC operation

In HVDC transmission system, the voltage application includes DC turn-on, steady state with positive polarity, DC voltage polarity reversal (DCPR) to change direction of power flow and steady state with negative polarity, as shown in Figure 1-5 [14], [19]. During DC turn-on, the distribution of electric field across the transformer insulation is capacitive in nature. At this time the field is determined by permittivity (ϵ) of composite insulation system. When voltage reaches DC steady state in positive polarity, the electric field is guided by conductivity (σ) of the insulation system [20].

However, the electric field distribution during polarity reversal becomes much higher than in steady state and turn-on, which can be understood as follows. The electric field across the transformer insulation system can be mathematically represented by Laplace equation as shown in equation 1.1 [15].

$$\left(\varepsilon \frac{\partial}{\partial t} + \sigma\right)(\nabla^2 V) = 0 \tag{1.1}$$

Where, σ : conductivity, ε : permittivity of insulation system, V: potential

This equation considers the effect of conduction current, governed by electrical conductivity and displacement current which is mainly influenced by dielectric permittivity.

During DC turn on, the time dependent displacement current is more significant. While, under the steady state operation of DC conductivity is dominant, as time varying component in equation 1.1 becomes zero. However, during the voltage polarity reversal, which is achieved by converter control for reverse power flow, both conduction and displacement currents become significant, thus subjecting the insulation of transformer to combined stress of steady state DC in addition to changing stress from +DC to -DC which is two times the stress due to peak AC voltage. This can increase the risk of flashover.

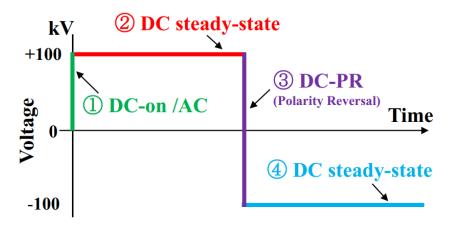


Figure 1-5: Voltage application in an HVDC transmission link during (1) turn on, (2) steady state, (3) during voltage polarity reversal and (4) steady state after polarity reversal (source: [19])

For high voltage application, the resistivity of the insulating liquids should be in the range of 10^{12} to $10^{16} \Omega$.m [14]. In their pure state, some liquids possess this property but in practice, it is very difficult to keep dielectric liquids in service totally free from contaminants such as dissolved gases, solid pollutants, oxidation product and moisture caused due to ageing and temperature changes [16][17].

During the service life of transformer, the resistivity of transformer oil changes due to increased moisture content. Also, resistivity of paper and oil decreases with increasing temperature, as shown in Figure 1-6. This can have direct impact on electric field distribution of transformer insulation system. As can be observed from the figure, at higher temperature (around 100 °C), the electrical stress can be expected to be evenly distributed between both oil and pressboard, as their resistivities fall in the same range (Figure 1-6). But at lower temperature, this gap widens, leading major part of stress on the paper due to its higher resistivity [14], [19].

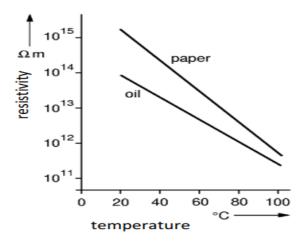


Figure 1-6: Comparison of resistivity of oil and paper as function of temperature. Note: Different oil and pressboard/paper can show different characteristics (source: [14])

Figure 1-7 presents the stress due to electric field for a simplified transformer windings under AC, DC and during DC polarity reversal (PR). As can be clearly observed, under DC voltage and during DCPR the electric field in the pressboard barriers are quite enhanced than in AC [21]. The uneven distribution of electric field at the interface of liquid/solid can greatly affect the discharge mechanism of the insulation system under HV stress [22].

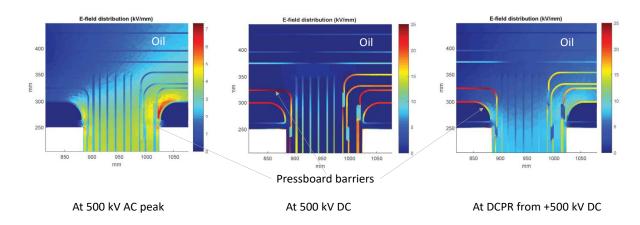


Figure 1-7: Electric field distribution on the insulation system of a converter transformer at 500 kV AC (peak), at 500 kV DC during steady state and during DC polarity (from +500 kV to -500 kV) ([21])

Moreover, mineral oils, which is mainly used in large transformers are non-biodegradable and pose a threat to the environment. In this situation, substitutes with low carbon footprint should be explored without compromising essential characteristics of transformer insulation system.

1.1.2. Need for alternative solution

To meet the increasing demands of energy, the power ratings of transformers have increased from almost 1 MVA in 1920 to almost 1000 MVA in the year 2000 and continue increasing further [18]. The increasing dimension of high power rating transformer demands large quantity of dielectric liquid.

Studies like [23] and [24] have suggested synthetic esters as an alternative to mineral oils, as their comparable dielectric strength and high flash point makes them an attractive choice (Table 1-1). Besides this, natural esters also appears to be a promising solution as dielectric liquid for transformers, based on the experimental works made in [25][26]. Table 1-1 provides key characteristics of synthetic ester and natural ester as compared to mineral oil.

Table 1-1: Some key properties of mineral oil (Nytro 4000X), synthetic ester (Midel 7131) and natural ester (FR3) taken from [27]–[29]

Properties	Mineral oil (Nynas Nytro 4000X)	Synthetic ester (MIDEL 7131)	Natural ester (ABB Biotemp)
Dielectric breakdown (kV)	> 70	> 75	> 75
Flash point (°C)	146	260	330
Water content recommended values (ppm)	< 20	Typical 50 Maximum 200	< 150
Maximum water solubility (ppm) (Typical values)	55	2600	1100
Dissipation factor (At 90 °C)	< 0.01	< 0.008	0.014
Relative permittivity (Er)	2.2	3.2	3.2

Apart from dielectric strength and flash point, the moisture content of the dielectric liquid used in the transformer is a primary concern. Excessive moisture dissolved or mixed with dielectric liquids can bring down the breakdown voltage, leading to early failure of asset. The electrolytic dissociation of water molecules can increase the conductivity of oil by increasing more charge carriers after dissociation. As can be seen from the Table 1-1, esters have higher water solubility as compared to mineral oil under standard atmospheric conditions. Higher solubility of water in esters make them insensitive to moisture in contrast to mineral oil which reduces their probability of breakdown under AC voltage [29]. Besides this, the difference in relative permittivity of esters and pressboard (ϵ_r =4.4) is less, which can modify the stress distribution due to electric field at the ester/pressboard interface, as compared to mineral oil. Therefore,

biodegradable substitute like synthetic ester offering higher flash and fire point with promising thermal stability could be a good choice [29] [30].

1.2. MVDC transmission

While the high voltage is transmitted either by HVAC or HVDC schemes, the distribution of electricity takes place with medium voltage (MV) AC grids. This is largely due to the availability of highly efficient transformers which step down the high voltage transmission line to lower distribution line voltage [31]. The AC network functions at 50/60 Hz and the passive components such as capacitors and inductors are quite bulky. Moreover, in such configuration, often two grids cannot be interconnected straightaway due to reasons like difference in phase angles, frequency of feeder line and higher harmonic content in one grid than in the other [32][33].

Owing to the aforementioned shortcomings of AC network and the move towards the adoption of renewable sources of energies like solar and wind farms, interconnection of energy storage systems (ESS), datacenters for future smart grid projects, MVDC grids are being looked upon as a promising solution. A DC cable occupies less space and carries more power than its AC counterpart, which makes it strategically advantageous. The MVDC grid can act as a backbone of future grid infrastructures by integrating distributed renewable sources, connecting remote loads, interconnection of existing AC substations and converting AC to DC lines to significantly increase the power capacity.

Figure 1-8 shows an example of interconnection of renewable generating stations, HVDC link, electric vehicle (EV) infrastructure, ESS and AC load (representing consumers) through an MVDC line. The common component in all these interconnections is the energy conversion unit which is either a DC/DC converter or a DC/AC inverter. The recent development of power electronic devices and the need for distributed generating stations are the keys towards the realization of MVDC schemes [4], [31]–[33].

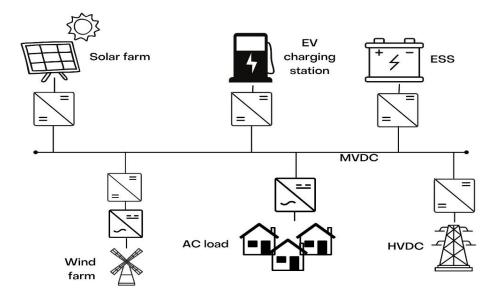


Figure 1-8: Example of interconnection of renewable source of energy (wind and solar farms), AC load, electric vehicle (EV) infrastructure, energy storage systems (ESS) and HVDC link to MVDC line

Considering the classical configuration of offshore wind power plants (Figure 1-9), the voltage generated by wind turbines generator (typically 690 V) is stepped up to medium voltage AC (usually 33 kV) by transformer [34]. The power from different offshore stations is collected at AC substation at offshore platforms, which is then transported to land grids. Often the transformer and passive components like capacitor in the AC substation are large.

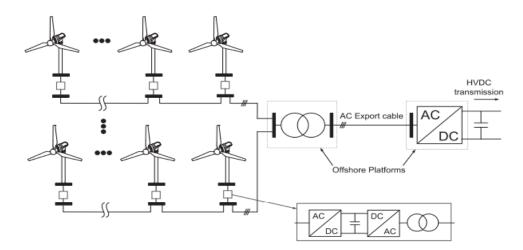


Figure 1-9: Radial collection configuration at windfarm and its connection to offshore AC substation (source:[35])

To reduce the weight and volume of substation and achieve higher efficiency, the collection and transport of power using MVDC grid have been proposed in recent studies [4] [35]–[37]. Figure 1-10 presents one such scheme for DC offshore wind power plant. In this scheme, the wind turbine feeder includes a step-up DC/DC stage after AC/DC, which increase the voltage level

before delivering to offshore platform. At offshore platform there is another step-up DC/DC which transports the power generated to the shore. As reported in [33], an MVDC grid of 5-10 kV rating near windfarms can improve the efficiency of power collection and reduce the total cost.

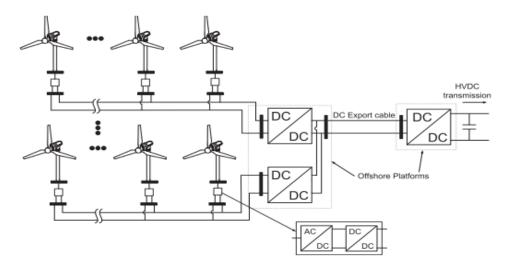


Figure 1-10: A proposed scheme for offshore wind power plant with step-up DC/DC for each wind turbine feeder which then connects to another DC/DC converter at offshore platforms (image source:[35])

The main component of MVDC distribution grid is a DC/DC converter for which dual active bridge converters (DAB) are one of the insulated DC/DC conversion techniques. Several such converters can be connected in series/parallel to interconnect a low voltage generating station with MVDC network [38].

The architecture of DAB includes an inverter and rectifier at extreme ends with a coupling transformer in the central position which isolates primary side from secondary as shown in Figure 1-11. In DAB architecture, the rectifier and inverter comprise of valves to convert DC to AC and vice versa. The leakage inductance (L) shown in the figure forms the part of medium frequency transformer (MFT). The operation in the medium frequency range (usually tens of kHz) by DC/DC converter can provide weight and volume reduction of the substation and increase the power density. As discussed in [39], a 3 MW 500 Hz transformer was evaluated to be 3.5 times lighter than a 3 MW 50 Hz AC transformer.

The WBG materials such as silicon carbide (SiC) based converter possessing high switching speed, higher electric breakdown field (3-5 MV/cm), improved thermal conductivity, ability to operate at hundreds of kHz and reduced conduction losses makes them more efficient than their silicon based counterparts (such as IGBT). The experimental comparison made between Si-IGBT and SiC-Mosfet in [40] of same voltage rating ($V_{DS} = 1.2 \text{ kV}$) in an isolated bidirectional resonant DC/DC converter, have shown DC/DC converter implementing SiC-Mosfet can reach

system efficiency of about 98 %, which was 1-2 % higher than that of Si-IGBT. These properties make SiC devices most suitable for switching designs of power converters (AC/DC and DC/DC) in both medium and high voltage applications [5], [41].

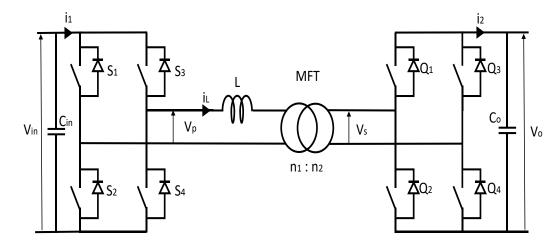


Figure 1-11: Schematics of a dual active bridge (DAB) converter implementing medium frequency transformer (MFT)

To have a look at the high switching speed of WBG devices, Figure 1-12 shows the rising front of a commercially available SiC-Mosfet (G2R1000MT33J from GeneSiC semiconductor) with blocking voltage of 3.3 kV. The spice model of the HV switch thus available from the semiconductor supplier was put across a capacitive load of 30 pF (representing a device under test or DUT in a laboratory scale). As can be seen from figure, the rising front of waveform generated by a single SiC-Mosfet switch across the capacitive load has dV/dt of more than 100 $kV/\mu s$.

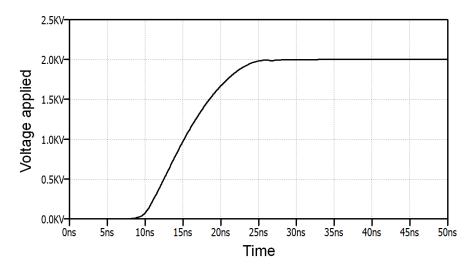


Figure 1-12: Fast rising front of output voltage waveform across a 30 pF capacitive load using a model of a commercially available high voltage SiC-Mosfet switch (G2R1000MT33J from GeneSiC)

1.2.1. Electrical stress on medium frequency transformer

Often the studies have been performed to analyze the input and output waveforms of DC/DC topology but the electrical stress across the windings of MFT due the serialization of DAB converters is quite missing in the literatures. Therefore, to conduct a simulation study in this regard, the specification of an insulated DC/DC topology with four DAB converters, provided in [4] was considered. The input side voltage taken in the study was 5 kV to generate output voltage of 20 kV after serialization of DAB converters.

To replicate this situation in simulation, at first DAB converter was developed with 1:1 transformation ratio for MFT (same as shown in Figure 1-11). The Mosfet switch blocks were used to design both inverter and rectifier bridges. Switching frequency was set at 10 kHz. Then, a structure as shown in Figure 1-13 was created, which comprised of four stages of DAB converters. The DAB converters were connected in parallel at input side (V_{in}) while the other end was serially connected to obtain 20 kV output (V_{out}) .

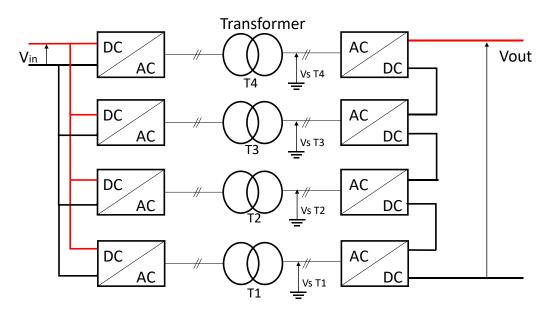


Figure 1-13: Serialization of DAB converters in isolated DC-DC topology to attain high voltage output (Vout)

In the DC/DC topology, both the primary and secondary side of transformer (V_p and V_s as shown in Figure 1-11) are exposed to fast rising square shaped voltage waveforms due to high speed switching of semiconductor device. An interesting part here is to look at the voltage stress across the transformer at different stages (T1 to T4) with respect to the ground.

Figure 1-14 demonstrates the voltage stress across the secondary side (V_{out} side) of MFTs with respect to the ground. As the level of transformer increases from bottom to top in the topology

(T1 to T4), the secondary side winding is stressed with DC offset voltage in addition to fast rising square waveform (see Figure 1-13 for layout and Figure 1-14 for voltage stress). The DC offset across the secondary winding of MFT at T2 is 25 %, T3 is 50 % and at T4 is 75 % of total MV line. As the stage of MFT increases in the topology, it would be highly stressed by electric field due to constant DC voltage apart from fast repetitive voltage impulses.

The insulation system of transformer operating in MF would depend upon its voltage requirement. For higher voltage application, it is expected that MFT may be insulated with dielectric liquid, as it has better cooling properties than solid insulators [42], [43].

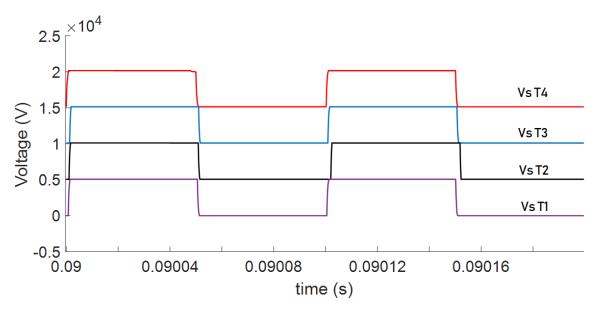


Figure 1-14: Simulation result of voltage stress across secondary winding of transformer with respect to ground at each stage of in DC-DC topology (see Figure 1-13) in steady state

The reliability of the insulation system under fast repetitive voltage impulses is already an ongoing research for more than a decade [44]–[47] for inverter fed induction motors. The enameled wire insulation used in motors when exposed to such complex waveforms during continuous operation has been reported to have accelerated degradation. The premature ageing has been mainly attributed due to increased partial discharge activities and dielectric losses.

The issues discovered for the insulation of inverter fed induction motors, puts a reliability concern for the insulation system of MFT due to the implementation of fast switches in DC/DC conversion techniques. The MF operation of transformer in DC/DC topology has attracted the attention of some research groups [6], [48]–[50] in past few years. However, not a lot of studies are available with liquid/solid insulation under repetitive square waveforms. In [48], experiments made on resin impregnated aramid fibers showed a reduction in breakdown voltage (BDV) when

sinusoidal voltage was increased from 50 Hz to 10 kHz. The study made in [50], has also reported decreasing breakdown voltage for paper/oil insulation system under fast rising square voltage waveform. From these investigations, the deteriorating effect of frequency can be noticed, which can be due to increase in dielectric losses at high frequency. The loss tangent (tan δ) is frequency dependent and insulation losses (P_{δ}) can be given by

$$P_{\delta} = 2\pi f C. U^{2}. \tan \left(\delta(f)\right) \tag{1.2}$$

where, U is the applied voltage, f is frequency of applied voltage, C is insulation capacitance

Unlike in AC, with square waveform, the dielectric losses should be summed for each harmonic content [42], [51] which may lead to a different dielectric behavior. This raises the necessity of monitoring the insulation system under MF square waveform.

1.3. Monitoring methods of the insulation systems

The quality of insulation system for conventional transformer degrades during its service time with continuous operation. Therefore, to ensure the functionality of transformer the insulation system should be examined regularly. Studies evaluating the insulation stress have proposed different diagnostic tools to monitor insulation health such as measurement of breakdown voltages (BDV), partial discharges (PD), leakage current and dielectric losses. Further, the assessment of furanic compounds can be a key indicator of cellulose condition [18]. The International Electrotechnical Commission (IEC) has provided standard measurement techniques to assess the insulators under continued operation. The testing engineer should select the characterization technique based upon the requirements.

In past four decades, the PD measurement of an insulation system has proved to be an excellent technique for quality assessment of HV equipment. It has been widely accepted by several utilities as a diagnostic test for quality control [52]. The PD activity is supposed to grow with increasing voltage or with time which can lead to final breakdown (explained further in chapter 2). PD tests can therefore be used to recognize serviceability, reliability as well as to predict the insulation issues quite well before its breakdown. A PD pulse is characterized by sharp rise in pulse amplitude which occurs in a very short span of time (range of nanoseconds or ns) as shown in Figure 1-15. It has a typical magnitude in the range of picocoulomb (pC).

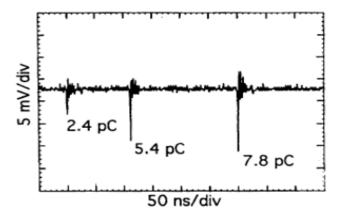


Figure 1-15: Partial discharges in dielectric liquid [53]

PD tests are well established under AC excitation. The norm IEC60270 describes the method and procedure to realize PD tests under alternating voltages up to 400 Hz. The measurement setup of includes a high voltage supply, high voltage filter (to suppress noise from supply), a device under test (DUT), coupling capacitor (C_k), measuring impedance (Z_{mi}) and measuring instrument MI as presented in Figure 1-16.

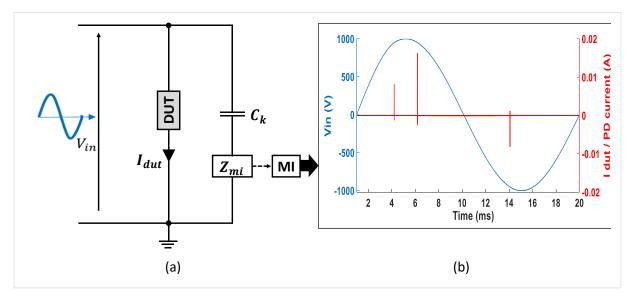


Figure 1-16: (a) PD measurement circuit as per IEC60270 (b) PD current and voltage measured across DUT

 C_k and Z_{mi} together constitute the coupling device for PD measurement. C_k serves the dual purpose of transmitting the high frequency PD signal detected across the terminals of the DUT to the coupling device and attenuating down the applied voltage to a measurable magnitude. C_k is meant to be PD-free and retain low inductance to avoid adding up perturbing oscillations to the PD signal. During the occurrence of PD, there is a sudden drop of voltage across the DUT. This voltage drop is compensated by coupling capacitor C_k which releases apparent charge in the circuit to counteract the voltage drop, thereby resulting a small transient current in the circuit.

Due to its high frequency content, PD current is differentiated from the input low frequency AC voltages using bandpass filters. The PD event is thus measured as a voltage signal by the measuring instrument (MI) as shown in Figure 1-16 (b).

PD measurement could be an important part of acceptance tests to address the insulation design of MFT [44], [54]–[56]. In [49], the insulation design of MFT with synthetic ester is validated by PD measurements at 50 Hz. Knowing that various factors like fast rise time, switching frequency and duty cycle of square waveform can influence the PD mechanism of material as found in other literatures, the isolation test in AC 50 Hz does not look sufficient to characterize insulation for MFT. Further, the miniaturization of the MFT creates a direct challenge on its dielectric design due to high electric field at reduced gap. Moreover, in a winding part of transformer, voltage distribution due to MF waveforms with high dv/dt can be significantly different from AC 50 Hz. So, to assess the discharge phenomenon with fast rise time, high switching frequency for MFT, experimental verification would be necessary under square waveform.

Studies like [56] have reported difficulty in PD detection under square voltage with IEC 60270 based schematic. To understand this better, the IEC 60270 circuit as shown in Figure 1-17 is developed in Simscape power system and simulated by generating a PD during rise time (more details about PD signal is in Appendix A). As shown in Figure 1-17, the PD generated during rise time overlapped with the displacement currents occurring due to fast switching.

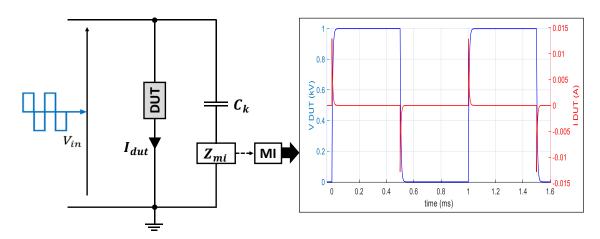


Figure 1-17: (Left) Square voltage waveform fed to PD measurement circuit as per IEC60270; (right) 1 kV square voltage with rise time of 3 µs and displacement current obtained across DUT; a 50 pC PD generated during rise time is not visually identified

Another drawback of using IEC60270 schematic under square voltage is the dV/dt across the DUT slows down due to the presence of coupling capacitor (typically 1 nF) in parallel to very small value of DUT (tens of pF). Therefore, to address the impact due to fast rising voltage from WBG switches (as shown in Figure 1-12), this circuit would need modification such as using a

coupling capacitor of value close to DUT. But, for better sensitivity of PD detection, the condition $C_k >> C_{dut}$ should be satisfied as recommended in IEC 60270.

The PD detection with fast WBG devices may even worsen due to overlapping of frequency content of displacement current and PD pulse. To assess this condition, a schematic was developed (see Appendix A) in Simscape power system producing rise time of 250 ns across a 30 pF DUT load at 20 kV (for high dV/dt). Three conditions were simulated namely displacement current without any PD pulse, displacement current overlapped with PD pulse and PD pulse during DC voltage plateau of square voltage (20 kV). Then from the recorded traces, fast Fourier transforms (FFT) of displacement current due to fast rising voltage and a PD event were analyzed.

As can be seen from the FFT spectrum presented in Figure 1-18, the frequency content of PD pulse which occurred during DC voltage plateau of square waveform falls in same range as displacement current without PD current. Also, the FFT spectrums of displacement current with and without PD overlap with each other. By reducing the background noise down to a permissible limit, PDs occurring during voltage plateau might be detected, however, a low magnitude PD occurring during the rising time of square voltage will blend completely with the high magnitude displacement current. Therefore, designing a filter is more challenging under square waveform and would depend on rise time in the set-up.

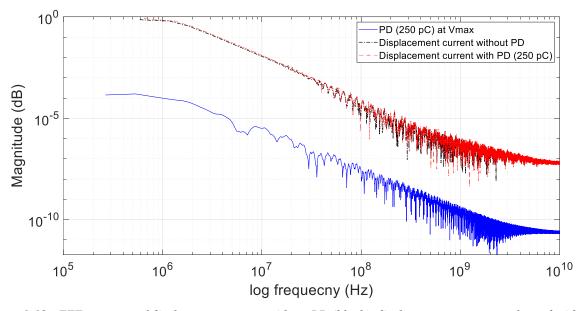


Figure 1-18: FFT spectrum of displacement current without PD (black), displacement current overlapped with PD of 250 pC (red) and PD of 250 pC generated at voltage plateau (blue) for a 20 kV square voltage waveform with rise time of 250 ns across a DUT of 30 pF

Looking at this situation, to detect the PDs under fast rising voltage, other methods are required to be explored. Different studies have presented the implementation of non-intrusive measurement techniques such as high frequency current transformer (HFCT) and ultra-high frequency (UHF) antenna [57], [58]. However, these techniques might as well be impacted by strong electromagnetic interference (EMI) produced by displacement current. Some other articles have proposed post processing methods like wavelet transformation, stochastic approach of PD detection and standard deviation to separate PDs under square waveform with short rise time [59]–[61]. Another technique is optical detection which offers decent sensitivity and immunity against EMI [55], [62]. Studies like [62] has showed the implementation of photomultiplier tube (PMT) for PD detection of printed circuit board embedded in insulating liquid. But it can detect PDs only in transparent mediums, which is one of its main limitation (more discussion in Chapter 2).

1.4. Motivation and objective

For future smart grid projects, new power conversion techniques are gaining popularity. The isolated DC-DC converter topology based on DAB is a promising solution for interconnecting renewables with a MVDC line. The MFT, which forms the central part of such isolated DC-DC topology, is going to play a major role by providing high power density flow at improved efficiency with a reduction in weight and volume. Conversely, due to fast switching and high frequency operation of power converters, the insulation of the MFT will be exposed to a kind of electrical stress which is quite different from conventional sinusoidal AC waveform. Studies on the insulation system of induction fed motors have shown that these fast-rising voltages can accelerate their degradation. Due to high dV/dt, high frequency and rather higher operating voltages, the insulation system of power electronic components like MFT is not clear today.

In HVDC LCC schemes, the transformer insulation system is continuously stressed by voltage waveforms with high harmonic content. Several research works have addressed its reliability and have tried to understand the discharge mechanism. Yet, with the development of high rating power devices for HVDC links, the electrical insulation performance of the transformers needs to be enhanced. Moreover, alternative recyclable solutions should be explored due to growing environmental threats posed by mineral oil in large HVDC transformers, without compromising essential performances such as heat dissipation and high thermal stability.

In these situations, the insulation system of transformers requires an investigation for high voltage applications and assess its reliability under fast rising complex voltages. This would be necessary to improve the insulation system of existing HVDC transformers and investigate the insulation reliability of power conversion equipment in MVDC schemes such as MFT. Therefore, a study under fast rising voltage would assist in their insulation design for this upcoming technology. Partial discharge measurement is widely used to examine pre-breakdown

phenomenon of insulators and therefore can be used as a defect monitoring tool for estimating the health of insulation system.

Thus, this thesis aims at investigating the insulation system using partial discharge measurements for power electronic applications such as MFT under square voltage waveform. Another goal is to evaluate the potential substitute of liquid/solid insulation for LCC application. These objectives will be addressed by investigation of PDs under fast rising square voltages with the approach dictated below:

- Explore different PD measurement techniques under square voltage waveform from publications
- Design of device under test (DUT) to represent transformer insulation system at laboratory scale. Choose insulating materials to be tested
- Definition of a test bench generating square waveform with high dV/dt at various switching frequencies
- Implementation and evaluation of PD measurement technique(s) in real set-up
- Comparisons of various insulation systems with regards to PD activity in AC and square waveforms conditions
- Assessment of PD activity by changing the parameters of square voltage such as rise time, switching frequency and duty cycle

1.5. Outline of thesis

With the approach define above, this thesis has been divided into six chapters. The first chapter (background and context) has described the issues and concerns for the chosen applications and problems encountered with conventional PD detection techniques under fast rising voltages. It has further discussed the concerns over reliability of insulation system for power electronic applications, the necessity of investigation and thereby the motivation behind the thesis.

The second chapter will provide a literature review of the partial discharge phenomenon in dielectric liquids, its characteristics and measurement techniques under fast rising voltages. A simulation study will be presented for some PD measurement techniques to provide a comparative analysis on their potential of PD detection under square waveform.

Chapter three will deal with the definition of the DUT (a composite insulation system) using the finite element method. It will discuss about the validation of the selected DUT from electrostatic point of view and impact of parameters like permittivity, thickness and needle tip on the electric field.

Chapter four will introduce the experimental set-up of PD measurement in AC 50 Hz using electrical and optical detection techniques. The methodology of validating optical detection technique against the standard electrical detection technique will be discussed.

Chapter five will describe a test setup to generate square waveforms, as well as preliminary test results using different PD detection techniques. The advantages and limitation of each detection technique will be presented and finally narrowing down the choice to one measurement technique for comparison between AC and square voltages.

In chapter six, the methodology (such as voltage profile) will be investigated to ensure consistency with AC measurements. Then comparative analysis between square and AC excitation will be provided using PD measurements. The impact of rise time, switching frequency and duty cycle will also be investigated.

Finally, the general conclusion will summarize the contribution and perspective drawn from this thesis. The references, appendices, abbreviations and notations can be found towards the end of this manuscript.

This thesis assembles the work done in three years in a joint venture between Power Electronics & Converter program of SuperGrid Institute, Villeurbanne, France and Laboratoire Ampère, Ecully, France. The experimental set-up has been developed in Ampère laboratory for PD measurements.

2. Literature review on partial discharge phenomenon and measurement techniques

To monitor the health of high voltage equipment, PD has been proved to be good indicator over past few decades. In case of dielectric liquids, the discharge mechanism mainly starts from a micro bubble. While in solid/liquid insulation system it is driven by the complex nature of insulation system. As seen in the last chapter, the detection of PDs under square waveform is difficult with conventional electrical technique, therefore studies have proposed different unconventional techniques.

This chapter deals with all above-mentioned topics. It starts with the general definition of PDs and condition required for PD occurrence. Then the PD phenomenon in dielectric liquid and solid/ liquid insulation system has been presented. Following this, an improved schematic representing the PD model has been proposed. Using this model, some measurement techniques available in studies were analyzed using simulation tool and arguments have been provided regarding their feasibility and limitations.

After this, different factors impacting the PD dynamics under fast rising time has been discussed as found in literatures. This chapter finally closes by introducing the PD measurement set-up and first results in AC, using simultaneously electrical and optical detection, which was the first step towards PD comparison between AC and square waveform.

2.1. Partial discharge

In dielectric materials small gas filled voids can arise due to defects in manufacturing, processing or aging. Due to their lower permittivity from surrounding solid or liquid materials, these voids become a weak point as it is prone to early breakdown in the presence of high electric field [52], [63]. The standard IEC 60270 [58] has defined partial discharge or PD as localized discharges which can partially bridge the insulation between conductors. The occurrence of PDs in a void degrades the insulating material by chemical, thermal and mechanical processes. This continuous degradation can weaken the insulation from inside due to formation of electrical tress, leading to early breakdown of insulation as shown in Figure 2-1 [64], [65]. Therefore, PD can be considered as a pre-breakdown phenomenon which can eventually lead to failure of HV equipment if not addressed at right time.

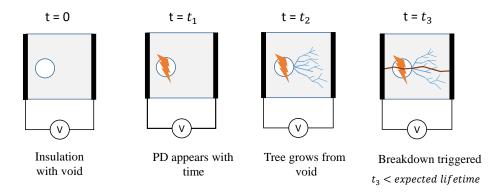


Figure 2-1: Representation of breakdown triggered by a partial discharge before the expected lifetime due to continuous degradation of insulation medium under voltage stress

The occurrence of a partial discharge has been described as stochastic process in different studies. In general, there are two necessary conditions for PDs to occur: first is the availability of a free electron to initiate the electron avalanche and second is the critical electric field necessary to trigger a discharge. The first free electron can come from the background radiation, due to field emission from void surface or from a previous discharge event [63], [64], [66].

Based on the location of occurrence, PD events can be classified as (i) internal discharges occurring inside the voids of insulation medium (both in solid and dielectric liquid), (ii) external discharges such as corona in air and (iii) surface discharges which can occurring at the interface of two dielectric materials. During a PD event, energy exchange takes place which can be exhibited in different ways such as current pulse, mechanical waves, electromagnetic radiation or chemical reactions. By exploiting one of the energy transfers from a discharge process, PD can be detected by using electrical, optical, acoustic sensor or ultra-high frequency sensor like antenna [67].

2.1.1. Quantities derived from PD activity

The occurrence of PDs is intermittent therefore it is recommended to use a digital instrument to measure partial discharges. The inception and extinction of PD determine stress tolerance level of an insulator, thereby making it an important quality indicator for insulation systems [15], [67], [68]. Here, only the terminologies used in this thesis have been described.

• PDIV and PDEV: The inception voltage of partial discharge (PDIV) is defined as the voltage level where the first PD event occurs while increasing the voltage from a lower voltage level where no such PDs existed. On the other hand, the partial discharge extinction voltage (PDEV) is the minimum voltage at which PD events cease to occur while decreasing the voltage from a higher level where PDs were occurring.

- PRPD: In phase resolved partial discharge (PRPD) pattern, the PDs occurring over a certain period of voltage cycles are accumulated and displayed as a function of phase. The integral value of PD pulse current is calculated and demonstrated as dots as shown in the PRPD pattern in Figure 2-4. The PRPD pattern makes it possible to perform deeper analysis of charge magnitude, number and phase of PDs by looking at the trend of PD occurrence with respect to voltage phase.
- Number of PDs (NPDs): It is the frequency of PDs occurring per second at a constant test voltage.
- Average charge magnitude (Q_{avg}) : Q_{avg} is the average charge magnitude of all the PDs occurring over a time interval at a constant test voltage.

2.1.2. PD activity in dielectric liquids

To study the pre-breakdown mechanism in dielectric liquids, many literatures like [69]–[71] have reported the initiation and formation of conductive channels under voltage stress. These conductive channels called streamers is mainly studied in inhomogeneous electric field using a needle as shown in Figure 2-2.

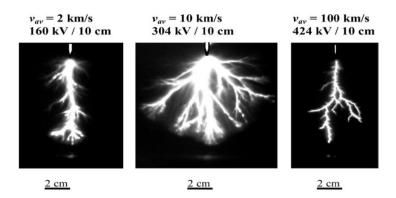


Figure 2-2: Increasing average velocity of positive streamers from 2 km/s to 100 km/s in mineral oil with increasing voltage across the needle for an inter electrode gap of 10 mm [image source: [69]]

The study of streamers is usually performed by using highspeed cameras. The streamers propagate towards the opposite plane electrode at an average velocity (v_{av}) which can vary from 100 m/s to 100 km/s in high voltage conditions. Its study is important to understand the physicochemical process involved in the initiation of discharges. While PD measurement provides the information about the charge transferred to the external circuit during a discharge event and is a more industrially accepted diagnostic tool to monitor insulation health. The PD can occur due to ionization caused by high electric field, impurities or microbubbles present in

liquid. In the scope of this thesis the discussion here will be limited to PDs however the concept of streamers will be used while describing the physicochemical process involved with PDs.

In laboratory conditions, PD phenomenon is mainly studied by subjecting dielectric liquid to either inhomogeneous (using needle-plane) or homogeneous (using plane-plane electrodes) electric field. With needle-plane geometry, the PD events in dielectric liquids generally occur from bubbles or gas voids which may be either already present or created by the divergent field at the needle tip.

In dielectric liquids, the PD occurs in the following steps: under the influence of high electric field, the free electrons or those detached by field emission accelerates towards the positive electrode. The electrons either neutralize at the positive electrode or hit an atom which releases a positive ion and an electron. The electrons drift rapidly while the heavier positive ions move slowly. This ends up creating a cluster of positive space charge as shown in Figure 2-3, which can weaken the total electric field across the void. In this case, as the externally applied electric field increases and total stress across the void reaches the critical electric field, a PD occurs in the presence of an initial electron. The minimal value of stress for discharge depends on difference in the permittivity, shape, temperature and pressure of the gaseous cavities from the surrounding insulator medium [67], [71], [72].

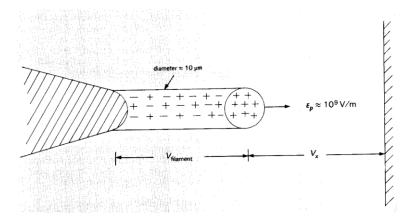


Figure 2-3: Model of positive discharge growth with a positive extended filament tip (image source:[72])

The discharge phenomenon in dielectric liquids can differ from one liquid to other due to differences in their chemical composition and physical properties. This becomes quite evident by looking at the discharge patterns as shown in Figure 2-4, which presents the PRPD patterns for mineral oil and synthetic ester from [67] at same voltage (25 kV), in a needle-plane configuration with 40 mm gap. It can be noticed from the PRPD patterns that the number of PDs and PD magnitude is higher in synthetic ester as compared to mineral oil under same voltage conditions. Almost all PDs occurred during the positive half cycle between phase angles 30° and 120°. The study attributes the strong charge propagation ability of positive PDs in the divergent field for

the observed PD phenomenon. As discussed earlier, the presence of positive space charges near the tip may also lead to enhanced PD activity in positive cycle. The higher moisture content can also be the reason of higher PD activity in synthetic ester [73].

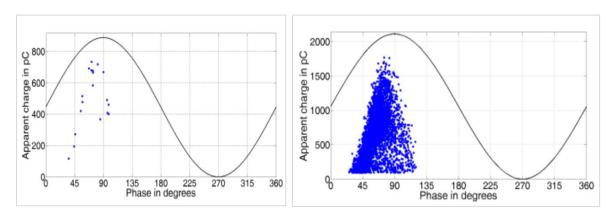


Figure 2-4: PRPD patterns of mineral oil (left) and synthetic ester (right) at 25 kV in needle-plane configuration [image source: [67]]

2.1.3. PD activity in oil/pressboard

To study the PD behavior with pressboard in oil, the electrode geometry can vary depending on the research objective. Needle is kept along the pressboard to mainly study the surface discharges until flashover while needle is kept perpendicular to pressboard surface to study the complete breakdown of insulation system as shown in Figure 2-5.

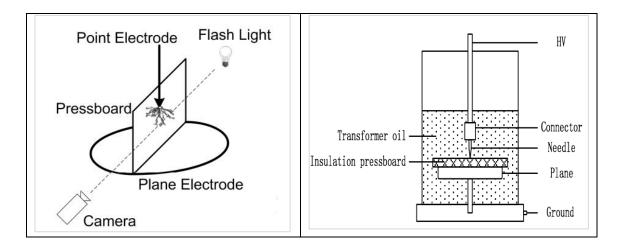


Figure 2-5: (Left) Orientation of needle along the pressboard to study surface discharges [74] and (right) needle perpendicular to pressboard to study complete breakdown of insulation system [75]

As reported in literatures [22], [70], the discharge inception and streamer propagation in the dielectric liquid is affected by the introduction of a solid insulation such as pressboard. Besides

the difference in permittivity of liquid and solid, the orientation of solid with respect to the externally applied electric field (as shown in Figure 2-5) also contributes to this phenomenon.

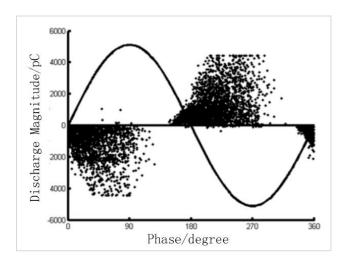


Figure 2-6: PRPD pattern of needle-plane with pressboard in mineral oil at 25 kV [75]

Figure 2-6 presents the PRPD pattern of needle-plane with pressboard in mineral oil from [75]. One can notice the concentration of PDs in first and third quadrants. PDs are occurring in negative cycle in presence of pressboard as compared to previously shown positive discharges in open oil gap. Moreover, PDs even appeared near 0° phase angle with pressboard as compared to open oil gap shown in previous section. The Cigre report [76] has also discussed about the enhancement of PDs in negative cycle with pressboard in the oil gap as compared to open oil gap for needle-plane configuration. In the presence of pressboard, the heterocharges and residual bubbles are formed from discharges in previous half cycle. The existence of heterocharges and bubbles promotes the PDs in negative half cycle and around the smaller phase angles, leading to a phenomenon known as promotion effect. This effect can further augment the PDs in negative half cycle which increases the risk of flashover. Also, this effect has been found more prominent in esters than in mineral oil, due to its higher viscosity as reported in the same report.

In AC, the PD behavior of oil/pressboard insulation is mainly reported under long term voltage application above PDIV and less than BDV to understand the electrical deterioration over time until insulation system completely collapses [74], [75]. As discussed in [75] for needle perpendicular to pressboard, under long term voltage application above PDIV, initially the discharges occur in the oil region near the tip and therefore PD characteristics have resemblance to oil discharges. With time the bubbles are formed by discharge process with charges deployed on them, which seems to be due to promotion effect as explained before. As the number of

bubbles grow with time, a column can be formed between two electrodes which eventually forms a conducting path leading to the complete breakdown of insulation system.

As discussed in previous chapter, in the HVDC network, the transformer insulation system is stressed by both AC and DC waveforms. Unlike in sinusoidal AC waveform, the PD dynamics can change under the long application of DC voltage. Considering the pressboard/oil insulation in a divergent electric field, the phenomenon under DC can be understood with the help of Figure 2-7 as explained in [77].

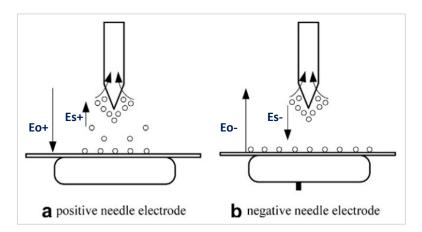


Figure 2-7: Space charge distribution under needle-plane electrode configuration (image: [77])

When the needle is at positive polarity (Eo+), the PDs can result in generation of free charge carriers such as electrons and ions in oil. The generated electrons are attracted towards the positive electrode while the ions move to the pressboard forming a positive space charge (Es+).

In the same way, during the negative polarity of needle (Eo-), the electrons are injected from the needle into the oil, and they move towards pressboard surface. Due to its higher affinity, more electrons get attached to the pressboard surface than positive ions. As a result of this, the reverse electric field (Es-) created by the space charges on the pressboard during negative polarity is stronger than Es+ created during positive polarity. This leads to a different PD dynamic than alternating AC waveforms and can impact the PDIV under the application of positive and negative DC voltages. The PD experiments under DC are a part of future test program.

Moving to the PD dynamics under square voltage, most of the studies available today have aimed the inverter fed motor insulation system (enameled wires). But not a lot of study have been found to address phenomenon of oil/pressboard insulation. In [15], the PD phenomenon for oil/pressboard insulation system was investigated under square voltage, but the rise time was quite slow (around 0.1 ms). The study made in [50] is one of the few studies which investigated PD phenomenon under square voltage waveforms. It presents PDIV and BDV results for rise time in the range of 200 to 1000 ns and frequency in the range of 1-10 kHz for impregnated kraft

paper in plane-plane configuration. However, the PD dynamics in oil/pressboard insulation system under square voltage is not quite clear and seems to be governed by several parameters like fast rise and fall time, repetition rate and duty cycle, which is quite different from AC voltage characteristics. The continuing section talk about these factors to develop understanding in this domain from available studies.

2.2. Factors impacting PDs under repetitive square voltages

This section discusses the impact of voltage amplitude, rise time, repetitive frequency and duty cycle of square voltage waveform on PD mechanism, found in different publications.

2.2.1. Voltage amplitude

To understand the impact of voltage amplitude with square shaped voltage a dedicated study was performed [54], with a needle to generate corona in air. For, this the rise time was fixed at $10 \,\mu s$ and voltage was increased from a value where no PDs appeared. The result from the study is shown in Figure 2-8.

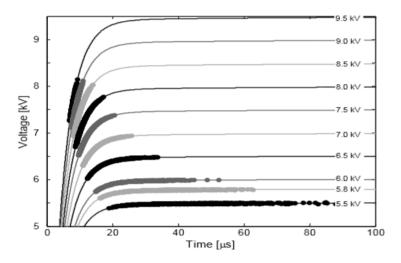


Figure 2-8: PDs measured for needle in air under increasing square voltage level with same rise time [54]

It can be observed from the figure that the PD occurrence is dependent on voltage level for given device under test. At 5.5 kV, the PD appeared at voltage plateau. While at higher voltage levels (like 9.5 kV), PDs started appearing during the rising voltage. The dV/dt increases with increasing voltage level. The concentration of charge carriers might have increased with increasing dV/dt leading to a higher probability of PD events during rising voltage.

2.2.2. Rise time

As explained in [78], fast rising voltage pulses can have direct impact on discharge phenomenon. With fast rising time, the voltage increases until the field is large enough to incept a PD event. However, the PD will be incepted only when the other condition, that is the presence of a free electron, is fulfilled as well. Usually, there is a delay between the moment when the inception field (or critical voltage) is high enough and the moment when PD occurs. Due to this statistical delay, the PD is fired at a voltage higher than critical voltage. This is especially noticeable with shorter rise times as shown in Figure 2-9. As can be noticed from the figure, the critical voltage is attained quite early with shorter rise times, but PD is fired at a higher voltage due to delay of free electron(s).

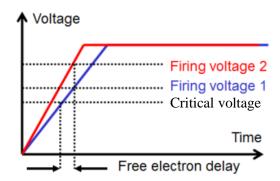


Figure 2-9: Effect of fast rising impulse voltage on PDIV (adapted from [78])

For enameled wires, several contributions like [45], [58], [60], [79] are available which discuss the impact of rise time on PD phenomenon. Figure 2-10 shows the impact of rise time on PD magnitude and PD firing voltage for enameled wires under bipolar square waveform.

It shows a higher PD firing voltage at shortest rise time of 200 ns as compared to longer rise times, which complies with reasoning provided in the beginning of this section. Also, the highest PD magnitude can be observed at 200 ns, which decreased for longer rise times. The higher firing voltage at short rise time explains the higher PD magnitude.

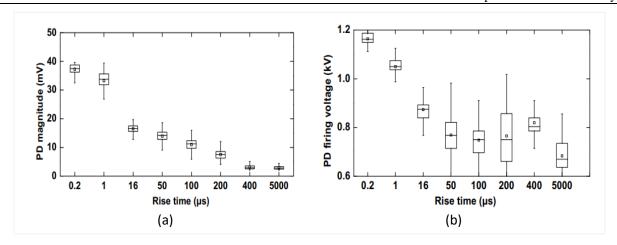


Figure 2-10: (a) PD magnitude as function of rise time and (b) PDIV as function of rise time for crossed pair of wires [58]

For transformer insulation materials, the impact of rise time has not been discussed extensively. The PD tests performed on impregnated 60 µm thick kraft paper embedded between Rogowski electrodes in [50] is one such instance as shown in Figure 2-11. The PDIV was presented in terms of scale parameters (a) of Weibull distribution fitting the experimental datasets. For impregnated kraft paper, the PDIV showed dependance on the rise times, for all switching frequencies tested in that study. This trend is not the same if compared to enameled wires.

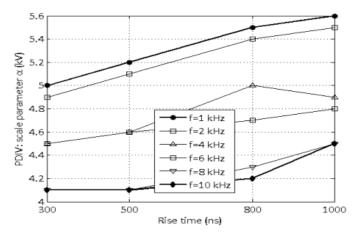


Figure 2-11: PDIV as a function of rise time for Kraft paper impregnated in mineral oil (Shell Diala B) [50]

From these studies, it is quite evident that changing rise time has an influence on PDIV, but it can vary with insulation medium and testing conditions.

2.2.3. Effect of frequency

The study conducted in [80] assessed PDs for an insulating pressboard in air between planeplane electrodes, to represent the windings of dry-type high frequency transformer. The PDIV thus obtained under sinusoidal waveform for frequency up to 12 kHz showed an increasing trend until 10 kHz before arriving at a constant value (see Figure 2-12).

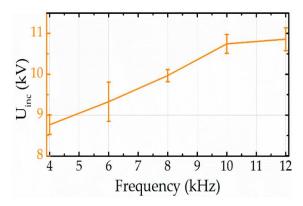


Figure 2-12: PDIV with increasing frequency of sinusoidal waveform [80]

While the investigation performed in [50], under square voltage waveform at higher frequencies showed an opposite relationship between PDIV and frequency (Figure 2-13). The tests were performed with $60 \, \mu m$ thick impregnated kraft paper, sandwiched between two pseudo rogowski electrodes.

Here it can be hypothesized that besides high pulse frequency, the high harmonic content of square voltages is favoring the PD activity. This could be due to increased dielectric losses under square voltage which could have led to the formation of bubbles in impregnated kraft paper and oil, thus favoring PD activity.

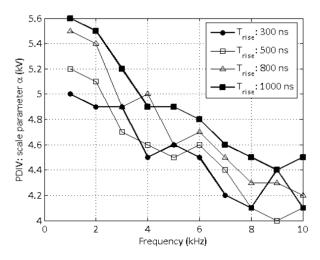


Figure 2-13: PDIV as a function of frequency for Kraft paper impregnated in mineral oil (Shell Diala B) [43]

2.2.4. Duty cycle

In [81], the duty cycle of square voltage was studied for crossed pair of enameled wires. The voltage applied had peak-peak value of 2.7 kV, switching frequency of 50 Hz and a rise time of $1 \text{ }\mu\text{s}$. The tests were conducted by varying the duty cycle from 0.005 % to 50 % to vary the pulse duration of applied voltage from $1 \text{ }\mu\text{s}$ to 10 ms at 50 Hz. The result thus obtained (Figure 2-14) showed an increasing trend in PD magnitude up to $100 \text{ }\mu\text{s}$ for both rising and falling flanks.

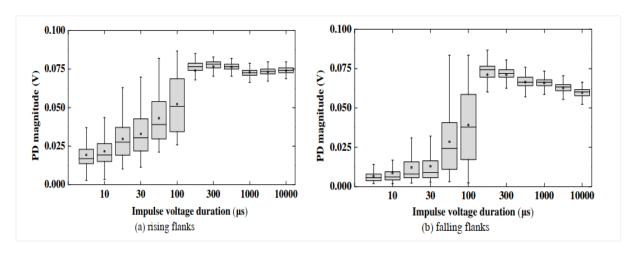


Figure 2-14: (a) PD magnitude as a function of voltage duration in crossed pair of cables during (a) rising flank and (b) falling flank of square voltage [114]

Another study [54], investigating the influence of duty cycle for corona discharges in air, found higher probability of PD occurrence when duty cycle was decreased. The hypothesis provided in the study is related to the distribution of charges, which might change either due to recombination of ions or due to diffusion.

2.2.5. Summary

Due to limited research work with transformer insulation system, the influence of square voltage waveform on PD mechanism is not very clear. Various effects seem to be influencing the PD mechanism, which can also vary with respect to the DUT configuration and testing conditions. Therefore, an experimental verification seems necessary to characterize the transformer insulating materials under square waveform.

2.3. Measurement techniques under square waveform

As discussed in Chapter 1, the measurement of PDs with fast rising voltage is difficult due to the interferences created by the switching currents, whose frequency content can fall in the same range as PD signal. Therefore, to investigate PDs under fast rising square voltages, different publications have suggested different measurement techniques such as optical detection, antenna, HFCT [58], [62] [82]. Some others literatures like [60], [61] have proposed techniques to extract

PDs using their stochastic nature. This section discusses the principle of these approaches and argues about their feasibility for PD detection under high dV/dt.

2.3.1. Optical detection

The PD events are accompanied with light emission, whose wavelength differ from one insulation to other. As stated in [83] [84], the wavelength of faint corona in air is usually less than 400 nm, which majorly falls in ultraviolet (UV) range. While the spectral region exhibited by transformer oil is in range of 350 nm to 700 nm which may further vary depending upon its chemical composition. These emitted optical signals are considered as good indicator of PD events.

The optical measurement technique works on the principle of detection of these lights or photons emitted during discharge process. As the light spectrum from PD activity varies with insulation, the choice of optical sensor should be made accordingly. Optical detection must be performed in a dark room to ensure capturing of lights emitted from PD events and not any other source. In case of transformer oil, the 1st mode of streamer generates a faint light which is quite difficult to capture with high speed cameras. Such events can be captured by photomultiplier (PM) tube [69].

A study [62] demonstrates the successful implementation PM tubes for detection of PDs under fast (100 ns) rising square voltage in mineral oil. Figure 2-15 shows the set-up from this study in which two PM tubes were placed in the line of sight for PD detection. The PM tubes were connected to Omicron system for PD acquisition. The figure also presents the optically obtained PDs (as dots) for fast rising square voltage at 10 kV.

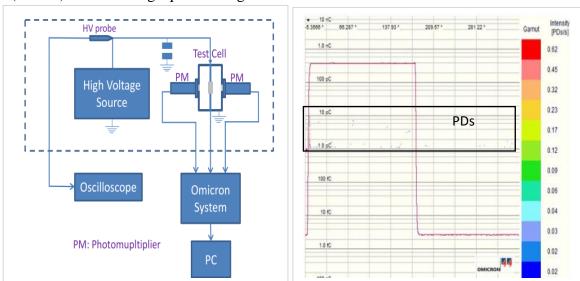


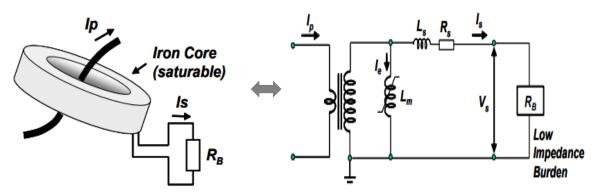
Figure 2-15: Circuits with optical detection of PDs under square voltage (left) using photomultiplier tubes in a test cell containing dielectric liquid and; (right) optically obtained PD using PM tubes ([62])

Another study [55] has also discussed about optical method of PD detection, for metal-air insulation interface defect, representing insulation of MV converter as shown in Figure 2-18. It employed a silicon PM (SiPM) sensor (besides an HFCT as discussed in next section) to detect PDs under unipolar square voltage waveform.

But this technique has certain limitations. It is limited to transparent media such as some gases and dielectric liquids; in opaque media, it can detect surface discharges but not the PDs occurring inside the dielectric. Another drawback is the lack of calibration standard for optical measurement. Therefore, it can detect the PD events, but does not provide charge magnitude associated with the PDs.

2.3.2. High frequency current transformer (HFCT)

HFCT is an inductive sensor which unlike other detection techniques can be used without altering the acquisition circuit for PD measurement. It offers galvanic isolation and can be clamped around the cable connecting the test object to the voltage supply or to the ground, to measure the current pulses. An HFCT represents a single turn primary and multi-turn secondary coil wound around a ferromagnetic core adapted to high frequency (upto few hundreds of MHz) signal measurements (Figure 2-16). [85], [86].



Where, Ls: secondary leakage inductance; Rs: secondary winding resistance; Lm: secondary magnetizing inductance; R_B : output resistance; I_p : current in primary coil/cable; I_s : current in secondary winding

Figure 2-16: Representation of an HFCT with a single turn primary with current Ip and multi-turn secondary across a resistive load and its equivalent circuit ([86])

The study made in [57] shows the detection of PDs using HFCT at cable joints under impulse voltage with rise time of 3 µs (Figure 2-17). It shows the PD detection using HFCT only during fall time. During rise time, the PD detection was hindered by the disturbances caused by the impulse voltages. As further discussed in the same study, the detection of some PDs was possible for rise time longer than 3 µs by implementing band-pass filters at the end of HFCT. Two filters

having bandwidth of 114 kHz - 48 MHz and 1.38 MHz - 90.2 MHz respectively were implemented after HFCT to attenuate the disturbances due to high impulse currents at fast rising voltage. However, the acquisition was performed at the expense of losing low magnitude PDs which were suppressed by the filters.

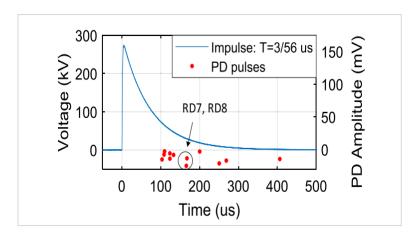


Figure 2-17: PDs detected only during fall time under impulse voltage using HFCT for cable joints [57]

The study made in [55] shows the PD detection with HFCT under unipolar square voltage (Figure 2-18). In this study, both SiPM and HFCT were used for PD detection for voltage with rise time between 1-40 μ s in the range of 0-25 kV. As can be seen in the figure, HFCT detected PDs at the same instant as SiPM.

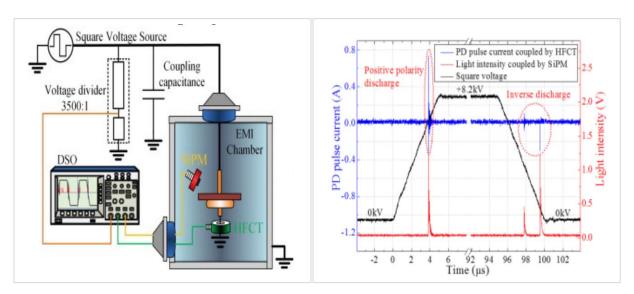


Figure 2-18: (Left) Representation of set-up for PD detection using SiPM and HFCT sensor for metal-air insulation defect model; (right) successful detection of PDs by SiPM and HFCT under unipolar square voltage at 8.2 kV, 2 kHz with 5 \(\mu s \) as rise time [55]

Looking at these studies, the HFCT seems to be an option for electrical detection of PDs under square voltage waveforms. However, the EMI induced by fast rising voltage would need greater attention during its implementation.

2.3.3. Antenna

The energy associated to PDs can generate high frequency electromagnetic (EM) signals (typically 300 MHz – 3 GHz). These high frequency signals can be detected using antenna as shown in Figure 2-19 and differentiated from low frequency components which usually holds true in case of AC excitation. For PD measurement with square waveforms, the bandwidth of the antenna should be selected considering the PD spectra, those of the EMI by the fast switching currents and the background noise [58], [83].

The work done in [58] utilized a horn type antenna to detect the PDs for crossed pairs of enameled wires. The test showed that the high dV/dt can impact the signal received by the antenna. As can be seen from Figure 2-19, the signal acquired by the antenna at a longer rise time (> 16 μ s) was not impacted by disturbances, while the other one with short time of 200 ns was influenced by the disturbances created by switching currents.

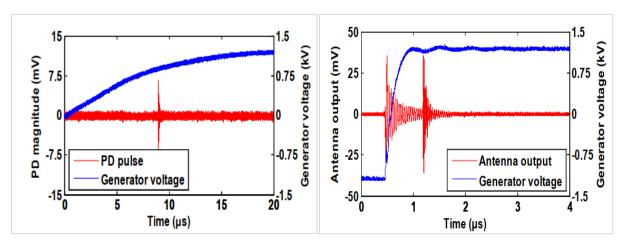


Figure 2-19: (Left) Detection of one PD pulse by antenna for a rise time of 16 µs; (Right) the antenna output impacted by switching current for a rise time of 200 ns [58]

2.3.4. Other PD detection techniques

Besides the unconventional PD measurement techniques described above, some other techniques in the literature use the stochastic nature of PDs for their detection. These techniques have been discussed here below.

Standard deviation

In [61], an automated technique has been proposed to separate PDs from the disturbance caused by fast switching currents. The commutation noise which occurs during switching are repetitive in nature for the solid state switches, unlike PDs whose occurrence is stochastic. This behavior of PD occurrence was used to extract them from the signal recorded at a voltage higher than PDIV using standard deviation (SD).

To do so, N frames of switching events (or traces) each of interval T and equal timesteps t_j were recorded by using an acquisition system like antenna or HFCT. Then the SD at time t_j can be calculated by using the following expression:

$$Std \ dev(t_j) = \sqrt{\frac{\sum_{i=1}^{N} x(t_{i,j}) - \overline{x}(t_{i,j})}{N}}$$
 (2.5)

Where, $x(t_{i,j})$ is the recorded signal value for ith trace at jth instant.

The stochastic presence of PDs in the processed signal leads to higher values at some time instants while the repetitive occurrence of commutation noise results in low SD. Figure 2-20 shows the acquisition of signal traces using an antenna at a voltage level above PDIV. It shows signals overlapped with commutation noise and PDs. The signal processed with SD confirmed the existence of PDs in acquired signals.

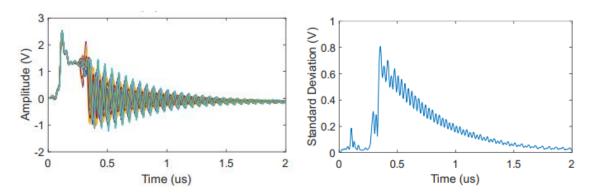


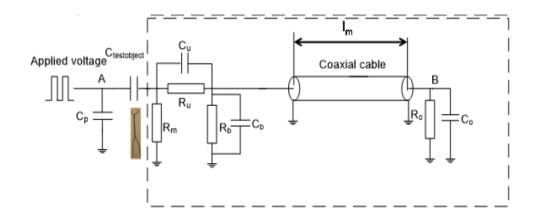
Figure 2-20: (Left) Signal traces measured by antenna at 2.8 kV which was higher than PDIV, shows overlapping of commutation noise and PDs; (right) signal traces processed with standard deviation provided evidence of PDs (source:[55])

Stochastic approach using PD decoupler circuit

The studies [60], [87], [88] show another technique of PD detection under square waveform. This technique works in two steps, as indicated here below, which is followed by its explanation:

- In the first step it utilizes a filtering circuit, which authors call as PD decoupler circuit to suppress the high frequency component in measured voltage signals
- To improve the possibility of PD detection, the measured signals are treated by moving average method in the second step.

The PD decoupler circuit as shown in Figure 2-21 is deployed in series with the object under test. In the PD decoupler circuit, the test object (C_{testobject}) along with resistance Rm forms the high pass filter. It is followed by voltage divider circuit constituted by Cu, Cb for high frequency and Ru, Rb for low frequency components in filtered signal. A coaxial cable connects this circuit to the oscilloscope. Ro and Co represent the channel impedance of oscilloscope where output signal is measured. As indicated in [60], it is possible to suppress the high frequency voltage signals of less than 20 MHz with complete PD decoupler circuit.



C _{testobject}	Rm	Ru	Rb	Ro	Cu	Cb	Со
15 pF	30 Ω	15 kΩ	0.2 kΩ	1 ΜΩ	10 pF	5 pF	15 pF

Figure 2-21: PD decoupling device proposed in [60]which can suppress high frequency component of up to 20 MHz in measured signal and the values assigned to the components of PD decoupling device

The acquired signals can still have high frequency components besides PD. Therefore, to further increase the probability of PD detection, the accumulated signals at Ro are calculated using moving average $(u_{acc}(k-1))$, and then subtracted from the currently measured signal $u_{Ro}(k)$ which is supposed to include PD(s). This eliminates the high frequency repetitive component mainly due to switching event. The final signal $u_{diff}(k)$ thus calculated as per given expression should only contain PD signals.

$$u_{diff}(k) = u_{Ro}(k) + u_{acc}(k-1)$$
 (2.6)

Figure 2-22 demonstrates the implementation of this technique. The Figure 2-22 (a) shows the moving average (average) of previous signals and latest trace with PD. Figure 2-22 (b) is

obtained after deduction of moving average signal from latest PD trace, which revealed two PD signals (PD1 and PD2). The PD1 and PD2 detected were reported to have 3.5 and 1 nC of charge magnitude. The study has presented the possibility of PD detection for a rise time as short as 15 ns with this technique.

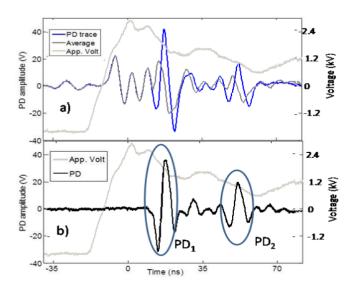


Figure 2-22: (a) Signal treated with moving average and a latest PD trace; (b) PDs recovered after subtraction of moving average waveform from latest PD trace ([60])

Balanced bridge configuration

The study made in [89] has discussed about a strategy of acquiring PDs using a balanced bridge circuit under square voltage waveform. In the study, the tests were performed on motor-coil samples under square voltage with slew rate of 0.4 kV/µs. To prepare the set-up of balanced bridge circuit, an identical sample without void is put in parallel to the void sample as shown in Figure 2-23. The voltages thus acquired across the shunt resistors are fed to the differential amplifier to eliminate the impact of impulse disturbance and detect PDs. In the same figure, the output of differential amplifier shows negative peak during switching event.

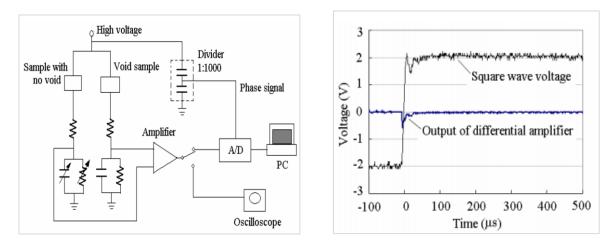


Figure 2-23: (Left) Measuring set up to detect partial discharges using balanced bridge circuit; (right) Square wave voltage and output of differential amplifier without PD events ([89])

Figure 2-24 illustrates the PD pulses obtained using this technique at 5 kV as provided in [89]. As can be seen, by implementing this technique PDs were detected, which is quite separated from the small negative peak during switching instant.

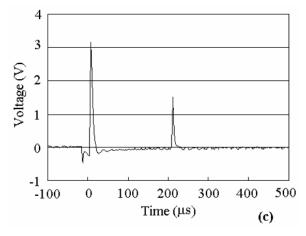


Figure 2-24: PD pulses obtained using balanced bridge circuit under square waveform at 5 kV (source: [89])

2.3.5. Summary

The studies show different PD detection techniques under fast rising square voltage. The optical method can be used for PD detection in transparent media at very short rise times, but there is no calibration method available. If the PDs detected by it are standardized, it can prove to be a decent PD indicator with dielectric liquid.

Unconventional techniques like HFCT would be easier to implement during online PD measurement of equipment like MFT. Also, PDs measured electrically by HFCT can be

quantified, which makes it more interesting. In this regard, simulation studies can provide necessary insights to ensure the applicability of electrical methods such as HFCT and some other found in studies. Hence to do this, following steps were undertaken:

- At first, a PD model and a circuit generating square waveform was developed in Simscape power system. Then, a high bandwidth HFCT probe available in testing facility was modeled, as described in section 2.4.
- After this an evaluation of HFCT model and other techniques found in studies were performed, to check their applicability for PD detection under high dV/dt.

These approaches are described in proceeding sections.

2.4. Simulation approach for PD detection

The PD prototype is usually modelled using three capacitors as shown in the Figure 2-25, termed as "three capacitor" or ABC model [67], [90]. Due to shortcomings of ABC model, another model called the ABCD model is proposed in this section and will be discussed just after the ABC model. This is followed by HV circuit generating square voltage. Finally, the methodology to obtain the transfer function of the HFCT is discussed.

2.4.1. ABC model

The concept of charge acquisition is based on measuring apparent charge from the object under the test and not the real charge occurring in the cavity. Often ABC model is used to represent this phenomenon as shown in the Figure 2-25. To understand this, lets consider a bubble cavity inside a dielectric liquid which is under voltage stress. Then the healthy part of the liquid insulation can be represented by capacitor C_a (= $C'_a + C_a$ ") whereas the portion of liquid insulation which surrounds the cavity can be represented by C_b (= $[C_{b'}C_{b''}/(C_{b'} + C_{b''})]$). The capacitor C_c denotes the cavity itself. C_a being the healthy part of insulation, is usually quite larger than C_b and C_c .

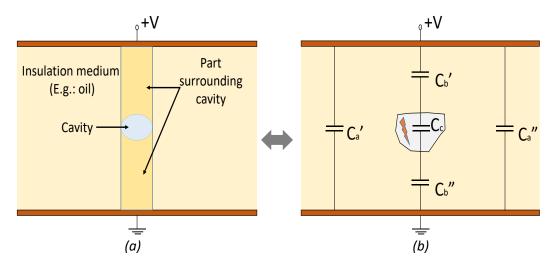


Figure 2-25: (a) Illustration of a cavity inside an insulation medium and (b) its representation as three capacitor model

As the voltage applied across the terminals of the object under the test increases, the electric field across the cavity would be strongly enhanced due to difference in permittivities and shape. The phenomenon of a PD event, leading to generation of apparent charge is depicted by the discharging of the capacitance in this model. The equivalent circuit of the discharge phenomenon is simulated with a resistor, capacitors and the switch S to represent spark gap as shown in Figure 2-26. As discussed in [91], R represents conductivity of weakly ionized thin channel due to streamer breakdown in void. Therefore, its value is set as so as to complete the discharge process in a short interval (in ns range). The capacitor discharges through the resistor, thus replicating the internal discharge process which generate a PD pulse as shown in Figure 1-15.

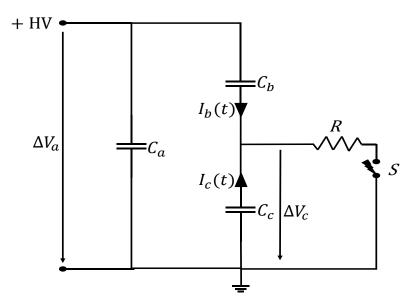


Figure 2-26: Equivalent circuit of partial discharge mechanism using three capacitor model

During the discharge process, there is a voltage drop (ΔV_c) across the capacitor C_c and charge lost internally is replenished by the capacitor C_a . The amount of real charge across the cavity (q_r) lost during discharge process can be expressed as:

$$q_r = \left(\frac{C_a C_b}{C_a + C_b} + C_c\right) \cdot \Delta V_c \approx (C_b + C_c) \cdot \Delta V_c \tag{2.1}$$

However, as said earlier, it is the apparent charge (q_a) value which can be detected across the terminals of the object under test. The (q_a) measurable across the terminals is the time integral of the current $I_b(t)$ shown in Figure 2-26. Under these circumstances, as discharge occurs, the voltage drop ΔV_a appearing across C_a is directly proportional to the capacitive divider ratio due to C_a and C_b . This can be expressed as:

$$\Delta V_a = \frac{C_b}{C_a + C_b} \cdot \Delta V_c \tag{2.2}$$

As $\mathcal{C}_a >> \mathcal{C}_b$, the q_a measurable across the test object can be expressed as:

$$q_a = C_a \cdot \Delta V_a \approx C_b \cdot \Delta V_c \tag{2.3}$$

Combining equations (2.1 and 2.3), a relation between (q_a) and (q_r) can be written as,

$$q_a = q_r \cdot \left(\frac{C_b}{C_c + C_b}\right) \tag{2.4}$$

As can be clearly observed from above equations, the apparent charge is a fraction of real charge and dependent on applied voltage. But as described earlier, some PDs have been found to be occurring at zero voltage due to presence of hetero charges, which cannot be simulated by this model as it is voltage dependent.

2.4.2. ABCD model

To simulate PDs even at zero voltage, an improved version of ABC model was developed and named as ABCD model. With this model, it was possible to generate a PD of own choice at any instant of time, even zero voltage. To do this, at first an impulse current generator was modeled which could produce charge of any value in pC. Then, with the inclusion of a capacitor Cd, the ABC model was modified as shown in Figure 2-27.

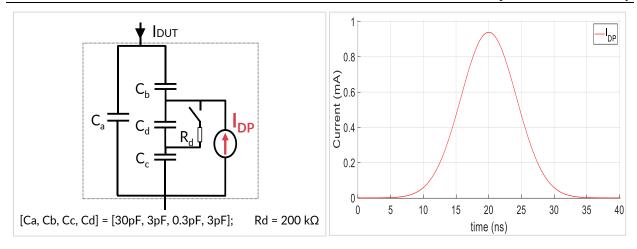


Figure 2-27: (Left) Circuit of ABCD model and values assigned to its components; (right) IDP of 10 pC generated in ABCD model using gaussian function

In the ABCD model, initially the switch remains closed and resembles like an ABC model with Ca, Cb and Cc. At the instant of a PD event, the switch opens, and the charge (I_{DP}) is injected to the circuit. Like this the charge of same magnitude as chosen for I_{DP} , could be measured across the model as apparent charge. After the PD event, the charge is damped through the resistor R_d as switch is closed again.

 I_{DP} is a current source whose amplitude and instant of occurrence can be controlled. To do so, function codes are written in Matlab. The user provides the instant of PD occurrence, amplitude, pulse width, number of PDs and type of PD (gaussian/ exponential) as input. These inputs are then sent as input to current controlled source block in Simscape, to generate the I_{DP} . Figure 2-27 also shows the I_{DP} of 10 pC generated in ABCD model. For the simulation studies presented later in this chapter, the gaussian type of PD is used, as shown in the same figure.

The ABCD model is then tested by generating a 20 pC PD 100 ns after the switching event. The values provided in Figure 2-27 are assigned to ABCD model.

Figure 2-28 shows the comparison between switching current (IDUT) with and without PD using this model. It can be observed that both switching currents, with and without PD overlap with each other except for the region with negative peak, which is the instant when PD is produced in the model. The negative peak can be seen by enlarging the region where PD occurred. This step ensured that ABCD model is suited for analysis of PD.

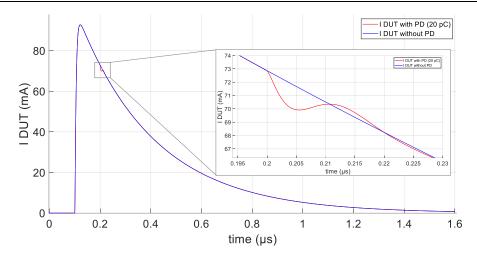


Figure 2-28: Comparison of switching current flowing through the DUT (IDUT) with and without PD using ABCD model; dV/dt across $DUT \approx 2 \ kV/\mu s$

2.4.3. Modeling of HFCT

As the HFCT can be used without modifying the electrical circuit, it makes it an attractive choice for PD detection.

With this notion, a high bandwidth HFCT (model: Solar 9123-1N), available in testing facility is modeled in Simulink, to better understand its performance and limitations. The bandwidth of this HFCT probe ranges from 10 kHz to 500 MHz and its transfer impedance is 1 to 5 Ω above 150 kHz as per its datasheet [92]. This work was done in collaboration with an intern from SuperGrid Institute.

For modeling the HFCT probe following steps were taken:

- Step 1: Characterization of HFCT using S-parameters
- Step 2: Conversion of S-parameters to equivalent Z-parameters
- Step 3: Determination of transfer function
- Step 4: Validation of the response of the transfer function

Additional explanation about S-parameters and related equations are in Appendix G.

Step 1: Characterization of HFCT using S-parameters

For components operating in radio or microwave frequencies, the characterization is often performed using S-parameters for which commonly used instrument is Vector Network Analyzer (VNA). Studies like [85] recommends to use a metallic box (also known as jig) for S-parameter

measurements of HFCT probe (Figure 2-29) to provide electromagnetic shielding. The copper cable passing through the aperture of HFCT links the input channel port P1 of VNA and 50 Ω matching resistor. The output response from HFCT is recorded at port P2 of VNA.

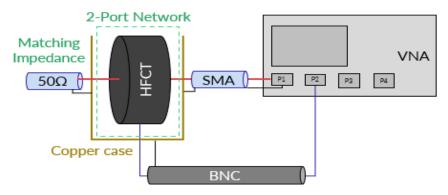


Figure 2-29: Block diagram of the set-up for measuring S-parameters of the HFCT probe

The S-parameters, thus measured between the frequencies 300 kHz to 3 GHz have been plotted in Figure 2-30. As can be seen, the transmission coefficients (S21 = S12) are identical (in amplitude and phase) indicating the HFCT obeys the reciprocity property; but reflection coefficients are not (S11 \neq S22). This is consistent with a passive component like this one.

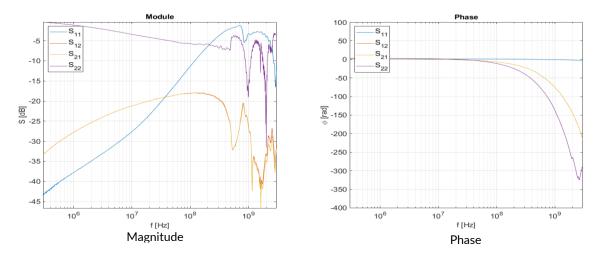


Figure 2-30: Magnitude and phase of S-parameters as a function of frequency

Step 2: Conversion of S-parameters to Z-parameters

By rearranging the linear equations, the S-parameters can be converted to Z-parameters which relate waves to voltage and currents at the two ports. the S-parameters can be converted to Z-parameters using the equations presented in Appendix G [93]. The Z-parameters thus obtained from the S-parameters are plotted in Figure 2-31.

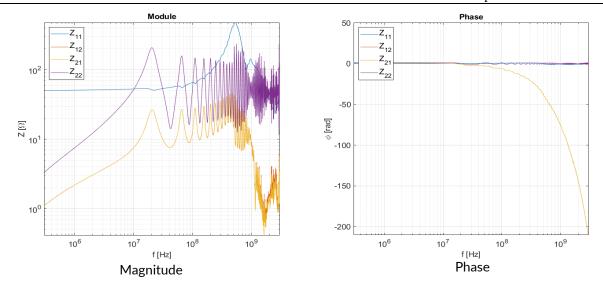


Figure 2-31: Magnitude and phase of Z-parameters as a function of frequency

The conversion to Z-parameters impedances shows similar behavior to S-parameters with Z21 = Z12 and Z11 \neq Z22.

Step 3: Determination of transfer impedance in MATLAB

The simulation environment (MATLAB Simulink) allows the modelling of differential equations and continuous functions. For this purpose, a function called tfest() (transfer function estimation) available in the "System Identification Toolbox" under MATLAB is used. This function estimates the transfer function from the measurement data in the form:

$$H(s) = \frac{N(s)}{D(s)} = \frac{b_m s^m + b_{m-1} s^{m-1} + \dots + b_1 s + b_0}{a_n s^n + a_{n-1} s^{n-1} + \dots + a_1 s + a_0}$$
(2.5)

Where, a and b: real coefficients; s: Laplace operator

With: $n \ge m$ for a physically feasible system.

The transfer function thus estimated with different number of poles and zeros are plotted in Figure 2-32. Finally, one model with 15 poles and 12 zeroes is selected which is a good trade-off between the model accuracy and simulation timing.

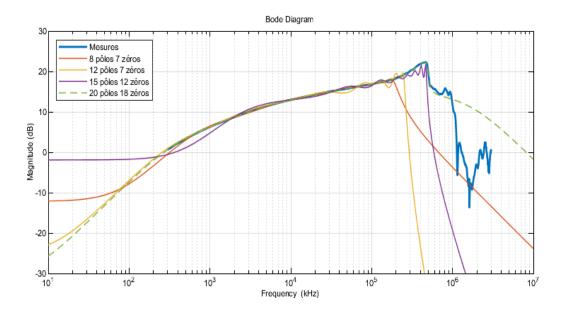


Figure 2-32: Comparison of estimated transfer functions of different orders

Step 4: Validation

To validate the performance of the selected model (15 poles and 12 zeros) with the real HFCT probe, a test like calibration is performed. The Omicron PD calibrator is used to provide a charge of known value and its voltage response from HFCT probe (Vmeas) is recorded using the oscilloscope. The recorded PD calibrator signal is also fed to the HFCT model in Simulink which generated a response Vsim, as shown in Figure 2-33.

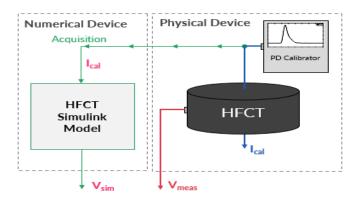


Figure 2-33: Set up for performance evaluation of the Simulink model with the HFCT

The output signal thus obtained from the HFCT model is compared with the response of real HFCT probe for 10 pC and 100 pC. It can be observed from the Figure 2-34, the simulated response from HFCT model (V_{simulated}) overlaps the curve of V_{measure} obtained by real HFCT probe for both 10 pC and 100 pC charge.

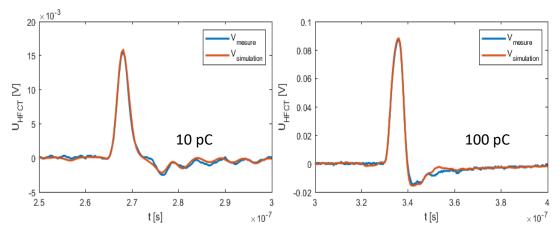


Figure 2-34: Comparison of HFCT model and real HFCT response for two pulses from calibrator

Through this step, the estimated model is validated, which can be used to study the behavior of real HFCT probe in simulation environment.

2.4.4. Circuit for generating square waveform

The modeling of square waveform test bench served the dual purpose. First was to use it for simulation with developed ABCD and HFCT model. While second was to create a schematic for development of a test bench with single HV switch to attain higher voltages in the test bench which will be discussed in Chapter-5. For generating square voltage waveform, the schematic as shown in Figure 2-35 was used.

The circuit thus proposed includes a high voltage DC generator (DC), the resistors (R1, R2 and R3), a capacitor bank (C), single HV switch and the device under test C_{DUT}. L1 represents the cable inductance connecting DC source to capacitor C, while L3 is the inductance of cable connecting HV switch to DUT. According to the datasheet of a HV switch [94], the rise time is between 1-20 ns. A resistor (Rn) and capacitor (Cn) are put across the ideal switch block available in the Simscape library, to achieve the realistic switching time behaviour in the simulation circuit.

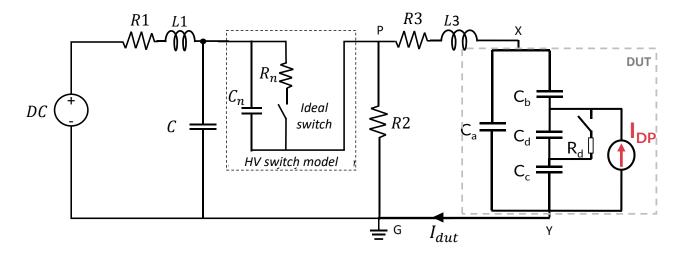


Figure 2-35: Schematics for PD detection under square waveform with ABCD model

Table 2-1: Values assigned to different parameters in the schematics with single HV switch

DC	R1/L1	C	Cn	Rn	R2	R3/L3	CDUT
1 kV	1mΩ/ 1μH	4 μF	100 pF	50 Ω	$2 M\Omega$	2.5 kΩ/1 μH	10 pF

The circuit operates on charging and discharging of capacitors. Its working principle has been explained in chapter-5 when this circuit will be implemented in the test bench to generate unipolar square waveform. The values considered for simulation has been presented in Table 2-1. With Ca as 10 pF, a rise time of about 57 ns was achieved across the DUT during simulations.

2.5. Assessment of electrical methods of PD detection

To understand the feasibility of electrical methods like HFCT for future test campaign under square voltage waveform, the HFCT model and some other presented in section 2.3, are assessed in simulation environment as discussed further.

2.5.1. HFCT

For this study, the HFCT model was put between nodes "Y" and "G" in the circuit shown in Figure 2-35 in Simscape electrical. Other parameters of the circuit were kept constant as indicated in Table 2-1. The rise time of voltage across DUT in HV circuit is close to 57 ns for an applied voltage of 1 kV across DUT. So, a 10 pC PD was produced 40 ns after the switching instant of voltage to assess the possibility of PD detection during a switching event.

Using the HFCT model in simulation, the trace with PD was recorded. After this the second trace was recorded without any PD. The HFCT signal with PD, without PD and voltage across DUT thus recorded are plotted together in Figure 2-36. The voltage starts rising at 0.1 µs. Both HFCT signals, with and without PD almost overlapped with each other, making it almost impossible to visually distinguish the PD in HFCT signal. This observation shows the difficulty in detecting 10 pC PD during rise time even with such a large bandwidth HFCT probe.

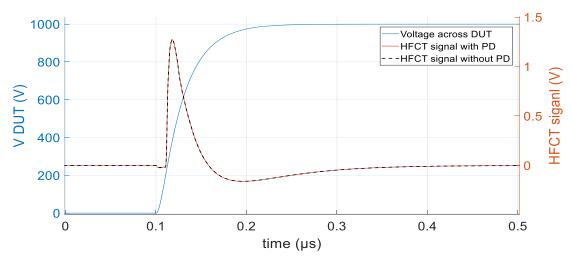


Figure 2-36: HFCT signals with a PD of 10 pC and without PD during voltage rise time

Then, the standard deviation or SD technique as discussed in section 2.3, is implemented to treat the recorded traces. To do so, the standard deviation function (std (A)) in Matlab is used. This function returns the standard deviation of the elements of matrix A, along one dimensional array. The HFCT signals, with and without PD formed the matrix A and treated using std (A) function. Figure 2-37 demonstrates the signal recovered using the standard deviation and the fast rising square voltage.

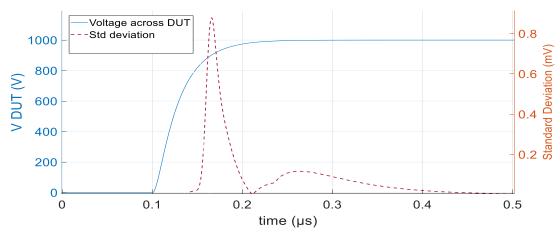


Figure 2-37: PD signal recovered using standard deviation

As can be seen in Figure 2-37, the standard deviation approach provides evidence of PD event, which occurred during a switching event. However, the standard deviation result presented above is true in ideal scenario. Therefore, to verify the applicability of this technique under experimental conditions, some sensitivity checks are performed.

In real experiments, the switching event may be impacted by jitter leading to a variable turn-on instant for each voltage cycle. As per the HV switch datasheet from Behlke [95], a typical turn-on jitter of up to 3 ns can be expected. This means, during real experiments, the traces recorded by HFCT probe can have variations in switching instants due to jitter.

To evaluate this scenario in simulation, the switching instant is delayed by 1 ns as compared to previous scenario and the HFCT signal is recorded without any PD. Thus, there are two traces (both without PD) from simulations, with switching instants 100 ns and 101 ns respectively, both captured by HFCT model. Then, the SD technique is applied on these two traces. The result thus obtained is plotted in Figure 2-38.

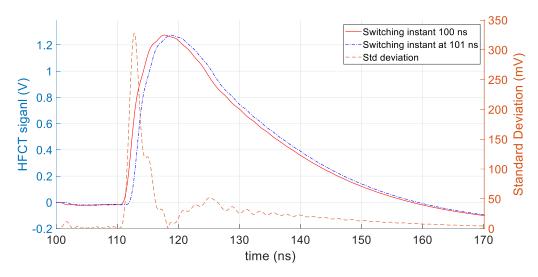


Figure 2-38: Standard deviation of two HFCT traces at two different switching instant without PD

As can be seen from Figure 2-38, from SD technique, a 1 ns delay due to jitter produces 300 mV, while the 10 pC PD shown earlier produced only a 0.8 mV. This means that a small magnitude PD of 10 pC, can be masked by large peak generated by SD technique under the impact of jitter.

During experiments, the slight variations can also occur in voltage level due to various reasons such as tolerance of components and parasitic elements. To check the applicability of SD technique under such circumstances, two traces from HFCT model are recorded at 990 V and 1000 V, both without PD. The 10 V variation accounts for 1 % change in voltage level. The voltage across DUT and HFCT traces at two voltage levels are plotted in Figure 2-39. The

magnified view at the tip of HFCT signals shows a small difference between them due to variation in voltage level.

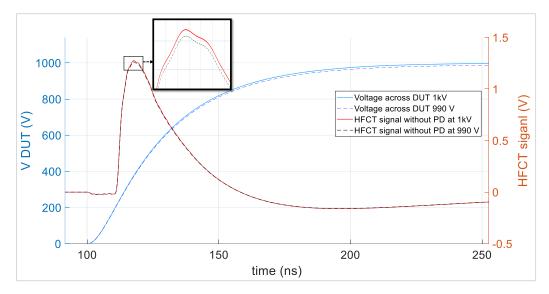


Figure 2-39: Traces of HFCT signal without PDs, recorded during rise time at 1 kV and 990 V keeping all other parameters constant

Applying SD technique on two HFCT traces yielded a peak of about 8 mV as shown in Figure 2-40. Again, this peak voltage obtained without any PD can be assumed to a PD signal.

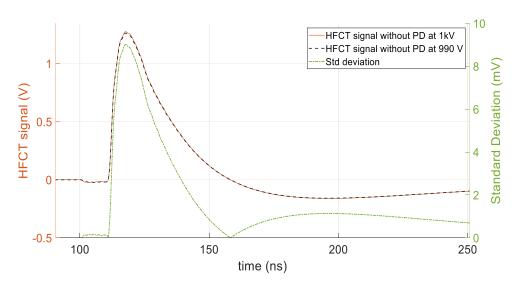


Figure 2-40: Standard deviation of two HFCT traces (without PD) obtained at two different voltage level

The interpretation of such voltage peaks from SD technique can be disguising. Therefore, it will be necessary to consider issues like jitter and small changes in dV/dt to ensure if the signal interpreted after standard deviation is a PD or not.

2.5.2. Other methods of PD detection

Other techniques like PD decoupler and balanced bridge are also studied to check their feasibility in detecting low magnitude PDs during rise time.

PD decoupler from [60]

The PD decoupler circuit is developed in Simscape Simulink with same values as in Figure 2-21, and added in series with the ABCD model as shown in Figure 2-41. The parameters of circuit generating square waveform remained same as stated in section 2.4.4.

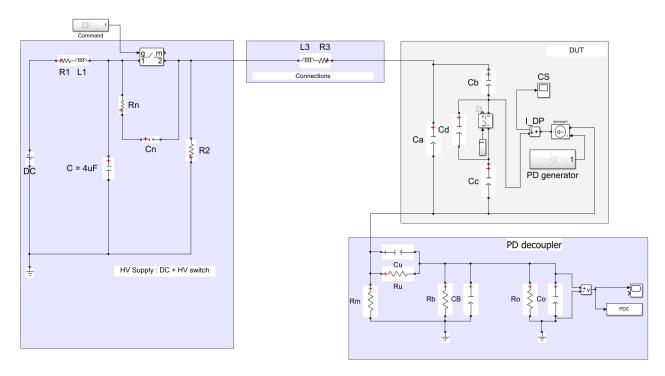


Figure 2-41: Circuit simulated in Simscape with PD decoupler circuit

Then, at first, the output signal from the PD decoupler (across Ro in PD decoupler) is recorded without any PD (Vnpd) to represent the accumulated trace of the measured signal. In the next step, a 10 pC charge is generated 40 ns after rising instant of voltage. The voltage from PD decoupler (Vpd) is recorded to represent the signal with PD. Figure 2-42 displays the Vpd and Vnpd recorded from PD decoupler. As can be observed that it is difficult to visually distinguish PD in Vpd signal and both Vpd and Vnpd quite overlap each other.

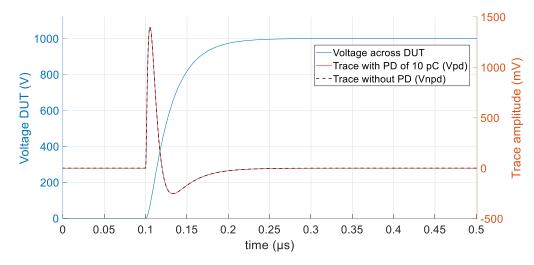


Figure 2-42: Signal traces with PD (Vpd) and without PD (Vnpd) recorded using PD decoupler circuit

Considering the ideal conditions of simulation, the moving average is not applied on the recorded Vnpd trace. As the averaging would return same result as the Vnpd trace itself. Then, as dictated in the study, Vnpd is subtracted from Vpd to retrieve the PD signal. The result thus obtained shows the presence of PD (Figure 2-43).

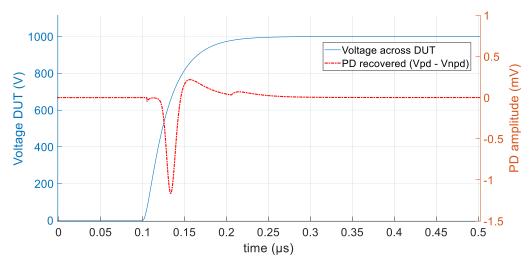


Figure 2-43: PD signal recovered by subtracting the previous signal trace (Vnpd) from the current trace (Vpd)

This shows the detection of low magnitude PDs occurring during rise time in ideal conditions. However, this may not be enough to consider this technique for implementation. Like the SD technique, this technique as well is tested by varying voltage and switching (jitter) conditions.

Considering the issue of jitter, following steps are taken to check the potential of this technique:

• Firstly, signal trace without any PD is recorded from PD decoupler, with switching instant as 101 ns (called as Vnpd101).

• The previously recorded signals from PD decoupler at 100 ns are named as, Vpd (with PD) and Vnpd100 (without PD at 100 ns instant).

To check if PD can be recognized in presence of jitter, Vnpd101 is subtracted from Vpd and Vnpd100, one by one. The idea behind this is to check if the PD event can be recovered even under impact of jitter.

As can be noticed from Figure 2-44 and Figure 2-45, there is hardly any difference between recovered signals in the two figures. The recovered signal has a peak of 500 mV which seems to have masked the 10 pC PD which has a peak of 1 mV (Figure 2-43).

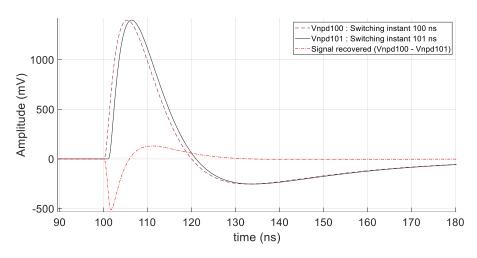


Figure 2-44: Signal recovered when Vnpd101 (signal without PD at 101 ns) is deducted from Vnpd100 (signal without PD at 100 ns)

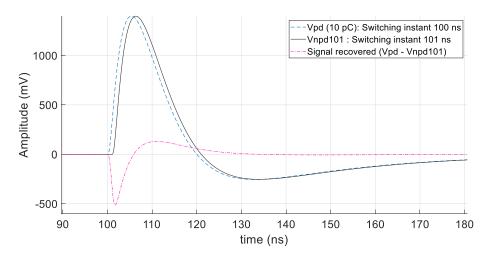


Figure 2-45: Signal recovered when Vnpd101 (signal without PD generated at instant 101 ns) is deducted from Vpd (signal with 10 pC PD generated at 100 ns)

Further, the applicability of this technique with varying voltage level is also checked. To do this, two traces, with PD, are recorded from PD decoupler circuit; one at 1 kV (called as *Vnpd1kV*) and other at 990 V (*Vnpd990*), to represent 1 % variation in voltage level as shown in Figure 2-46. The *Vnpd1kV* and *Vnpd990* seems to be overlapping until magnified.

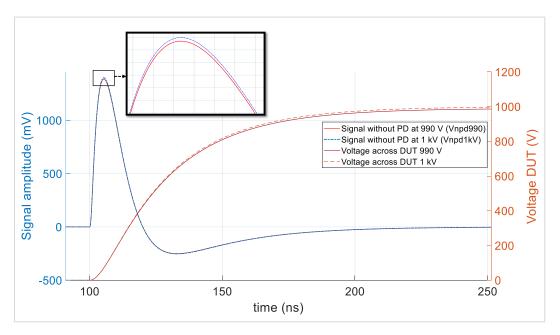


Figure 2-46: Signal traces (without PD) obtained at two different voltage level

In the next step, the *Vnpd1kV* is subtracted from *Vnpd990*, resulting in a negative peak of about 13 mV as shown in Figure 2-47. The recovered signal may give a false indication of an PD event.

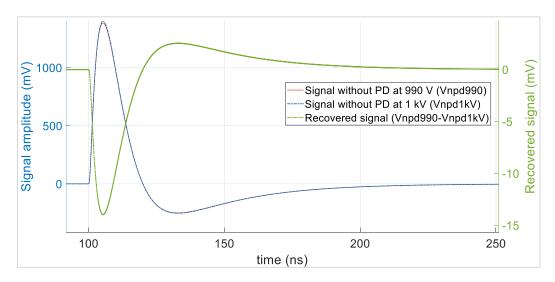


Figure 2-47: Signal traces (without PD) obtained at two different voltage level and recovered signal after deduction

Balanced bridge

Theoretically, this technique of PD detection appears quite attractive, but it requires two important conditions to be fulfilled: firstly, two DUTs of same value. Secondly, one of them should be PD free. For this assessment, an unmatched capacitor value (C1) was chosen to eliminate the criteria of identical DUT and still attaining a balanced bridge by adapting resistive shunts (Rsh1 and Rsh2). A balanced bridge circuit was thus constructed with the values indicated in Figure 2-48.

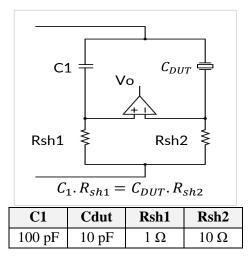


Figure 2-48: Balanced bridge circuit used in simulation

CDUT represents ABCD model from Figure 2-35. Other parameters of the circuit were same as in previous cases. Due to inclusion of 100 pF (C1) capacitor, the rise time of voltage across DUT was around 593 ns. The PD was generated 40 ns after voltage rise time. The voltage wavefroms thus recorded across Rsh1, Rsh2 and across DUT have been plotted in Figure 2-49. As can be observed, here as well it is difficult to visually identify the PD generated.

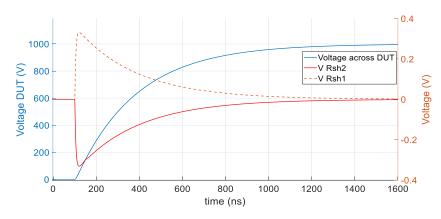


Figure 2-49: Voltage measured across Rsh1 and Rsh2 during switching in balanced bridge circuit

To replicate the differential amplifier in simulation environment, VRsh1 was subtracted from VRsh2 using the 'Sum' block in Simulink. The signal thus obtained, shows the possibility to detect PD with this technique during rise time of voltage, as plotted in Figure 2-50.

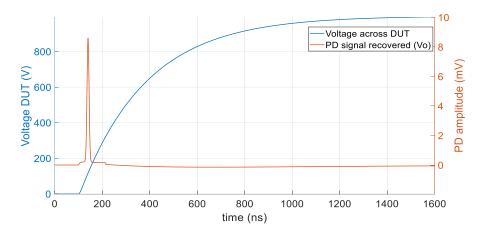


Figure 2-50: PD signal recovered using balanced bridge technique by cancellation of voltages across Rsh1 and Rsh2 due to commutation

Here as well, in ideal simulation environment, it was easy to extract the PD using this technique. But, at high frequency operation the resistor value may change due to skin effect. Also, usually the resistors have tolerance values of 5 % or 10 %. To assess if this technique can be useful in real set-up, the value of Rsh1 is changed to 1.05 Ω from 1 Ω , considering 5 % tolerance. Then simulation is performed without generating any PD event. The output voltage thus recovered at Vo is plotted in Figure 2-51.

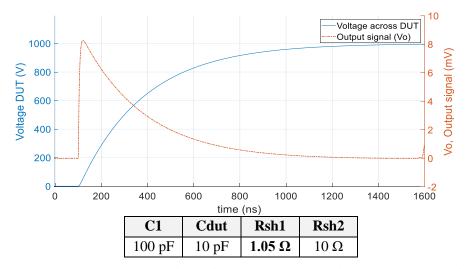


Figure 2-51: Output voltage waveform (Vo) obtained after subtraction of voltages across Rsh1 and Rsh2 when Rsh1 was changed to $1.05~\Omega$, considering 5 % tolerance in resistor value

As can be observed from Figure 2-51, the output signal obtained due to error in resistance gives the impression of a PD event. Therefore, this technique can complicate the acquisition of PD events during real experiments.

2.5.3. Discussion on electrical detection of PDs

The simulation studies performed here gave necessary insights regarding the capability of PD detection under high dV/dt. With HFCT model it is not possible to differentiate the PD occurring during rise time. The signal processing principles of PD detection such as standard deviation and moving average seems promising methods to recover PDs, but in ideal conditions. Impact of voltage waveshape, jitter must be taken into account while implementing these techniques which can, either mask low magnitude PDs or even be misinterpreted as an PD event. From both techniques, standard deviation and moving average method, the recovered PD signal had a peak voltage of about 1 mV for a PD charge of 10 pC. Detection of such low magnitude PDs in experimental set-up can be challenging in presence of background noise and disturbance caused by high dV/dt.

This situation puts up the question such as: what magnitude of PD can be recovered by these techniques in real experimental conditions? What conditions should be considered while implementing such techniques? Dedicated investigations will be necessary to understand this.

The balanced bridge circuit have showed the ability to cancel the commutation noise due to fast switching actions. But using this technique with dielectric liquid means preparation of PD (bubble) free DUT. Also, the tolerance of passive components like shunt resistor can lead to misinterpretation during PD detection.

2.6. Statistical analysis of measurement results

A classical approach to perform the statistical analysis on datasets available from BDV and PD tests is the calculation of average (\bar{x}) and standard deviation (SD) values. The average calculates the arithmetic mean of all the observations in a dataset while the SD indicates the spread from the average value. The range of observations included by one SD above and below average (expressed as { $\bar{x} \pm SD$ }) covers almost 68 % of observations, which is useful in comparing two datasets.

During experiments, often the number of tests conducted are limited. If the average values of two different experiments (such as tests with two different dielectric liquids) differs only slightly, it becomes important to assess if the average from two datasets are significantly different or same.

In other words, if the difference in average value for the limited number of tests just occurred by chance.

The SD is usually a measure of variability between two datasets, and therefore a useful indicator of scattered observations. For example, the extent of overlapping of the SD bars in two graphs, gives a clue about the significant difference between datasets. When the SD bars overlap considerably, the difference may not be statistically significant. When it overlaps a bit or doesn't overlap, there is a higher probability that difference in average values is significant. But this clue is not enough to draw a clear conclusion. In this situation, statistical analysis such as t-test can be used to ascertain if the difference between average values from two datasets is statistically significant [96]. The following section provides the steps to perform t-test.

2.6.1. Steps to perform t-test

The t-test is performed in following steps [96] [97], [98]:

- a. In the first step, the null hypothesis is considered. Usually, it means that there is no difference between the average of datasets from two groups or average of one dataset compared to some reference.
- b. Then, t-score is calculated based on one or two groups being studied, as discussed in paragraph 2.6.2.
- c. Like in other tests of significance, the measure of likelihood of the difference in the average from two datasets, is done by usually assuming p-value of 5 %. The p-value is evidence against the null hypothesis.
- d. The p-value is then estimated by a t-distribution table which corresponds to a p-value for known degree of freedom, which is also discussed in paragraph 2.6.2.
 - If the p-value from final calculation after running t-test is less than assumed 0.05, the null hypothesis is rejected, meaning that there is a significant difference between the average values of two datasets.
 - If the p-value is greater than 0.05, the null hypothesis cannot be rejected and it means that average of two groups are almost same.

2.6.2. Types of t-test

The t-test are categorized based on one or two groups being analyzed, which are as follows:

- Single or one sample t-test
- Two sample t-test

Paired sample t-test

A single t-test (t) is performed to compare the average of population of a group to a theoretical average value (\bar{x}_{th}) , and is calculated as:

$$t = \frac{\bar{x} - \bar{x}_{th}}{s / \sqrt{n}} \tag{2.6}$$

where, $\bar{x} = \text{sample average}$; $\bar{x}_{th} = \text{theoretical average value}$; s = sample standard deviation; n = sample size

The two sample t-test is used to compare the average between two groups of datasets obtained from two independent samples. For the case when variance is different, 't' is calculated as:

$$t = \frac{(\bar{x}_1 - \bar{x}_2)}{\sqrt{(\frac{s_1^2}{n_1} + \frac{s_2^2}{n_2})}}$$
(2.7)

where, \bar{x}_1 = first sample average; \bar{x}_2 = second sample average;

 s_1 = first sample standard deviation; s_2 = second sample standard deviation;

 n_1 = first sample size ; n_2 = second sample size

In case, if variance of two independent samples is equivalent, $s_1=s_2$ in equation 2.7.

When two different datasets are available from same sample, paired sample t-test is performed, which is given by:

$$t = \frac{\bar{x} - \Delta}{s / \sqrt{n}} \tag{2.8}$$

where, \bar{x} = average of sample of differences; Δ = average difference postulated in null hypothesis; s = standard deviation of sample of differences; n = size of sample of differences

The degree of freedom refers to the number of values which can vary in a study. Usually, it depends upon the size of dataset. Hence, for single t-test, degree of freedom is (n-1), while for two samples t-test it is $(n_1 + n_2 - 2)$.

To evaluate the experimental data obtained from PD tests, the t-test score is calculated using T.TEST() function in Microsoft Excel in this thesis. The T.TEST() function requires four parameters, array 1, array 2, type of tail distribution and type of sample (paired or two samples). The array 1 and array 2 are the two datasets being compared. Two tailed distributions have been chosen which is considered appropriate for attaining significance using t-test method. The use of paired or two sample is taken into account while calculating t-tests.

2.7. Summary

In this chapter, the partial discharge phenomenon has been discussed with a focus on dielectric liquids and liquid/solid insulation systems. Studies have shown that, the introduction of solid barrier in a dielectric liquid can lead to a different PD phenomenon than liquid itself in AC. This can be due to formation of space charges and residual bubbles from previous discharges in presence of a solid barrier.

The PD phenomenon under square waveform is influenced by various factors like dV/dt, switching frequency and duty cycle, which can lead to a different PD phenomenon than in AC 50 Hz. Due to limited research work with transformer insulation system, the PD mechanism is not very clear under square waveform. Hence, an experimental verification seems important to assess the transformer insulating materials under square waveform.

Following this, different PD measurement techniques under high dV/dt have been discussed, especially their capability and shortcomings as found in literatures. With the interest in electrical detection of PDs, simulation study was conducted. As found in studies, the PDs can be generated at even zero voltage which is not possible with classical ABC model. To overcome this issue, a new model (ABCD) has been introduced, which can generate PDs, even at zero voltage crossing, with the magnitude of choice. Further, a high bandwidth (up to 500 MHz) HFCT available in testing facility has been modelled to understand its behaviour in simulation environment.

The simulation studies were performed with the objective of PD detection during rise time. The simulation results infer that PD detection will not be easy even with an HFCT of large bandwidth. Some other approaches, such as the standard deviation, moving average and balanced bridge techniques have also been tried to recover PDs. The simulation results have shown the effectiveness of these techniques in cancelling commutation noise, but in ideal conditions. However, it has been seen that under the impact of jitter and variation in voltage waveshape, the recovery of signal using these techniques can either mask low magnitude PDs (such as 10 pC) or be disguised as PDs. Further, background noise and EMIs caused by switching events, can add further challenges during PD detection in real set-up.

From different measurement techniques found in publications, the optical measurement seems to be offering good immunity under high dV/dt and can detect PDs in dielectric liquids. Standardizing this technique may transform it into a good PD indicator in dielectric liquid.

Often, the experimental results are represented using average and standard deviation. But sometimes, it is not enough to state if the difference is significant when the averages of two sample sets have only slight difference. Therefore, a statistical tool called t-test will be used to evaluate the experimentally obtained results, in chapter-4 and chapter-6. The p-value thus

calculated using t-test assists in decision making if there is a significant difference between the average values of two datasets.

3. Device under test for partial discharge detection

This chapter discusses the design of the device under test (DUT) to perform the partial discharge (PD) measurements both in AC 50 Hz and square waveform. First, a literature review of different electrode configurations incorporating solid/liquid insulation system is provided. Following this, a needle-plane configuration completely immersed in liquid with barrier is chosen as the DUT.

Considering the voltage level of the testing facility, the electric field generated at the needle tip is compared with literature values to ensure the generation of PDs from an electrostatic point of view. This is done by creating the model of the selected configuration in a finite element method (FEM) software.

After the validation step of chosen DUT configuration, FE simulations are performed for different combinations of solid/liquid insulators, varying tip radius, gaps and barrier thicknesses to analyze their impact on the electric field generated at the tip of needle and at the liquid/solid insulation interface. As discussed earlier, synthetic esters can be a substitute to mineral oil for high voltage equipment. Therefore, both mineral oil and a synthetic ester are considered for these simulations.

Following the investigation in FE simulation, a DUT with needle-barrier plane configuration is decided for the partial discharge measurements. The choices of electrode geometry, solid barriers and dielectric liquids are made based on the observations from simulation results. The preparation of DUT, treatment of dielectric liquid and solid barriers are discoursed towards the end of this chapter.

3.1. DUT design methodology

Following steps are taken for designing the DUT configuration:

- Study of different configurations (plane-plane and needle-plane) from literature which are widely used to investigate PDs for transformer insulation system
- Selection of an appropriate electrode geometry suiting the voltage and testing requirements of the experimental test bench
- Selection of dielectric liquids and solid barrier materials with different properties such as permittivity.
- Analysis of selected DUT by comparing it with a study, using FEM simulations, to ensure the occurrence of PDs within 25 kV (maximum voltage limit of set-up)

3.1.1. Different types of configurations

The insulation of high voltage equipment like transformers mainly experiences uniform or quasiuniform electric field [99]. Studies like [14] and [18] have investigated the insulation performance of oil/pressboard combination under HVDC by using rogowski plane-plane configurations to generate a uniform electric field, as shown in Figure 3-1.

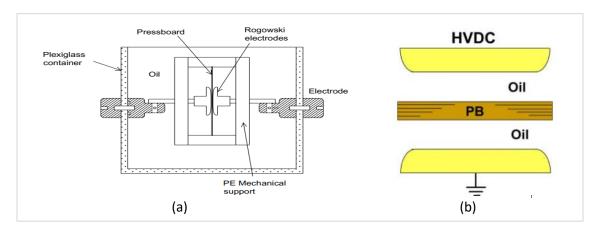


Figure 3-1: DUT models with pressboard in oil in plane-plane configuration from [14] and [18] used for investigating insulation performance under HVDC

While some other working groups like [71] and [90] have presented the characterization of oil/pressboard under divergent electric field using a needle-plane geometry as discussed in previous chapter (Figure 2-5). This kind of geometry is used to study the local enhancement of the electric field by sharp points, impurities or gas voids present at the interface or in the

dielectric liquid. In needle-plane geometry, the divergent electric field created at the tip (E_{tip}) with voltage (V) is given by the equation 3.1 [15], [101],

$$E_{tip} = \frac{2 \cdot V}{r \cdot \ln\left(1 + 4d/r\right)} \tag{3.1}$$

where,

V is the instantaneous applied voltage (in volt)

r is the radius of needle tip (in m)

d is the gap spacing between needle tip and plane electrode (in m)

The tip radius used in investigations by different research groups have ranged from 1 to 100 μ m to create a very high electric field. The technical report IEC61294 [102] which provides guidelines to measure PDIV in dielectric liquids recommends to use needles with tip radius of 3 μ m. Apart from tip radius, the gap 'd' if reduced can increase the electric field at the tip which is relevant from the equation 3.1.

The choice of electrode geometry, gap between electrodes and type of insulation under test have a significant role in determining the parameters of test bench, mainly regarding the voltage requirements. A higher voltage range would be necessary to study insulation behavior under uniform electric field with larger gaps as compared to divergent electric field with small gaps. Since the maximum attainable voltage is limited to 25 kVrms for the AC test set-up and 30 kV for the square-wave setup in the testing facility, the DUT must be designed to ensure the possibility of PD generation at a compatible voltage level.

3.1.2. Selection of DUT configuration

Looking at the studies addressing insulation of transformer and considering the attainable voltage level of the test benches, a DUT with needle-plane electrode configuration with barrier looked practical as shown in Figure 3-2. The needle tip of 1 μ m radius is considered to create a high local electric field with the plane measuring (BO in figure) 20 mm in diameter.

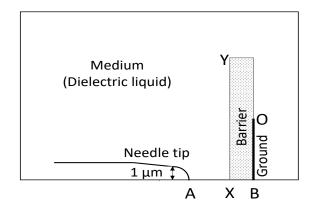


Figure 3-2: Design of axis-symmetric model of selected needle-barrier plane DUT (note: not to scale)

For comparative analysis, mineral oil and synthetic ester are considered. Also, different types of barriers like polyvinyl chloride (PVC), aluminum nitride (AlN) and pressboard (PB) are considered due to their differences in material properties, permittivity and surface homogeneity. Pressboards are widely used in power and distribution transformers [18], [22]. Therefore, it could be the first choice for MFT application. AlN ceramic finds its application in HV power modules [62]. The choice of PVC is driven by its low relative permittivity ($\varepsilon_r = 2.24$ which is quite close to the relative permittivity of mineral oil), as its availability. Table 3-1 provides some of the properties of these barriers found in literatures [17], [19], [103], [104].

Barriers	Relative permittivity (ε_r)	Tan delta	Туре
PVC	2.24	0.0017	Polymer based
AlN	8.5	0.0021	Inorganic
Pressboard (PB)	4.4	0.12	Organic

Table 3-1: Permittivity of the chosen barrier materials

3.1.3. Analysis of DUT with finite element method (FEM)

This section describes the modeling and simulation of the selected configuration using finite element method. The first objective here is to compare the electric field generated at the tip of needle with study to verify if field generated is sufficient to initiate PD events in the selected DUT configuration. The simulation using FEM are performed in FEMM 4.2 software which is an open-source finite element package.

Generally, for solving electrostatic problems, FEMM utilizes the scalar potential (V), to define the electric field intensity (E), as follows

$$E = (-\nabla \cdot V) \tag{3.2}$$

From the Maxwell's equation we have,

$$\nabla . E = \rho / \varepsilon \tag{3.3}$$

 ρ : charge density in an enclosed volume and

 $\boldsymbol{\varepsilon}$: permittivity of material

For the simulation studies, all dielectrics are considered perfect; spaces charges are not considered. Only relative permittivity values provided in Table 3-1 are used. Therefore, the charge density in this case becomes zero and combining (3.2) and (3.3), the differential equation solved by FEMM will be [105]

$$\nabla^2 \cdot V = 0 \tag{3.4}$$

The following subsection discusses the geometrical modeling and simulation results obtained.

The study in [67] provides the investigation of PDIV and PD inception field (PDIF) in needle-plane configuration at different gaps in dielectric liquids, using a 3 μm needle tip and a grounding plane of 50 mm diameter. As reported in the study, the PDIFs in mineral oil and synthetic ester can range between 1200 kV/mm and 1600 kV/mm for gap spacings of 5 mm to 50 mm.

The generation of such high electric field does not seem possible in a plane-plane configuration with the maximum voltage level available in test bench. Even at maximum voltage of 25 kV, a perfect plane-plane electrode configuration with a gap spacing of 1 mm would produce a uniform field of 25 kV/mm. The inclusion of barrier would make it almost impossible to generate PDs in plane-plane configuration. This also fortifies the choice of needle-barrier plane configuration for PD investigation.

For a gap of 10 mm, the study [67] reports the PDIV and PDIF of about 14 kVrms and 1600 kV/mm respectively in Gemini X (mineral oil). As the PDs of maximum apparent charge are detected at 90° of phase angle, therefore study has reported the PDIF calculations by using peak value of PDIV, which corresponds to about 20 kV. This case is chosen for comparative analysis. To do this, at first the axis-symmetric geometry of the DUT from the study (Figure 3-3) is developed in FEMM.

In the next step, the selected DUT configuration (Figure 3-2) with a barrier, 1 µm tip radius and gap spacing of less than 1 mm is created. The voltage applied across the needle during FEM

simulations is instantaneous and hence quoted in peak (and not rms). For mesh sizing around the tip curvature, the minimum possible segment size in FEMM software is chosen for finest discretization. The smallest mesh size thus achieved around 1 µm tip is 0.5 nm. Away from the tip (in dielectric medium), the automatic meshing is chosen which increases in size (see Figure 3-4). This is a trade-off in simulation time and accuracy of the tip field. For the selected configuration, a longer length of barrier (XY) than grounding plane (BO) is considered. The values of parameters for the models are provided in Table 3-2.

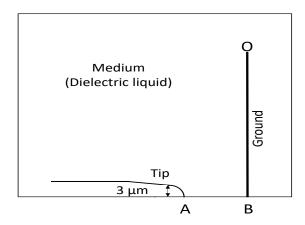


Figure 3-3: Representation of axis-symmetric model of needle-plane DUT adapted from study [67](not to scale)

Table 3-2: Values used for constructing axis symmetric models of a DUT from study and selected model of DUT in FEMM

Parameters	Needle plane (adapted from Study [67])	Needle-barrier-plane (selected DUT configuration)	
Tip radius	3 μm	1 μm	
Barrier length (XY)	-	20 mm	
Barrier thickness	-	1 mm (XB) (considering a PVC barrier of $\varepsilon_r = 2.24$)	
Grounding plane (BO)	25 mm	10 mm	
Gap (AB)	10 mm	1.7 mm (AX + XB)	
Dielectric medium	Mineral oil ($\varepsilon_r = 2.2$)	Mineral oil $\varepsilon_r = 2.2$	
Voltage applied	20 kV	10 kV	

For the DUT in study [67], the FEMM model yielded a tip field of about 1724 kV/mm at 20 kV, which is quite in same range with the PDIF mentioned in the study (1600 kV/mm at same voltage level). Also, the theoretical estimation of tip field using equation 3.1, for this configuration is 1404 kV/mm. Therefore, it can be observed that the tip field simulated with FEMM is in same range as literature and theoretical values. The difference is mainly due to the small variation in needle length and tapering of needle constructed in FEMM.

While the selected DUT configuration in FEMM, produced a tip field of $2476 \, kV/mm$ at only 10 kV. A comparison between fields generated by 3 μm tip from the study and 1 μm tip from chosen DUT configuration can be seen in Figure 3-4 and Figure 3-5.

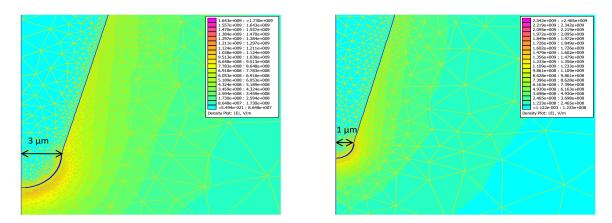


Figure 3-4: (Left) 3 µm tip built in FEMM from study [67] produced a tip field of 1724 kV/mm at 20 kV; (right) 1 µm tip built in FEMM for selected DUT configuration produced a tip field of 2476 kV/mm at 10 kV

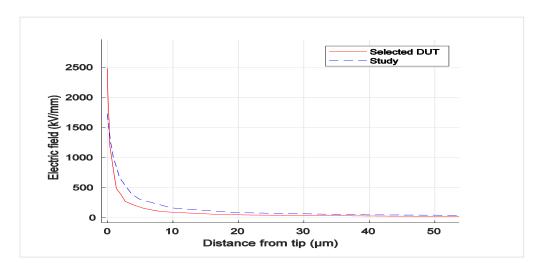


Figure 3-5: Comparison of electric fields at needle tip between selected DUT with 1 μ m tip radius at 10 kV and the DUT from study [67] with tip radius of 3 μ m at 20 kV

As can be clearly seen in Figure 3-5, the tip field for the selected DUT radius is quite higher than the PDIF generated in the model from the study [67]. This should result in generating PDs at even lower voltage than 10 kV used in this simulation. Indeed, other parameters like impact of space charges or material conditions are neglected in these simulations. Thus, the FE simulations performed here supports the choice of DUT configuration and shows the possibility to generate PDs with selected barrier and dielectric liquid as provided in Table 3-2.

3.2. Additional investigation with selected DUT configuration

After the validation of selected DUT configuration, same model (with needle-barrier-plane configuration, completely immersed in dielectric liquid) is considered for further studies. Here the aim is to study the impact of various parameters like permittivity, thickness of barrier, gap and tip radius on the electric field at the tip and interface of liquid/solid insulation. Therefore, barrier materials possessing different characteristics and permittivity are chosen. The barrier materials and dielectric liquids discussed in section 3.1.2 are chosen for the study.

The parameters of needle-barrier plane (or selected DUT) configuration in

Table 3-2 correspond to the "reference DUT" for all the simulations below. Thus, unless specified otherwise, the geometry has a tip radius of 1 μ m, a gap between tip and barrier of 0.7 mm and 10 mm-wide grounding plane; the needle tip is set at +10 kV while the grounding electrode (plane) is assigned 0 V; the liquid dielectric is considered to be a perfectly insulation medium with zero charge value; a 1 mm-thick and 20 mm-long block is modeled as the barrier, which has the permittivity value of PVC. The boundary conditions remained same for all the analyses.

Due to huge difference in dimension of the tip radius (1 μ m) and the barrier length (20 mm), it is not possible to demonstrate their dimensions in the same figure. Therefore, a magnified image of the needle in the simulated model from FEMM is also included in Figure 3-6.

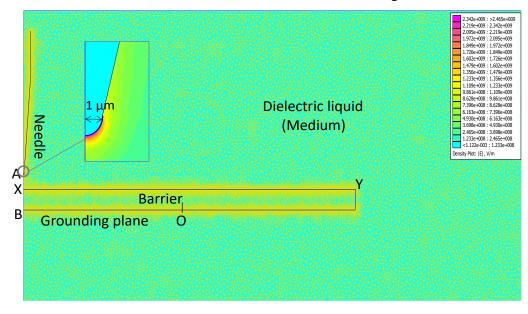


Figure 3-6: Full view of the DUT configuration with electric field and meshing around the tip in FEMM with a magnified view of needle tip

The points marked in the figure represent the following elements of the configuration:

• AX : Gap between tip and barrier (0.7 mm)

• XB : Thickness of barrier (1 mm)

• BO : Half-Length of grounding electrode (10 mm wide)

• XY : Barrier half-length (20 mm)

The electric field distributions are studied by varying one parameter at a time such as the length of barrier, tip radius, permittivity of materials and thickness of barrier. The data files thus obtained from FEMM are processed in Matlab. These results are discussed in the following sections.

3.2.1. Selection of barrier dimension

With needle-barrier plane configuration, there are chances that discharges appearing at needle tip propagate towards the edges of the barrier [106] if barrier size is less than grounding plane. This can lead to flashover if voltage increases above PDIV. For experiments, it is intended to avoid any flashover event, more importantly to carry out PD tests under square waveform, as the datasheet of the HV switch recommends avoiding any short circuits and sparkovers [95].

Therefore, the objective here is to determine the barrier dimension to prepare for PD tests. As the diameter of the grounding plane in the reference DUT is 20 mm, barriers of 30, 40 and 50 mm are studied here. 1 mm thick PVC immersed in mineral oil is considered for simulation. Being an axis-symmetric model, only half-lengths (i.e., 15, 20 and 25 mm) are modeled. To study the field distribution along the barrier surface, tangential electric field is measured. The tangential electric field is analyzed from point X to the farthest end Y as shown in Figure 3-6.

The results thus obtained have been plotted in Figure 3-7. As can be observed in the graph, the peak of electric field always occurs at point X (0 on horizontal axis). This is due to high local electric field created at the tip. Tangential electric field decreased exponentially along the surface of the barrier up to point O (edge of grounding plane). After this point, there is a further drop in field along the barrier surface.

From this graph, it can be assumed that a barrier longer than grounding electrode (i.e. more than 20 mm), should be a sufficient to avoid any flashover at or above PDIV, due to low electric field intensity at farthest end of barrier surface.

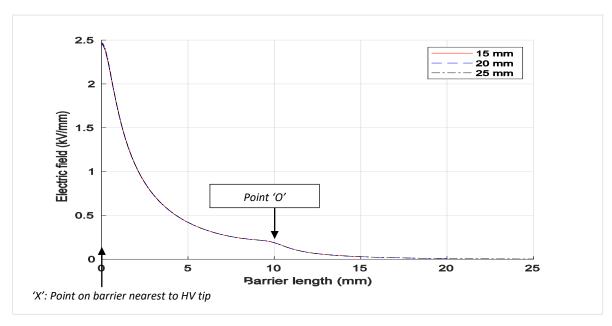


Figure 3-7: Tangential electric field along the barrier surface for different lengths of barrier

3.2.2.Impact of tip radius

Here, tips of 1 μ m, 10 μ m and 100 μ m radius are modeled and studied in FEMM, still using the reference DUT for all other parameters values. The electric field is analyzed vertically from the HV needle tip to the grounding electrode i.e. from "A" to "B" as marked in Figure 3-6. The electric field values along this line are plotted in Figure 3-8.

As can be observed from the graph, the maximum electric field occurred at the tip of 1 μ m radius. By increasing the tip radius from 1 μ m to 10 μ m and 100 μ m, the electric field at the tip reduced by about 83 % and 97 % respectively, under same voltage conditions. This phenomenon is consistent with equation 3.1 as the electric field is highest for the smallest tip radius. Here, it should be noted that the electric field at the tip calculated from equation 3.1 would be different from what is shown in the graph, as the formula does not consider the presence of barrier with a different permittivity than fluid. It should also be noted from Figure 3-8 that for a 1 μ m tip, the electric field drops by more than 95 % just 25 μ m away from the tip compared to the field at the tip.

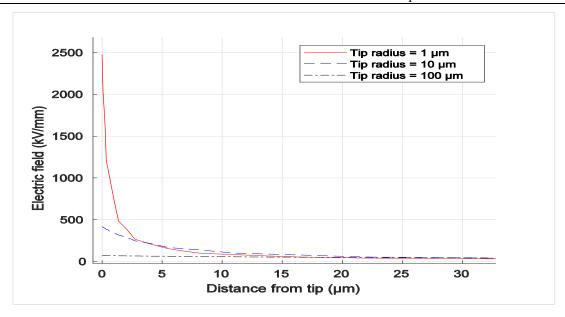


Figure 3-8: Impact of tip radius on the electrical field near the tip

On the other hand, the electric field at liquid/solid interface (Figure 3-9) shows a different trend and values much lower than at the tip. Considering the PDIF value of more than 1200 kV/mm from the study used for verification of DUT, the field at the interface (around 3 kV/mm) seems quite small to trigger a PD event in ideal conditions (in the absence of impurities and space charges).

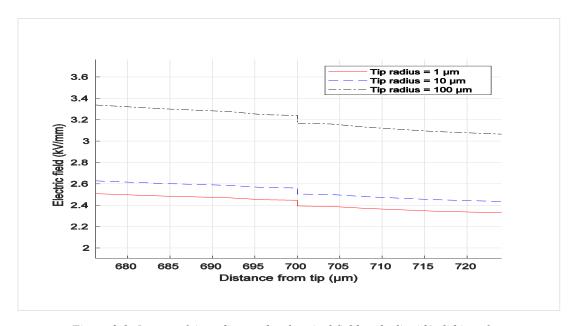


Figure 3-9: Impact of tip radius on the electrical field at the liquid/solid interface

So, for the selected electrode configuration, the 1 μ m tip radius is crucial in triggering a discharge event in the region around the tip as compared to larger tip radii for the voltage level

considered here in simulation (10 kV), due to the high local electric field created. A higher voltage level would be necessary to generate PDs with a larger tip radius. This is verified with experiments as discussed in the next chapter.

3.2.3.Impact of permittivity of barriers

The distribution of electric field when the flux is normal at the interface of two dielectrics, is given by the following expression [15],

$$\frac{\varepsilon_{br}}{\varepsilon_{oil}} = \frac{\overrightarrow{E_{oil}}}{\overrightarrow{E_{br}}} \tag{3.5}$$

where,

 ϵ_{br} : permittivity of barrier ϵ_{oil} : permittivity of oil $\overline{E_{oil}}$: electric field in oil $\overline{E_{br}}$: electric field in barrier

The above expression mainly holds true for electric field under parallel plate configuration.

To study the impact of varying permittivity for needle-barrier plane configuration, the relative permittivity of the barrier is varied to represent the permittivity of PVC, pressboard (PB) and AlN in accordance with Table 3-1, keeping the thickness of barrier constant (1 mm). The permittivity of surrounding dielectric liquid was also changed to replicate mineral oil (MO, ε_r = 2.2) and synthetic ester (SE, ε_r = 3.2). The electric field is analyzed from "A" to "B" as shown in Figure 3-6.

Moving away from the tip, the electric field can be seen to be decreasing exponentially for all cases in Figure 3-10. A magnified view of tip field has also been presented in the same figure.

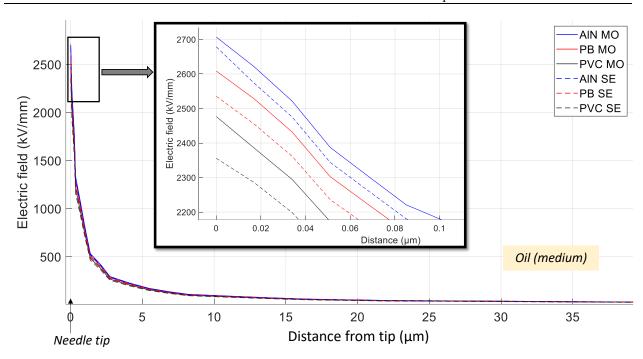


Figure 3-10: Electric field as a function of distance from needle tip, with a magnified view near the tip, for barriers of different permittivity in mineral oil (MO) and synthetic ester (SE)

While Figure 3-11 presents the electric field at the liquid/solid interface for different barriers in mineral oil (MO) and synthetic ester (SE). The observations from the graph can be segregated as follows:

- The electric field at the needle tip is found to be higher when the difference between the relative permittivity of barrier and dielectric liquid is larger. For instance, the electric field at the tip for AlN in mineral oil is about 2700 kV/mm (ε_r are 8.5 and 2.2 respectively) while for PVC in synthetic ester is about 2350 kV/mm (ε_r are 2.24 and 3.2 respectively).
- At the liquid/solid interface (0.7 mm away from needle tip), a sudden change in electric field at the liquid/solid interface can be observed. This change of electric field is maximum for AlN in mineral oil (about 75 % drop) while least for PVC in mineral oil (about 4 %), who have almost same relative permittivities (2.24 and 2.2 respectively). While for PVC in synthetic ester, the electric field increased inside the barrier as compared to that in dielectric liquid.

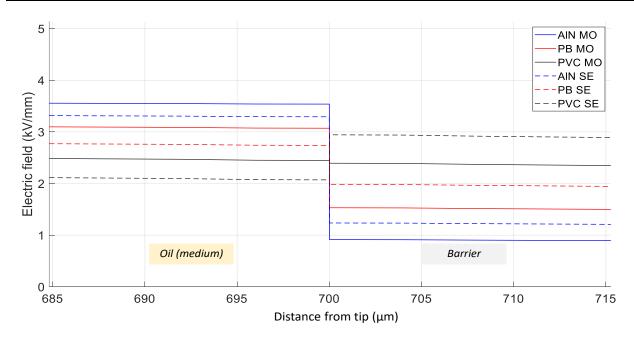


Figure 3-11:Electric field at the interface of liquid/solid insulation, for barriers of different permittivity in mineral oil (MO) and synthetic ester (SE) as dielectric medium

Equation 3.5 can be used to explain the electric field distribution at the interface of two dielectrics: the electric field decreases while passing from a medium of lower permittivity to a medium of higher permittivity and vice versa. This can be observed for all liquid/solid combinations as shown in Table 3-3. In the table, the permittivity values of barrier are provided in top row, while for two oils (MO and SE) are in extreme right column. As can be seen, the ratio between the electric fields in oil and barrier at interface obtained from simulations are almost same as the ratio between the relative permittivities of barrier and oil.

Table 3-3: Calculation of ratio of permittivity in barrier and oil and comparison with ratios of electric fields obtained from simulations in oil and barrier at the interface

Barrier $(\varepsilon_{r_barrier})$	PVC (2.24)	Pb (4.4)	AlN (8.5)	Oil (ε_{r_oil})
$rac{arepsilon_{r_barrier}}{arepsilon_{r}}$	1.02	2	3.86	MO (2.2)
(calculated using permittivity values)	0.70	1.38	2.66	SE (3.2)
$rac{E_{oil}}{E_{barrier}}$	1.02	2.01	3.92	MO (2.2)
(calculated from simulation)	0.70	1.38	2.67	SE (3.2)

Another observation is made while comparing tip field in synthetic ester and mineral oil for changing barrier permittivity. When the permittivity of the barrier almost doubles (PVC to Pb), the electric filed at the tip increases by about 5 % for mineral oil, while it increases by about 8 %

with synthetic ester. However, considering the doubling of permittivity, this change in tip electric field seems rather small.

3.2.4.Impact of barrier thickness

For this investigation, the thickness of barrier is varied between 1 mm to 4 mm to analyze its impact on electric field distribution, using the reference DUT described above. The oil gap between needle tip and barrier is kept constant (0.7 mm) and the electric field is measured from point "A" to "B" shown in Figure 3-6.

Table 3-4 presents the electric field at the tip obtained from simulation for varying barrier thicknesses. It can be observed that for a thinner barrier, the electric field is highest at needle tip. Considering the electric field for 1 mm thick barrier as reference point, when the barrier thickness increases by 100 % (1 to 2 mm), the electric field at tip diminishes by about 7 %. While it decreases by about 11 % and 14 % when thickness is changes by 200 % (1 to 3 mm) and 300 % (1 to 4 mm) respectively. As the percentage reduction in electric field is quite small with respect to percent increase in barrier thickness, the PDIV may not be very sensitive with barrier thickness in selected DUT configuration.

Table 3-4: Electric fields at the tip (Etip) obtained from simulations for varying thickness of barrier; and the approximate percentage decrease in tip field with respect to increase in barrier thickness

Barrier thickness (mm)	Etip (kV/mm) (from simulation)	% increase in thickness	% decrease in E _{tip} field
1	2476		
2	2307	100	7
3	2202	200	11
4	2123	300	14

However, this investigation exhibits the possibility of generating PDs in the selected DUT configuration even with thicker barriers (at least up to 4 mm) at 10 kV. It thus aids in selecting the range of thickness of barrier samples for PDIV tests, which is discussed in section 3.3.

3.2.5.Impact of varying gap between tip and barrier

Prior to the PDIV investigation, the impact of error on gap spacing was not clear. Therefore, to understand its impact the electric field distributions are simulated at 0.5 mm, 0.7 mm and 1 mm

gap spacing. While modeling the geometry of the DUT, the ground plane and barrier are shifted, keeping all other dimensions constant (and consistent with the reference DUT).

Electric field at the tip thus obtained from simulation are presented in Table 3-5. As can be seen from the table, when gap spacing increases by 40 % (from 0.5 to 0.7 mm), the tip field (E_{tip}) falls by about 1 %. Similarly, for a 43 % increase in gap (from 0.7 mm to 1 mm), tip filed reduced by about 2 %.

Gap spacing (mm)	% increase in gap spacing	Etip (kV/mm) (from simulation)	% decrease in Etip
0.5		2500	
0.7	40	2476	0.96
1	43	2427	1.98

Table 3-5: Electric fields at the tip (Etip) obtained from simulations by varying gap spacing

From the above table, it can be observed that a small gap variation from reference value (0.7 mm) does not change the tip field largely, so it may not have a significant influence on PDIV for selected DUT configuration.

Nevertheless, the gap spacing should be set carefully to ensure consistent testing. For PD measurements, a specific gap spacing procedure is adopted during the DUT preparation as discussed further in section 3.4. Also, the analysis of the effect of gap length is reproduced experimentally for verification in the next chapter.

3.2.6. Observations from FEM analysis

The FEM simulations show that the selected needle-barrier plane configuration can generate high enough tip field to trigger a PD event at 10 kV. Moreover, it provides an understanding of the electric field distribution as a function of changing permittivity, barrier thickness, tip radius and gap. The main observations made from FEM analysis can be summarized as follows:

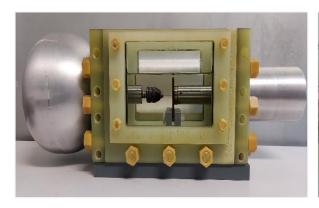
- It is possible to generate PDs with 1 µm tip radius and gap spacing of less than 1 mm for selected needle-barrier plane configuration at 10 kV. It is an important verification considering the voltage limitation of the test benches in AC and square waveform.
- For the chosen DUT configuration, the tangential electric field reduces exponentially
 along the surface of barrier. Therefore, a barrier wider than the grounding plane should
 avoid any flashover, which is an important criterion as per the datasheet of high voltage
 switch.

- The tip radius could be an important factor in triggering a discharge event in the region around the tip. An increase in tip radius from 1 μm to 10 μm and 100 μm can diminish the electric field at tip by 83 % and 97 % respectively.
 - On the other hand, the electric field at the interface is found to be quite small as compared to the field generated at the tip at same voltage. Assuming the absence of space charges, only the tip field might play a significant role in triggering a PD event.
- A large difference in permittivity of barrier and surrounding dielectric liquid leads to uneven distribution of electric field in the composite insulation system. The highest electric field at the tip has been witnessed for AlN in mineral oil. Also, a large variation in electric field has been observed at the liquid/solid interface for AlN in mineral oil (about 75%) while least for PVC in mineral oil (about 4%).
- The increasing thickness of barrier diminishes the electric field at the tip. By considering the streamer initiation due to high electric field at the tip, increasing the thickness might elevate the inception voltage. However, this effect remains small, with a 14% reduction in electric field for a 400% increase in barrier thickness (from 1 to 4 mm). Nevertheless, in the selected DUT, high enough electric field can be generated to produce PDs even with a barrier as thick as 4 mm in ideal conditions.
- The slight variation in gap spacing can influence the electric field at the tip, but this
 change may not have a substantial impact on PDIV. However, for coherent testing with
 different combination of liquid/solid insulation, the gap spacing during DUT preparation
 must be carefully controlled.

3.3. DUT for PD measurements

The FE simulation shows the possibility of triggering a PD event with the selected needle-barrier plane configuration from a purely electrostatic point of view. Hence, it is decided to use a DUT with a needle tip of 1 μ m radius and gap spacing of 0.7 mm, as it is compatible with the voltage level available in our testing facilities.

The DUT cell thus chosen is made of resin reinforced with glass fiber with a Pyrex glass window for visualization as shown in Figure 3-12. Its inner dimensions are 18 cm x 9 cm x 10 cm (length x width x height). The two ends of the DUT cell have cylindrical metallic shields. The one on the side of needle (with larger diameter) is connected to the high voltage. As the shield is electrically connected to same potential, it minimizes the effect of corona discharges.



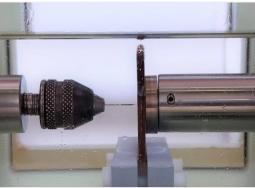


Figure 3-12: (left) Device under test with needle-barrier plane configuration completely immersed in mineral oil used for all partial discharge measurements (right) magnified view of the small gap between needle tip and barrier

In the DUT, the solid dielectric barrier rests against the grounding electrode, completely immersed in dielectric liquid. The tungsten needle is clamped using a small mandrel and connected to high voltage potential. The plane ground electrode of 20 mm diameter is fabricated with stainless steel.

During the DUT preparation, the needle tip was found to get deformed when pushed against with hard surfaced barrier like AlN. Therefore, a gap between tip and barrier is achieved by using a 0.7 mm thick FR4 (glass reinforced epoxy) spacer. The needle is always carefully mounted in the DUT to avoid any contact with hard surface (such as grounding plane). The tip is then slowly approached until it touches the FR4 spacer, which is then removed, and mandrel is tightened.

As discussed earlier in section 3.1, different combinations of liquid/solid insulations which could find application in high voltage equipment with varying properties are considered for this work. Nytro 4000X (mineral oil) and Midel7131 (synthetic ester) are used as dielectric liquid; impregnated pressboard, PVC and AlN as barriers. As the barrier dimension should be wider than the grounding electrode (i.e., more than 20 mm) to avoid any flashover, the dimensions of the barriers are chosen accordingly. The dimension, thickness and number of barrier samples chosen for tests are provided in Table 3-6.

Barrier samples	Thickness (mm)	Sample size (mm × mm)	Samples tested with Nytro 4000X	Samples tested with MIDEL 7131
PVC	1	40 × 40	5	5
	2	40 × 40	5	5
AIN	0.63	40 × 40	3	3
	1	40 × 40	3	3
Impregnated Pressboard	2	36 × 36	5	NA

Table 3-6: Specification of tested solid barriers

3.4. DUT preparation

This section discusses the steps taken to prepare the DUT cell for the partial discharge measurements under AC 50 Hz and square waveforms.

Treatment of barriers

Prior to the PD measurements, the barrier samples are treated. PVC does not absorb water. On the contrary, dry pressboard and AlN are hygroscopic in nature. The high moisture content in the barrier samples can increase the dielectric constant and can influence the discharge inception [22]. Therefore, AlN barrier samples are cleaned with isopropanol and then dried for 4 hours at 45°C in an oven before being stored in airtight boxes. The same cleaning and drying process is applied with PVC, to keep similar condition for tests as well to keep its surface free from impurities.

The impregnated pressboards in Nytro 4000X are available from other tests in laboratory. For impregnation, the pressboards are first dried for one day at 105°C followed by two days of drying under vacuum (≈1mbar) at 85°C. At the end of this step, the moisture contents are verified for both dielectric liquid and pressboard, to comply with normative values. Then in next step, the pressboard with mineral oil is left in vacuum at 85°C for several days until it is completely impregnated.

Conditioning and monitoring of dielectric liquids

Before PD tests, the dielectric liquids are filtered using a porosity grade 4 sintered glass (or P4) filter with a pore diameter in the range of $10\text{-}16\,\mu\text{m}$. A vacuum pump is used during filtration to reduce pressure down to less than 1 mbar. Additional details on the filtration process are provided in Appendix D.

After the treatment, the dielectric liquid is characterized. To do this, two samples of treated dielectric liquid are taken, one for water content measurement using a coulometric Karl Fischer titration [107] and another sample is poured in a test cell for breakdown voltage (BDV) measurements. The BDV tests are performed in compliance with IEC60156:1995 recommendations in a commercially available BAUR DTA 100C set-up.



Figure 3-13: Dielectric liquid in Baur cell with sphere-sphere electrodes maintained at 2.5 mm gap

As per norm IEC 60156, stirring of dielectric liquid during BDV tests is optional, however recommended. In the initial phase, BDV tests are performed both with and without stirring to understand the impact of stirring on BDV measurements. A discussion on same have been provided in Appendix D. For the BDV test results provided here, continuous stirring process is chosen as it seemed to provide better homogeneity.

After finishing PD tests with one type of barrier sample (details in chapter 4), the dielectric liquids were treated every time in batches to continue the PD measurements with next set of barrier samples as per

Table 3-6. The characterization processes (both breakdown and water content measurement) were repeated for every batch of treated dielectric liquids, for both mineral oil and synthetic ester.

Figure 3-14 and Figure 3-15 present the average breakdown values of liquid samples taken from ten different batches of treated mineral oil and synthetic ester. Each bar represents an average of thirty BDV tests, while the error bars represent the standard deviation. The number of BDV tests varied from one literature to another. Therefore, in order to perform statistical analysis, it is decided to perform thirty BDV tests with one sample from every batch. As per their respective datasheets, the average BDV test values after treatment should be more than 70 kV for Nytro 4000X and more than 75 kV for Midel 7131 (see Table 1-1). The results thus obtained are found to be compliant with their respective datasheet values.

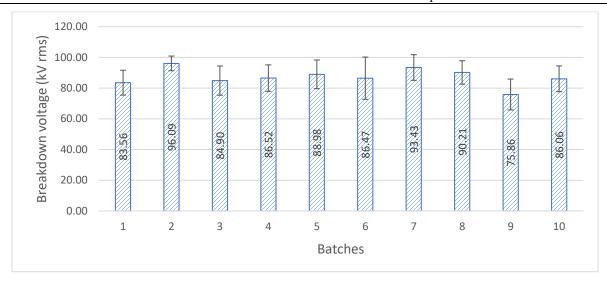


Figure 3-14: Average and standard deviation of breakdown tests of treated mineral oil (Nytro 4000X) for ten different batches

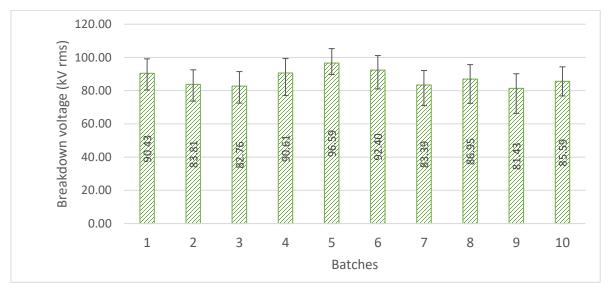


Figure 3-15: Average and standard deviation of breakdown tests of treated synthetic ester (Midel 7131) for ten different batches

Table 3-7 shows the average value of two water content measurements performed using coulometric Karl Fischer (KF) titration (Appendix D) for every batch of liquid after treatment. It can be seen from Table 3-7 that the absolute water content in Midel 7131 is quite higher than Nytro 4000X. As discussed in chapter-1, the solubility of water in synthetic ester is almost 30 times more than mineral oil. Therefore, the assessment of water content while comparing different dielectric liquids is usually done in relative terms rather than using absolute values. The relative saturation (RS) is the actual amount of water measured in dielectric liquid with respect to its solubility at a given temperature, which is given by,

$$RS = \frac{W_c(ppm)}{S_O(ppm)} \times 100\% \tag{3.6}$$

 S_0 = Solubility of water in dielectric liquid

 W_c = measured water content (ppm)

As we know that the water solubility in Nytro 4000 X is 55 ppm and 2600 ppm in Midel7131 (see Table 1-1); the relative water content (RS) of treated mineral oil (Nytro 4000X) and synthetic ester are calculated using the above expression. As can be seen in Table 3-7, the relative water content of Midel7131 is quite less for all batches (less than 5 %) as compared to Nytro 4000X which range between 13-24 %.

Batch	Water content of Nytro 4000X (ppm)	% RS Nytro 4000X	Water content of MIDEL 7131 (ppm)	% RS Midel7131
1	13.15	23.9	68.6	2.64
2	10.7	19.45	57.4	2.21
3	12.8	23.3	85.95	3.31
4	9.5	17.3	53.4	2.05
5	12.9	23.45	91.15	3.51
6	8.5	15.45	129	4.96
7	7.6	13.8	93.1	3.58
8	7.8	14.18	90.5	3.48
9	11.7	21.27	79.8	3.07
10	7.7	14.0	105	4.04

Table 3-7: Measured water content of dielectric liquids for different batches

However, note that during the characterization process, measured water content is used as the validation criterion, by comparing the value quoted in the datasheet of the liquids (see Table 1-1).

3.5. Summary

This chapter presents a literature review on different configuration of DUTs, with the objective of designing a representative model of the composite insulation system in transformer. In the first step, a needle-barrier plane configuration is selected considering the voltage limitation of the test benches. To ensure the generation of PDs in the selected configuration, the analyses with FE simulation is performed. This ensured the production of tip electric fields higher than the PDIF values, as found in the literature. With the selected needle-barrier plane configuration, it is

anticipated that a sufficient tip field can be generated at less than half the maximum voltage limit of test benches, with a needle of 1 µm tip radius.

Following the verification of the selected configuration from an electrostatic point of view, the FEM analysis is extended to study the impact of different parameters like tip radius, permittivity, thickness, and gap spacing between tip and barrier for the selected configuration. This study aids in the selection of barrier dimensions and provides the influence of aforementioned parameters on electric field distribution.

For PD experiments, a needle-barrier plane configuration with 1 μ m tip radius and a gap of 0.7 mm is chosen as DUT. Apart from pressboard, which is widely used in transformers, other barrier materials (AlN and PVC) with varying material properties, are also chosen for investigation and comparative analysis. A commonly used transformer oil (mineral oil) and a biodegradable alternative (synthetic ester) are chosen as surrounding media.

In the end, this chapter presents the *modus operandi* for the conditioning and monitoring of the dielectric liquids, the treatment of barriers and dielectric liquids have been discussed. The BDV and water content measurement of the dielectric liquids produces reproducible results and agree with the corresponding datasheet values.

4. Partial discharge measurements in AC 50 Hz

This chapter introduces the experimental set-up for PD measurement in AC 50 Hz. The measurement techniques include a photomultiplier tube (PMT) for optical detection of PDs besides the conventional electrical method. The optical PD detection is chosen in preparation for future tests with square-shaped waveforms, for which electrical detection of PDs is more difficult.

Then the correlation of the optical PD detection technique with the standard electrical method is discussed. This starts by the simultaneous detection of PDs in air and dielectric liquid using optical and electrical technique. It is followed by PD measurements with different barriers in mineral oil and synthetic ester.

The results thus obtained are presented and discussed towards the end of this chapter. To validate the optical PD technique against electrical method, the phase resolved partial discharge (PRPD) patterns and partial discharge inception voltage (PDIV) obtained from both detection techniques are examined and compared. Also, the PD patterns and PDIV obtained from different combination of solid/liquid insulation system are analyzed.

4.1. Experimental set-up for PD detection under AC 50 Hz

Following the guidelines of IEC60270 standard, an AC test bench is developed for PD measurement with the assistance of other researchers in Ampere laboratory (Figure 4-1). It consists of two major parts: a high voltage circuit and a PD measurement circuit.

The high voltage is generated using a PD-free transformer (230 V/ 25 kV) located inside the faraday cage. The voltage applied and its profile (ramp, stepwise, rate of rise of voltage) across the DUT is controlled from outside the cage.

The PD measurement circuit comprises of an Omicron PD detector (MPD600) for electrical measurement (see section 1.3 for working principle) and a photomultiplier tube (PMT R943-02 from Hamamatsu) which detects the photons emitted during the discharge processes. The spectral response of the PMT ranges from 160 to 930 nm, which includes the light emitted by corona and PDs in transformer oil as discussed in chapter 2. The DC supply of PMT is controlled by a negative DC bias supply, which has been optimized and is maintained at -1.3 kV for all PD

measurements. As discussed in handbook of PMT from Hamamatsu [108], by increasing the supply voltage of PMT, the dark current increases. Also, it states that the PMT provides the best signal to noise ratio for a supply voltage between -700 V and about -1.3 kV. These dark currents are not observed with oscilloscope as only one period is acquired, unlike the Omicron system, in which multiple periods superimpose which makes the random background noise quite visible. More details about this are provided in section 5.3.5 in Chapter 5. Appendix F reports some preliminary tests, performed with an LED light source to validate the operation of the PMT, the impact of the insulating medium (air, dielectric liquid) and the distance between the test object and the PMT lens.

The DUT is placed inside a small dark metallic box (within big faraday cage) which improved the capturing capability of the PMT. Two MPD 600 units are used to acquire PDs simultaneously from electrical and optical detection techniques. The voltages quoted in this chapter are in root mean square values (rms) unless specified.

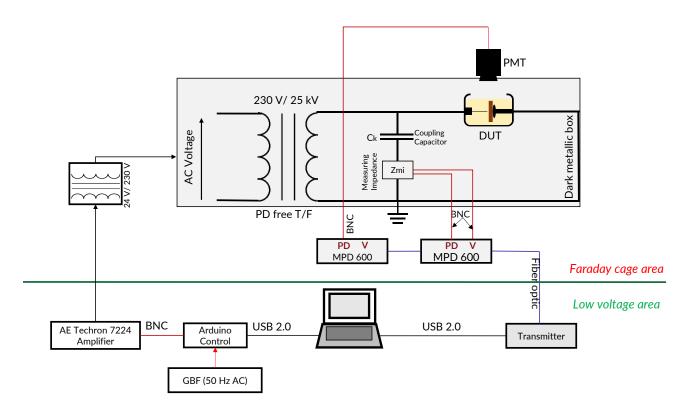


Figure 4-1: Schematics of PD test bench in AC 50 Hz

4.2. Determination of background noise

Regarding the electrical measurement of partial discharges, the background noise level of the test bench is determined by increasing the voltage across a DUT without its needle (but including a barrier sample immersed in mineral oil). The noise level is found to be less than 300 fC (femto coulomb) up to 16 kV (rms) as shown in Figure 4-2. But discharges appeared at 17 kVrms and

above, as shown in same figure. As DUT is without needle, the discharges acquired electrically above 17 kVrms could be mainly due to the HV set-up connection, such as between transformer and Ck. The discharges seen at 17 kVrms with electrical detection are not observed optically even at higher voltage levels (see Figure 4-3).

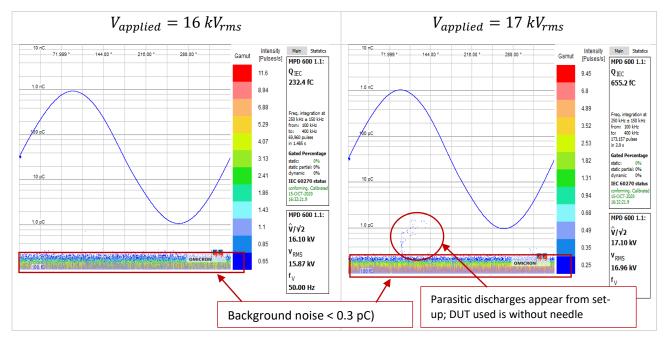


Figure 4-2: Background noise check for electrical measurement with DUT filled with oil and pressboard without needle

As the PMT counts the photon emitted during the discharge process, its measurements are reported here using arbitrary unit (a.u.). The optical detection is not found to be impacted at all by the applied voltages and its background noise always remained below 0.2 pa.u. (pico arbitrary unit) (reported as 0.2 pC by the Omicron acquisition system) as shown in Figure 4-3.

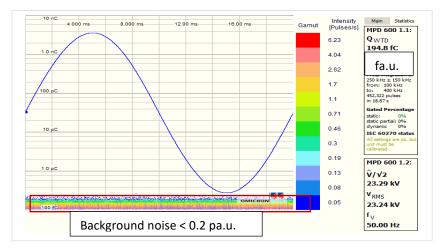


Figure 4-3: Background noise estimation with the gain of PMT set at DC bias of -1.3 kV using a DUT without needle

After determining the background noise some tests are performed in air and dielectric liquid. The first objective of these PD tests is to match the results obtained with publications. These tests are simultaneously performed with both electrical and optical detection techniques to check the correlation between both techniques. Before all tests, the voltage calibration is done with a high voltage probe across the DUT. The charge calibration of electrical measurement system is performed with an industrial charge calibrator from Omicron (reference: CAL 542), in compliance with IEC60270.

4.3. Corona discharge in air

For this test, a needle-plane configuration in air is used. The needle tip radius measured 1 μ m, maintaining a gap of about 10 mm from the plane grounding electrode. As the background noise have been found to be less than 0.3 pC up to 16 kVrms in electrical detection, the threshold is set at 0.5 pC. For this threshold, the corona discharges in air incepts at 1.6 kVrms as shown in Figure 4-4. The PD events are found to be occurring at a phase angle of 270° during the negative half-period of the sinewave. The PRPD pattern thus obtained from electrical detection matches the results presented in studies such as [66].

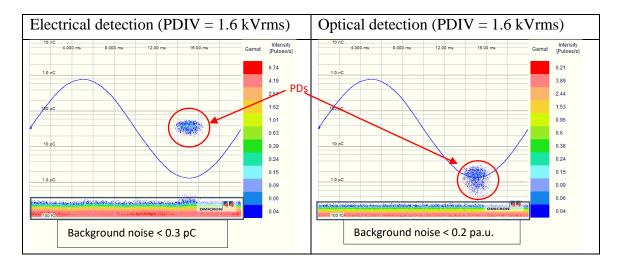


Figure 4-4: PRPD pattern for corona discharge in air using needle-plane electrode configuration for 10 mm gap in AC 50 Hz from (left) electrical detection and (right) optical detection

With the PMT, the PDs are detected at the same phase angle as with the electrical detection. The threshold is set at 0.5 pa.u. (reported as 0.5 pC by the Omicron unit), resulting in a PDIV of 1.6 kVrms, identical to that obtained electrically. Also, the tests are found to be reproducible.

To further verify the simultaneous acquisition of PDs from various detection techniques, measurements are also performed using an oscilloscope (Tektronix: MDO34). Z_{mi} , the PMT and the HFCT probe are connected to the input channels of the oscilloscope. Additionally, a high

voltage probe is connected across the DUT to monitor the applied voltage. As can be seen from Figure 4-5, same PD event is captured by all three detection techniques.

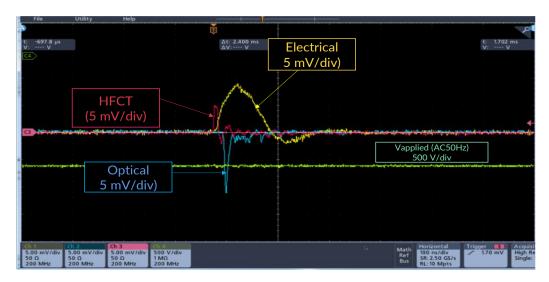


Figure 4-5: Correlation in PD detection using electrical, optical and HFCT at 1.5 kV (rms) for DUT with needleplane in air. Horizontal scale: 100 ns/div (1 µs total)

4.4. Partial discharge in dielectric liquid

In the next step, the PDs are investigated with mineral oil (Nytro Taurus) in needle-plane configuration. Same as before, a 1 μ m tip radius and 10 mm gap between tip and grounding plane is used (Figure 4-6). The voltage is increased at a rate of 1 kV/s in compliance with standard IEC61294 [102].

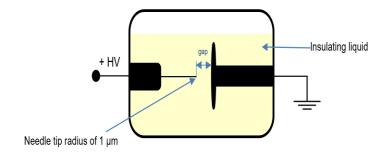


Figure 4-6: Needle-plane configuration in dielectric liquid used for PD tests

Figure 4-7 presents the PRPD pattern obtained from both electrical and optical detection. With electrical detection, the threshold value is set at 100 pC in compliance with IEC 61294, resulting in a the PDIV of 14.25 kVrms. The PRPD pattern matches the results from the studies in chapter-2.

With optical detection, the PDIV is found to be 14.25 kVrms, with the detection threshold set at 5 pa.u. (reported as 5 pC in Omicron). The PDs detected by optical method have the same phase as those detected electrically.

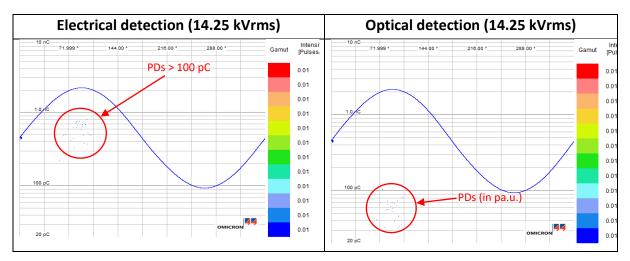


Figure 4-7: PRPD pattern for PDs in mineral oil using needle-plane electrode configuration for 10 mm gap in AC 50 Hz from (left) electrical detection and (right) optical detection

Like previously done in case of corona discharges (Figure 4-5), some verifications are performed with an oscilloscope to confirm the simultaneous acquisition of PD by all detection techniques. Figure 4-8 shows the acquisition of same PD event by all detection techniques at 11 kVrms. The vertical scale is reduced to 2 mV/div as compared to 5 mV/div for corona discharge.

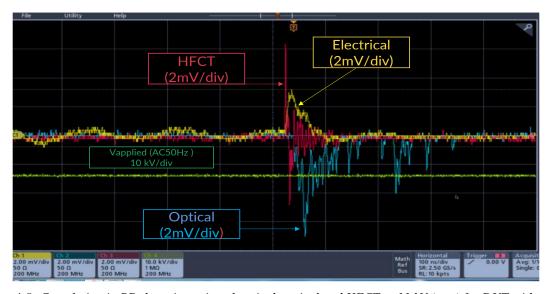


Figure 4-8: Correlation in PD detection using electrical, optical and HFCT at 11 kV (rms) for DUT with needleplane in mineral oil. Horizontal scale: 100 ns/div (1 µs total)

4.5. PD test with needle-barrier plane configuration

Following the tests in air and dielectric liquid, PD tests are carried out with the DUT of interest as reported in section 3.3. This section discusses the measurement protocol such as the reusability of the needle and other procedures before presenting experimental results.

The 1 μm needle tip should be replaced from time to time due to deformation caused by discharge events. Therefore, some preliminary tests with needle-barrier plane configuration are conducted to estimate the maximum number of times a needle can be used without impacting PDIV. For a needle with a 1 μm tip, it is concluded that a maximum of ten PDIV measurements can be performed. This is discussed in detail in Appendix C.

The DUT specimen comprised of treated dielectric liquid, barrier sample and new needle. To verify the reproducibility of PD tests, six tests were performed with each DUT specimen. After six PD tests, the needle, dielectric liquid and solid barrier sample are replaced by pristine ones. This is repeated for all barrier samples of each barrier type as per

Table 3-6. Once the tests have been performed for one type of barrier (such as 1 mm PVC), the DUT cell is cleaned and dried before testing another type of barrier. The used dielectric liquids thus collected after PD tests were retreated and monitored in batches whose results are presented in Figure 3-14 for mineral oil, Figure 3-15 for synthetic ester and Table 3-7 for water content measurement in chapter 3 (batch 1 to batch 5). Batch 6 to 10 correspond to the results of the conditioned dielectric liquid used for tests under square waveform as discussed in chapter-6.

The PMT bias is set at -1.3 kV throughout the test. As there is no existing method to calibrate the optical detection technique, an attempt has been made in this work, which is further discussed in this chapter. The PDIV values presented here are average and standard deviation (error bars) of thirty measurements for PVC and pressboard barriers and eighteen measurements for AlN (3 samples of each thickness are tested) as mentioned in

Table 3-6. During the PD tests of needle-barrier plane configuration, the voltage applied across the DUT is increased in steps of 1 kV with a rising rate of 1 kV/s. This is followed by a waiting time of 30 s at high voltage level before decreasing it to zero with a falling rate of 1 kV/s. A rest interval of 30 s is provided at zero voltage before increasing the voltage again across the DUT as shown in Figure 4-9. This continued until PDIV is reached.

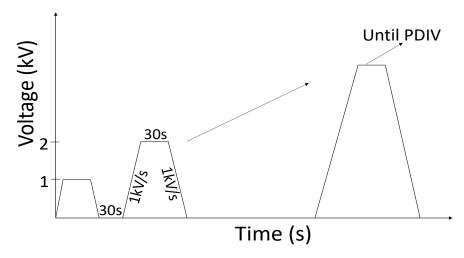


Figure 4-9: Voltage application profile across DUT for PD test in AC 50 Hz

Following the definition of DUT specimen and voltage application across the DUT, the PD experiments in AC are performed. The results thus obtained are discussed in following sections which are classified as,

- correlation of PDIV results from electrical and optical measurements
- phase resolved partial discharge (PRPD) patterns acquired for different cases
- PDIV comparison of different barriers tested in both dielectric liquids

A discussion about additional tests with varying gap and tip radius is also provided towards the end of this section to understand their impact on obtained PDIV results.

4.5.1. Correlation between electrical and optical measurements

Figure 4-10 shows the PRPD patterns (PD clusters) obtained from electrical and optical detection techniques at the same instant for a 2 mm thick pressboard in mineral oil at 12 kV (rms). It can be observed from the figure, that the PMT detected PD events during the same phase (between 0°-90° and 180°-270°) as the electrical detection.

As discussed before, the PD parameters shown in Figure 4-10 from optical measurements are in a.u. The maximum magnitude of electrical PDs reached more than 1 nC while those obtained optically could reach up to 100 pa.u. Moreover, low magnitude PDs (less than 1 pC) acquired electrically could not be detected by the PMT for many tests.

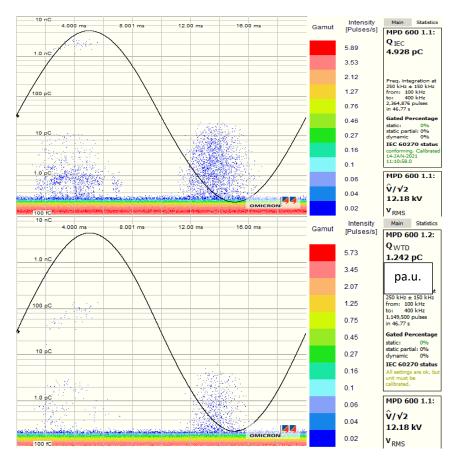


Figure 4-10: PRPD pattern of 2 mm thick pressboard in Nytro 4000X taken at same instant from electrical (top) and optical (bottom) detection at 12 kV (higher than PDIV)

In the next step, the number of PDs (NPDs) acquired from two detection techniques are compared for same DUT i.e. pressboard in mineral oil. Starting from PDIV, the voltage is increased in steps using the same voltage profile as presented earlier. At the end of tests with one DUT specimen, the needle, barrier sample and dielectric liquid sample are replaced. During this experiment, five DUT specimens are used. Thus, each point in the graph in Figure 4-11 corresponds to an average of five NPDs acquired at each voltage level from five DUT specimens.

The background noise is suppressed so as not to skew the PD count. It is found that the PMT starts detecting PDs only when electrical PDs begin to exceed 2 pC. This is explained further in the next section. Hence, for the calculation of NPDs, a minimum threshold value is set at 2 pC for the electrical detection, while it is set at 0.25 pa.u. for optical detection (i.e. just above background noise of PMT). As can be seen from the graph in Figure 4-11, the electrical NPDs are higher than those acquired optically. However, both of them follow the same trend.

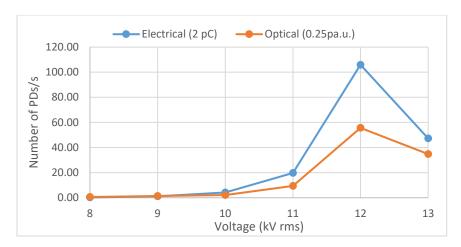


Figure 4-11: Comparison of number of PDs for pressboard in Nytro 4000X from both electrical and optical measurements by increasing the voltage in steps above PDIV

Both phenomena, reduction in NPDs and magnitude of PDs with the optical detection as compared to the electrical detection, can be explained by the attenuation of the light emitted by the PD events in the dielectric liquid. A reduction in magnitude of the PMT peak output voltage is also observed for an LED after it is immersed in dielectric liquid, as discussed in Appendix F.

To further inspect the signals generated by the various PD detectors, time-domain measurement is conducted using the same oscilloscope as earlier. During this test, the DC bias of the PMT is set at -1.5 kV. Figure 4-12 shows the measurement taken for 2 mm thick pressboard in mineral oil at 9 kV(rms). As can be clearly seen in the figure, the same PD event is captured by electrical, optical and HFCT methods, at the same instant.

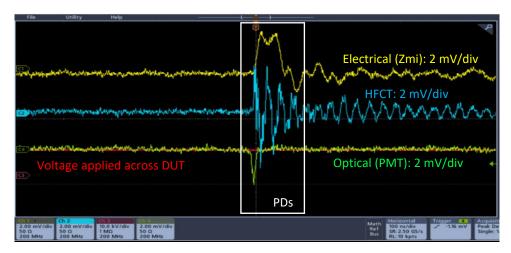


Figure 4-12: Correlation in PD detection among electrical measurement, optical measurement and HFCT at 9 kV (rms) for DUT with pressboard in mineral oil: horizontal time scale at 100 ns/div; total 1 µs

As described above, PDs are detected optically only when they exceed a certain level. Thus, the PD recordings are analyzed for different combinations of solid/liquid to correlate the PD magnitude obtained from optical detection (in a.u.) with that from electrical detection (in pC).

It is found that in case of mineral oil, 0.25 pa.u. with the optical measurement nearly corresponds to the threshold of 2 pC with the electrical measurement. This is found to be true almost for all barrier types in mineral oil. For example, as shown in Figure 4-13, with a threshold set at 2 pC for electrical detection and 0.25 pa.u. for optical detection, PDs can be seen occurring during same phase angles. The PDIV thus obtained electrically and optically are same (10 kV) for pressboard in mineral oil, in the given figure.

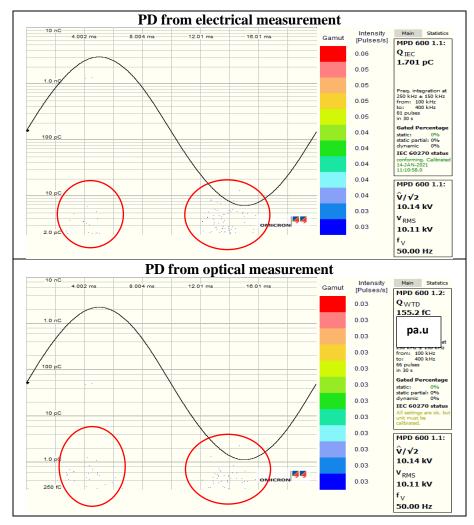


Figure 4-13: Correlation in PD events for 2 mm thick pressboard barrier in mineral oil at 10 kVrms. (top) PDs observed with threshold set at 2 pC with electrical measurement and (bottom) PDs observed with threshold at 0.25 pa.u. with optical detection

Considering these thresholds for PD detection, the PDIV for each barrier type in mineral oil is obtained. The average PDIV thus calculated is plotted in Figure 4-14. It can be observed that the

average PDIV values acquired electrically and optically are almost in same range for each barrier type.

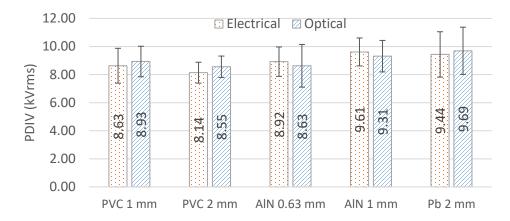


Figure 4-14: Correlation between PDIV observed from electrical with threshold of 2 pC and optical detection in mineral oil (Nytro 4000X) for different barriers

A similar correlation is found between PDIVs obtained from electrical and optical measurement with the synthetic ester (Midel 7131). With this liquid, the 0.25 pa.u. with optical detection is found to correspond to a PDIV threshold of 10 pC with the electrical measurement. This indicates higher light attenuation with the synthetic ester than the mineral oil. The average PDIV values for different barriers tested in synthetic ester have been plotted in Figure 4-15 which are almost in same range for each barrier type.

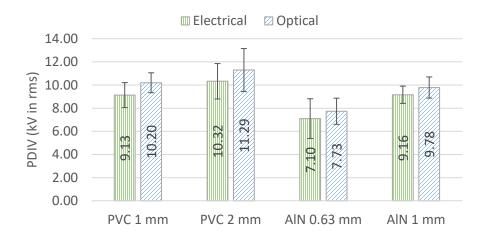


Figure 4-15: Correlation between PDIV observed from electrical with threshold of 10 pC and optical detection in MIDEL7131 for different barriers

Figure 4-16 shows the PDs obtained from two detection techniques for 1 mm thick AlN barrier with synthetic ester. With the chosen threshold values for both measurement techniques, the average PDIV obtained optically are found comparable to those acquired electrically.

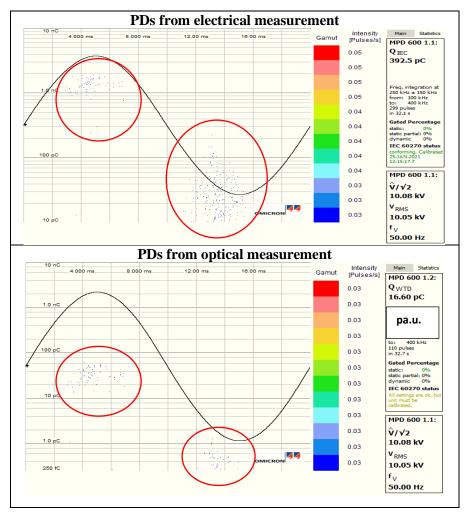


Figure 4-16: Correlation in PD events occurring for 1 mm thick AlN barrier in synthetic ester. (top) PDs acquired electrically with threshold set at 10 pC and (bottom) PDs obtained optically with threshold set at 0.25 pa.u. at 10 kVrms

From above correlations, it can be inferred that the magnitude of 0.25 pa.u. obtained from optical detection nearly corresponds to 2 pC with mineral oil while it is 10 pC with synthetic ester. Additionally, two major conclusions can be drawn:

- for the electrode configuration with barriers in dielectric liquid, the PMT detected PDs with the same phase angle as the electrical measurement and
- PDIVs obtained optically matches the electrical PDIV values, provided appropriate detection threshold are set for both types of dielectric liquids tested here.

So, optical detection using PMT can be considered as a decent indicator to confirm the occurrence of PD activity for composite insulation system as well. Moreover, unlike electrical

detection technique, as it is not found to be impacted by electromagnetic interferences (EMI) at higher AC voltages, therefore, it can be a suitable technique to detect PDs under complex non-sinusoidal waveforms.

4.5.2. PRPD patterns

For most of the test cases, the PD activity initiated with the appearance of PDs at the crest of negative polarity. Figure 4-17 shows the PD initiation at the negative polarity for 1 mm thick PVC barrier in synthetic ester. Same is found to be true for most of the cases with other barriers tested in two dielectric liquids.

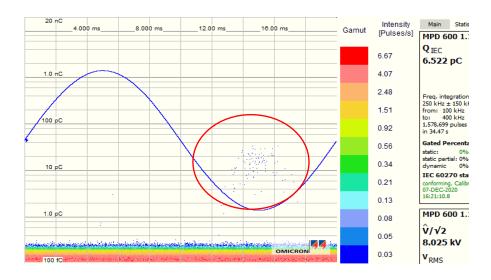


Figure 4-17: PRPD pattern of 1 mm thick PVC in synthetic ester at PDIV from electrical detection

To understand this further, Figure 4-18 shows evolution of PRPD pattern for pressboard in mineral oil with increasing voltage. By increasing the voltage above PDIV, PD events mainly occurred during the first and third quadrants of the sinusoidal waveform. Moreover, the PDs in positive cycle are found to have larger amplitude as compared to those in negative cycle. In the following subsections, these phenomena have been discussed.

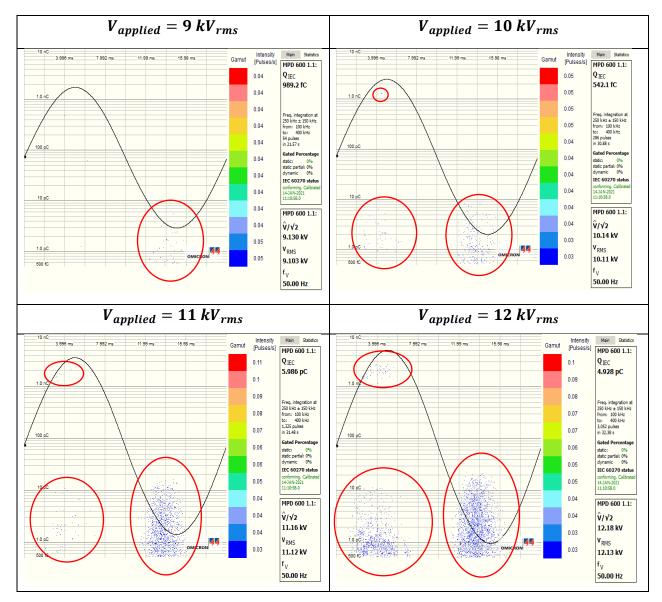


Figure 4-18: Evolution of PRPD pattern with increasing voltage above PDIV for pressboard (1 mm thick) in Nytro 4000X (mineral oil) in needle-barrier plane configuration for same DUT specimen

Initiation of PDs in negative AC cycle

For needle-plane configuration in dielectric liquid, studies like [109], [110] have reported that the inception voltages can be higher in positive polarity as compared to negative polarity. During the positive polarity of AC cycle, the slow-moving cluster of positive ions are formed as discussed in section 2.1.2. This forms an extended tip, resulting in the reduction of total field across a void, thus elevating the inception voltage with positive half cycle.

On the other hand, during negative cycle, an avalanche of electrons is injected from the tip to the liquid, leading to the initiation of PDs in negative half cycle. Same has been explained in [111] for pressboard in dielectric liquid. The occurrence of PDs during negative half cycle at PDIV has been found to be quite consistent with all oil/solid combination.

High magnitude of PDs in positive cycle at a voltage higher than PDIV

In [99], a relationship between the apparent charge and stopping length of streamer (length between needle tip and streamer tip) has been established by the synchronized measurements. In a divergent field, an increase in voltage can lead to the radial growth of positive streamers from the tip. The larger charge transfer associated with positive PDs leads to its stronger propagation ability, than negative ones, leading to longer stopping length. Thus, a PD with high apparent charge in divergent field can be attributed to a farther propagating streamer.

PDs in first and third quadrant at a voltage higher than PDIV

As explained in the section 2.1.3 (in chapter-2), the physicochemical process involved behind this phenomenon can be mainly due to presence of space charges and residual bubbles from previous half cycle. In presence of the charge carriers from previous cycle, as soon as sufficient inception field is reached (at higher voltage than PDIV), PDs start occurring during rising time of sinusoidal voltage. Also, the heterocharges and residual bubbles promotes the PD events in negative half of voltage cycle. This hypothesis may explain the occurrence of PDs in first and third quadrant.

With time the positive ions slowly drift in the direction of electric field and settle on the barrier surface. Such distribution of charges may create a quasi-uniform field between barrier and plane electrode [112], resulting in increase of inception voltage. Further, as sinusoidal voltage begins to fall to zero in second quadrant, the extinction conditions could be reached. This may cease the PDs to occur in second quadrant.

As explained in [71], [110], the negative streamers thus formed have different mechanisms than positive one due to higher injection of electrons. This might lead to the differences observed in NPDs or PD amplitude, observed during negative cycle as compared to positive one.

4.5.3. Comparison of PDIV and PRPD patterns in two dielectric liquids

This section compares the average PDIV values and the PRPD pattern obtained from electrical PD measurements for two dielectric liquids.

PRPD pattern in two dielectric liquids

Figure 4-19 shows PRPD patterns of 0.63 mm thick AlN barrier in mineral oil (Nytro 4000 X) and synthetic ester (Midel 7131) respectively, acquired after 30s of recording at 10 kV, from electrical measurement. It can be observed that the magnitude of PDs reached as high as 1 nC for both mineral oil and synthetic ester at same voltage. Also, in positive cycle, the ester shows higher number of PDs, while in negative half cycle it shows higher charge magnitude than in mineral oil.

As synthetic ester is more viscous than mineral oil, the PD activity might have increased due to promotion effect as discussed in chapter-2. Also, the absolute water content of synthetic ester is higher than mineral oil (see Table 3-7). The high-water content favors the PD activity as mentioned in [100].

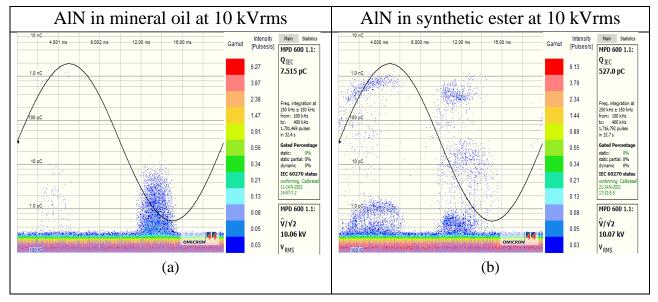


Figure 4-19: (a) PRPD pattern of AlN (0.63 mm thick) in mineral oil (Nytro 4000X) and synthetic ester (Midel 7131) at 10 kV from electrical detection

PDIV comparison between two dielectric liquids

From the available recordings, the electrically acquired PDIV values are extracted by setting threshold value at 0.5 pC as presented in Figure 4-20. This threshold value is just above the background noise level for electrical detection (0.3 pC) and makes possible to detect PD events occurring just above this range. The graphs provide average and standard deviation of PDIVs for different barriers tested in two dielectric liquids. The first point that can be noticed from the graph is the average PDIVs for all combination of liquid/solid are less than 10 kV. This is quite consistent with FEM simulations, where the same was anticipated for selected DUT specimens.

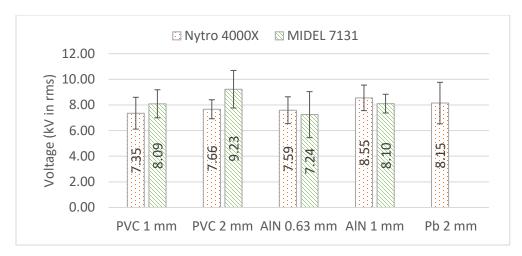


Figure 4-20: Comparison of PDIV values for different barriers in Nytro 4000X and MIDEL7131 from electrical detection with threshold at 0.5 pC

In the next step, the electric field generated at average PDIV for each combination is evaluated. The reference DUT model with 1 μ m tip and 0.7 mm gap length as discussed in Table 3-2 (Chapter-3) is used. The barrier thickness, its permittivity and permittivity of dielectric liquid are adapted for each case and electric fields are measured at experimentally obtained average PDIVs (as in Figure 4-20). The electric field thus measured between tip and barrier surface are plotted in Figure 4-21.

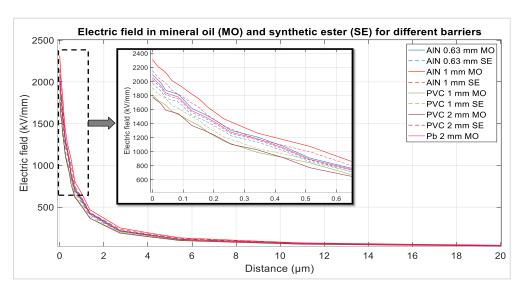


Figure 4-21: Electric field for different barriers in mineral oil and synthetic ester for corresponding average PDIV found experimentally, obtained from FE simulation

It can be noticed that tip electric field for all cases are above 1700 kV/mm, which is above PDIF value for PD generation. The highest tip field is observed for 1 mm AlN, while lowest for 2 mm 107 | Page

PVC in mineral oil. The AlN barrier with the highest permittivity among all barriers tested shows highest tip field, which was also found during FEM analysis, followed by pressboard and PVC.

Coming back to the graph of Figure 4-20, it can be observed that average PDIVs have minor differences as the standard deviation bars overlap for many cases. For example, for 0.63 mm AlN in two liquids, the overlapping of SD bars give the impression that mean difference in PDIVs is not significant. To verify this, t-tests are performed to compare if there is an impact of permittivity, thickness and dielectric liquids on average PDIVs, as discussed in following section.

For t-tests, p-value considered is 0.05. Apart from p-value, the standard deviation (SD), 95 % confidence interval (CI), upper bound (UB) and lower bound (LB) are also calculated. In the following sections, the t-test results are provided and then discussed.

Impact of dielectric liquids on PDIV

The null hypothesis considered is that the average PDIVs in mineral oil (MO) and synthetic ester (SE) are equal for same type of barriers. Table 4-1 shows the average (Avg), SD, 95 % CI, UB, LB and p-value.

As can be seen, the PVC barriers of both thicknesses show p-value of less than 0.05 in MO and SE. This gives enough evidence to reject the null hypothesis as there is a significant difference in the average PDIVs obtained from two dielectric liquids.

Impact of dielectric liquids								
Barriers	PVC 1 mm		PVC 2 mm		AIN 0.63 mm		AIN 1 mm	
Dielectric liquid	МО	SE	МО	SE	МО	SE	МО	SE
Avg (kV)	7.35	8.09	7.66	9.23	7.59	7.24	8.55	8.10
SD (kV)	1.32	1.09	0.93	1.46	1.39	1.80	1.15	0.73
95 % CI	7.85	8.50	8.01	9.77	8.28	8.14	9.12	8.47
UB/LB	6.86	7.68	7.31	8.68	6.94	6.35	7.98	7.74
p-value	2E-	-02	1E-	-05	5E-	-01	2E-	-01

On the other hand, the p-value obtained for AlN barriers are more than 0.05, for both thicknesses. Therefore, for these cases, there is no difference between PDIVs obtained from two dielectric liquids.

Impact of barrier thickness on PDIV

In this case, the null hypothesis considered is there is no difference in average PDIVs when barrier thickness changes. From Table 4-2, the p-value is less than 0.05 for AlN in mineral oil and PVC in synthetic ester. While for other two cases, there is no significance difference in average PDIV.

Impact of thickness								
Dielectric liquid	Mineral oil				Synthetic ester			
Barriers	PVC AIN			P\	/ C	AIN		
Thickness	1 mm	2 mm	0.63 mm	1 mm	1 mm	2 mm	0.63 mm	1 mm
Avg (kV)	7.35	7.66	7.61	8.55	8.09	9.23	7.24	8.10
SD (kV)	1.32	0.93	1.39	1.15	1.09	1.46	1.80	0.73
95 % CI	7.85	8.01	8.28	9.12	8.50	9.77	8.14	8.47
UB/LB	6.86	7.31	6.94	7.98	7.68	8.68	6.35	7.74
p-value	3E-01		3E-02		1E-03		7E-02	

Table 4-2: Analysis of difference in average value of PDIVs between barrier thickness in AC 50 Hz using t-test

Impact of permittivity on PDIV

To analyze the influence of permittivity on PDIV, the barriers of same thickness, but different permittivities (such as PVC and AlN) are compared using t-test as shown in Table 4-3. As can be seen from the p-values calculated, a significant difference can be observed between barriers of different permittivities in mineral oil, but not in synthetic ester.

Table 4-3: Analysis of difference in average value of PDIVs for changing permittivity of barriers in AC 50 Hz using
t-test

Impact of permittivity							
Liquid	Mineral oil				Synthetic ester		
Thickness	1 mm 2 mm			1 mm			
Permittivity	PVC AIN		PVC	Pb	PVC	AIN	
Avg (kV)	7.35	8.55	7.66	8.15	8.09	8.10	
SD (kV)	1.32	1.15	0.93	0.91	1.09	0.73	
95 % CI UB/LB	7.85	9.12	8.01	8.48	8.50	8.47	
	6.86	7.98	7.31	7.81	7.68	7.74	
p-value	2E-03		4.7E-02		10E-01		

Discussion

The experimentally obtained PDIV values are less than 10 kV which complies with the findings of FEM simulations. The average PDIVs are in almost same range and SD bars are found to be overlapping for some cases.

To go further into the analysis, the tip fields are calculated using FEM for experimentally obtained average PDIV values. The tip field thus obtained are higher than required PDIF of 1600 kV/mm for PD production.

Further, the significance analysis using t-test is performed, to check if differences in mean values of PDIV occurred by chance. The results from t-tests have shown that there is no real impact of permittivity, thickness and dielectric liquid for the selected electrode configuration. The dispersion of data could be due to different reasons such as different types of specimens tested and measurement precision. The electric field generated by 1 µm tip radius at a gap of 0.7 mm seems to play a significant role for triggering a PD event. To understand the impact of tip radius and error of gap spacing on PDIV, some complementary experiments are performed as discussed further.

4.5.4. Impact of varying tip radius

To assess the impact of tip radius on PDIV, PD measurements are conducted with tip radii of 1 μ m, 10 μ m and 100 μ m. The tests are performed with 1 mm thick PVC barrier with untreated mineral oil (Nytro 4000X) maintaining a constant gap of 0.7 mm between tip and barrier. Five PD measurements are performed with each tip radius. The barrier and oil are changed with different tip radius. The threshold used for PD detection is 0.5 pC.

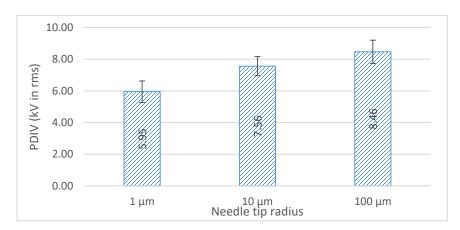


Figure 4-22: Comparison of PDIV values for different tip radius from electrical measurement

As can be seen from the graph presented in Figure 4-22, the PDIV increases with increasing tip radius. Considering the 1 μ m tip as reference point, an increase in tip radius from 1 to 10 μ m, increases PDIV by 27 %, while the increase to 100 μ m raises PDIV by 42 %. The discrepancy in average PDIV obtained for 1 μ m tip (5.95 kVrms) than in Figure 4-20, could be due to impurities present in untreated oil, which brought down the PDIV value.

In the next step, the tip fields are calculated at the experimentally obtained average PDIVs using FE simulation. As can be seen from Figure 4-23, the electric field at the tip is highest for 1 μ m radius at 5.95 kV, almost reaching 1500 kV/mm. For 10 and 100 μ m tip radius, the tip field are quite less than 400 kV/mm at their corresponding PDIVs.

In FEM, the tip fields are calculated under ideal conditions. The major reason for this discrepancy seems to be construction defect in tip radius. This has been later verified by measuring a new 1 μ m needle tip (Figure 6-4, in chapter 6), whose tip measured less than 1 μ m and is not hemispherical in shape. Further, the 100 μ m tip is found to have radius of about 50 μ m as shown in Appendix C. The construction defect of the tip and the impurities in untreated liquid could have led to discrepancies between FEM and experimentally obtained results.

Nevertheless, the increasing trend of PDIV for bigger tip radius validates the FE simulations.

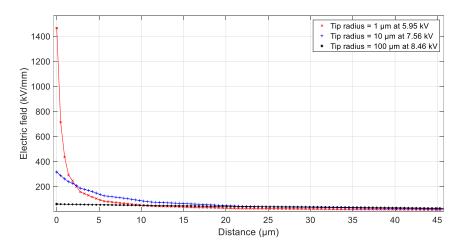


Figure 4-23: Tip fields obtained from FE simulation at average PDIVs for three tip radii tested

4.5.5. Impact of gap variation

To investigate the effect of variation in gap spacing on PDIV, additional tests are performed at gaps of 1 mm, 0.7 mm and slightly less than 0.7 mm. The gap of 0.7 mm and 1 mm are created using plastic spacers. The gap of less than 0.7 mm is created by setting the gap to 0.7 mm using the corresponding spacer, removing it, and turning the micrometric screw by two turns. Tests are performed with 1 μ m tip with 1 mm thick PVC barrier in mineral oil, which was not treated. Five tests are performed for each of the three gap spacings. The components of DUT (needle, oil and barrier) are changed to perform measurements at each gap.

Figure 4-24 shows the mean PDIVs and standard deviation as error bars thus obtained for the selected gaps from electrical measurements. A threshold value of 0.5 pC is used for all these measurements.

Considering the gap of 0.7 mm as reference point, it can be noticed that the mean PDIV measured at the gap less than 0.7 mm is about 7 % lower, while at 1 mm gap is about 6 % higher than the PDIV at 0.7 mm (6.04 kVrms). Also, as the standard deviation bar at 0.7 mm quite overlaps with the SD bars for other two cases, the difference in average PDIV does not seem significant.

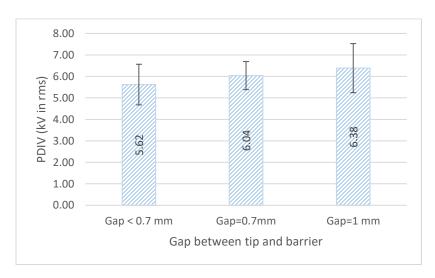


Figure 4-24: Comparison of PDIV values at different gaps from electrical measurement

The average PDIV values thus obtained at different gaps are used for calculating tip fields in FE simulations. To do this, the PDIV voltage obtained from experiments are assigned for corresponding gaps, keeping other parameters same as reference DUT model (1 μ m tip, PVC barrier in mineral oil). For the gap less than 0.7 mm, 0.5 mm gap is considered in simulation considering the fact that micrometric screw was turned two times after creating the gap of 0.7 mm.

The tip field thus obtained from FE simulation are 1548 kV/mm at 1 mm, 1487 kV/mm at 0.7 mm and 1421 kV/mm at 0.5 mm, as marked in Figure 4-25. When the gap is increased to 1 mm or decreased to 0.5 mm from reference point (0.7 mm), the variation in tip field is between 4-5 %, which corresponds to a variation between 5-7 % in terms of PDIV.

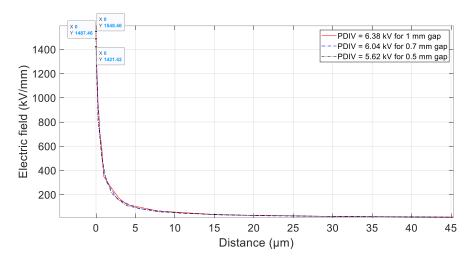


Figure 4-25: Comparison of PDIF values at different gaps for corresponding average PDIVs

From the above discussion, it can be said that small tolerances in gaps, as used in this investigation may not have a major impact on PDIV. This also validates the finding of FE simulation discussed in Chapter-3.

4.6. Summary

In this chapter, the optical detection of PDs is used simultaneously with the electrical detection. The electrical detection technique shows a noise band of 0.3 pC up to 16 kV. Above this voltage, it shows some discharges generated due to HV connections in the set-up. While the PMT shows a noise band of less than 0.2 pa.u. at all voltages. First PD tests are performed in air and dielectric liquid to verify the consistency with published data. This is followed by tests in needlebarrier plane configuration to investigate the PD phenomenon in composite insulation system.

The PMT is found to detect PDs at the same instants as the electrical method, but only relatively large magnitude PD events are detected optically. A correlation is established between PDIVs acquired electrically and optically. This means the PDs of 0.25 pa.u. acquired optically would correspond to 2 pC of charge in mineral oil and 10 pC of charge in ester respectively.

Further, the PRPD patterns and PDIV results obtained from different combination of solid/liquid insulation are presented. The PD events occur mainly during the first and third quadrants in the presence of barriers. The PRPD patterns of synthetic ester show large PD magnitudes. The experimentally obtained PDIVs have been found at less than 10 kV and tip fields thus calculated at PDIVs are in same range, which is quite consistent with FEM simulations earlier made in Chapter-3. The PDIV results obtained from different solid/liquid combinations show no considerable effect for various parameters including permittivity of the liquid, of the barrier, or barrier thickness. Towards the end of this chapter some complementary tests to assess the impact

of variations in gap and changes in tip radius are discussed. The PD appearance is mostly triggered by the modest 1 µm tip radius and 0.7 mm gap separation.

The major outcomes of these investigations are:

- The DUT configuration with 1 µm tip radius and gap length of 0.7 mm described in chapter 3 can generate PDs with the different combinations of solid/liquid insulation well within 10 kV. This demonstrates the exactness of DUT configuration thus designed using FEM simulation.
- Establishment of optical detection as an alternative technique to monitor PDs. Except for a lower sensitivity, which can be associated with some absorption of light by the dielectric liquid, results are remarkably consistent between optical and electrical detection.

The following chapter discusses the implementation of optical detection technique to detect PDs under square waveform.

5. Methodology for partial discharge detection under square voltage waveform

WBG semiconductor devices such as SiC MOSFETs offer several advantages over Si-devices in terms of breakdown voltage, operating frequency, fast switching speed and reduced switching and conduction losses. The repetitive voltage pulses generated from WBG-based converters is expected to have slew rates of $100 \text{ kV/}\mu\text{s}$ and can reach switching frequencies of 500 kHz [113]. So far, the impact of repetitive pulses on insulation system has been mainly investigated only for slew rates of up to $20 \text{ kV/}\mu\text{s}$ and repetition frequency of 10 kHz [50], [58]. The lack of knowledge about the effect of repetitive pulses such as those generated by WBG devices on the insulation system could be a significant obstacle in future development of power system applications. To answer some of these issues, this chapter discusses an approach to measure partial discharges under very high dV/dt (about $50 \text{ kV/}\mu\text{s}$).

Initially a dV/dt between 10-100 $kV/\mu s$ with repetition of about 10 kHz is considered to match the conditions of square voltages generated in power electronic application incorporating fast switches. As the square voltage across the MFT in an isolated DC-DC topology is bipolar in nature, therefore, the first choice was to perform investigation under bipolar square voltage waveform. Due to the difficulty in finding a suitable commercial solution and considering the cost and time to develop such test bench with enough voltage level (tens of kV), it was decided to focus on unipolar square waveforms in the beginning and expand it to bipolar square waveforms in the future.

With unipolar square waveform, two solutions have been tested within the timeframe of this thesis. The first is a commercial solution from RLC Electronics (Nanogen 3), which is a 30 kV pulse generator in a half-bridge configuration. While the second is a single HV switch from Behlke rated at 140 kV max. voltage. Table 5-1 summarizes key characteristic of the two solutions.

As shown in Figure 5-1, the pulse generator from RLC Electronics could produce an output voltage waveform of around 71 ns as tested across a DUT without needle. The voltage applied for this test is 3 kV with a repetition frequency of 10 kHz at 25 % duty cycle. However, this commercial solution proved to be fragile and failed after only few tests.

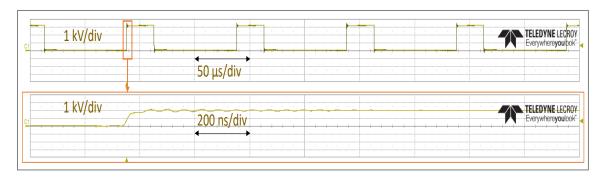


Figure 5-1: (Top) Output voltage waveform from pulse generator across a DUT without needle and (bottom) magnified view of same waveform with a rise time of 71 ns

Solution 1 (Nanogen) Solution 2 (HV switch) **Parameters BEHLKE** Pump & reservoir **Active radiator** HTS switch with DLC Configuration Half-bridge Single switch HV switch HTS 301-10-GSM (Behlke) HTS 1401-10-LC2 (Behlke) reference Output voltage 30 kV 140 kV 50 A (at 1 kHz and 1 % duty 100 A Output current cycle) Remote control Integrated inside the Nanogen Developed in laboratory circuitry (Plug and play) Pulse frequency 100 kHz Up to 500 Hz

Table 5-1: Characteristics of pulse generator (Nanogen) and HV single switch

As a result of the failure of the Nanogen system, a custom set-up with a single HV switch is built for this thesis. A discussion about the test circuit, its operation principle and component selection are provided. To ensure the PD measurement under square waveform, measurements are taken to improve the electromagnetic compatibility (EMC) of the test bench. After the realization of test bench, some preliminary PD measurements are performed under unipolar square waveform, using the DUT designed as presented in chapter-3.

5.1. Schematics for generating square waveform

As discussed in chapter 1, due to the fast switching action of semiconductor devices, it is difficult to perform PD measurement with square voltage waveforms using the same schematics as mentioned in IEC 60270. Hence, a new test bench is developed to generate square voltage waveform. The steps taken to do so are discussed here after.

5.1.1. Proposed schematics of the test bench

In the first step, a schematic for generating fast rising square voltage waveform with single HV switch from Behlke is proposed (Figure 5-2).

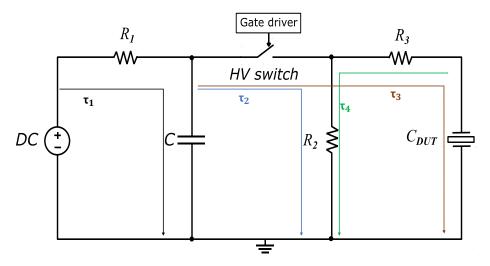


Figure 5-2: Simplified schematics proposed to generate square voltage waveform

The circuit thus proposed includes a high voltage DC generator (DC), three high voltage resistors (R1, R2 and R3), a capacitor bank C, one HV switch and the device under test C_{DUT} . The circuit operates in the following ways:

- a) Initially the HV switch remains open.
- b) R1 is a HV resistor which limits the current from DC source and charges the capacitor C with a time constant.
- c) Once the capacitor is fully charged, the HV switch can start operating at the chosen switching frequency.
- d) R2 is a high value resistance to let all the current pass through the DUT when switch closes and allow discharging of DUT when HV switch opens.

- e) R3 is a current-limiting resistor to keep the current below the rating of the switch in case the DUT fails. Also, R3 can influence the rise time of voltage across the DUT (V_DUT).
- f) DUT charges and discharges based upon the switching frequency chosen for the switch.

5.1.2. Component selection

To begin with, a DC generator rated at 30 kV/5 kW and the HV capacitor rated at 4 μ F/50 kV available in the laboratory are considered for the test bench.

For the HV resistors (R1, R2 and R3), cylindrical shaped resistors are decided to be used to avoid any corona discharge in air due to sharp edges at high voltages. As per HV switch datasheet, its switching frequency is limited to 500 Hz. Therefore, the resistor R2 needed be chosen in such a way that,

- the voltage drop across R2 is minimal so that all voltage from capacitor bank appears across the DUT.
- it allows complete discharging of the DUT when HV switch turns off

R1 and R3 are current limiting resistors. R3 being in series with DUT also act as wave shaping resistor. From several values of HV resistors available in laboratory, the selection is made based upon the simulation as discussed further. A 30 pF value for C_{DUT} is a typical value and is therefore considered as a starting point for the simulations.

5.1.3. Simulation and validation of proposed schematic

As some parameters such as DC source, capacitor bank, DUT are known, therefore this step aided in optimizing the values of components wherever necessary.

According to the HV switch datasheet [94], its turn-on rise time is in the range of 1 to 20 ns. To comply with the values, a resistor (Rn) and capacitor (Cn) are added across the ideal switch block available in the Simscape electrical. The time constant of RC circuit (Rn = 50Ω and Cn = 100 pF) is chosen in such a way to produce a rise time of 11 ns across the resistor R2 (V_R2). The circuit thus created in Simscape electrical as shown in Figure 5-3 is simulated and the components with values in Table 5-2 are finalized. In the circuit, L1 and L3 are included to replicate the inductance of cable connection.

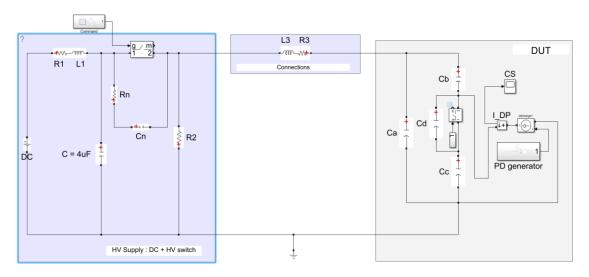


Figure 5-3: Image of the circuit simulated in Simscape electrical for generation of unipolar square voltage waveform using HV switch from Behlke

Table 5-2: Values assigned to different parameters for unipolar square waveform circuit

Parameter	Values
DC source	0-30 kV (maximum)
R1/L1	8.5 kΩ / 1 μH
R2	2 ΜΩ
R3/L3	5 kΩ / 1 μH
Cn / Rn	100 pF / 50 Ω
С	4 μF
C _{DUT} (ABCD model)	30 pF
HV Switch	MOSFET switches (HTS 1401-10-LC2) 140 kV/100 A
Switching frequency	500 Hz (maximum from datasheet)

In an RC circuit, the time required to reach from 10 % to 90 % of final value is 2.2 time constant (2.2τ) . The charging and discharging of capacitors with the given values of component are thus calculated as provided in Table 5-3.

Table 5-3: Time constant of RC present in schematics of test bench of partial discharge

Time constant	Time	Remarks
$\tau_1 = 2.2 \cdot R_1 \cdot C$	74.8 ms	Charging time of C
$\tau_2 = 2.2 \cdot R_2 \cdot C$	17.6 s	Discharging time of C
$\tau_3 = 2.2 \cdot C_{DUT} \cdot R_3$	330 ns	Rise time across DUT
$\tau_4 = 2.2 \cdot (R_2 + R_3) \cdot C_{DUT}$	0.13 ms	Discharging of C _{DUT}

As can be seen in Figure 5-4, the rise time across R2 when HV switch turns on is about 10.6 ns and rise time across the DUT (V_DUT) is about 284 ns (as measured in Simscape electrical), which are quite close to the values calculated analytically.

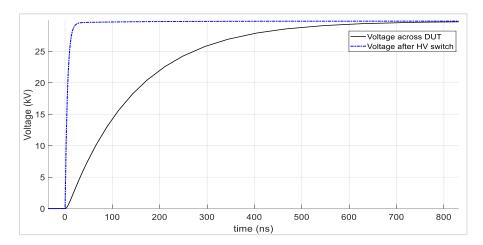


Figure 5-4: Rising front of square voltage after high voltage switch (across 2 $M\Omega$ resistor) and across DUT of 30 pF from simulation

With R2 as 2 M Ω , the V_DUT is then checked at the maximum switching frequency of 500 Hz. As can be seen in Figure 5-5, the DUT can be considered as discharged after 2 ms (approx. 3% of the max. voltage remaining).

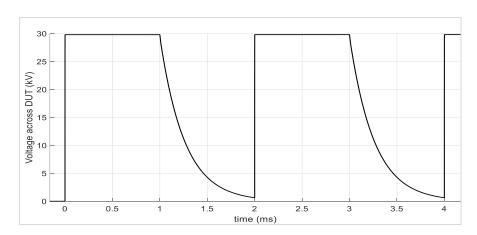


Figure 5-5:Output voltage across DUT at switching frequency of 500 Hz with R2 as 2 M Ω from simulations

The output waveforms thus generated from the simulations allowed to go ahead with test bench development.

5.2. Development of square waveform test bench

From the schematics used in Simscape electrical, the test bench to generate unipolar square voltage (USV) waveform is developed as shown in Figure 5-6. The whole set-up can be broadly divided into three parts: high voltage circuit, remote control circuit and measurement circuit. The following section briefs about all these parts.

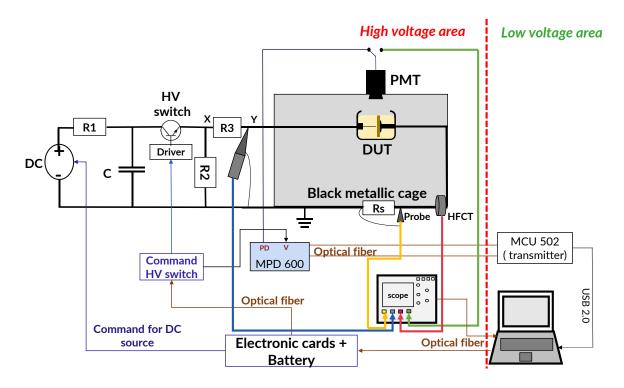


Figure 5-6: Schematics of HV test bench to generate USV waveform using a single HV switch with photomultiplier tube (PMT), high frequency current transformer (HFCT) and resistive shunt (Rs) for PD detection

5.2.1. Components of high voltage circuit

High voltage circuit

The DC generator, capacitor bank, HV switch and HV resistors of the values defined in Table 5-2 are installed in the set-up for generating the USV waveform. The HV switch from Behlke which comprises of MOSFETs, incorporated four accessories namely the pump, radiator, driver unit and HV switch itself. The details about the switch and other components of the test bench can be found in Appendix E.

At node "X" and "Y" as shown in Figure 5-6, the high voltage connections are enclosed by metallic shields to avoid occurrence of corona discharges from sharp edges (see set-up photo in

Figure 5-8). The usage of long wires in the HV circuit is avoided to reduce the EMI transmission through long wires during high speed switching. The DUT is placed inside a small dark metallic cage to improve the capturing capability of the photomultiplier tube and the whole set-up is inside a big Faraday cage. The set-up also allows the co-existence of AC test equipment for PD measurements.

Interface for remote control

To control DC source generator and the HV switch from outside the cage, the printed circuit board (PCB) interfaces are developed in Ampère laboratory with the help of experts. The frequency, duty cycle of HV switch and voltage output from DC source are controlled by implementing a customized PCB with Arduino. A graphical user interface (GUI) software, as shown in Figure 5-7, let the operator to send instructions through an optical fiber cable.

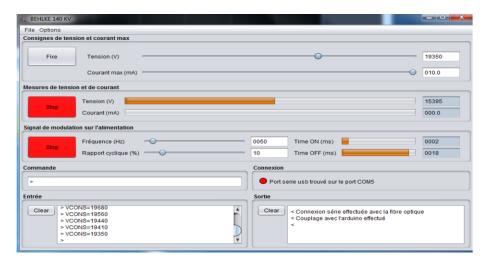


Figure 5-7: Photo of GUI software to communicate with DC source and HV switch with the help of PCBs placed inside the Faraday cage

To improve the immunity of the control boards to EMI from transients, the electronic cards inside the cage are powered using batteries. This is discussed in detail in section EMI management.

Measurement circuit

The partial discharge measurements can be made using PMT, HFCT and resistive shunt (Rs). The HFCT is put over the grounding cable from the DUT, while a 56 Ω shunt is connected to the grounding terminal of the DUT (Rs in Figure 5-6). The signal acquisition is made by either connecting all detectors to an oscilloscope, or by connecting the PMT to the Omicron system.

Due to the bandwidth limitation to 2.16 kHz for the MPD 600 unit and an input impedance mismatch with the HV probe (Tektronix P6015A), it is not possible to acquire the voltage with the Omicron system (or MPD 600). Therefore, to have an image of the square voltage waveform (for example to measure the phase angle of the PRPD patterns), the low voltage control signal transmitted to the HV switch is sent to the MPD 600 unit.

With the oscilloscope, the input impedances (Zin) of detection techniques and HV probe are chosen in accordance with their respective datasheet values, as provided in Table 5-4:

Table 5-4: Input impedance chosen in the oscilloscope while connecting the different detection techniques

$Zin = 1 M\Omega$	Low voltage probe across Rs; 56 Ω non-inductive resistor in series with grounding cable of DUT
$Zin = 50 \Omega$	HFCT
$Zin = 1 M\Omega$	HV probe to measure applied square voltage waveform
$Zin = 50 \Omega$	PMT

Figure 5-8 shows the photograph of the test bench developed in Ampère laboratory (Ecully, France). The same test bench can be used for PD measurement under both AC and square waveform.



Figure 5-8: Photograph of the square voltage test bench developed in Ampère laboratory, Ecully, France

5.2.2.EMI management in design phase of test bench

The transients produced by the fast switching action of power electronic devices can produce electromagnetic pulses. These pulses can propagate in the form of radiation or conduction, which might interfere with PD measurements and even disturb control circuits developed to communicate remotely with DC generator and HV switch. Hence, applying EMC principles to minimize the impact of EMIs was necessary in the initial design phase of this test bench. With this, the critical elements in the set-up such as placements of high energy sources, cable routing, signal cables and grounding structures can be addressed to minimize the impact due to EMIs. Here below are those measures which were adopted during the development of test bench to counter the impact of EMIs:

- Implementation of metallic shields around high voltage connections to reduce the effect of corona discharges in air.
- Optical fiber isolation: As shown in Figure 5-6, the communication from outside the cage
 is established with optical fiber cables for both command and measurement circuit. The
 transmission of data through optical fiber provides complete galvanic isolation. It reduces
 EMI coupling and avoid ground loops which would occur with copper wire.

Also, the PCB for driver unit (Command HV switch block) is isolated from the main PCB (Electronic cards) using an optical fiber cable as shown in Figure 5-6 to avoid EMI propagation between the two PCBs.

- The PCBs and accessories of the HV switch (pump and radiator) are powered using the batteries.
- The PCBs are kept inside metallic boxes and connection between boxes are made using shielded cables to minimize the impact of EMIs.

Even though EMC principles have been adopted at the early stages of development to minimize EMIs, disturbances are observed on the measurement circuits during preliminary checks. After consulting with EMC experts in the laboratory, it seems to be due to common mode current problems and EMIs generated during high speed switching. Therefore, some additional measures are taken to minimize the effect of EMI. They are discussed in Appendix E.

5.2.3.Output waveforms from test bench

In the next step, the waveform generated from the test bench are checked. The output voltages are measured by placing the HV probe at nodes 'X' (VR2) and 'Y'(V_DUT) respectively as shown in the schematics (Figure 5-6), with needle-barrier plane in dielectric liquid. The output

voltage waveform 'VR2' at 20 kV with 10 % duty cycle at a switching frequency of 50 Hz is presented in Figure 5-9.

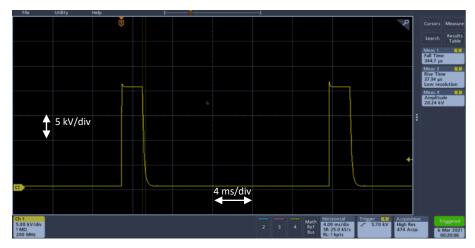


Figure 5-9: Unipolar square voltage waveform (VR2) measured at 20 kV with a switching frequency of 50 Hz at a duty cycle of 10 %

The rise time of VR2 is measured to be about 28 ns while for V_DUT it is around 256 ns as shown in Figure 5-10. Using, 2.2 τ as time constant for rise time across DUT with resistance R3 being 5 k Ω , the capacitance of DUT used in set-up can be estimated to be 23.3 pF.

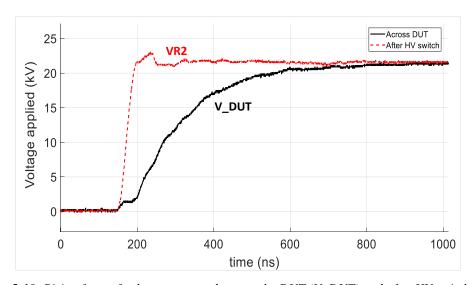


Figure 5-10: Rising front of voltage measured across the DUT (V_DUT) and after HV switch (VR2)

In the simulation, the rise time across DUT is found to be 284 ns (to reach 10-90 % of final value), which is only slightly different from what is measured in the set-up. This difference is due to the larger DUT capacitance considered in simulation compared to the experiment (30 pF vs 23.3 pF).

Furthermore, in Figure 5-10, some distortion can be observed in the waveform with fast rising time. As discussed in the manual of the HV probe [114], a resonance can occur due to the capacitance of the probe and ground lead inductance under fast transient signals. It may cause the overshoot and distortion observed in the measured voltage.

Figure 5-11 shows the image captured from the scope for the voltage across DUT at a switching frequency of 460 Hz at 20 kV. The longer falling time of about 350 µs (measured by scope) is due to the large value of resistance R2 in the circuit, which also limits any further increase in switching frequency.

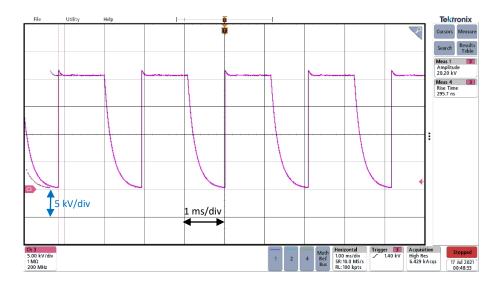


Figure 5-11: Voltage measured across DUT at 460 Hz at 20 kV using HV probe with scope

It can be observed from above discussion that the waveforms generated from test-bench have similar dynamics as found during electrical simulations.

5.3. Preliminary tests with unipolar square waveform

To assess the performance of the set-up under varying conditions and have the first experience of PD measurements under USV waveform, some preliminary tests are performed. The applicability of various PD detection techniques is also assessed through these tests.

At first the impact of resulting switching currents on three detection techniques (PMT, HFCT and Rs) using both an oscilloscope and the Omicron system as shown in Figure 5-6, is investigated. As mentioned in the beginning of this chapter, the resistor R3 which is in series with DUT can influence the rise time. Hence, tests are carried out with different resistors as R3 available in laboratory. Additional tests are also performed to measure the synchronization between the control signal sent to the driver unit and the square voltage generated.

This is followed by PD measurements. For this, at first a simple electrode configuration comprising of a needle-barrier plane in air is tested. The barrier between needle and plane is kept to avoid any breakdown event, so as to prevent damage to HV switch as recommended in its datasheet [94].

Finally, the dielectric liquid is poured in the DUT for PD measurements. The major outcomes from these preliminary tests are summarized at the end of this section.

5.3.1.Impact due to fast switching action of HV switch

In the set-up, the EMI produced by fast switching action of HV switch is found to impact all detection techniques. Under AC excitations, the PMT signal is not found to be impacted even at voltages more than 20 kV. However, under square waveform it is not completely true.

To mitigate this problem, the cable connecting the PMT to oscilloscope is shortened to less than 10 cm. Due to placement limitations of instrument it was not possible to reduce it further. Although this reduced the amplitude of commutation noise on PMT signal, it is still found to be impacted by the EMIs, as shown in Figure 5-12. Also, a test by switching DC bias of PMT is performed to check its impact on the PMT signal, which is provided in section E3 of Appendix E.

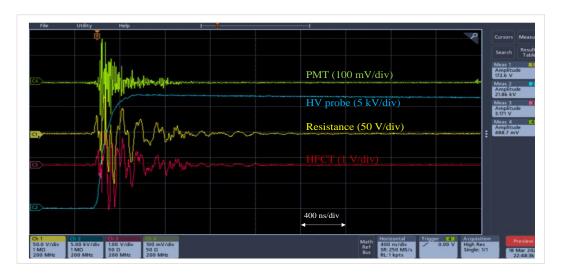


Figure 5-12: Impact of fast switching action of HV switch on all detection techniques at 20 kV

Other techniques, HFCT and Rs are also impacted by the fast switching actions in the circuit at 20 kV as can be seen in Figure 5-12. In terms of amplitude, the resistive shunt is found to be the most impacted, while the PMT signal is found to be the least impacted (note that the vertical scales of the three detection techniques are adjusted accordingly).

The disturbance of the PMT signal is also checked by connecting the 10 cm long BNC cable with MPD600 unit. As can be seen in Figure 5-13, the disturbances from the switching action are found to produce a peak of less than 0.4 pa.u. (on Omicron) at an applied voltage of 20 kV even with the DC supply of PMT turned off. Apart from this, a background noise band of less than 0.2 pa.u. is found to exist, which is same as under AC as discussed in Chapter-4.

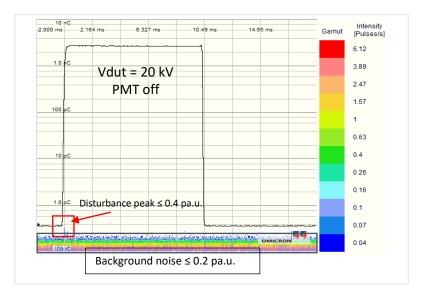


Figure 5-13: Disturbance peak due to fast switching action of HV switch observed with PMT when connected to Omicron system at 20 kV besides the background noise

From the investigation with oscilloscope, it is concluded that, the EMIs due to fast switching action of HV switch has an impact on all measurement techniques (PMT, HFCT and Rs). As the PMT signal is found to be least impacted among all techniques, it might be the first choice for PD detection. However preliminary tests are conducted before confirming this, as discussed further in this section.

With MPD600 unit, the disturbance peak of PMT signal is less than 0.4 pa.u. and is seen only around the rising part of control signal, which can be suppressed by elevating the threshold value. Moreover, with Omicron, the PDs occurring at phase angles other than disturbance peak can be recorded.

5.3.2. Varying rise times

To change the rise time across the DUT (with needle barrier plane in dielectric liquid), tests are performed by varying the resistance R3 in the set-up as presented in Table 5-5.

Table 5-5: R3 values and corresponding measured rise times across the DUT

R3	2.7 kΩ	5 kΩ	10 kΩ
Rise time	160 ns	256 ns	560 ns

The corresponding waveforms at 20 kV are plotted in Figure 5-14. Here it should be noted that, the dV/dt for R3=2.7 k Ω is about 125 kV/ μ s at 20 kV.

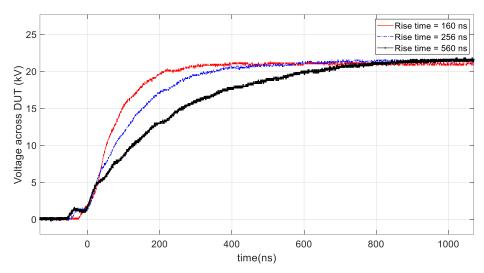


Figure 5-14: Rising voltage across the same DUT comprising of needle-barrier plane with dielectric liquid, for R3 resistor values of 2.7, 5 and 10 k Ω

To produce even higher dV/dt across the DUT, a smaller R3 resistor (100 Ω) is used. As can be seen from Figure 5-15, at an applied voltage of 16 kV, the voltage exhibits an overshoot which exceeds 30 kV, followed by a damped oscillation. This ringing could be due to the stray inductance resonating with the capacitance of the DUT (the low R3 value being insufficient to completely damp the oscillations).

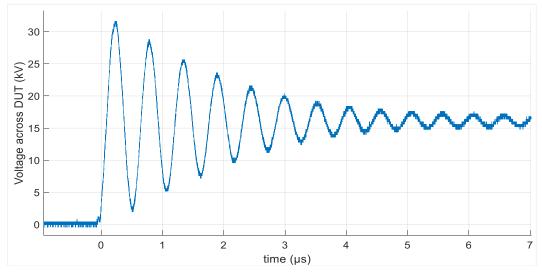


Figure 5-15: Rising front measured across DUT with R3 = 100Ω

The above assumption is verified by performing electrical simulation with the model developed in Simscape electrical. To investigate this, an inductance and capacitance are added in series with resistance R3 in the simulation circuit of Figure 5-3. With some adjustments, it is found that with an inductor and capacitor of 250 μ H and 250 nF respectively in series with 100 Ω , almost same oscillations can be generated across the V_DUT as found during experiments. The waveforms thus generated from simulations with 5 k Ω and 100 Ω as R3 with above mentioned values of series inductance and capacitance are plotted in Figure 5-16.

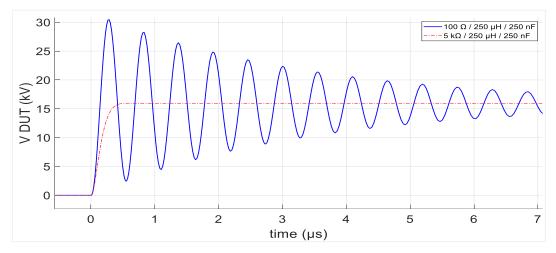


Figure 5-16: Voltage across DUT obtained from simulation for $100~\Omega$ and $5~k\Omega$ resistors as R3 with series inductance and capacitance of $250~\mu\text{H}$ and 250~nF respectively for both cases

The stray inductance obtained from simulation is quite high and the oscillations due to it resonate with capacitance in the circuit. These oscillations are not damped by 100Ω resistor, unlike $5 k\Omega$.

5.3.3. Synchronization between control signal and voltage output

As stated earlier, to synchronize the PD detection with the square waveform, the control signal transmitted to the driver unit of the HV switch is transmitted to the MPD 600. It is known that the MOSFET switches exhibit some turn-on delay because of internal capacitances and impedance of their gate drive circuit (refer Appendix E for more details). Hence, the investigation below aims at analyzing the delay between the control signal of the driver unit and V_DUT. This is to ensure PD events can be located accurately with respect to the HV waveform.

As shown in Figure 5-17, the control signal of 3 V sent to the driver unit of HV switch and corresponding V_DUT of 13.2 kV, appeared to be synchronized for 50 Hz switching frequency with 50 % duty cycle.

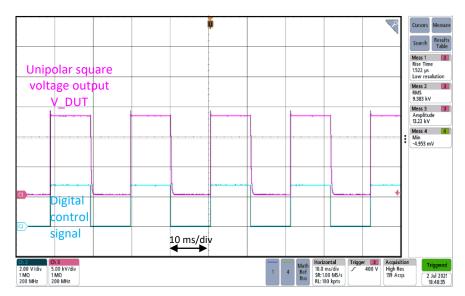


Figure 5-17: Synchronization between PWM signal (of 3 V) sent to driver control unit of HV switch and the output voltage waveform (of 13.2 kV) generated across the DUT

But when focused on a shorter time span around the rising front of the unipolar square waveform (Figure 5-18), a delay of 400 ns is observed between the control signal and the output voltage across DUT. This delay is close to the typical value of 250 ns for a resistive load stated in the Behlke HV switch datasheet.

Also, in Figure 5-18, large transients are found to be impacting the digital control signal. These occur only during the switching operation at high voltage, and their magnitude is found to increase with the voltage level.

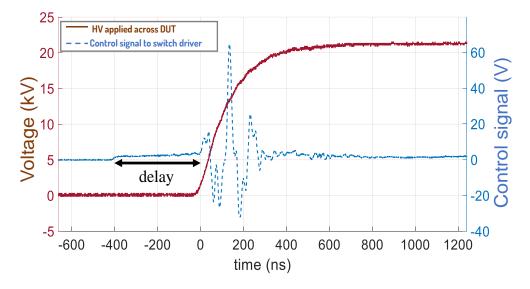


Figure 5-18: Transients observed with control signal being fed to driver unit during switching operation of HV switch

The remote control operation was found to be impacted by these perturbations. The EMI generated during switching might have conducted to the driver, impacting the remote control. Proper operation is restored by separating the wiring harnesses and batteries used for powering the PCBs (Command HV switch and electronic cards in Figure 5-6) corresponding to the driver unit and DC generator (as opposed to having a single supply for both). Although this does not remove perturbations from the control signal, no more problem is observed with the remote control operation. Keeping in mind this issue, an improved version of the PCB is being designed by an expert in the laboratory at the time of writing this manuscript.

As said earlier, due to bandwidth limitations of MPD600 unit, the control signal displayed on Omicron has very long rise time (about 200 µs as shown in Figure 5-19). Compared to 400 ns delay, this is quite large.

Therefore, with Omicron, the PD detection around the rising part of control signal, cannot be referred to the PDs during rise time of actual V_DUT, even if PDs are higher than disturbance peak. However, the acquisition of several voltage cycles and PD pattern study becomes easier with Omicron.



Figure 5-19: Rise time of about 200 µs observed for control signal on Omicron due to low bandwidth of MPD600 (timescale on top)

5.3.4. PD tests with needle-barrier plane configuration in air

For preliminary PD tests, a needle-barrier plane in air is considered, which is quite less complicated to implement and can ensure the occurrence of PDs at a relatively lower voltage than a DUT with dielectric liquid. The barrier is used to prevent breakdown events which could damage the HV switch. Here, a 0.7 mm thick FR4 barrier is placed against the grounding plane.

A gap of 2 mm is kept between needle tip and barrier surface. The parameters used during these measurements are summarized in Table 5-6,

Table 5-6: Parameters of the needle-barrier plane configuration in air used for preliminary PD tests

Electrode configuration	Needle- FR4-plane
Needle tip radius	1 μm (new)
Barrier	FR4 sample (0.7 mm thick)
Plane diameter (grounded)	20 mm
Medium	Air
Gap (needle tip to barrier)	2 mm
Detection technique	PMT (DC supply at -1.3 kV), HFCT and resistive shunt
Voltage waveform	Unipolar square/50 Hz/ 10 % duty cycle

The voltage is increased slowly from zero to detect PDs. At 5.4 kV, a negative peak appeared on PMT signal which corresponds to the emission of photons from a PD event (Figure 5-20). The acquisition of PD events (as opposed to that of an EMI) is confirmed by removing the needle: as no PD event is then found to occur even at a voltage higher than applied voltage, keeping other parameters of the DUT and DC supply of PMT constant. Another verification is made by turning the DC supply of the PMT off for the same DUT, with needle: no PDs are detected. This demonstrates that the output signal from the PMT corresponds to an actual detection of photons produced by PDs.

It can be observed that all three detection techniques are impacted by the EMIs generated by fast switching. The PMT (least impacted by EMI) detects the PD event which occurs just at the end of rising front at maximum voltage. Even after several attempts, it is difficult to detect the PD event using the HFCT and resistive shunt, which are masked by the perturbations.

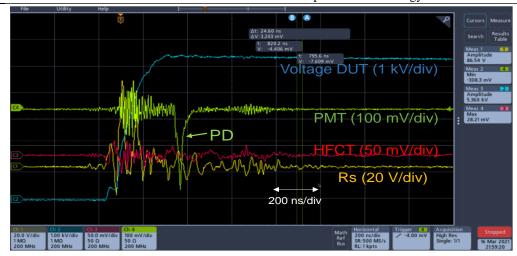


Figure 5-20: PD acquisition at 5.4 kV tried with PMT, HFCT and Rs near the rising front of square voltage for needle-FR4 plane configuration in air

Figure 5-21 presents the acquisition of a PD event during the plateau of USV. It can be observed that all three detection techniques are able to identify same PD event in the absence of perturbations.

From above observations, it can be concluded that the impact of perturbation on PMT signal is small and that it could detect PDs, just after rise time and during the plateau of USV. While with HFCT and Rs, the detection of PDs is only possible during voltage plateau. The EMIs due to fast switching largely impacted the acquisition of PDs with HFCT and Rs even just after rising voltage.

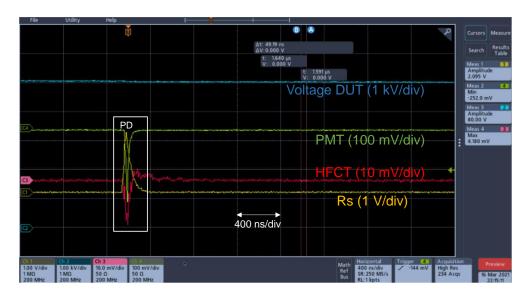


Figure 5-21:Image of the acquisition of PD events for needle-FR4 plane configuration in air at 5.4 kV using PMT, HFCT and Rs at maximum voltage for the chosen configuration

As with the AC 50 Hz tests, acquisition of PDs is tried under USV by connecting the PMT to the MPD 600 unit. Figure 5-22 shows the PDs events acquired for the same DUT after 30s of recording at 4.4 kV. As compared to the oscilloscope observations, PDs are detected at slightly lower voltage with Omicron. The occurrence of PDs is confirmed in the same way as discussed before (i.e., by turning off DC bias of PMT and removing the needle).

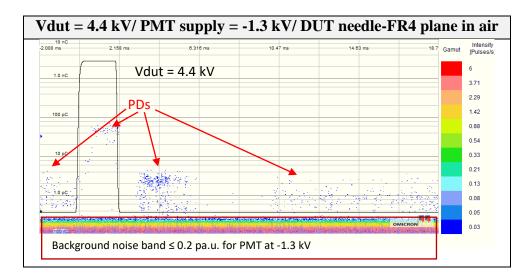


Figure 5-22: Detection of PD events by using the PMT with Omicron system acquired after 30 seconds of recording at 4.4 kV

As said earlier, the square voltage waveform shown by the Omicron system is the control signal fed to driver unit of HV switch and therefore is not the real square voltage applied across the DUT. For monitoring purposes, the HV probe is placed at node "Y" in Figure 5-6, which measures the V_DUT using the oscilloscope.

5.3.5. PD tests with needle-barrier plane configuration in dielectric liquid

In the next step, PD measurements are performed with needle-barrier plane configuration immersed in dielectric liquid. For these tests, the gap of 0.7 mm is maintained, which is same as used for PDIV measurements under AC 50 Hz. The parameters of the DUT and detection techniques used for this investigation are summarized in Table 5-7.

The measurements are performed with all detection techniques using the oscilloscope, followed by PMT connected to Omicron system. Considering the dispersion of optical signals while passing through the dielectric liquid medium, the DC supply of PMT is set at -2 kV to improve its detection capability with both oscilloscope and Omicron system.

Table 5-7. Parameters	s of the needle-harri	ier nlane configu	ration in synthetic a	ester used for preliminary l	PD tests
Tubic 5 7. Turameters	, of the needle barri	er piane conjigui	anon in symmetic c	csici uscu joi preiminary i	Dicord

Electrode configuration	Needle- FR4-plane
Needle tip radius	1 μm (new)
Barrier	FR4 sample (0.7 mm thick)
Plane diameter (grounded)	20 mm
Medium	Midel7131 (Synthetic ester)
Gap (needle tip to barrier)	0.7 mm
Detection technique	PMT, HFCT and resistive shunt
Voltage waveform (s)	Unipolar square/50 Hz/ 50 % duty cycle

With V_DUT at 20 kV, it can be seen again in Figure 5-23, all three detection techniques are impacted by the fast-switching action of semiconductor device. The first PD (marked as PD1) is detected, approximately 500 ns after the rising front of V_DUT. The PD1 cannot be viewed with HFCT and resistive shunt signals. The PD2 detected by PMT represents the large negative peaks acquired by PMT. PD3 represents set of PD events which are acquired by all three detection techniques.

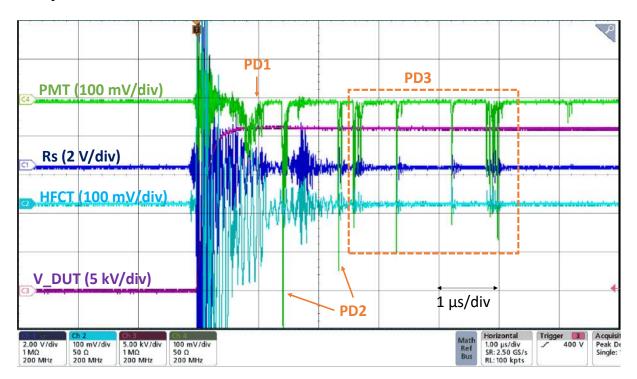


Figure 5-23: Image of the acquisition of PD events at 20 kV for needle-FR4 plane configuration in synthetic ester using PMT, HFCT and Rs during rising voltage across the DUT

This is more clearly visible in Figure 5-24, away from the rising front, all three detection techniques are found to detect PD events at same instants during the plateau. Regarding the shape of the signals, the detection of PDs by the PMT always generate negative peaks, while the HFCT and Rs produce oscillatory signals. This is different from the signals observed during the voltage plateau in air for the HFCT and Rs.

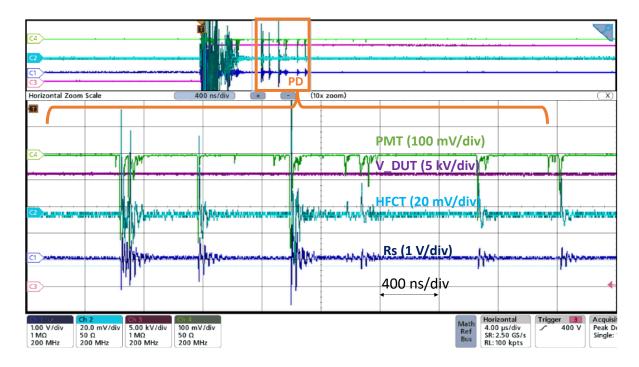


Figure 5-24: Image of the acquisition of PD events at 20 kV for needle-FR4 plane configuration in synthetic ester using PMT, HFCT and Rs at maximum voltage across the DUT

The occurrence of PD events is confirmed by turning off the DC supply of PMT and removing the needle from the DUT, while keeping the applied voltage at same level. The waveforms thus saved from the oscilloscope are plotted together as shown in Figure 5-25. It can be observed that the negative peaks (PD1, PD2, PD3, PD4, PD5, PD6) can only be seen when the DC supply of PMT is at -2 kV with a needle in the DUT. The first PD event, PD1, generated just after rising voltage is found to have a low negative peak value as compared to long peaks (PD2, PD4 and PD5) detected during voltage maximum. Also, these PDs mainly occur just few microseconds after the rising front of USV waveform.

For other conditions, i.e., DC supply of PMT turned off and needle removed, with the same voltage applied, no PD events are detected. The perturbation can be seen overlapping with each other from three different cases, i.e. DUT with needle, DUT without needle and PMT off.

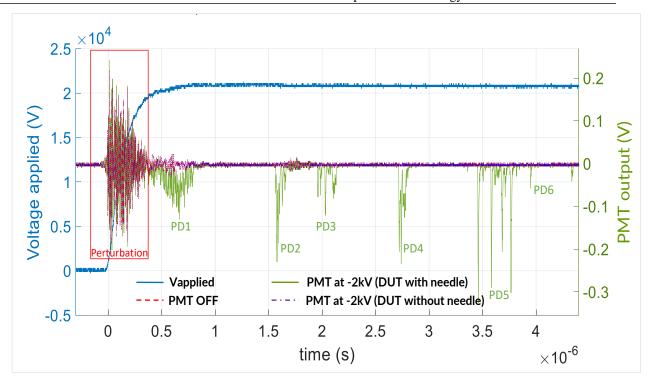


Figure 5-25: Verification of the acquisition of PDs by keeping DC supply of PMT at -2 kV with DUT, turning off DC bias of PMT with same DUT and removing the needle from the DUT at 20 kV

The tests are further continued for same DUT by coupling PMT with MPD600 unit, with PMT DC supply at -2 kV. It can be observed in Figure 5-26 (a), PDs are mainly occurring near the ascending part of the control signal. With the oscilloscope (Figure 5-25), the PDs are found to be occurring at least 500 ns after the V_DUT rise time, therefore PDs which appear near the ascending part of control signal may be assumed to be occurring after this interval. The PD occurrence with Omicron is confirmed as well, by turning off the PMT and removing the needle from the DUT, while keeping the V_DUT at same level (see Appendix F).

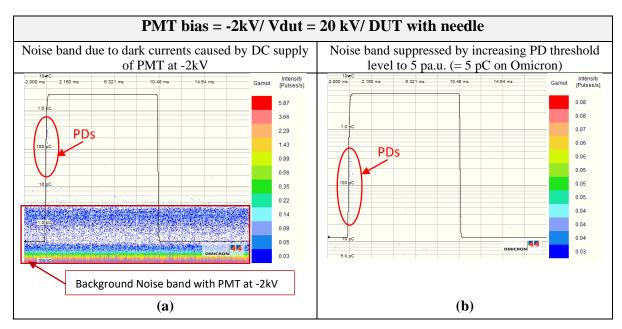


Figure 5-26: Acquisition of PD events at 20 kV for needle-FR4 plane configuration in synthetic ester with PMT coupled to MPD600 from Omicron shows (a) noise band with -2 kV DC supply of PMT and (b) noise band suppressed by adjusting threshold to 5 pa.u. in Omicron for same DC supply of PMT

Also, as can be seen in Figure 5-26, the background noise band is reaching up to 5 pa.u. due to increased dark current generated by the PMT at -2 kV (as said earlier in section 4.1, Chapter-4). To suppress this noise band and visualize only the PD events, the PD threshold of 5 pa.u. is chosen in Omicron. The result thus acquired after 30s of acquisition is presented in Figure 5-26 (b).

After this, the PDs are also acquired by PMT by keeping its DC supply at -1.3 kV, which is the same value used for detection of PDs under AC 50 Hz. When the supply voltage of PMT is increased from zero to -1.3 kV, the noise band remained less than 0.2 pa.u. (same as observed during AC tests). Beyond this level, the background noise increased above 0.2 pa.u.

The tests thus performed with DC supply of PMT at -1.3 kV is presented in Figure 5-27 for same DUT. The PDs are found to be detected with this DC supply of PMT. The background noise is less than 0.2 pa.u. and only noise peak of about 0.4 pa.u. due to switching occurred at 20 kV.

Further, from Figure 5-26 (PMT supply voltage at -2 kV) and Figure 5-27 (PMT supply voltage at -1.3 kV), it can be noticed that by increasing the DC supply of PMT, the captured PD events have higher magnitude (around 100 pa.u.) at -2 kV as compared to those (around 10 pa.u.) at -1.3 kV. Increasing the DC supply of PMT scaled up the magnitude of almost same set of PD events, along with the noise band. As PD detection is possible at -1.3 kV without increasing noise band, hence -1.3 kV is chosen as DC supply of PMT when coupled to Omicron, for PD detection.

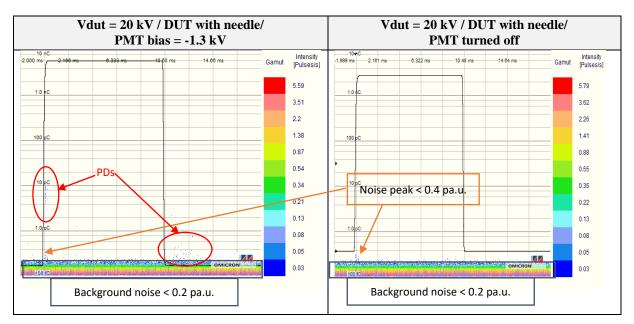


Figure 5-27: Acquisition of PD events at 20 kV for needle-FR4 plane configuration in synthetic ester with PMT connected to Omicron (left) with DC supply voltage of PMT at -1.3 kV and (right) with supply voltage of PMT turned off

In case of oscilloscope, by keeping DC supply of PMT at -1.3 kV, it was not easy to trigger at low magnitude PDs due to large amplitude of commutation noise generated by EMIs during fast switching, which seems to be impacting the PMT measurement circuit. As can be seen in Figure 5-28, with DC supply of PMT at -1.5 kV, the PD triggering with oscilloscope was only possible when V_DUT is increased to 23 kV. This is because, as voltage increased, the PD amplitude (or negative peak with PMT) became larger than the amplitude of commutation noise. Hence, with scope, if DC supply of PMT is reduced from -2 kV to -1.5 kV, the V_DUT needed to be increased for PD detection.

The PMT is chosen for PD measurement as it is found best among all detection techniques tried under USV waveform. But next is to choose between acquisition systems: oscilloscope or Omicron. For this, all the measurements made with oscilloscope and Omicron are summarized as provided in Table 5-8. As can be seen from table, the PDs could not be detected by PMT coupled with scope, with DC supply as -1.3 kV, due to large amplitude of commutation noise which hinders the detection of low magnitude PDs as said earlier. The PD detection with scope is possible when DC supply of PMT is increased (such as to -2 kV). However, with Omicron, the PD detection is possible with DC supply of PMT at -1.3 kV. Moreover, the noise band remained less than 0.2 pC at this PMT supply, same as during AC tests.

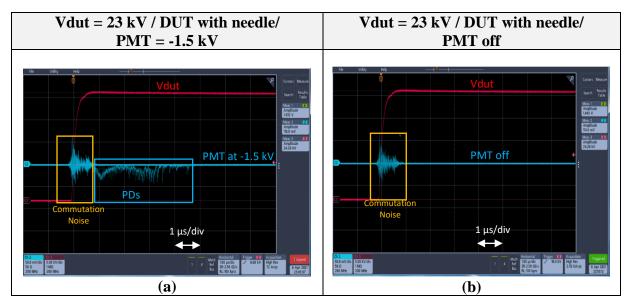


Figure 5-28: PD detection with PMT at 23 kV (a) with supply voltage of PMT at -1.5 kV and (b) PMT turned off

Table 5-8: Comparison of voltage across DUT and supply voltage of PMT used for PD investigation using oscilloscope and Omicron system

Test case	Voltage across DUT	DC input of PMT	DUT status	Observation with Oscilloscope	Observation with OMICRON system
1	20 kV	-2 kV		PDs detected	PDs > 10 pa.u. detected. Background noise ≤ 5 pa.u.
2	23 kV	-1.5 kV		PDs detected (for lower DC input of PMT, a higher voltage across DUT was required than in test case 1)	Not tested
3	23 kV	-1.3 kV	With needle	Difficult to trigger at low value PDs due to high amplitude of commutation noise on PMT signal	Not tested
4	20 kV	-1.3 kV		Not tested	PDs > 1 pa.u. detected. Perturbation peak ≤ 0.4 pa.u. Background noise ≤ 0.2 pa.u
5	20 kV	0 V		No PDs detected. Only perturbation impacting PMT signal observed	No PDs detected. Perturbation peak ≤ 0.4 pa.u. Background noise ≤ 0.2 pa.u.
6	20 kV	-2 kV	Without	No PDs detected. Only perturbation impacting PMT signal observed	Not tested
7	20 kV	-1.3 kV	needle	Not tested	No PDs detected. Perturbation peak ≤ 0.4 pa.u. Background noise ≤ 0.2 pa.u

From the above discussion, it can be observed that the acquisition of PDs with Omicron system can be done at lower voltage across DUT by maintaining optimal value of DC supply of PMT

(i.e., -1.3 kV). Apart from this, the PDIV voltage and PRPD pattern thus obtained by using PMT with Omicron can be directly compared to the results obtained with AC 50 Hz for same DUT. Even though, oscilloscope provides waveforms (negative peak) of PDs with PMT, locating the initial PDs at inception voltage seemed easier with Omicron system. Also, the Omicron can record several periods which can be used for further analysis even after finishing the tests.

Considering the above advantages of using Omicron system, the PDIV investigations with USV waveform are decided to be performed by coupling PMT with Omicron system for further tests. However, the oscilloscope is used for voltage measurements across DUT as control signal is sent to Omicron.

5.3.6. Conclusions from preliminary tests

Some preliminary tests were performed to assess the performance of test bench and acquire first experience of PD investigations under square voltage waveform. The acquisition of PDs was tried with PMT, HFCT and resistive shunt. The PDs were acquired by connecting PMT, HFCT and Rs to oscilloscope as well as by linking the PMT to the Omicron system. For investigations, at first a simple configuration comprising of needle-barrier plane in air was used. This was followed by the PD investigation of needle-barrier plane in dielectric liquid. The major outcomes of the preliminary tests can be summarized as follows:

- A 100 Ω resistor as R3 in the set-up, can lead to an overshoot of about two times (30 kV) the applied voltage (16 kV), followed by oscillations in the square voltage waveform across the DUT. From simulation, it was observed that a 250 μ H inductance in series with 250 nF capacitance can produce same overshoot and oscillations as found during test with 100 Ω resistor. Similar overshoot and oscillation were not observed with 5 k Ω resistor and same value of series inductance and capacitance.
- The total turn-on delay between the control signal and output voltage waveform is 400 ns. The fast-switching action of the switch has been found to be impacting the control signal.
- The EMI generated due to fast switching action of semiconductor devices impacts all
 detection techniques, but the PMT is found to be less sensitive to EMI than HFCT and
 Rs.
- Among all detection techniques, the PMT detected PD events both after rising front and during the voltage plateau. The HFCT and Rs could detect PDs only during the plateau.
- The acquisition of PD signals by connecting the PMT to the Omicron system has been found to be easier and more sensitive as compared to using an oscilloscope. Therefore, this method is used for further investigations.

5.4. Summary

This chapter discusses the two options considered for square waveform generation. Following the failure of commercial pulse generator, a square waveform test bench is designed and built using a single HV switch in the timeframe of this thesis. The component selection is based on simulation and is found to be compatible in the real set-up with the needle-barrier plane configuration in dielectric liquid.

PD measurements with unipolar square waveform are performed with three different detection techniques namely PMT, HFCT and Rs. Although precautions are taken to minimize the impact of EMIs in the test bench, the high-speed switching of the HV switch is found to impact all three detection techniques, with the PMT signal being impacted the least.

During preliminary measurements, a needle-barrier plane configuration in air as well as the DUT with needle-barrier plane in dielectric liquid are tested. Among all detection techniques, PMT detects PD events both after rising front and during the voltage plateau. The HFCT and Rs can only detect PDs only during the voltage plateau. The incapability of PD detection during fast rising voltage with HFCT is also in line with the findings of simulations presented in chapter-2.

The comparison between Omicron and oscilloscope aided in understanding the treatment of the signals acquired by Omicron. Under USV waveform, the commutation noise observed with oscilloscope can be related to disturbance peak observed with Omicron. Further, the acquisition of PD signals by coupling PMT with MPD600 is found to be easier as compared to oscilloscope, due to ease of triggering, recording several periods and analyze the data after finishing the tests.

The capability of USV test bench is further illustrated in following chapter where the PD measurements under AC and USV will be presented for different combination of liquid/solid insulations and changing parameters of USV waveform (such as switching frequency, rise time).

6. Study of partial discharges in unipolar square voltages

Following the development of partial discharge test bench with unipolar square voltage (USV) waveform, experimental plans are designed to address two major objectives:

- Examine the PDs for various liquid/solid insulation under USV waveform and compare the findings with the results obtained under AC 50 Hz.
- PD detection under varying parameters of the USV waveform such as rise time, switching frequency and duty cycle.

This chapter discusses all the steps taken to fulfill these objectives. A different test method is used to allow PD comparison between AC and USV waveform.

At first a consistency measurement between AC and USV waveform is performed with a DUT specimen to define the strategy for PD comparison. Then, with the defined strategy, a test campaign is launched with different combination of liquid/solid insulations under AC and USV waveform. Some complementary tests by changing tip radius under USV waveform are also presented.

Following this, the investigations under USV waveform is presented by varying switching frequency, rise time and duty cycle. The observation has been summarized at the end of each section and the chapter closes with a general discussion on obtained results and conclusion.

The PDIV results are presented as bar graph which shows the average value whereas the error bars represent the standard deviation. To understand the statistical difference between the average of PDIVs, t-test are used considering p-value of 0.05. The t-test is performed using the T.Test () function in Microsoft Excel. The standard deviation (SD), upper and lower bound of average PDIV by taking 95 % of confidence interval (CI), are also stated with p-values.

All tests are carried out with series resistor (R3 in Figure 5-6) of 5 k Ω except during the evaluation of rise time effect. The PMT coupled with commercially available MPD600 (from Omicron) is used for all PD measurements. The PDIV measurements thus performed with Omicron is compliant with IEC60270 standard, which means the PDIV is the minimum voltage above which PD of specified (or threshold) value occurs. As the square voltage displayed by Omicron is a control signal, the actual voltage across DUT (V_DUT) is measured using an HV probe and an oscilloscope.

6.1. Procedure of PD comparison between AC and unipolar square voltages (USV)

To define the procedure of PD measurements, a consistency check is performed between AC 50 Hz and USV 50 Hz with 10 % duty cycle. As found during preliminary tests peak of commutation noise due to EMI impacting the PMT signal acquired by Omicron reaches 0.4 pa.u. at 20 kV. Therefore, the threshold value of 0.5 pa.u. is chosen under both AC and USV for PDIV comparison.

Following steps are taken to define the procedure for PD comparison under AC and USV:

- Definition of test method which can be used under both kinds of waveforms.
- Define the number of tests that can be performed with same DUT cell without degrading it under both kinds of waveforms
- Report the first outcomes of consistency check

6.1.1. Test method for PDIV comparison

Due to long discharging time through 2 M Ω resistor, it is difficult to use the voltage profile defined during AC test campaign (Figure 4-9), with USV waveform as well. Therefore, the voltage profile as shown in Figure 6-1 is adopted for comparative analysis between AC and USV; which is explained below:

- Step 1: The voltage is first increased by ramp to find the first PDIV.
- Step 2: After finding the PDIV value, the voltage is increased to 60 % of PDIV found in previous step. Then, the voltage is raised in steps of 1 kV with a waiting time of 30 seconds at each step. The voltage is increased until PDIV is reached.
- Step 3: Step 2 is repeated five times with an interval of 30s at zero voltage between two successive voltage applications.

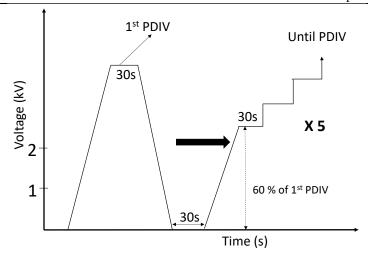


Figure 6-1: Voltage profile chosen for PDIV comparison between square and AC voltages

6.1.2. Device under test for PDIV comparison

During this investigation, needle-FR4-plane in mineral oil (Nytro 4000X) was used as DUT. For this consistency check between AC and USV waveform, the dielectric liquid was not treated. The parameters of DUT cell, acquisition technique and threshold condition used during this investigation have been provided in Table 6-1.

Table 6-1: Parameters of the DUT used for PDIV consistency checks between AC and USV

Electrode configuration	Needle- FR4-plane
Needle tip radius	1 μm (new)
Barrier	FR4 sample (0.7 mm thick)
Plane diameter (grounded)	20 mm
Medium	Mineral oil (Nytro 4000X- untreated)
Gap (needle tip to barrier)	0.7 mm
Detection technique	Photomultiplier with MPD600 (Omicron)
Voltage waveform (s)	 USV/50 Hz/ 10 % duty cycle AC 50 Hz
PD threshold	0.5 pa.u.

For comparative analysis, the same DUT cell should be tested under both waveforms. As noticed earlier during PD tests with AC excitations, a 1 µm tip could be used to perform ten PDIV measurements without noticeable impact on the PDIV results. To ensure if this holds true regardless of the waveform and assess the degradation of the DUT during PDIV tests under AC and USV waveform, the following steps are taken:

1. At first a DUT specimen as defined in Table 6-1 is taken and named as DUT n°1

- 2. Four series (one series = 5 PDIV tests) of PDIV measurements are performed in the following order:
 - a. Test series 1: under USV waveform (TS1_Sq)
 - b. Test series 2: under AC voltage (TS2_AC)
 - c. Test series 3: under USV waveform (TS3_Sq)
 - d. Test series 4: under AC voltage (TS4_AC)
- 3. After this, another DUT specimen is taken and called as DUT n°2
- 4. With DUT n°2, two series of PDIV measurements are performed; but test order is reversed, as follows,
 - a. Test series 1: under AC voltage (TS1_AC)
 - b. Test series 2: under USV waveform (TS2_Sq)

Reversing the test order with DUT n°2 provided the possibility to check the influence of fastrising square voltage on PDIV results as discussed in next section. Further, tests are discontinued to check the needle from DUT n°2 under microscope after two series of PD tests. This step was taken after noticing higher PDIV values for TS3_Sq and TS4_AC for DUT n°1, as discussed ahead.

6.1.3. Results and discussion

To compare the PDIV results between two waveforms, voltage obtained in AC 50 Hz is reported as peak-peak values (= $2\sqrt{2} \times V_{rms}$). For USV, the amplitude value has been considered (zero to peak). The representation of PDIV in peak-peak values allow comparison of PDs occurring in a complete cycle between two kinds of waveforms. The comparison using peak-peak between AC and unipolar square voltage is also in compliance with literatures such as [58], [62].

Figure 6-2 presents the comparison of average PDIVs obtained from four series of PD measurements with DUT n°1. It can be observed that the:

- PDs occurred at a lower voltage amplitude under unipolar square waveform than in AC.
- The average PDIV for TS1_Sq is less than TS2_AC.
- $PDIV_{TS3_Sq} > PDIV_{TS1_Sq}$ and $PDIV_{TS4_AC} > PDIV_{TS2_AC}$. The needle tip could have deformed due to heating effect caused by the PDs leading to higher PDIV values for test series 3 and test series 4.

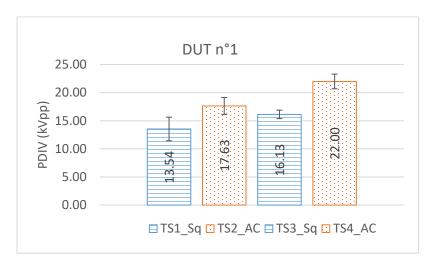


Figure 6-2: PDIV results for DUT n°1 under USV and AC at 50 Hz

Further, to check if the fast-rising USV waveform has an impact on PDIV results, the order of tests with second DUT (DUT n°2) is reversed, that is, the PD tests under AC is performed first under USV. The idea behind reversing the test order is if USV waveform deforms the needle tip after five PD tests, the average PDIV in AC with new tip for DUT n°2 would be lower than TS2_AC of DUT n°1. The average PDIV results thus obtained for DUT n°2 are plotted in Figure 6-3.

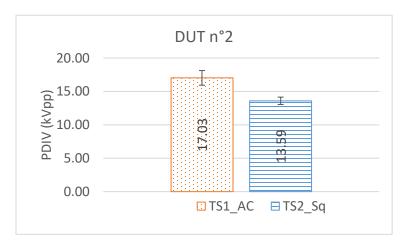


Figure 6-3: PDIV results for DUT n°2 under square waveform and AC 50 Hz

Comparing the average PDIV values of DUT n°1 and DUT n°2, it can be observed that:

- $Average_PDIV_{TS1_AC_DUTn^{\circ}2} \approx Average_PDIV_{TS2_AC_DUTn^{\circ}1}$ and,
- $Average_PDIV_{TS2\ Sq\ DUTn^{\circ}2} \approx Average_PDIV_{TS1\ Sq\ DUTn^{\circ}1}$

This investigation demonstrates that the same DUT cell can be used for ten PDIV measurements with five tests under each waveform for comparison of PDIVs. Also, after ten PD tests the DUT should be replaced.

Also, to verify the assumption of deformation of needle tip, two different needle tips, a new one and another after ten PD measurements (from DUT n°2) are examined under scanning electron microscope (from Vega3 Tescan) in laboratory. As can be observed from the images presented in Figure 6-4, as compared to new tip, the one after ten PD measurements have undergone deformation. This might be the reason of higher average PDIV values obtained for TS3_Sq and TS4 AC with DUTn°1.

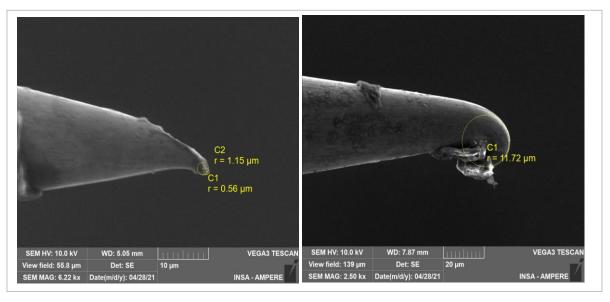


Figure 6-4: (Left) A new 1 µm needle tip and (right) tip after 10 PDIV tests viewed under microscope

6.1.4. Outcomes from consistency tests

Following outcomes are derived from the consistency check between AC and USV waveforms,

- The adopted voltage application facilitated the PD comparison between AC and USV.
- The average PDIV of USV is lower than in AC for tested DUT.
- A DUT specimen can be used for a maximum of ten PD measurements, with five tests each under AC and USV. The DUT specimen should be replaced by a new one for further measurements to avoid any deformation of needle tip.

Following the definition of test procedure, following investigations are planned,

• PD comparison between AC and USV waveforms for different solid/liquid insulations

- Compare PD parameters between two dielectric liquids tested under USV
- Assess PD phenomenon under USV by changing the parameters of USV waveform

All these are discussed in succeeding sections.

6.2. PD comparison between AC and unipolar square waveform

With the procedure defined in section 6.1, the PD measurements are carried out with different combinations of solid/liquid insulation under AC 50 Hz and USV 50 Hz with a duty cycle of 50 %. During these investigations, both mineral oil (Nytro 4000X) and synthetic ester (Midel7131) are used. They are conditioned and monitored according to the procedure described in Appendix D. For reference, the BDV test results of mineral oil and synthetic ester are provided in Figure 3-14 and Figure 3-15 respectively, while the water content measurement are in Table 3-7 in chapter 3 (batch 6 to batch 10).

For these tests, FR4 (0.7 mm and 1.3 mm thick) and 3 mm thick pressboard barriers were also included to the list of previously used barriers under AC. FR4 is a glass fiber-epoxy composite used in printed circuit boards and may find application in power modules with WBG devices as suggested in [110]. Table 6-2 presents the list of barriers used during this investigation.

Barrier samples	Thickness (mm)	Sample size (mm × mm)	Samples tested with Nytro 4000X	Samples tested with MIDEL 7131
PVC	1	40 × 40	5	5
FVC	2	40 × 40	5	5
FR4	0.7	40 × 40	5	5
rk4	1.3	40 × 40	5	5
A INI	0.63	40 × 40	3	3
AlN	1	40 × 40	3	3
Impregnated	2	36 × 36	5	
Pressboard	3	40 × 40	5	

Table 6-2: Solid barriers used for PDIV comparison between AC and USV waveform

With the aim to calibrate the optically acquired PDs, electrical and optical detection techniques are used simultaneously for PD measurements under AC 50 Hz. The correlation strategy is similar to the one described in section 4.5 (Chapter-4).

The charge and voltage calibration are done every time before starting the PD tests under AC. Ten PD measurements are performed with each DUT specimen, five each under AC and USV waveforms. A DUT specimen comprised of treated dielectric liquid, a new needle and a barrier sample. At the end of ten PD tests, the dielectric liquid, needle and barrier sample in the DUT specimen are changed. For statistical analysis of PD measurements, five DUT specimens are tested for each solid/liquid combination, except for AlN barriers for which only three DUT specimens are examined (see Table 6-2).

It is worth mentioning here that the order of tests is reversed from one DUT specimen to the next; i.e. if PD tests started under AC for first DUT specimen, then it began with USV for second specimen.

6.2.1. Estimation of charge magnitude from optical detection

Figure 6-5 and Figure 6-6 presents the average PDIV obtained under AC and USV for different barriers tested in mineral oil (Nytro 4000X) and synthetic ester (Midel7131) respectively. The PD tests under AC are performed simultaneously with electrical and optical detection, while under USV only optical detection is used. Each bar represents the average, and the error bars are the standard deviation of twenty-five PDIV measurements except for AlN barrier for which only fifteen PD tests are performed.

In the first step, a correlation between electrically and optically acquired PDs is established. From the AC tests, it is found that the optically acquired PDs of 0.5 pa.u. magnitude corresponds to about 2 pC in mineral oil. This is true for all barriers tested in mineral oil. A similar correlation is established with synthetic ester, in which PDs of 0.5 pa.u. from optical detection corresponds to about 10 pC of apparent charge measured from electrical detection.

Using the above mentioned threshold values for electrical and optical detection in mineral oil and synthetic ester, the average PDIV thus obtained are found to be quite same, as can be seen in the graphs plotted in Figure 6-5 and Figure 6-6.

Comparing the AC results obtained here with the results from the previous AC test campaign, (section 4.5 in Chapter 4), some differences can be observed in average PDIV. This variation could be due to differences in the test methods for the two test campaign. In the previous test campaign under AC (chapter 4), the voltage was always reduced to zero volt (see Figure 4-9). However, here, the voltage profile has to be adapted to allow PD comparison under AC and USV as discussed in paragraph 6.1.1. With this voltage profile (see Figure 6-1) the DUT is continuously stressed until PDIV is reached. The influence of test methods on PDIV is discussed in studies like [17] and [99].

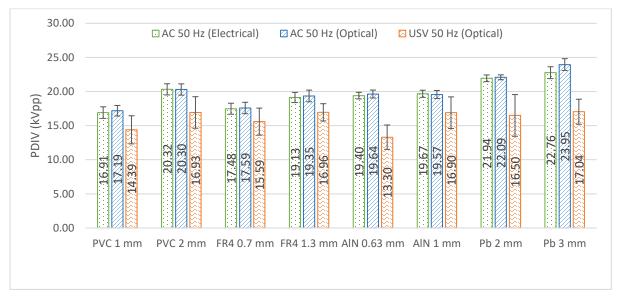


Figure 6-5: Average PDIV (in peak to peak) for different barriers tested in mineral oil; using electrical detection only in AC and optical detection in both AC and USV; the threshold set in electrical detection is 2 pC while for optical detection is 0.5pa.u.

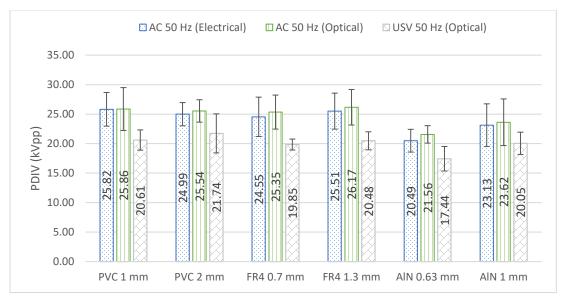


Figure 6-6: Average PDIV (in peak to peak) for different barriers tested in synthetic ester; using electrical detection only in AC and optical detection in both AC and USV; the threshold set in electrical detection is 10 pC while for optical detection is 0.5pa.u.

6.2.2. PD comparison between AC and USV waveforms

Looking at the graphs plotted in Figure 6-5 and Figure 6-6, it can be observed that the average PDIVs under USV waveforms are lower than in AC. To assess if the difference in average value

of PDIV is significant between AC and USV, t-test method is used, considering the null hypothesis that PDIV average values are identical under AC and USV for each barrier.

The result is provided in Table 6-3 and Table 6-4 for mineral oil and synthetic ester respectively.

	Mineral oil															
Barriers	PVC 1	mm	PVC 2 mm FR4 0.7 mm F		FR4 1.3 mm AIN 0.63 mm		AlN 1 mm		Pb 2mm		Pb 3mm					
	AC	USV	AC	USV	AC	USV	AC	USV	AC	USV	AC	USV	AC	USV	AC	USV
Avg (kV)	17.19	14.39	20.30	16.93	17.59	15.59	19.35	16.96	19.64	13.30	19.57	16.90	22.09	16.50	23.95	17.04
SD (kV)	2.19	2.06	2.35	2.31	2.36	1.99	2.41	1.26	1.64	1.79	1.66	2.31	1.02	3.06	2.46	1.84
95 % CI	18.09	15.24	21.27	17.89	18.56	16.41	20.35	17.48	20.55	14.29	20.48	18.18	22.51	17.76	24.96	17.80
UB/LB	16.28	13.54	19.33	15.98	16.61	14.77	18.36	16.43	18.73	12.32	18.65	15.62	21.67	15.24	22.93	16.28
n-value	2.23F	-04	2.43	F-05	6.16	F-04	6.47	F-04	2.82	F-07	2.10	F-03	2.86	F-08	5.91	F-11

Table 6-3: Estimation of difference in average value of PDIVs between AC and USV for mineral oil using T-test

Synthetic ester												
Barriers	PVC 1 mm		PVC 2 mm		FR4 0.7 mm		FR4 1.3 mm		AIN 0.63 mm		AlN 1 mm	
	AC	USV	AC	USV	AC	USV	AC	USV	AC	USV	AC	USV
Avg (kV)	25.86	20.61	25.54	21.74	25.35	19.85	26.17	20.48	21.56	17.44	23.62	20.05
SD (kV)	3.64	1.72	1.90	3.31	2.89	0.93	3.01	1.53	1.48	2.08	3.96	1.89
95 % CI	27.36	21.32	26.33	23.10	26.54	20.23	27.41	21.11	22.38	18.59	25.81	21.10
UB/LB	24.36	19.90	24.76	20.37	24.15	19.46	24.93	19.85	20.74	16.29	21.43	19.01
p-value	1.69E-08 6.83E-06		E-06	3.45E-09		3.35E-08		8.12E-08		1.13E-03		

Table 6-4: Estimation of difference in average value of PDIVs between AC and USV for synthetic ester using T-test

As can be observed from these tables, for each barrier tested under AC and USV waveforms, the p-value is less than 0.05. This is true in both dielectric liquids. This indicates that there is a significant difference in average PDIV values between AC and USV for all barriers.

To compare the PDIVs, the reduction in average PDIV in USV as compared to AC is calculated using following expression:

$$\% \ reduction = \frac{(Average_PDIV_{AC} - Average_PDIV_{USV}) \times 100 \ \%}{Average_PDIV_{AC}}$$

^{*} Avg: Average, SD: Standard Deviation, CI: Confidence interval, UB: Upper bound, LB: Lower bound

^{*} Avg: Average, SD: Standard Deviation, CI: Confidence interval, UB: Upper bound, LB: Lower bound

The results are shown in Table 6-5.

Table 6-5: Decrease in PDIV observed	l in unipolar squa	re waveform for	different barriers tested

Barriers thickness	PVC 1 mm	PVC 2 mm	FR4 0.7 mm	FR4 1.3 mm	AlN 0.63 mm	AlN 1 mm	PB 2 mm	PB 3 mm
% Reduction (Mineral oil)	16	17	11	12	32	14	25	29
% Reduction (Synthetic ester)	20	15	22	22	19	15	NA	NA

^{*}Note: result rounded to nearest integer value

From the PDIV comparison between AC and USV, the largest reduction can be noticed for 0.63 mm AlN in mineral oil (32% reduction in PDIV). Also, for the pressboard barriers in mineral oil, the average PDIV reduces by more than 25 % under USV. In synthetic ester, the highest reduction in average PDIV occurs for FR4 barriers (22%), and is larger than for the same barriers in mineral oil (11-12%).

Then, the optically acquired PRPD patterns obtained for one type of liquid/solid insulation are analyzed. Figure 6-7 shows the PRPD pattern of same DUT specimen (with 2 mm thick pressboard in mineral oil), taken after 30 seconds at PDIV. In AC, PDs mainly appeared under voltage crest and around first and third quadrants of sinusoidal voltage. This pattern is similar to the findings of previous AC tests (Chapter-4). As said earlier, the Omicron displays the control signal and due to bandwidth limitations the 'rising edge' does not represent the real rise time of USV waveform. Therefore, here the 'ascending part', 'voltage plateau' and 'descending part' as marked in Figure 6-7 are used for referring control signal displayed by Omicron system.

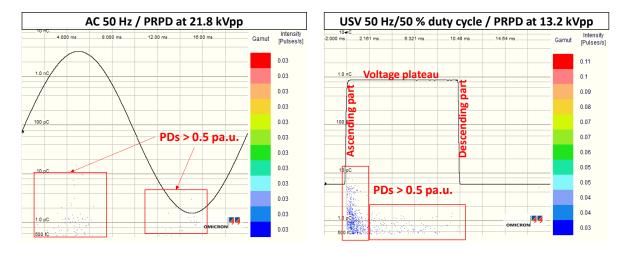


Figure 6-7: Optically acquired PRPD pattern in AC and USV for 2 mm thick pressboard in mineral oil at inception voltage; after a recording time of 30 seconds

In the PRPD pattern (Figure 6-7), the ascending part shows a high concentration of PDs. PDs can also be seen under maximum voltage plateau but less intense than ascending part. During descending part of waveform, hardly any PD can be observed.

In the given example of PRPD patterns, PDs look quite intense under USV waveform, which indicates a higher PD activity. Therefore, to compare the PD activity between USV and AC; number of PDs (NPDs) occurring per second and average charge magnitude (Qavg) are analyzed for 2 mm thick pressboard in mineral oil. Figure 6-8 and Figure 6-9 shows the scatter plot of NPDs and Qavg for twenty-five PD tests (from five DUT specimen) under AC and USV respectively. Each point in these plots is taken after 30 seconds at PDIV with PD threshold at 0.5 pa.u.

From the NPDs plot in Figure 6-8, it can be seen that for DUT n°1, the number of PDs occurring per second are more dispersed under USV than in AC. For other DUT specimens (DUT n°2 to n°5), the NPDs of USV are almost same as in AC.

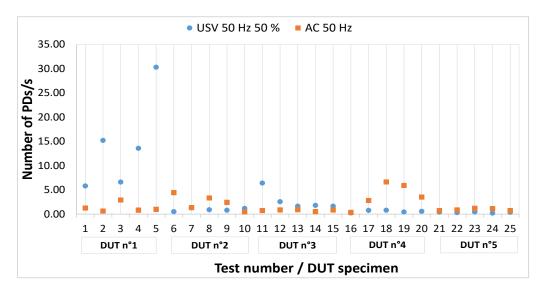


Figure 6-8: Comparison of number of PDs (NPDs) for needle-pressboard plane in mineral oil under AC and USV

Under AC, the Qavg (Figure 6-9) does not seem to vary a lot from mean value for all PD measurements. Contrarily to the NPD observations in Figure 6-8, Qavg is relatively flat for first five PD measurements under USV but exhibits more randomness for other DUT specimens (test number 6 to 25), with a maximum of 14.4 pa.u. for the last PD test. This shows high unpredictability in Qavg observed under USV waveform.

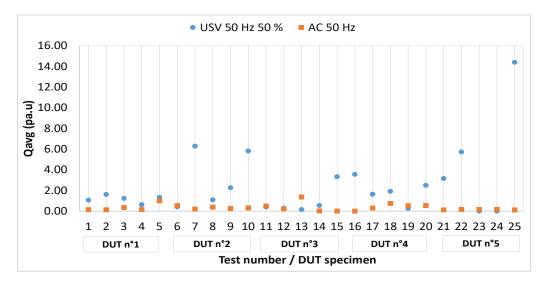


Figure 6-9: Comparison of average charge magnitude (Qavg) for needle-pressboard plane in mineral oil under AC and USV

It has been observed during the tests, that the PDs extinguish when voltage is maintained at PDIV level. The same is also stated in IEC60270. As a result of this, the values of NPDs and Qavg for many cases are low which is average over 30 s.

Considering the Qavg is a measure of PD activity, the higher Qavg found for many tests under USV means higher PD activity than in AC. This may accelerate the degradation of insulator under USV waveform than in AC. Also, the low PDIV under USV means early arrival of PD activity as compared to AC.

6.2.3. PD comparison between dielectric liquids under USV

In the next step, the PDIVs obtained from two dielectric liquids under USV waveform are compared. The PD threshold for both liquids are kept at 0.5 pa.u. As can be observed in the Figure 6-10, the average PDIV in synthetic ester is quite higher as compared to mineral oil for the same barrier. The largest increase in PDIV can be noticed for 1 mm PVC (about 43 %) while smallest for 1 mm AlN barrier (about 18 %).

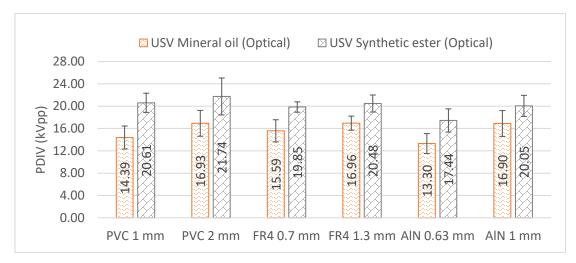


Figure 6-10: PDIV comparison between synthetic ester and mineral oil in unipolar square voltage at 50 Hz and 50 % duty cycle

T-test is used to evaluate the difference in PDIVs between two dielectric liquids under USV waveform. The same null hypothesis as before is considered (average PDIVs are the same in both dielectric liquids). The fact that the experiments are performed with different DUT specimens is considered for the t-test calculation.

Table 6-6 provides the results in the form of SD, 95 % CI and p-value from t-test. The low p-value gives enough evidence to reject the null hypothesis as there is a significant difference in the average PDIVs obtained from both dielectric liquids.

Table 6-6: Estimation of difference in average value of PDIVs between mineral oil and synthetic ester in USV using
T-test

Barriers	PVC 1	l mm	PVC 2	2 mm	FR4 0.7 mm		FR4 1.3 mm		AIN 0.63 mm		AIN 1 mm	
	МО	SE	МО	SE	МО	SE	МО	SE	МО	SE	МО	SE
Avg (kV)	14.39	20.61	16.93	21.74	15.59	19.85	16.96	20.48	13.30	17.44	16.90	20.05
SD (kV)	2.06	1.72	2.31	3.31	1.99	0.93	1.26	1.53	1.79	2.08	2.31	1.89
95 % CI	15.24	21.32	17.89	23.10	16.41	20.23	17.48	21.11	14.29	18.59	18.18	21.10
UB/LB	13.54	19.90	15.98	20.37	14.77	19.46	16.43	19.85	12.32	16.29	15.62	19.01
p-value	2.5	-15	4.5	E-07	2.4E-11		-11 1.4E-11		3.01	-06	3.5E	-04

^{*} Avg: Average, SD: Standard Deviation, CI: Confidence interval, UB: Upper bound, LB: Lower bound, MO: Mineral oil, SE: Synthetic ester

A similar behaviour is observed under AC 50 Hz with t-test as well as can be seen in Table 6-7. The low p-value means that there is a difference between average PDIVs from two dielectric liquids.

	AC 50 Hz											
Barriers	PVC 1 m	ım	PVC 2 mm		FR4 0.7 mm		FR4 1.3 mm		AIN 0.63 mm		AlN 1 mm	
	МО	SE	МО	SE	МО	SE	МО	SE	МО	SE	МО	SE
Avg (kV)	17.19	25.86	20.30	25.54	17.59	25.35	19.35	26.17	19.64	21.56	19.57	23.62
SD (kV)	2.19	3.64	2.35	1.90	2.36	2.89	2.41	3.01	1.64	1.48	1.66	3.96
95 % CI	18.09	27.36	21.27	26.33	18.56	26.54	20.35	27.41	20.55	22.38	20.48	25.81
UB/LB	16.28	24.36	19.33	24.76	16.61	24.15	18.36	24.93	18.73	20.74	18.65	21.43
p-value	1.2E-1	2	2.9	E-11	1.11	E-13	1.91	E-11	2.21	E-03	1.7	E-03

Table 6-7: Estimation of difference in average value of optically obtained PDIVs between mineral oil and synthetic ester in AC using T-test

The threshold for optically detected PDs is same (0.5 pa.u.) in both MO and SE liquids. But as said earlier, 0.5 pa.u. corresponds to 2 pC in MO and 10 pC in SE. Ideally, higher magnitude of PDs can be attributed to higher voltage, and this can be one of the reasons of higher PDIV in ester than MO, using optical detection.

For some cases such as shown in Figure 4-20, the PDIV is found to be same in MO and SE (such as AlN barrier), using electrical method. This means PD of same magnitude can occur at same voltage in both liquids. But as PMT detects stronger PD in SE than in MO; a higher PDIV will be observed for SE when using optical detection, for this situation as well.

Then, one type of barrier is selected for comparing PRPD pattern between two dielectric liquids. Figure 6-11 shows optically acquired PRPD pattern for 1 mm thick AlN in mineral oil and synthetic ester acquired at same voltage of 20 kV. PDs can be seen occurring at zero voltage level, around the ascending part as well as during the voltage plateau of the USV waveform in Omicron. A similar trend can be observed with the synthetic ester. Moreover, PDs at zero voltage could be due to the presence of space charges. These patterns are quite different from the patterns in AC at PDIV, where PDs are mainly observed under voltage crest or around the 1st and 3rd quadrants of voltage cycle. The USV waveform with high dV/dt might be influencing the PD mechanism in liquids leading to a different pattern than in AC.

In the same figure, the control voltage signal shows different levels in Omicron which is due to display adjustments made while recording the data. The PD tests with MO and SE were performed at different times.

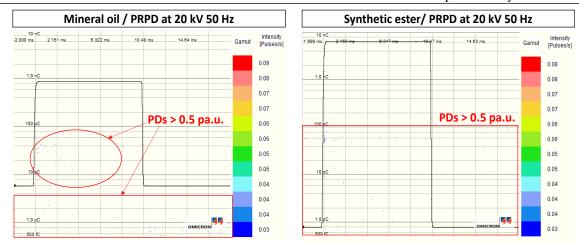


Figure 6-11: Optically acquired PRPD pattern obtained at PDIV (20 kV) for 1 mm thick AlN barrier in mineral oil and synthetic ester

To go further, the NPDs and Qavg for 1 mm thick AlN barrier are evaluated for mineral oil and synthetic ester. Figure 6-12 and Figure 6-13 presents the NPDs and Qavg respectively, where each point is taken after 30 seconds with PD threshold at 0.5 pa.u. The graphs present results of fifteen PD tests from three DUT specimens, DUTn°1, DUTn°2 and DUTn°3, as only three 1 mm AlN barriers are tested (see Table 6-2).

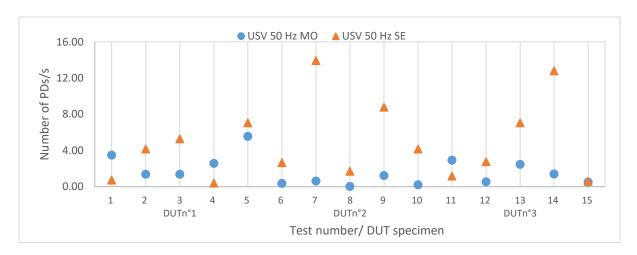


Figure 6-12: Comparison of number of PDs (NPDs) between mineral oil (MO) and synthetic ester (SE) for needle-AlN plane under USV

In Figure 6-12, the NPDs in synthetic ester are higher than mineral oil for some instants with DUT n°2 and DUT n°3 in ester. But the Qavg in synthetic ester are noticeably higher for DUTn°2 (Figure 6-13). For DUTn°3, it is almost same in both liquids.

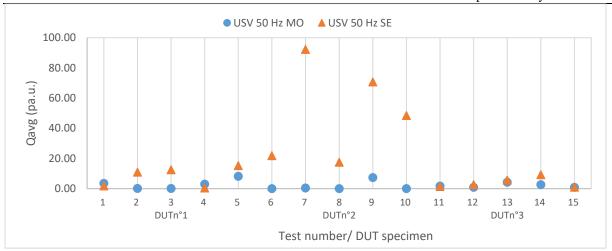


Figure 6-13: Comparison of average charge magnitude (Qavg) between mineral oil (MO) and synthetic ester (SE) for needle-AlN plane under USV

From these graphs it could be seen that results are quite distinct for every DUT specimen for two liquids. One of the parameters which is not same in two liquids are their water content (Table 3-7), which is higher in ester than mineral oil. Studies like [73] states that PD initiation in esters are favored by higher water content than in mineral oil. Moreover, the transmission of light from PD event differs in two dielectric liquids, which might have also impacted the obtained results. To ascertain this, investigation should be done with same amount of water content in two dielectric liquids.

At this stage, with the available experimental data, it can be said that the PDIV is higher in synthetic ester due to higher attenuation of optical signals than in mineral oil. The space charges under USV seems to have an impact as PDs occurred at zero voltage as shown in PRPD patterns (Figure 6-11). However, additional tests such as aging and breakdown tests would be necessary to assess their performances under repetitive square voltage waveforms.

6.2.4. Influence of barrier thickness, permittivity and tip radius on PDIV in USV

Influence of barrier thickness on PDIV

From the PDIV results presented in Figure 6-5 and Figure 6-6, it can be observed that the average PDIV slightly increases with the barrier thickness under USV waveforms. Among them, the most significant increase can be noted for AlN in mineral oil, for which average PDIV increases by 27 %, when changing the thickness from 0.63 mm to 1 mm. In esters, a 15 % increase in average PDIV can be observed for the same barrier.

To assess if differences in PDIV is significant for different barriers, a t-test is used again. Table 6-8 and Table 6-9 shows the result obtained in mineral oil and synthetic ester respectively. The p-value > 0.05 suggests that difference may not be statistically significant. This is the case of pressboard in mineral oil (in Table 6-8), and PVC and FR4 in synthetic ester (in Table 6-9).

Table 6-8: Estimation of difference in average value of PDIVs for changing barrier thickness in mineral oil under USV using T-test

	USV 50 Hz / 50 % duty cycle in Mineral oil								
Barriers	PVC		FR4		AIN		Pb		
Thickness	1 mm	2 mm	0.7 mm	1.3 mm	0.63 mm	1 mm	2 mm	3 mm	
Avg (kV)	14.39	16.93	15.59	16.96	13.30	16.90	16.50	17.04	
SD (kV)	2.06	2.31	1.99	1.26	1.79	2.31	3.06	1.84	
95 % CI	15.24	17.89	16.41	17.48	14.29	18.18	17.76	17.80	
UB/LB	13.54	15.98	14.77	16.43	12.32	15.62	15.24	16.28	
p-value	1.6	1.6E-04		5.8E-03		6.1E-05		4.53E-01	

^{*} Avg: Average, SD: Standard Deviation, CI: Confidence interval, UB: Upper bound, LB: Lower bound

Table 6-9: Estimation of difference in average value of PDIVs for changing barrier thickness in synthetic ester under USV using T-test

USV 50 Hz / 50 % duty cycle in Synthetic ester							
Barriers	PVC		FF	R4	AIN		
Thickness	1 mm	2 mm	0.7 mm	1.3 mm	0.63 mm	1 mm	
Avg (kV)	20.61	21.74	19.85	20.48	17.44	20.05	
SD (kV)	1.72	3.31	0.93	1.53	2.08	1.89	
95 % CI	21.32	23.10	20.23	21.11	18.59	21.10	
UB/LB	19.90	20.37	19.46	19.85	16.29	19.01	
p-value	1.4	E-01	8.5	E-02	1.2E-0	3	

^{*} Avg: Average, SD: Standard Deviation, CI: Confidence interval, UB: Upper bound, LB: Lower bound

The FE simulations in chapter 3 showed that the electric field generated at 1 μ m tip only reduces slightly with increasing barrier thickness in ideal conditions for the "reference DUT" (i.e. PVC in mineral oil). For many cases, the experimentally obtained results validates the finding of FE simulation.

However, the AlN shows a significant difference in average PDIVs in both dielectric liquids under USV, when barrier thickness changes. Therefore, this case is further investigated in FEM to understand from electrostatic point of view. For this, the reference DUT model in FEMM is adapted for two barrier thicknesses, 0.63 mm and 1 mm respectively. The permittivity of mineral oil (MO) and synthetic ester (SE) are used: for assessing respective case. The gap spacing of 0.7 mm is kept for all cases. The experimentally obtained average PDIV under USV is used in simulation. The electric field thus determined is shown in Figure 6-14.

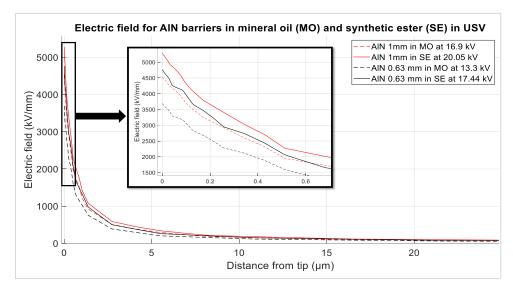


Figure 6-14: Electric field obtained in FEM at experimentally obtained PDIV values for AlN barriers of different thicknesses in USV

The tip fields at experimentally obtained PDIV values are quite higher than PDIF (of about 1600 kV/mm). The tip fields are higher for thicker AlN barrier in both liquids. Also, relative tip fields are higher for AlN in SE than in MO. In the next step, for corresponding increase in PDIV under USV for both dielectric liquids, the percent increase in tip field is calculated as shown in Table 6-10.

Table 6-10: Comparison of tip field obtained at PDIV and PDIV for increasing thickness of AlN barrier in mineral oil and synthetic ester under USV

Barrier	AIN	0.63 mm	1 mm	% increase
Tip field	МО	3693	4533	23
(kV/mm)	SE	4764	5280	11
Avg PDIV	МО	13.3	16.9	27
(kV)	SE	17.44	20.05	15

It can be observed that, under USV, for an increase in thickness of about 58 % (from 0.63 mm to 1 mm) of AlN barrier, the PDIV value increased by 27 % in mineral oil and 15 % in synthetic ester. This increase in PDIV corresponds to an increase in tip field of about 23 % in mineral oil and about 11 % in synthetic ester.

It should be noted here that, during AC tests (Chapter-4), a difference in PDIV was observed for varying thickness of AlN barriers only in mineral oil and not in synthetic ester (see Table 4-2). This could be an indication that the USV waveform can influence the PDIV, for varying barrier thickness, if barrier permittivity is higher than surrounding medium in tested DUT configuration. More tests with different configurations (such as tip radius, gap) would be necessary to further explore this part.

Influence of permittivity

Employing t-test method for assessing the impact of permittivity under USV waveform, did not yield significant difference in PDIV for most of the cases (Table 6-11).

This follows the FE simulation to a greater extent, which did not forecast any large difference in tip field with changing barrier permittivities in reference DUT configuration.

Table 6-11: Estimation of difference in average value of PDIVs for different barrier permittivities in both mineral oil and synthetic ester under USV waveform using T-test

Impact of permittivity							
Liquid	Mineral oil S					Synthetic ester	
Thickness	1 n	nm	2 n	nm	1 mm		
Barrier (different ε _r)	PVC	AIN	PVC	Pb	PVC	AIN	
Avg (kV)	14.39	16.90	16.93	16.50	20.61	20.05	
SD (kV)	2.06	2.31	2.31	3.06	1.72	1.89	
95 % CI	15.24	18.18	17.89	17.76	21.32	21.10	
UB/LB	13.54	15.62	15.98	15.24	19.90	19.01	
p-value	1.86	E-03	5.8	E-01	3.60E-01		

^{*} Avg: Average, SD: Standard Deviation, CI: Confidence interval, UB: Upper bound, LB: Lower bound

Influence of tip radius on PDIV

The aim of this investigation is to analyze the PDIVs under USV as a function of tip radius, and to compare them to those obtained under AC for the same DUT specimen. The tests are performed with a FR4 barrier (0.7 mm thick) in mineral oil. Two DUT specimens are used, one with 1 μ m and another with 100 μ m tip. New needle and barrier samples are used in both DUT specimens. The dielectric liquid is not treated.

With each DUT specimen, ten PDIV tests are carried out, five each under USV 50 Hz at 10 % duty cycle and AC 50 Hz. The average PDIVs and standard deviations thus calculated are displayed in Figure 6-15.

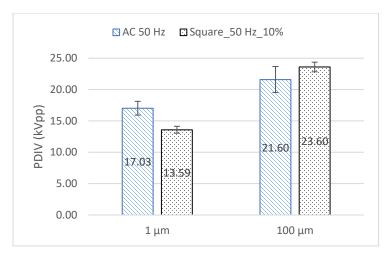


Figure 6-15: Comparison of PDIVs obtained for varying tip radius under USV and AC waveform

From the graph following observations can be made:

- The average PDIV is lower when the tip radius is reduced from $100~\mu m$ down to $1~\mu m$ (by 21~% in AC and by 42~% in USV). This decrease in PDIV is consistent with the higher tip field generated by the $1~\mu m$ tip as compared to $100~\mu m$, as demonstrated with FE simulation in chapter 3.
- For 1 μm tip, the average PDIV in AC is about 25 % higher than the PDIV in USV. For 100 μm tip, although the average PDIV in AC is lower than USV, but this may not be significant as standard deviation bars overlap quite a bit.

From these tests, it seems that high dV/dt may have an impact on PDIV, especially for the sharpest needles, as compared to AC. However, to understand the discrepancy between AC and USV at 1 μ m and 100 μ m, the tests must be completed (using more DUT specimens, and treated oil). Complementary investigations such as PD tests with different tip radii may also be needed.

6.2.5. Summary of PD comparison

- By simultaneously deploying electrical and optical detection techniques under AC 50 Hz, optically acquired PDs of 0.5 pa.u. have been correlated to 2 pC in mineral oil and 10 pC in synthetic ester, under given experimental conditions. Differences in the optical properties of two dielectric liquids influence the light transmitted through them.
- Using a statistical tool (t-test), the average PDIV is found to change significantly:

- Between USV and AC 50 Hz for all combination of liquid/solid insulations tested.
 These results indicate that, as compared to AC, PD activity starts at lower voltage under unipolar square waveform for the used DUT configuration.
- Between both dielectric liquids under USV waveform.
 However, the higher PDIV obtained with ester could be due to higher voltage necessary to detect stronger PDs in ester than in mineral oil, with PMT.
 Additional investigations are required to understand the long-term effects on liquid degradation.
- From the PRPD patterns, the PDs are more clustered around ascending part and voltage plateau of the USV waveform, while in AC, they occur mainly in the first and third quadrants of the voltage cycle, at PDIV. The PDs occurring around zero voltage (Figure 6-11) shows the existence of space charges with USV waveform.
- The NPDs and Qavg plots for 2 mm thick pressboard in mineral oil suggest large variations, sometimes from one test to another and for some cases one DUT specimen to another. Evaluation of NPDs and Qavg with other DUTs might make it clearer.
- Using t-test, no definite conclusion can be drawn on the impact of permittivity and barrier thickness under USV waveform for tested DUTs. There is a statistical difference in average PDIVs for some cases, but not for all. The 1 µm tip and small gap of 0.7 mm are the driving factor for PD activity in used DUT configuration.
- As expected, the average PDIV decreases when tip radius is changed from 100 µm to 1 µm, both under USV and AC waveform. The effect is found to be more profound under USV waveform from experiments conducted. However, additional tests with the same tip are required to understand the discrepancies between AC and USV.

6.3. Assessment of PD under varying parameters of USV

To fulfill the second objective of these investigations and improve the understanding of PD phenomenon under USV waveform, investigations are conducted under varying parameters of USV, i.e. switching frequency, duty cycle and rise time.

To assess the switching frequency and duty cycle, two DUT specimens are used, whose details are provided in Table 6-12. Each DUT specimen underwent fifteen PD test, in the following order:

- 5 PD tests at 50 Hz with 50 % duty cycle
- 5 PD tests at 460 Hz with 50 % duty cycle, and

• 5 PD tests at 50 Hz with 5 % duty cycle.

A DUT configuration with 100 μ m tip radius is chosen for these investigations as preliminary tests showed tip to be quite robust to PD stress (see Appendix C). Such large radius was not used for the previous tests, as it produces lower tip field, and may not produce PDs considering the voltage limitations of the test bench. An instance where 100 μ m tip limited the PD generation is discussed in section 6.3.4.

Electrode configuration	Needle- pressboard-plane		
Needle tip radius	100 μm (new)		
Barrier	Pressboard sample (3 mm thick)		
Plane diameter (grounded)	20 mm		
Medium	Mineral oil (Nytro 4000X- treated)		
Gap (needle tip to barrier)	0.7 mm		
Detection technique	Photomultiplier coupled with Omicron		
	o USV/50 Hz with 50 % duty cycle		
Voltage waveform (s)	o USV/ 460 Hz/ with 50 % duty cycle		
	O USV/50 Hz with 5 % duty cycle		
PDIV threshold	0.5 pa.u.		

Table 6-12: Parameters of the DUT used for PD tests with varying switching frequencies and duty cycle

For changing rise time, another DUT is used as described in section 6.3.4.

6.3.1. Impact of switching frequency

The maximum frequency attainable in the set-up with USV waveform is 460 Hz as discussed in paragraph 5.2. The PDIV measurements thus conducted at 50 Hz and 460 Hz with 50 % duty cycle are shown in Figure 6-16. As can be observed from the graph, the average PDIV is lower at higher frequency for the chosen DUT.

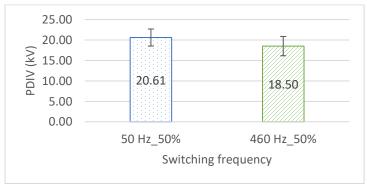


Figure 6-16: PDIV comparison performed with needle-pressboard plane configuration in mineral oil with varying switching frequency

To verify if the difference in average value of PDIVs is significant, a t-test is performed. From Table 6-13, it can be observed that p-value is 0.05, which means that there is not significant difference in average PDIVs at the tested frequencies.

Table 6-13: Estimation of difference in average value of PDIVs for varying frequencies under USV waveform using
T-test

Duty cycle	50%				
Frequency	50 Hz	460 Hz			
Avg (kV)	20.61	18.50			
SD (kV)	2.08	2.35			
95 % CI					
UB/LB	22.10	20.18			
	19.12	16.82			
p-value		0.05			

To further evaluate the influence of frequency on PD phenomenon, the NPDs and Qavg are extracted from the recorded data, as shown in Figure 6-17 and Figure 6-18. Each point is extracted after 30 s at PDIV (with threshold at 0.5 pa.u.).

As can be seen from Figure 6-17, the NPD occurring at 50 Hz is greater than at 460 Hz. Also, the range of values at 50 Hz is wider than 460 Hz. On the contrary, at 460 Hz more points are close to zero. The small pulse duration at 460 Hz could have led to reduced number of PD events during voltage plateau with USV as compared to at 50 Hz [117].

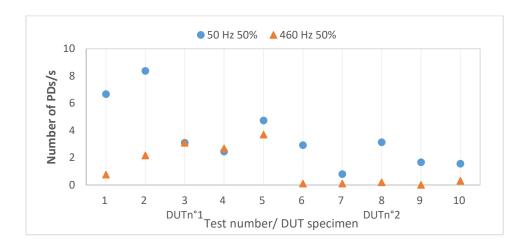


Figure 6-17: Number of PDs (NPDs) at 50 Hz and 460 Hz for needle-pressboard plane configuration in mineral oil under USV

The Qavg is quite randomly distributed for two DUT specimens as shown in Figure 6-18. For few cases, it is higher at 50 Hz while comparable for rest of cases.

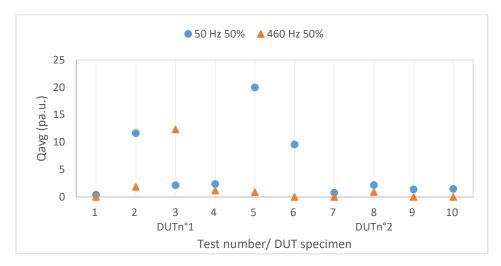


Figure 6-18: Average PD magnitude (Qavg) at 50 Hz and 460 Hz for needle-pressboard plane configuration in mineral oil under USV

As there is no difference between PDIVs for tested frequencies, the range of frequency should be widened (such as 1-10 kHz) to estimate the influence of frequency on PDs under USV waveform.

6.3.2. Impact of duty cycle

To assess the influence of duty cycle on PD activity under USV waveform, the results obtained at 5 % and 50 % duty cycle at 50 Hz are compared. The DUT is same as described in Table 6-12. The PDIV results thus obtained, are plotted in Figure 6-19.

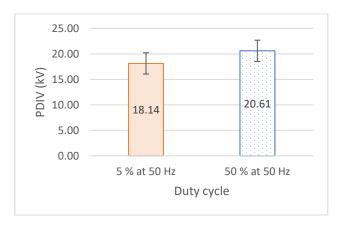


Figure 6-19: PDIV measurements at 5 % and 50 % as duty cycles with 50 Hz as switching frequency

Although PDIV results partially overlap for both duty cycle values, the t-test shows that the difference is significant (Table 6-14).

Table 6-14: Estimation of difference in average value of PDIVs at 5 % and 50 % as duty cycles with 50 Hz as switching frequency using T-test

Frequency	50 Hz			
Duty cycle	5% 50%			
Avg (kV)	18.14	20.61		
SD (kV)	2.09	2.08		
95 % CI	19.63	22.10		
UB/LB	16.65	19.12		
p-value	0.02			

To further investigate the impact of duty cycle on PD activity, the NPDs and Qavg are also evaluated for ten tests. As can be seen in Figure 6-20 and Figure 6-21, they are randomly distributed. Except for few cases, the NPDs and Qavg are almost same for both duty cycles.

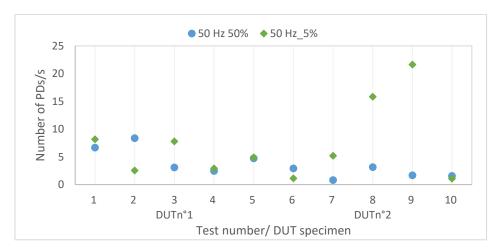


Figure 6-20: Number of PDs (NPDs) measured at 5 % and 50 % as duty cycles with 50 Hz as switching frequency

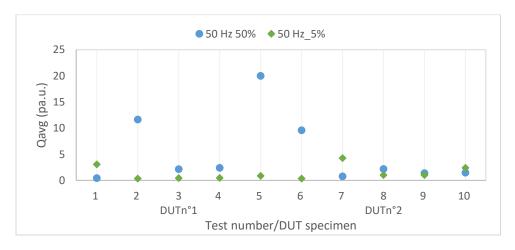


Figure 6-21: Average PD magnitude (Qavg) measured at 5 % and 50 % as duty cycles with 50 Hz as switching frequency

Further, the PRPD pattern of one DUT specimen is investigated at PDIV to have more insights. From the pattern shown in Figure 6-22 it looks like the low magnitude PDs (< 10 pa.u.) have higher count with 5 % duty cycle than at 50 %. While only few high magnitude PDs (> 10 pa.u.) can be seen with 5 % duty cycle while several of them exist at 50 %.

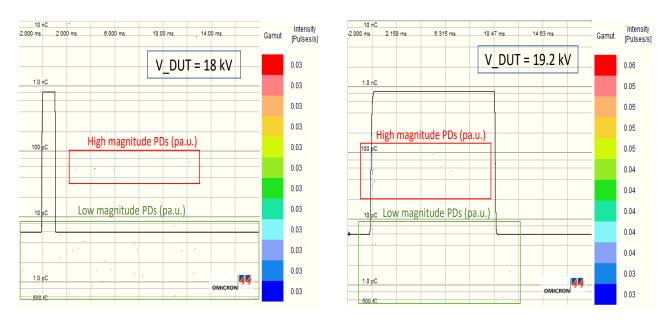


Figure 6-22: PRPD patterns taken at PDIV with 5% (top) and 50 % (bottom) duty cycles at 50 Hz for needlepressboard plane in mineral oil after 30 s

As said in IEC60270, the PDs can occur intermittently for some types of insulation, either it may rise rapidly or extinguish when voltage is maintained at PDIV. The stochastic occurrence of PDs with changing pulse period could have led to such distribution of results and obtained PD patterns.

6.3.3. Same pulse duration

The pulse duration with 50 % duty cycle at 460 Hz and 5 % duty cycle at 50 Hz are 1.08 and 1 ms respectively. Therefore, the results for both cases can be compared considering they have the same pulse duration. As can be observed from Figure 6-23, the average PDIVs are very close for both conditions.

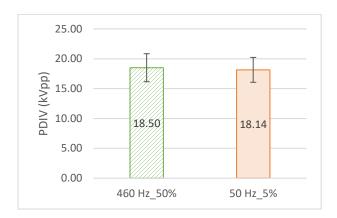


Figure 6-23: PDIV measurements for same voltage duration at maximum voltage plateau for different switching frequencies and duty cycles

Running the t-test confirms there is no significant difference in average PDIVs for these two cases as shown in Table 6-15.

Table 6-15: Estimation of difference in average value of PDIVs for almost same voltage duration at maximum voltage plateau with different switching frequencies and duty cycles using T-test

	460 Hz at 50%	50 Hz at 5 %	
Avg (kV)	18.50	18.14	
SD (kV)	2.35	2.09	
95 % CI	20.18	19.63	
UB/LB	16.82 16.65		
p-value	0.78		

For some cases, the NPDs are higher with 5 % duty cycle at 50 Hz, (Figure 6-24), but overall both NPDs and Qavg (Figure 6-25) between two cases are randomly distributed.

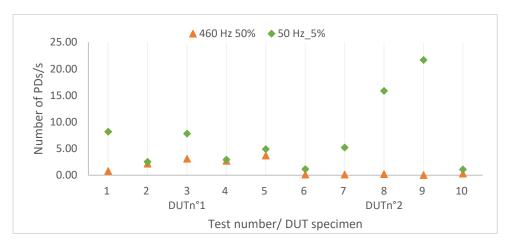


Figure 6-24: Number of PDs measured with same voltage duration at maximum voltage plateau for different switching frequency and duty cycle

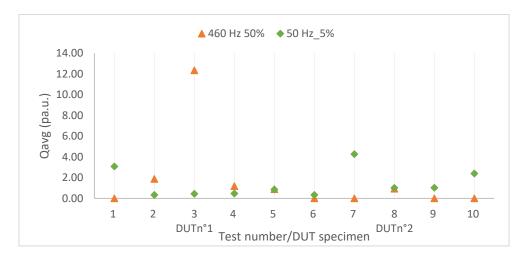


Figure 6-25: Average PD magnitude with same voltage duration at maximum voltage plateau for different switching frequency and duty cycle

Looking at the PRPD pattern obtained with 50 % cycle at 460 Hz (in Figure 6-26), less number of PDs are observed as compared to 5% duty cycle (shown in Figure 6-22). This supports the low NPDs at 460 Hz, found for some cases. The long rise and fall time of the control signal is due to bandwidth limitation of MPD600 unit as discussed in section 5.3.3 (chapter-5).

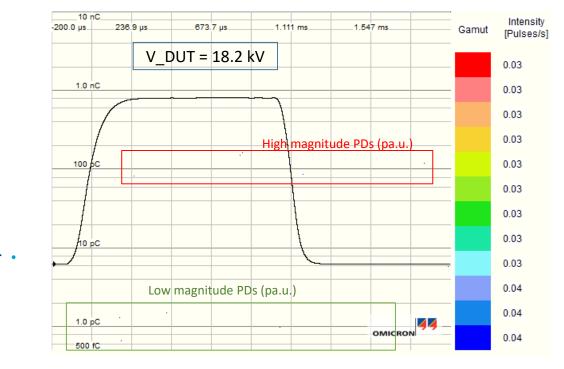


Figure 6-26: PRPD pattern taken at PDIV after 30 s, with 50 % duty cycle at 460 Hz for needle-pressboard plane in mineral oil

Overall, it can be concluded that there is no significant difference statistically for same pulse duration with used DUT configuration.

6.3.4. Impact of rise time

As seen in section 5.4 in chapter 5, with $100~\Omega$ resistance (R3), the voltage measured across DUT rises quickly (less than 100~ns) and overshoots noticeably; producing a dV/dt of more than $300~\text{kV/\mu s}$. Studies such as [60] considers voltage overshoot as one of the most important factors for premature ageing of insulators. With such a waveform, it would have been difficult to differentiate between the effect of rise time and overshoot on PD mechanism. Therefore, during this investigation, relatively longer rise times of (160 ns, 256 ns and 560 ns across the DUT section 5.3.2 in chapter 5) are considered, to focus solely on the influence of rise time on PD activity.

Initially, for this investigation, the DUT with 3 mm thick pressboard and 100 µm tip radius has been considered, as in the sections above. However, with the rise time of 560 ns, the PDIV could not be determined for some test, even at the maximum voltage level allowed by the test bench.

Consequently, to generate a sufficiently high tip field for PDs to occur, a DUT with $10 \mu m$ tip and 1 mm AlN barrier is chosen (see Table 6-16). A USV waveform of 50 Hz with 50 % duty cycle is used, with different rise times.

Table 6-16: Parameters of t	TOO I SDECHBER USED	ana osv waveloim	or mvesuvami	van ving rise iinies
	r			, , ,

Electrode configuration	Needle- AlN-plane
Needle tip radius	10 μm (new)
Barrier	AlN sample (1 mm thick)
Plane diameter (grounded)	20 mm
Medium	Mineral oil (Nytro 4000X- treated)
Gap (needle tip to barrier)	0.7 mm
Detection technique	Photomultiplier with Omicron
Voltage waveform (s)	USV/50 Hz/ 50 % duty cycle
Rise time tested	160 ns, 256 ns and 560 ns
PDIV threshold	0.5 pa.u.

Two DUT specimens are used, and five tests are performed at each rise time with each DUT specimen. With the first DUT specimen, the first five tests are performed at 160 ns, followed by 256 ns and finished with 560 ns. The order of tests with the second DUT specimen is reversed.

Hence, tests start with 560 ns and finish with 160 ns. The average of ten PDIV measurements obtained for each rise time value is plotted in Figure 6-27.

As can be noticed from the graph, the average PDIV seems to be increasing with rise time. But the t-test performed on the measured datasets reveals that differences are not significant (Table 6-17). To clearly assess the impact of rise time on PDIV for the given DUT, it may be interesting to investigate a larger range of rise time values.

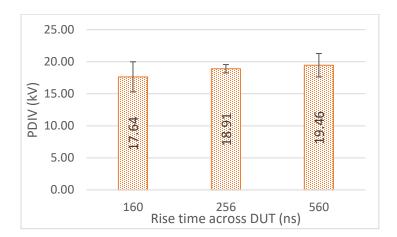


Figure 6-27: PDIV measurements at different rise time across the DUT

Rise time	160 ns	256 ns	560 ns
Avg (kV)	17.64	18.91	19.46
SD (kV)	2.35	0.65	1.82
95 % CI	19.32	19.37	20.76
UB/LB	15.96	18.44	18.15
p-value (160 ns and 256 ns)	0.19		
p-value (256 ns and 560 ns)	0.3		33
p-value (160 ns and 560 ns)			0.15

Table 6-17: Estimation of difference in PDIVs for varying rise times across DUT using T-test

To further evaluate the PD behavior at different rise times, the NPDs and Qavg are extracted after 30 seconds at PDIV, as shown in Figure 6-28 and Figure 6-29 respectively. Due to measurement error, there is a missing data with 160 ns for the second test with DUTn°1.

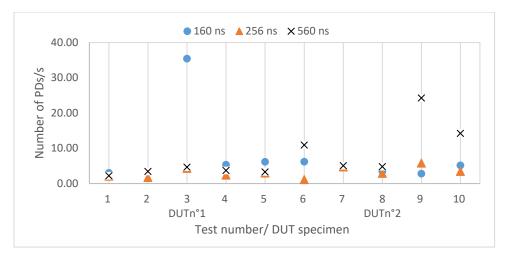


Figure 6-28: Number of PDs measured at different rise time across the DUT

From the NPD graph, it can be noticed that there is no definite trend they are almost in same range for most of the test cases. As compared to longer rise times, the Qavg are higher for about half of the tests at 160 ns (Figure 6-29).

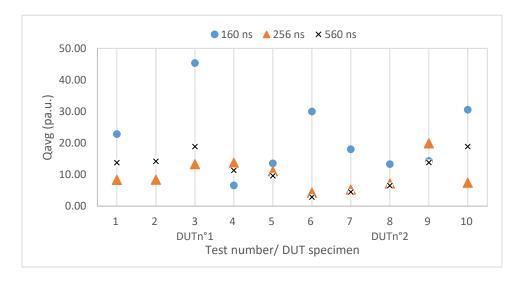


Figure 6-29: Average PD magnitude measured at different rise time across the DUT

To understand the impact of high dV/dt on PD phenomenon, it would be necessary to segregate the NPDs and Qavg around rise time, steady state plateau and fall time of USV waveform. Perhaps to see the differences in PDIV, the higher range of rise times (such as in the range of 100 ns to 1 ms) should be tested.

6.4. General discussion

Methodology of PD comparison

To facilitate the PDIV comparison between AC and USV waveforms, a new type of voltage application method is adopted during this campaign. Contrarily to the ramp increase of voltage across the DUT, the adopted method allows the data recording at PDIV. This data is used later for analyzing PD parameters such as NPDs and Qavg.

The microscopic examination of a 1 μ m needle tip reveals its deformation due to the discharge process. Also, even brand new 1 μ m tips do not exhibit a hemispherical shape. For all measurements, needles from the same manufacturer (Microworld) are used. Preliminary consistency tests are used to define the procedure for PDIV comparison between AC and USV waveform.

Interpretation of PD results

During this test campaign the optically acquired PDs are correlated to those acquired electrically. Under stated experimental conditions, the optical detection is found to be less sensitive than electrical detection as the photomultiplier tube could detect 2 pC in mineral oil and 10 pC in ester.

A lower average PDIV is found under USV waveform compared to AC. Taking the case of pressboard in mineral oil, the 25 % reduction in average PDIV under USV waveform, may have a detrimental effect on the long term reliability of mineral oil/pressboard insulation systems. Further, the Qavg and NPD are found to have high variability under USV waveform as compared to AC. The recorded results from other combination of liquid/solid insulations should be assessed to check if same trend is observed for NPDs and Qavg under USV; however due to time limitation this could not be done in the timeframe of this thesis.

Synthetic ester showed higher PDIV under USV waveform. In esters, a higher magnitude of PD (10 pC) is detected by the PMT than mineral oil (2 pC). This would have eventually elevated the PDIV of ester with optical detection. The NPDs and Qavg in ester are found quite random which needs to be explored whether it is the impact of DUT specimen, test order or intrinsic behavior of ester.

The high electric field created by 1 μ m tip and small gap seems to be the driving factor for PD generation for the investigated DUT configuration. This is experimentally shown when the tip

radius is changed from $100~\mu m$ to $1~\mu m$. On the contrary, barrier thickness and permittivity do not have a significant influence on PDIV.

No significant difference in PDIV is found between 50 Hz and 460 Hz. On the contrary, the duty cycle is found to result in significant PDIV difference. An interesting result is found for USVs with same pulse duration but different frequencies (5 % duty at 50 Hz and 50 % duty at 460 Hz): both conditions yield the same PDIV.

By changing the resistor in series with the DUT, different rise time of about 160 ns, 256 ns and 560 ns are achieved. Considering the average PDIVs obtained at three rise times, the DUT experienced dV/dt of about 110 kV/ μ s, 73 kV/ μ s and 34 kV/ μ s respectively. Again, no significant difference is observed in PDIVs for tested dV/dt.

Perspective

For PD measurement under repetitive voltage impulses, standard IEC61934 recommends determining repetitive PDIV (or RPDIV), which is the voltage when 5 PD pulses occur in same polarity in 10 voltage cycles. However, during this investigation the tests are performed as per IEC 60270 to find the first PDs above threshold value. This is done to establish the comparison between AC and USV, as well as to see first PDs under varying parameters of USV waveforms for different insulating materials. Determination of the RPDIV should be considered for future tests.

Probably, the space charges play a role in PD dynamics under USV waveform, which is evident from the PD occurring at zero voltage (see Figure 6-11). The outcomes presented in this chapter shows the path which can be adopted to understand the PD dynamics under USV waveform.

To elucidate the impact of varying USV parameters on PD dynamics, testing with wider range of switching frequencies and rise times should be done. To ensure ester's usability for power electronic applications, additional investigations such as aging and breakdown tests under repetitive square voltage will be necessary.

6.5. Conclusion

The investigations presented here are novel of its kind, with a high dV/dt (10-100 $kV/\mu s$) for composite insulation systems at roughly 20 kV employing an optical detection approach. The capabilities of USV test bench to measure PDs are illustrated to a large extent in this work. Also, tests are carried out for different USV waveform parameters, i.e. repetition rate, rise time and duty cycle. The major conclusions drawn from these investigations are:

- Optical detection is a decent indicator for PD measurement under unipolar square voltage waveform. A photomultiplier tube coupled with a commercially available Omicron system allowed extraction of PD parameters like NPDs and Qavg, besides PDIV.
- The optically acquired PDs are calibrated against electrical method for the tested DUT configuration under given experimental conditions.
- PD activity starts at lower voltage under USV than AC for tested DUTs which may accelerate degradation.
- The test bench developed under USV is capable of measuring PDs for varying rise time, switching frequencies and duty cycle of USV waveform.
- The role of space charges remains to be elucidated as a future work as the main objective here was to ensure the PD detection under fast rising voltage and then check the influence of varying parameters on PDIV. Dedicated investigation would be necessary to understand their impact on PD parameters.

7. Conclusion and perspective

This thesis contributes to addressing the problem of partial discharge measurements under fast rising square waveform. The application cases considered here are existing HVDC transformer and upcoming MFTs which insulation system are exposed to such kind of electrical stresses.

The major outcomes of this work are summarized below:

- Electrical detection techniques for PDs are very sensitive to the fast transients. The Simscape simulations with the HFCT model show that alone it may not detect PDs during fast rise time. This is confirmed experimentally under USV waveform, as only PDs which occur during the voltage plateau can be detected by the HFCT. Signal processing techniques such as moving average and standard deviation can be implemented to overcome this limitation, but they are prone to providing false PD signals if the waveform is impacted by jitter in real experiments.
- FEM simulation is as a valuable tool for designing the device under test. It ensures the generation of enough electric field for PD generation in the testing facility (which is limited to 25 kV). Also, it aids in defining the barrier dimension, choosing the tip radius and gap in the DUT cell for carrying out PD measurements. Experiments carried under AC confirmed the design of DUT.
- During the PD tests in AC, the optical detection technique proved to be a good alternative to electrical detection for tested DUT configuration (as oil and ester are found to be relatively transparent to the light emitted during the PD events).
- Following the successful implementation of optical detection under AC, it is implemented under fast rising square waveform. Despite careful implementation (use of separate battery supplies, fiber optics communication...), the PMT signal is found to be impacted by EMIs in square waveform set-up. Consequently, although PMT is said to be immune to displacement currents, in this work the PD detection after a few hundreds of ns after rise time is possible with it. It is not clear yet how this EMI issue can be overcome.
- Despite being impacted by EMIs, the optical detection proved to be the best among all detection techniques (high bandwidth HFCT and low inductive resistive shunt) tried in this work.

- From the PD tests, lower PDIV has been observed under USV for all combination of liquid/solid insulations. For pressboard in mineral oil, the reduction of PDIV under USV waveform is about 25 % in used DUT configuration.
- The PD dynamics in synthetic ester is not clear and more investigation will be required such as aging and breakdown tests under square waveform to evaluate its implementation for power electronic applications.
- The USV waveform test bench allows to change parameters such as rise time, switching frequency and duty cycle, to analyze their influence on PD activity. A significant difference is found between the average PDIVs of 5 % and 50 % duty cycles at 50 Hz. However, for the tested switching frequencies and rise times, there is no significant difference. Further the NPDs and Qavg show variability which makes PD analysis under USV waveform more complex than AC.

The test bench thus developed for PD measurements under different waveforms (AC and USV) is capable of testing PDs for various combination of liquid/solid insulations. The USV waveform can reach dV/dt between 10-100 $kV/\mu s$ for used DUTs. The results obtained here provide significant insights about the PD behavior in composite insulation system and is an initial step towards understanding the degradation process due to PDs.

Perspectives

From here, several perspectives can be foreseen. At first, one should take advantage of the existing unipolar square voltage test bench. This can be used to further improve the knowledge about discharge mechanism in different dielectric liquids under repetitive square voltages. The segregation of PD parameters during rising front, maximum voltage and falling flank might give better insight on PD mechanism.

Further improvements would be necessary to overcome the EMI issue impacting the optical detection. This can be then used to validate advanced electrical detection techniques such as HFCT with effective digital processing techniques. This is necessary to allow PD measurements for opaque insulation system and for online measurements for equipment like MFT.

Considering the full bridge configuration of power converters, the MFT insulation would be exposed to bipolar square voltage (BSV) waveform. PD measurements under BSV for same DUT would allow to have a comparative analysis between USV and BSV. Also, a direct comparison with AC 50 Hz will be possible with BSV. Moreover, a square waveform

superimposed over DC would constitute more realistic test conditions for many application cases.

Finally, beyond PD, other diagnostic methods like breakdown and aging tests with square voltage will provide more insights about the dielectric reliability. This requires profound changes to the test setup, to make it robust to current surge (during breakdown), or to allow for continuous and unsupervised operation (for the aging tests).

References

- [1] K. Meah and S. Ula, "Comparative Evaluation of HVDC and HVAC Transmission Systems," in 2007 *IEEE Power Engineering Society General Meeting*, Tampa, FL, USA, Jun. 2007, pp. 1–5. doi: 10.1109/PES.2007.385993.
- [2] O. Peake, "The History of High Voltage Direct Current Transmission," *Aust. J. Multi-Discip. Eng.*, vol. 8, no. 1, pp. 47–55, Jan. 2010, doi: 10.1080/14488388.2010.11464824.
- [3] "Electricity information: Overview (2020 edition)," *IEA*, pp. 1–23, 2020, [Online]. Available: https://webstore.iea.org/electricity-information-overview-2020-edition
- [4] T. Lagier and P. Ladoux, "A comparison of insulated DC-DC converters for HVDC off-shore wind farms," in 2015 International Conference on Clean Electrical Power (ICCEP), Taormina, Italy, Jun. 2015, pp. 33–39. doi: 10.1109/ICCEP.2015.7177597.
- [5] R. Adapa, "The Role of Power Electronics in the Future Smart Electric Grid," presented at the IEEE Power Electronics Society SCV Chapter meeting, Jun. 15, 2011. [Online]. Available: https://ewh.ieee.org/r6/scv/pels/archive/Role%20of%20Power%20Electronics%20in%20Future%20S MART%20Electric%20Grid.pdf
- [6] T. Guillod, R. Faerber, D. Rothmund, F. Krismer, C. M. Franck, and J. W. Kolar, "Dielectric Losses in Dry-Type Insulation of Medium-Voltage Power Electronic Converters," *IEEE J. Emerg. Sel. Top. Power Electron.*, vol. 8, no. 3, pp. 2716–2732, Sep. 2020, doi: 10.1109/JESTPE.2019.2914997.
- [7] T. Guillod and J. W. Kolar, "Medium-Frequency Transformers for Smart Grid Applications: Challenges and Opportunities," presented at the SCCER-FURIES Annual Conference, Power Electronic Systems Laboratory, ETH Zurich, Dec. 02, 2016. [Online]. Available: https://www.pes-publications.ee.ethz.ch/uploads/tx_ethpublications/workshop_publications/SCCER_2016_MF_Transformers_Guillod.pdf
- [8] T. B. Gradinger, U. Drofenik, and S. Alvarez, "Novel insulation concept for an MV dry-cast medium-frequency transformer," in 2017 19th European Conference on Power Electronics and Applications (EPE'17 ECCE Europe), Warsaw, Sep. 2017, p. P.1-P.10. doi: 10.23919/EPE17ECCEEurope.2017.8099006.
- [9] A. Rey, "Transport D'énergie Moutiers-Lyon Par courant continu à 50 000 volts," *Houille Blanche*, vol. 7, no. 10, pp. 229–235, Oct. 1908, doi: 10.1051/lhb/1908068.

- [10]"HVDC for Beginners and Beyond." ALSTOM. [Online]. Available: http://sarienergy.org/oldsite/PageFiles/What_We_Do/activities/HVDC_Training/Presentations/Day_7/ALSTO M_HVDC_for_Beginners_and_Beyond.pdf
- [11]P. Kundur, *Power system stability and control*,. Macgraw Hill Inc. Electric Power Research Institute, 1994.
- [12]R. S. Fieee and J. Hu, "SWITCHING IN DC SYSTEMS," presented at the IEEE Switchgear Committee 2018 Spring meeting, Apr. 29, 2018. [Online]. Available: https://www.ewh.ieee.org/soc/pes/switchgear/presentations/tp_files/2018-1_Smeets_Hu_Switching_in_DC_Systems.pdf
- [13]O. E. Oni and I. E. Davidson, "A Review of LCC-HVDC and VSC-HVDC Technologies and Applications," *IEEE 16th Int. Conf. Environ. Electr. Eng. EEEIC*, pp. 1–7, 2016, doi: 10.1109/EEEIC.2016.7555677.
- [14]P. Morshuis, A. Cavallini, D. Fabiani, G. Montanari, and C. Azcarraga, "Stress conditions in HVDC equipment and routes to in service failure," *IEEE Trans. Dielectr. Electr. Insul.*, vol. 22, no. 1, pp. 81–91, Feb. 2015, doi: 10.1109/TDEI.2014.004815.
- [15] C. G. A. Ramos, "Partial discharge phenomena in converter and traction transformers identification and reliability," PhD Thesis, Universita di Bologna, 2014.
- [16] A. Carlson, "Specific requirements on HVDC converter transformers." ABB Transformers AB, 1996. [Online]. Available: https://library.e.abb.com
- [17] M. S. Naidu and V. Kamaraju, *High Voltage Engineering*, Fourth. New Delhi: Tata McGraw Hill Education Private Limited, 2009.
- [18]N. Pattanadech, "Partial disharge inception voltage characteristics of mineral oil," PhD Thesis, Technische Universität Graz, Graz, 2013. [Online]. Available: https://diglib.tugraz.at/download.php?id=576d1bf0cd70e&location=browse
- [19]H. Okubo, R. Nakane, K. Takabayashi, and K. Kato, "Electric field distribution with dynamic charge activity in composite insulation systems under HVDC and DC-polarity reversal conditions," in 2017 IEEE Conference on Electrical Insulation and Dielectric Phenomenon (CEIDP), Fort Worth, TX, Oct. 2017, pp. 600–604. doi: 10.1109/CEIDP.2017.8257510.
- [20]E. Ildstad, "Challenges arising from use of HVDC," *Nord. Insul. Symp.*, p. 4, 2013, doi: 10.5324/nordis.v0i23.2443.

- [21]M. Yea, K. J. Han, J. Park, S. Lee, and J. Choi, "Design optimization for the insulation of HVDC converter transformers under composite electric stresses," *IEEE Trans. Dielectr. Electr. Insul.*, vol. 25, no. 1, Art. no. 1, Feb. 2018, doi: 10.1109/TDEI.2018.006629.
- [22] J. Kyunghoon, "Creepage Discharge Behaviour and Numerical Model Analysis at the Oil/Pressboard Interface with the Effect of Nano Composite Coating," PhD Thesis, Kyushu Institute of Technology, 2017. [Online]. Available: http://hdl.handle.net/10228/00006311
- [23] C. Thirumurugan, G. B. Kumbhar, and R. Oruganti, "Effects of impurities on surface discharges at synthetic ester/cellulose board," *IEEE Trans. Dielectr. Electr. Insul.*, vol. 26, no. 1, pp. 64–71, Feb. 2019, doi: 10.1109/TDEI.2018.007439.
- [24]D. Martin, "Evaluation of the Dielectric Capability of Ester Based Oils for Power Transformers," PhD Thesis, University of Manchester, 2008.
- [25]M. A. G. Martins, "Vegetable oils, an alternative to mineral oil for power transformers- experimental study of paper aging in vegetable oil versus mineral oil," *IEEE Electr. Insul. Mag.*, vol. 26, no. 6, pp. 7–13, Nov. 2010, doi: 10.1109/MEI.2010.5599974.
- [26] Y. Bertrand and L. C. Hoang, "Vegetal oils as substitute for mineral oils," in *Proceedings of the 7th International Conference on Properties and Applications of Dielectric Materials (Cat. No.03CH37417)*, Nagoya, Japan, 2003, vol. 2, pp. 491–494. doi: 10.1109/ICPADM.2003.1218460.
- [27] "Nytro 4000X: Datasheet." Nynas. [Online]. Available: https://www.barth-gmbh.at/resources/PDS_Nytro_4000X_EN.pdf?label=RESOURCE_PDS_Nytro_4000X_EN.pdf_EN
- [28] "MIDEL-7131-Product Brochure." [Online]. Available: https://www.midel.com/app/uploads/2018/05/MIDEL-7131-Product-Brochure.pdf
- [29] "Experience in service with new insulating liquids." CIGRE WG A2.35, Oct. 2010. [Online]. Available: https://e-cigre.org/publication/436-experiences-in-service-with-new-insulating-liquids
- [30] Y. Jing, I. V. Timoshkin, M. P. Wilson, M. J. Given, S. J. MacGregor, and T. Wang, "Dielectric Properties of Natural Ester, Synthetic Ester Midel 7131 and Mineral Oil Diala D," p. 9, doi: 10.1109/TDEI.2013.003917.
- [31] A. Giannakis and D. Peftitsis, "MVDC distribution grids and potential applications: Future trends and protection challenges," in 2018 20th European Conference on Power Electronics and Applications (EPE'18 ECCE Europe), 2018, p. P.1-P.9.

- [32]R. Bernacchi, "MVDC and Grid Interties: enabling new features in distribution, sub-transmission and industrial networks," Nov. 2019. [Online]. Available: https://library.e.abb.com/public/5fea768c835b4daeb8258bf950ddb05c/ABB%20MVDC_White%20paper.pdf?x-sign=X9LOXylnUBkKIMUPttFtrNFlHfODv7TYMZjoITkYE332BdplwYEgUSztjC9z/158
- [33] J. K. Steinke, P. Maibach, G. Ortiz, F. Canales, and P. Steimer, "MVDC Applications and Technology," in *PCIM Europe; International Exhibition and Conference for Power Electronics, Intelligent Motion, Renewable Energy and Energy Management*, Nuremberg, Germany, May 2019, p. 8.
- [34]O. Dahmani, S. Bourguet, M. Machmoum, P. Guerin, P. Rhein, and L. Josse, "Optimization of the Connection Topology of an Offshore Wind Farm Network," *IEEE Syst. J.*, vol. 9, no. 4, pp. 1519–1528, Dec. 2015, doi: 10.1109/JSYST.2014.2330064.
- [35]M. De Prada Gil, J. L. Domínguez-García, F. Díaz-González, M. Aragüés-Peñalba, and O. Gomis-Bellmunt, "Feasibility analysis of offshore wind power plants with DC collection grid," *Renew. Energy*, vol. 78, pp. 467–477, Jun. 2015, doi: 10.1016/j.renene.2015.01.042.
- [36] C. Meyer, M. Hoing, A. Peterson, and R. W. De Doncker, "Control and Design of DC Grids for Offshore Wind Farms," *IEEE Trans. Ind. Appl.*, vol. 43, no. 6, pp. 1475–1482, 2007, doi: 10.1109/TIA.2007.908182.
- [37]M. A. Bahmani, K. Vechalapu, M. Mobarrez, and S. Bhattacharya, "Flexible HF distribution transformers for inter-connection between MVAC and LVDC connected to DC microgrids: Main challenges," in 2017 IEEE Second International Conference on DC Microgrids (ICDCM), Nuremburg, Germany, Jun. 2017, pp. 53–60. doi: 10.1109/ICDCM.2017.8001022.
- [38] P. Dworakowski, A. Wilk, M. Michna, B. Lefebvre, and T. Lagier, "3-phase medium frequency transformer for a 100kW 1.2kV 20kHz Dual Active Bridge converter," in *IECON 2019 45th Annual Conference of the IEEE Industrial Electronics Society*, Lisbon, Portugal, Oct. 2019, pp. 4071–4076. doi: 10.1109/IECON.2019.8926695.
- [39] S. Meier, T. Kjelqvist, S. Norga, and H. Nee, "Design considerations for medium-frequency power transformers in offshore wind farms," in 2009 13th European Conference on Power Electronics and Applications, 2009, pp. 1–12.
- [40]C. Ma, K. Yoshida, and K. Honda, "Si-IGBT versus SiC-MOSFET 2014; An isolated bidirectional resonant LLC DC-DC converter for distributed power systems," in 2015 54th Annual Conference of

- the Society of Instrument and Control Engineers of Japan (SICE), Hangzhou, China, Jul. 2015, pp. 894–899. doi: 10.1109/SICE.2015.7285440.
- [41]I. Villar, "Multiphysical Characterization of Medium-Frequency Power Electronic Transformers," Ecole Polytechnique Federal de Lausanne, 2010.
- [42] A. Fouineau et al., "A Medium Frequency Transformer Design Tool with Methodologies Adapted to Various Structures," presented at the 2020 Fifteenth International Conference on Ecological Vehicles and Renewable Energies (EVER), Monte-Carlo, Monaco, Sep. 2020.
- [43]R. Moller, B. Soppe, and A. Schnettler, "Development of a test bench to investigate the breakdown voltage of insulation oil in a frequency range between 1 kHz and 10 kHz," in 2017 IEEE Second International Conference on DC Microgrids (ICDCM), Nuremburg, Germany, Jun. 2017, pp. 160–165. doi: 10.1109/ICDCM.2017.8001038.
- [44] P. Wang, G. C. Montanari, and A. Cavallini, "Partial Discharge Phenomenology and Induced Aging Behavior in Rotating Machines Controlled by Power Electronics," *IEEE Trans. Ind. Electron.*, vol. 61, no. 12, pp. 7105–7112, Dec. 2014, doi: 10.1109/TIE.2014.2320226.
- [45]E. Lindell, T. Bengtsson, J. Blennow, and S. Gubanski, "Influence of rise time on partial discharge extinction voltage at semi-square voltage waveforms," *IEEE Trans. Dielectr. Electr. Insul.*, vol. 17, no. 1, pp. 141–148, Feb. 2010, doi: 10.1109/TDEI.2010.5412012.
- [46] F. P. Espino-Cortes, Cherney EA, and S. H. Jayaram, "Impact of inverter drives employing fast-switching devices on form-wound AC machine stator coil stress grading," *IEEE Electr. Insul. Mag.*, vol. 23, no. 1, pp. 16–28, Jan. 2007, doi: 10.1109/MEI.2007.288451.
- [47] A. Cavallini, D. Fabiani, and G. Montanari, "Power electronics and electrical insulation systems part 2: life modeling for insulation design," *IEEE Electr. Insul. Mag.*, vol. 26, no. 4, pp. 33–39, Jul. 2010, doi: 10.1109/MEI.2010.5511187.
- [48]R. Moller and R. Puffer, "Investigation of the Breakdown Voltage of Resin Impregnated Aramid Fibers at Medium Frequency," in 2018 IEEE 2nd International Conference on Dielectrics (ICD), 2018, pp. 1-6, Budapest, Hungary, 2018, p. 6. doi: 10.1109/ICD.2018.8514666.
- [49]M. Jaritz and J. Biela, "Isolation design of a 14.4kV, 100kHz transformer with a high isolation voltage (115kV)," in 2016 IEEE International Power Modulator and High Voltage Conference (IPMHVC), San Francisco, CA, USA, Jul. 2016, pp. 73–78. doi: 10.1109/IPMHVC.2016.8012831.

- [50]T. Koltunowicz, A. Cavallini, D. Djairam, G. C. Montanari, and J. Smit, "The influence of square voltage waveforms on transformer insulation break down voltage," in 2011 Annual Report Conference on Electrical Insulation and Dielectric Phenomena, Cancun, Mexico, Oct. 2011, pp. 48–51. doi: 10.1109/CEIDP.2011.6232593.
- [51] A. Cavallini, D. Fabiani, and G. Montanari, "Power electronics and electrical insulation systems & Part 1: Phenomenology overview," *IEEE Electr. Insul. Mag.*, vol. 26, no. 3, pp. 7–15, May 2010, doi: 10.1109/MEI.2010.5482783.
- [52] "Guidelines for unconventional partial discharge measurements." CIGRÉ WG D1.33, 2010.
- [53]M. Pompili and R. Bartnikas, "On partial discharge measurement in dielectric liquids," *IEEE Trans. Dielectr. Electr. Insul.*, vol. 19, no. 5, pp. 1476–1481, Oct. 2012, doi: 10.1109/TDEI.2012.6311489.
- [54] E. Lindell, T. Bengtsson, J. Blennow, and S. Gubanski, "Measurement of partial discharges at rapidly changing voltages," *IEEE Trans. Dielectr. Electr. Insul.*, vol. 15, no. 3, pp. 823–831, Jun. 2008, doi: 10.1109/TDEI.2008.4543120.
- [55]C. Zhang, M. Dong, B. Wang, and M. Ren, "Partial Discharge Detection and Assessment of Surface defects under Fast Rising Repetitive Square Voltage for MV Converter Application," in 2019 IEEE Conference on Electrical Insulation and Dielectric Phenomena (CEIDP), Richland, WA, USA, Oct. 2019, pp. 311–314. doi: 10.1109/CEIDP47102.2019.9009626.
- [56]P. Romano *et al.*, "Partial discharges at different voltage waveshapes: Comparison between two different acquisition systems," *IEEE Trans. Dielectr. Electr. Insul.*, vol. 25, no. 2, pp. 584–593, Apr. 2018, doi: 10.1109/TDEI.2018.006782.
- [57] J. Wu, A. Rodrigo Mor, P. V. M. van Nes, and J. J. Smit, "Measuring method for partial discharges in a high voltage cable system subjected to impulse and superimposed voltage under laboratory conditions," *Int. J. Electr. Power Energy Syst.*, vol. 115, p. 105489, Feb. 2020, doi: 10.1016/j.ijepes.2019.105489.
- [58] Peng Wang, A. Cavallini, G. C. Montanari, and Guangning Wu, "Effect of rise time on PD pulse features under repetitive square wave voltages," *IEEE Trans. Dielectr. Electr. Insul.*, vol. 20, no. 1, pp. 245–254, Feb. 2013, doi: 10.1109/TDEI.2013.6451364.
- [59] C. Abadie, "On-line non-intrusive partial discharges detection in aeronautical systems," PhD Thesis, Université Paul Sabatier Toulouse III, Toulouse, 2017.

- [60] T. J. A. Hammarstrom, "Partial discharge characteristics at ultra-short voltage risetimes," *IEEE Trans. Dielectr. Electr. Insul.*, vol. 25, no. 6, Art. no. 6, Dec. 2018, doi: 10.1109/TDEI.2018.007445.
- [61]G. C. Montanari, R. Hebner, P. Seri, and R. Ghosh, "Noise rejection and partial discharge identification in PDIV tests of insulated wires under repetitive impulse supply voltage," in 2019 IEEE Electrical Insulation Conference (EIC), Calgary, AB, Canada, Jun. 2019, pp. 505–508. doi: 10.1109/EIC43217.2019.9046587.
- [62] A. A. Abdelmalik, A. Nysveen, and L. Lundgaard, "Influence of fast rise voltage and pressure on partial discharges in liquid embedded power electronics," *IEEE Trans. Dielectr. Electr. Insul.*, vol. 22, no. 5, pp. 2770–2779, Oct. 2015, doi: 10.1109/TDEI.2015.005411.
- [63] C. Forssén, "Modelling of cavity partial discharges at variable applied frequency," PhD Thesis, Electromagnetic Engineering, KTH Electrical Engineering, Stockholm, 2008.
- [64] P. H. F. Morshuis, "Partial discharge mechanism: Mechanism leading to breakdown, analyzed by fast electrical and optical measurements," PhD Thesis, Delftse Universitaire Press, Delft, 1993.
- [65] "Partial discharges and IEC standards 60840 and 62067: Simulation support to encourage changes," *Teh. Vjesn. Tech. Gaz.*, vol. 23, no. 2, Apr. 2016, doi: 10.17559/TV-20141118124625.
- [66] Suwarno, "Partial Discharge in High Voltage Insulating Materials," *Int. J. Electr. Eng. Inform.*, vol. 8, no. 1, pp. 147–163, Mar. 2016, doi: 10.15676/ijeei.2016.8.1.11.
- [67]Z. Liu, "Partial discharge and streamer characteristics of transformer liquids under AC stress," PhD Thesis, The University of Manchester, 2017.
- [68] M. Pompili, C. Mazzetti, and R. Bartnikas, "PD Pulse Burst Characteristics of Transformer Oils," *IEEE Trans. Power Deliv.*, vol. 21, no. 2, Art. no. 2, Apr. 2006, doi: 10.1109/TPWRD.2005.858776.
- [69]O. Lesaint, "Prebreakdown phenomena in liquids: propagation 'modes' and basic physical properties," *J. Phys. Appl. Phys.*, vol. 49, no. 14, Art. no. 14, Apr. 2016, doi: 10.1088/0022-3727/49/14/144001.
- [70] L. Lundgaard, D. Linhjell, G. Berg, and S. Sigmond, "Propagation of positive and negative streamers in oil with and without pressboard interfaces," *IEEE Trans. Dielectr. Electr. Insul.*, vol. 5, no. 3, Art. no. 3, Jun. 1998, doi: 10.1109/94.689428.
- [71] A. Beroual, "Pre-breakdown mechanisms in dielectric liquids and predicting models," in 2016 IEEE Electrical Insulation Conference (EIC), Montreal, QC, Canada, Jun. 2016, pp. 117–128. doi: 10.1109/EIC.2016.7548608.

- [72] W. G. Chadband, "The electrical breakdown of insulating oil," *Power Eng. J.*, vol. 6, no. 2, p. 61, 1992, doi: 10.1049/pe:19920015.
- [73] V.-H. Dang, A. Beroual, E. A. Al-Ammar, and M. Qureshi, "Comparative PD characteristics of pressboard/mineral oil and pressboard/vegetable oil insulating systems," in 2012 IEEE International Conference on Condition Monitoring and Diagnosis, Bali, Indonesia, Sep. 2012, pp. 890–893. doi: 10.1109/CMD.2012.6416294.
- [74] H. Zainuddin, P. L. Lewin, and P. M. Mitchinson, "Partial discharge characteristics of surface tracking on oil-impregnated pressboard under AC voltages," in 2013 IEEE International Conference on Solid Dielectrics (ICSD), Bologna, Italy, Jun. 2013, pp. 1016–1019. doi: 10.1109/ICSD.2013.6619774.
- [75]P. Peng, Y. Cui, S. Ji, F. Zhang, P. Cao, and L. Zhu, "Evolution of partial discharge of oil-paper insulation under long-term AC voltage," in 2016 IEEE International Power Modulator and High Voltage Conference (IPMHVC), San Francisco, CA, USA, Jul. 2016, pp. 166–170. doi: 10.1109/IPMHVC.2016.8012853.
- [76] "Ester insulating liquids for power transformers." CIGRE A2 209, 2012.
- [77]Y. Sha, Y. Zhou, L. Zhang, M. Huang, and F. Jin, "Measurement and simulation of partial discharge in oil-paper insulation under the combined AC–DC voltage," *J. Electrost.*, vol. 71, no. 3, pp. 540–546, Jun. 2013, doi: 10.1016/j.elstat.2012.11.013.
- [78] "Insulation degradation under fast, repetitive voltage pulses." WG D1.43 CIGRE, 2017.
- [79] Peng Wang, A. Cavallini, and G. Montanari, "The influence of repetitive square wave voltage parameters on enameled wire endurance," *IEEE Trans. Dielectr. Electr. Insul.*, vol. 21, no. 3, Art. no. 3, Jun. 2014, doi: 10.1109/TDEI.2014.6832275.
- [80] J. Jiang, M. Zhao, C. Zhang, M. Chen, H. Liu, and R. Albarracín, "Partial Discharge Analysis in High-Frequency Transformer Based on High-Frequency Current Transducer," *Energies*, vol. 11, no. 8, Art. no. 8, Aug. 2018, doi: 10.3390/en11081997.
- [81]P. Wang, A. Cavallini, and G. C. Montanari, "The influence of square wave voltage duty cycle on PD behavior," in 2015 IEEE Conference on Electrical Insulation and Dielectric Phenomena (CEIDP), Ann Arbor, MI, USA, Oct. 2015, pp. 338–341. doi: 10.1109/CEIDP.2015.7352006.

- [82]IEC 61934, "Electrical insulating materials and systems--electrical measurement of partial discharges (PD) under short rise time and repetitive voltage impulses.," International Electrotechnical Commission, Geneva, Technical Report, 2011.
- [83] Z. Wei, H. You, R. Na, and J. Wang, "Partial Discharge Detection Strategies under Fast Rise Time Voltages Generated by Wide-bandgap Semiconductor Devices," in 2019 IEEE Electrical Insulation Conference (EIC), Calgary, AB, Canada, Jun. 2019, pp. 75–78. doi: 10.1109/EIC43217.2019.9046572.
- [84]M. Muhr and R. Schwarz, "EXPERIENCE WITH OPTICAL PARTIAL DISCHARGE DETECTION," in *Int. Conf. Adv. Process. Test. Appl. Dielectr. Mater. Wroclaw Pol.*, Poland, 2007, pp. 26–29. [Online]. Available: https://graz.pure.elsevier.com/en/publications/experience-with-optical-partial-discharge-detection
- [85] X. Hu, W. H. Siew, M. D. Judd, and X. Peng, "Transfer function characterization for HFCTs used in partial discharge detection," *IEEE Trans. Dielectr. Electr. Insul.*, vol. 24, no. 2, Art. no. 2, Apr. 2017, doi: 10.1109/TDEI.2017.006115.
- [86] L. A. Kojovic and R. Beresh, "Practical Aspects of Rogowski Coil Applications to Relaying," IEEE PSRC Special report, 2010. [Online]. Available: https://www.pes-psrc.org/kb/published/reports/Practical%20Aspects%20of%20Rogowski%20Coil%20Applications%20to%20Relaying_Final.pdf
- [87] T. Bengtsson, E. Lindell, and T. Hammarstrom, "Stochastic detection of partial discharges," *IEEE Trans. Dielectr. Electr. Insul.*, vol. 20, no. 6, Art. no. 6, Dec. 2013, doi: 10.1109/TDEI.2013.6678871.
- [88] E. Lindell, T. Bengtsson, J. Blennow, and S. M. Gubanski, "Partial discharges measured at semi-square voltages," in 2006 IEEE Conference on Electrical Insulation and Dielectric Phenomena, Kansas, MO, USA, Oct. 2006, pp. 631–634. doi: 10.1109/CEIDP.2006.312011.
- [89] K. Wu, T. Okamoto, and Y. Suzuoki, "Effects of discharge area and surface conductivity on partial discharge behavior in voids under square voltages," *IEEE Trans. Dielectr. Electr. Insul.*, vol. 14, no. 2, pp. 461–470, Apr. 2007, doi: 10.1109/TDEI.2007.344627.
- [90]E. Lemke, "A critical review of partial-discharge models," *IEEE Electr. Insul. Mag.*, vol. 28, no. 6, pp. 11–16, Nov. 2012, doi: 10.1109/MEI.2012.6340519.

- [91]Z. Achillides, E. Kyriakides, and G. E. Georghiou, "Partial discharge modeling: an improved capacitive model and associated transients along medium voltage distribution cables," *IEEE Trans. Dielectr. Electr. Insul.*, vol. 20, no. 3, pp. 770–781, Jun. 2013, doi: 10.1109/TDEI.2013.6518947.
- [92]"EMI current measurement using Solar 9123-1N current probe." Solar Electronics, 1992.
- [93] W. A. Davis and K. K. Agarwal, *Radio Frequency Circuit Design*. New York, USA: John Wiley & Sons, Inc., 2001. doi: 10.1002/0471200689.
- [94]"Fast high voltage transistor switches." Behlke. [Online]. Available: https://www.behlke.com/pdf/general.pdf
- [95] "Fast high voltage transistor switch." Behlke. [Online]. Available: https://www.behlke.com/pdf/901-20-lc2.pdf
- [96]P. Dusart, "Cours de Statistiques inférentielles," Université de Limoges, 2018. [Online]. Available: https://www.unilim.fr/pages_perso/pierre.dusart/Probas/cours_stat_S4.pdf
- [97] S. GLen, "T Test (Student's T-Test): Definition and Examples," *StatisticsHowTo.com: Elementary Statistics for the rest of us.* https://www.statisticshowto.com/probability-and-statistics/t-test/
- [98] "SPSS Tutorials: Independent Samples t-test." Kent State University, Oct. 04, 2021. [Online]. Available: https://libguides.library.kent.edu/SPSS
- [99] Z. Liu, Q. Liu, and Z. D. Wang, "Effect of electric field configuration on streamer and partial discharge phenomena in a hydrocarbon insulating liquid under AC stress," *J. Phys. Appl. Phys.*, vol. 49, no. 18, p. 185501, May 2016, doi: 10.1088/0022-3727/49/18/185501.
- [100] V.-H. Dang, A. Beroual, M.-L. Coulibaly, and C. Perrier, "Investigation on creeping discharges propagating over pressboard immersed in mineral and vegetable oils submitted to lightning impulse voltages," in 2012 IEEE International Conference on Condition Monitoring and Diagnosis, Bali, Indonesia, Sep. 2012, pp. 404–407. doi: 10.1109/CMD.2012.6416465.
- [101] Z. Liu, J. S. Park, and Q. Liu, "Partial discharge inception voltages of an inhibited mineral oil in quasi-uniform electric fields," in 2015 IEEE 11th International Conference on the Properties and Applications of Dielectric Materials (ICPADM), Sydney, Australia, Jul. 2015, pp. 420–423. doi: 10.1109/ICPADM.2015.7295298.
- [102] IEC 61294, "Insulating liquids Determination of the partial discharge inception voltage (PDIV)
 Test procedure," International Electrotechnical Commission, Technical report, 1993.

- [103] V. W. L. Chin, T. L. Tansley, and T. Osotchan, "Electron mobilities in gallium, indium, and aluminum nitrides," *J. Appl. Phys.*, vol. 75, no. 11, pp. 7365–7372, Jun. 1994, doi: 10.1063/1.356650.
- [104] M. Florkowski, D. Krześniak, M. Kuniewski, and P. Zydroń, "Partial Discharge Imaging Correlated with Phase-Resolved Patterns in Non-Uniform Electric Fields with Various Dielectric Barrier Materials," *Energies*, vol. 13, no. 11, p. 2676, May 2020, doi: 10.3390/en13112676.
- [105] K. B. Baltzis, "On the usage and potential applications of the finite element method magnetics (FEMM) package in the teaching of electromagnetics in higher education." [Online]. Available: https://core.ac.uk/download/pdf/38301447.pdf
- [106] M. Michelarakis, P. Widger, A. Beroual, and A. (Manu) Haddad, "Electrical Detection of Creeping Discharges over Insulator Surfaces in Atmospheric Gases under AC Voltage Application," *Energies*, vol. 12, no. 15, p. 2970, Aug. 2019, doi: 10.3390/en12152970.
- [107] "Good titration practices for Karl Fischer titration," Mettler Toledo, Switzerland, Brochure, Apr. 2011. [Online]. Available: https://www.mt.com/dam/non-indexed/po/ana/titration/51725145B_V10.11_GTP_KF_Titr_HB_Complet.pdf
- [108] "Photomultiplier tubes: Basics and applications," Hamamatsu, Edition 3a. [Online]. Available: https://www.hamamatsu.com/resources/pdf/etd/PMT_handbook_v3aE.pdf
- [109] A. Beroual and R. Tobazeon, "Prebreakdown Phenomena in Liquid Dielectrics," *IEEE Trans. Electr. Insul.*, vol. EI-21, no. 4, pp. 613–627, Aug. 1986, doi: 10.1109/TEI.1986.348967.
- [110] O. Lesaint and R. Tobazeon, "Streamer generation and propagation in transformer oil under AC divergent field conditions," *IEEE Trans. Electr. Insul.*, vol. 23, no. 6, pp. 941–954, Dec. 1988, doi: 10.1109/14.16519.
- [111] L. Cui, W. Chen, A. S. Vaughan, B. Xie, J. Li, and Z. Long, "Comparative analysis of air-gap PD characteristics: Vegetable oil/pressboard and mineral oil/pressboard," *IEEE Trans. Dielectr. Electr. Insul.*, vol. 24, no. 1, pp. 137–146, Feb. 2017, doi: 10.1109/TDEI.2016.005911.
- [112] S. M. Lebedev, O. S. Gefle, and Y. P. Pokholkov, "The barrier effect in dielectrics: the role of interfaces in the breakdown of inhomogeneous dielectrics," *IEEE Trans. Dielectr. Electr. Insul.*, vol. 12, no. 3, pp. 537–555, Jun. 2005, doi: 10.1109/TDEI.2005.1453459.
- [113] M. Ghassemi, "Accelerated insulation aging due to fast, repetitive voltages: A review identifying challenges and future research needs," *IEEE Trans. Dielectr. Electr. Insul.*, vol. 26, no. 5, Art. no. 5, Oct. 2019, doi: 10.1109/TDEI.2019.008176.

- [114] "Instruction manual: P6015A 1000 X High voltage probe." Tektronix. [Online]. Available: https://download.tek.com/manual/070822305.pdf
- [115] A. B. Jorgensen, S. Beczkowski, C. Uhrenfeldt, N. H. Petersen, S. Jorgensen, and S. Munk-Nielsen, "A Fast-Switching Integrated Full-Bridge Power Module Based on GaN eHEMT Devices," IEEE Trans. Power Electron., vol. 34, no. 3, Art. no. 3, Mar. 2019, doi: 10.1109/TPEL.2018.2845538.
- [116] X. Wang, "Partial discharge behaviours and breakdown mechanism of ester transformer liquids under AC stress," PhD Thesis, The University of Manchester, 2011.
- [117] R. Acheen, "Determination and influence of the existence of partial discharges in a railway traction system using SiC-based components," PhD Thesis, Université Paul Sabatier Toulouse III, France, 2020.
- [118] M. Gruchalla and M. Thuot, "Managing Electromagnetic Interference in large instrumentation systems," Monterey, CA, USA, 2014. [Online]. Available: http://accelconf.web.cern.ch/AccelConf/IBIC2014/
- [119] F. Caspers, "RF engineering basic concepts: S-parameters." CERN, Geneva. [Online]. Available: https://cds.cern.ch/record/1415639/files/p67.pdf

Appendix A: Partial discharge model under AC 50 Hz and square waveform

A1. PD model under AC 50 Hz

To simulate the DUT with IEC60270 schematics, the ABC model was used. The ABC model was connected across a coupling capacitor and shunt resistance in series with it. The resistance and inductance represent the parasitic values of a short cable connection between PD model and high voltage circuit, as in laboratory set-up.

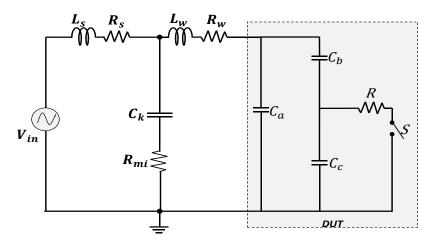


Figure A1: Circuit developed in Simulink for PD measurement under AC

The circuit elements, as shown in Table A2, are chosen in such a way so as to match the magnitude and dynamics of the PD curves with a commercially available pulse generating calibrator (CAL 542) from Omicron.

Table A1: Value	assigned in the PI	D measurement circu	it of Figure A1 under AC

Vin	Ls/ Rs	Lw/Rw	Ck	Rmi	Са	Cb	Сс	R
1 kV	1mH/ 1mΩ	$0.155 \mu H$ $/ 1 m \Omega$	1 nF	50 Ω	70 pF	0.07 pF	0.02 pF	2 kΩ

The PD curve (in blue) generated in the circuit and 50 pC pulse signal (in black) from the calibrator were plotted together as shown in figure A1. The area under PD curve was calculated using 'trapz ()' function in Matlab which returned 50.8 pC as output.

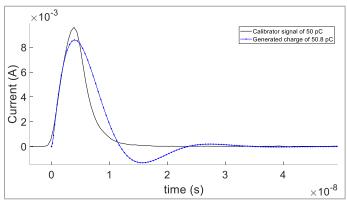


Figure A2: Comparison of 50 pC charge (in blue) generated by ABC model with a 50 pC pulse generated by the Omicron calibrator

A2. PD model under square waveform

Further, the same PD model (or ABC model) was implemented under a circuit generating square voltages. The circuit incorporates a H-bridge configuration using ideal switches available in Simscape electrical. The circuit parameters thus chosen to generate square voltage across the ABC model are in table A2.

Table A2: Value assigned in the PD measurement circuit of Figure A2 under square voltage

VDC	Ls/Rs	Ck	Rmi	Switching frequency	Duty cycle	Ca	Cb	Сс	R
1 kV	500 μH / 5 kΩ	1 nF	50 Ω	1 kHz	50 %	30 pF	0.07 pF	0.02 pF	500 kΩ

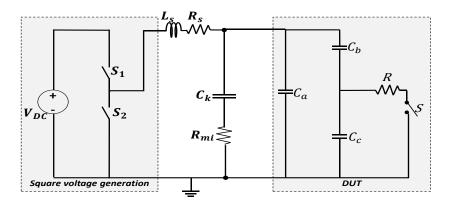


Figure A3: Circuit developed in Simulink for PD measurement under square waveform using coupling capacitor and measuring resistance

In order to analyze the FFT of displacement current due to fast rising voltage, the coupling capacitor and measuring impedance from Figure A3 were removed. FFT was performed using fft() in Matlab.

Appendix B: Modeling of DUT in FEMM

The selected configuration of needle-barrier plane was modeled using 3 μm tip (same as used in study [67]) in FEMM 4.2 software. The parameters and voltage used for modeling are in Table B1.

Needle tip	3 μm
Voltage applied at tip	20 kV peak
Plane	10 mm in axis-symmetry
Gap	0.7 mm
Barrier	1 mm thick pvc ($\varepsilon = 2.24$)
Medium	Mineral oil ($\varepsilon = 2.2$)
Boundary points (r, z)	(0,4000); (30000,4000); (0,18000); (30000,18000)
Mesh size (minimum)	0.5 nm around the curved tip

Table B1: Value used for modeling needle-barrier plane configuration with 3 µm tip

Tip field with 3 µm radius was found to be 2085 kV/mm.

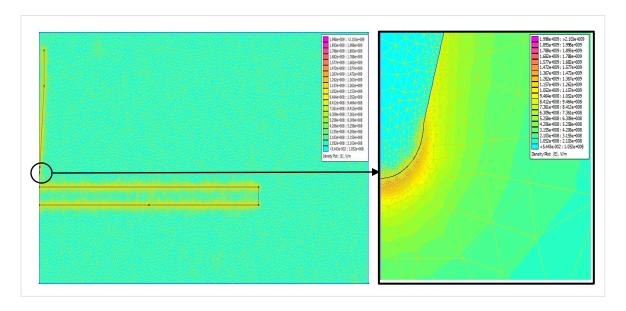


Figure B2: (left) Full view of needle barrier plane configuration with 3 µm tip at 20 kV (right) magnified view of 3 µm tip with size of 0.5 nm around the tip generating a tip field of 2085 kV/mm at 20 kV

Appendix C: Tip radius under microscope

In order to check the reusability of 1 μm needle tip, ten PDIV tests were performed with 1 mm thick PVC in mineral oil. As can be seen in Figure C1, the PDIV values are 6.8 ± 1.2 kV, where 6.8 kV is the mean value. From this experiment, it was concluded that for ten PDIV measurements the electric field generated by 1 μm tip was sufficient for each test to generate PDs in the given DUT.

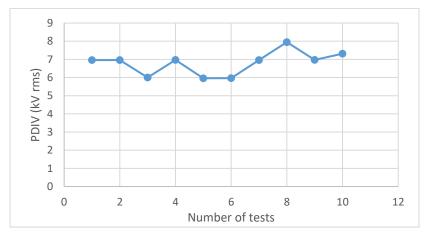


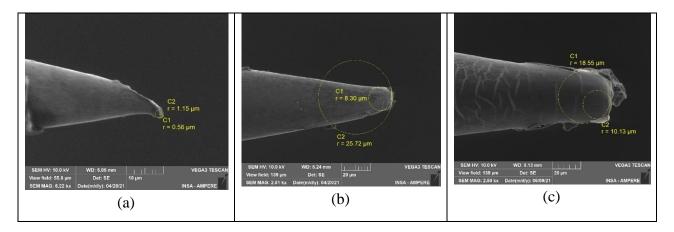
Figure C1: PDIV values obtained from ten measurements with 1 mm thick PVC in mineral oil for selected DUT

In another tests, the tip radius of a new needle, tip after five partial discharge tests were checked under scanning electron microscope (from Vega3 Tescan) available in the Ampère laboratory. As shown in Figure C2 (a), the tip of new 1 μ m needle was not found to be hemispherical in shape. Moreover, as compared to new tip, the tip after five PD tests was found to be somewhat flattened as shown in Figure C2(b).

In order to check, if the deformation occurred during the installation or due to melting of tip from discharge process, the same new needle tip as shown in Figure C2 (a) was mounted and unmounted casually with AlN barrier in the DUT cell. The gap of 0.7 mm was maintained as usual with the spacer. No PD tests were performed with this needle.

As can be observed in Figure C2 (c), the tip radius after installation was deformed. The tip deformation could have occurred by hitting hard surface of AlN barrier or grounding plane during mounting/unmounting actions. It seems that a careful mounting of needle tip in the DUT cell can avoid tip deformation.

Figure C2 (d) presents the image of new 100 μ m tip before PD tests and Figure C2 (e) provides the image of 100 μ m tip after 10 PD measurements. The 100 μ m tip was found to be more robust to mechanical stress during installation as well as to discharges.



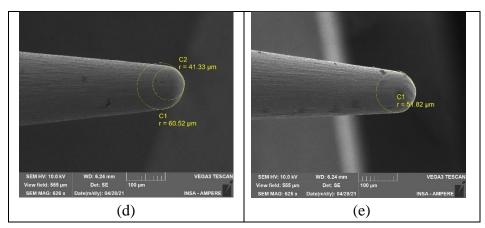


Figure C2: (a) New 1 μ m tip (b) 1 μ m tip after five PDIV measurements checked under electron microscope (c) 1 μ m after installation in DUT with no PD measurements performed (d) new 100 μ m tip (e) 100 μ m tip after 10 PDIV tests

Appendix D: Conditioning and monitoring of dielectric liquid

The treatment or conditioning of dielectric liquid was an important step to maintain the quality of dielectric liquid before using it for PD tests. This section presents the steps taken for conditioning dielectric liquid before partial discharge measurements.

The conditioning and monitoring of dielectric liquids were performed by taking following steps:

- 1) Filtration
- 2) Breakdown voltage (BDV) measurements
- 3) Water content measurements

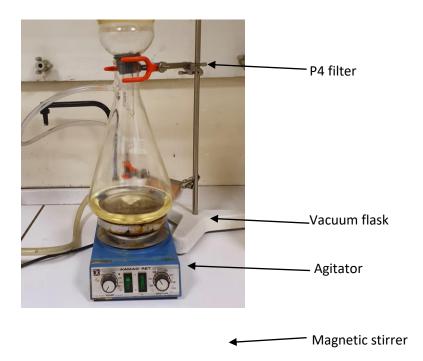


Figure D1: Components of filtration process of dielectric liquid

D.1 Filtration

The filtration was performed to remove foreign particles in the dielectric liquids. Prior to the filtration process, the filter and vacuum flask were cleaned and dried. Here below are laboratory components used to perform filtration:

1. Glass filter: The sintered glass filter used during filtration process was of porosity grade 4 (or P4). It has pores of dimensions 10 -16 μ m.

- 2. Pump: The pump (model: Adixen PASCAL 2010 C1) used during filtration can create low pressure of less than 1 mbar as per its datasheet.
- 3. Vacuum filtration flask: Capacity of 2 L
- 4. Magnetic stirrer: Set at 400 rpm

All the above mentioned components can be seen in Figure D1. The treated dielectric liquid was stored in clean dried container.

D.2Breakdown voltage measurements

In order to perform BDV tests, the IEC 60156 standard test option was always selected in Baur DTA 100C tester. The gap between sphere-sphere electrodes were always maintained at 2.5 mm using the standard spacer available with Baur kit. During BDV measurements, the rate of rise of voltage was 2 kV/s until breakdown as per IEC 60156: 1995 norm.

D.2.1 Impact of stirring during filtration

During the initial phase of dielectric liquid treatment, the stirring process was not adopted during filtration, which means the magnetic stirrer as shown in Figure D1 was not used.

The norm IEC 60156 provides the option of BDV tests 'with' and 'without stirring', therefore treated samples of dielectric liquids were tested with both stirring as well as without stirring to understand the influence of stirring on BDV tests.

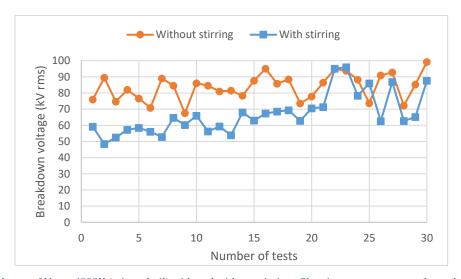


Figure D2: BDV tests of Nytro 4000X (mineral oil) with and without stirring; filtration process was performed without magnetic stirring

As can be seen from the Figure D2, the BDV tests without stirring were found to be more consistent and compliant with standard datasheet value of 70 kV. On the other hand, with stirring the BDV tests was found to be less than 70 kV for first fifteen tests. It however, improved during last fifteen tests. It seems that after filtration the dielectric liquid was either not homogenous enough or there were tiny particles present in liquid, which could be the reason of low BDV tests for first fifteen tests. Conversely, without stirring the dielectric liquid showed BDV values more than 70 kV for more than twenty-five tests out of thirty.

In order to understand the impact of stirring, the magnetic stirrer (as shown in Figure D1) was introduced in the second step. After the filtration of dielectric liquid with stirring, two samples were taken to perform BDV tests 'with' and 'without stirring'. The BDV measurements thus obtained have been provided in Figure D3.

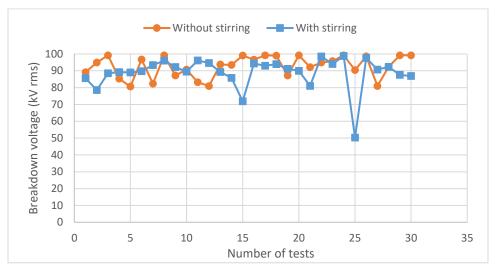


Figure D3: BDV tests of Nytro 4000X (mineral oil) with and without stirring; filtration process was performed with magnetic stirring

As a result of adoption of stirring process during filtration process, a major change in BDV test results of liquid sample with stirring was noticed. It seems that stirring process during filtration makes the dielectric liquid quite homogenous. Another point to note here is that the breakdown values of dielectric liquid did not degrade for thirty BDV tests, which can be attributed to not enough degradation of the liquid for these many tests.

Before PDIV tests, the filtration of dielectric liquid was performed with stirring as shown in Figure D1. Also, the BDV tests for different batches of dielectric liquids reported in Chapter-3 were performed with stirring.

D.3. Water content measurement

There are various methods for determining water content of dielectric liquids which uses chemical reactions, spectral analysis or electro-physical processes. Due to its accuracy, the Karl Fischer coulometric titration is widely used, which uses electrochemical reaction to determine water content [115][116]. In this method, the coulometric titration takes place, in which water (H_2O) reacts with iodine (I_2) and sulfur dioxide (SO_2) in the presence of methanol (ROH) and a base, such as imidazole (3RN), as per following general reaction:

$$H_2O + I_2 + SO_2 + 3RN + ROH \rightarrow (RNH)SO_4R + 2(RNH)I$$

The image presented in Figure D4 shows the set-up of Karl Fischer titration for water content measurement of dielectric liquid in Ampère laboratory. The generator electrode and measuring electrode as shown in the figure forms the anode and cathode of the electrolytic cell.

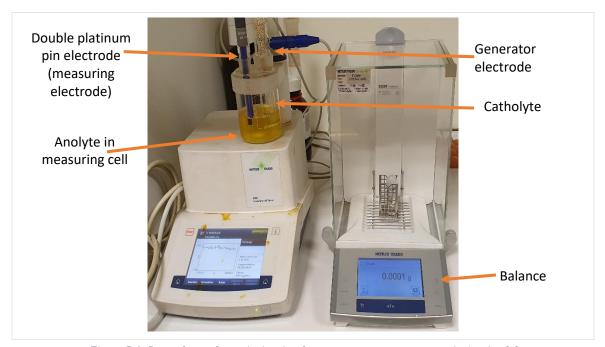


Figure D4: Set-up for coulometric titration for water content measurement in Ampère laboratory

The anode compartment contains the anolyte required for oxidation to generate iodine by applying current at generating electrode. At anode (or generator electrode), two iodide ions $(2I^-)$ are oxidized to an iodine molecule (I_2) , releasing two electrons $(2e^-)$ by the following half reaction,

$$2I^- \rightarrow I_2 + 2e^-$$

The cathode tube contains catholyte, which has the reagent to complete whole electrochemical reaction. In this technique the quantity of water is determined by the amount of current (converted to Coulomb) required to generate iodine. As we know that, in order to produce one

mole of a chemical substance, 96485 C of current are needed. In coulometric titration, the oxidation of iodine releases two electrons which reacts with water as per following,

$$2I^- \rightarrow I_2 \rightarrow H_2O$$

For each mole of water, two Faraday constant (2 x 96485 C/mol) is necessary. As the molar mass of H_2O is 18 g/mol, therefore it can be said that 1 mg of water corresponds to about 10 C of charge required at anode. Thus, iodine generation corresponds to the amount of water content in the solvent as per above stoichiometry of KF reaction.

While performing the water content measurement, first place the syringe with dielectric liquid sample inside the "balance", then start the sampling process in titrator. After this set the weight of balance to zero and then carefully inject the oil in "measuring cell". In the end, put the syringe back in the balance as depicted in the Figure D5.

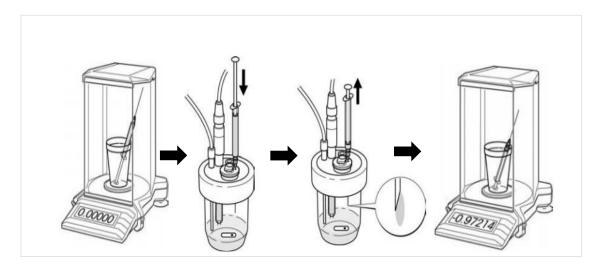


Figure D5:(Left to right) Put syringe on balance, inject oil into measuring cell, pull out empty syringe and put it back on the balance (image source: GTP brochure, Mettler Toledo)

Appendix E: Components of HV test set-up and EMC management

E1: Components of square waveform test bench

Figure E1 presents the assembly of HV switch from Behlke which includes radiator and a pump. The reservoir in the pump is filled with a dielectric liquid (galden) to dissipate heat during high voltage and high frequency operation. The pump and radiator required +12 V DC source for continuous operation. Further, the driver of HV switch required +3 to 10 V supply for operating. In the set-up the electronic cards, pump and radiator are powered using two 12V/ 38 Ah batteries. The HV switch itself is rated at 140kV/100A.



Figure E1: Assembly of a HV switch from Behlke similar to the one used for generating unipolar square waveform in Ampère laboratory (image source: Behlke website)

The DC generator in the set-up is rated as 30 kV/5 kW. Two high voltage capacitors rated at 2 μ F are connected in parallel to form a bank of 4 μ F.



Figure E2: DC generator from Technix (model:SR30KV-5kW) (image source: Technix)

E2: Steps taken to minimize the impact of EMIs in the test bench

In the set-up, different types of noise were observed interfering with the PD detection techniques. The additional steps taken to minimize the impact of EMIs have been discussed here below:

Using ferrite cores

As soon as the PCB assemblies is powered by batteries inside the Faraday cage, a periodically occurring repetitive perturbation is observed. As can be seen in Figure E3 (a), a repetitive pulse of small amplitude existed even without any high voltage application. This is found to be impacting detection techniques i.e. BNC cable connecting HFCT and PMT to the scope as shown in Figure E3 (b). This might be due to common mode (CM) current problems in the set-up which could have occurred in the absence of equipotential grounding between BNC cable (linked to scope) and HV probe. The absence of equipotential ground can introduce a capacitive coupling, giving small impedance path for radio frequency currents.

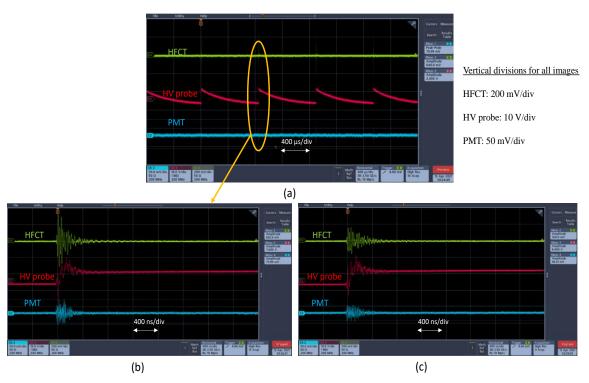


Figure E3: (a) Voltage detected at DUT using HV probe with only PCB circuit turned on and no HV applied (b) Magnified view of single event (c) reduction in noise observed with HFCT and PMT with ferrite cores on cable connecting PCB and driver unit of HV switch (scales unchanged in (b) and (c))

One of the classical approaches to counter CM current problems is to implement the common mode isolators (or ferrite cores) over the cables. The ferrite cores when put across the cables

offers high impedance to the currents flowing in the shield of cable. Also, it tries to equate the voltage in the signal and shield conductors by adding mutual inductance.

There are different ways to put ferrite cores across the signal cables to counter CM current problems. Either many cores can be put around the signal carrying cables or there can be multiturn (looping around the core) configuration as dictated in [118]. In our test bench, the multiturn configuration of the cables connecting 'PCB assembly to switch driver' and 'switch driver to HV switch' is found effective. Thus, amplitude of these perturbations reduced by some factor as shown in Figure E3(c).

E3: Influence of high speed switching on PMT signal

The PMT signal is found to be impacted by the EMIs generated by fast switching actions. To check if DC supply of PMT has an affect on PMT signal, a test is done by turning on and off the DC supply of PMT. In both situations the coaxial cable connecting PMT to oscilloscope is impacted by EMI due to high speed switching (see Figure E4).

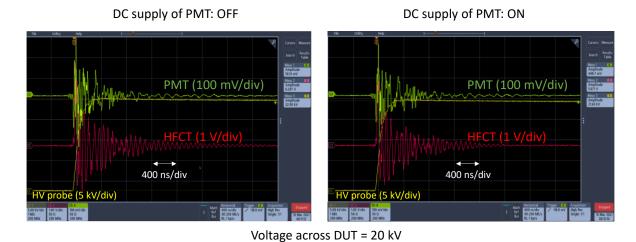


Figure E4: Impact on PMT signal due to EMIs generated by fast switching action of HV switch for conditions when DC supply of PMT is turned off (left) and turned on at -1.3 kV (right) at 20 kV for a DUT filled with dielectric liquid but without needle

E4: Turn on delay

The MOSFET device can be modeled as shown in Figure E5. As the voltage is applied across the gate (G), initially the input capacitance is charged from zero to a threshold value. Most of the current goes for charging the internal capacitors C_{gs} and C_{gd} . The drain current and voltage of the device remains unchanged during this period and is called as turn-on delay (t_d).

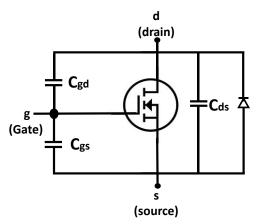


Figure E6: Model of MOSFET device

There is a further delay (tr) in which the voltage across the gate rises to a higher value which is sufficient to drive the MOSFET into on state. In this state the drain current rises from zero to its full rated value. Thus, total turn on delay (tdon) is the sum of td and tr.

Appendix F: Behavior of photomultiplier tube

F1: Tests to understand the PMT

Looking at the literatures we were sure of detecting first weak discharges with photomultipliers. However, we were not clear about the response of PMT to light emissions from a discharge process as a function of distance from PMT and media.

Therefore, to have initial experience of PMT to light emissions and understand its behavior in different conditions, some tests were made with light emitting diode (LED). The LED was put in a cell with dielectric media as air, mineral oil and synthetic ester under the PMT. The LED was powered by a function generator to produce a short duration pulsating signal at a high frequency of 10 kHz at 1 % duty cycle. The response of PMT and peak amplitude obtained were captured by oscilloscope as shown in figure F1.

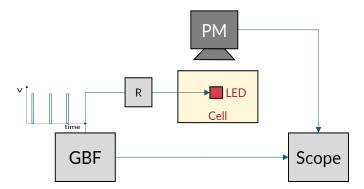


Figure F1: Set-up to study the response of PMT using LED

The DC supply of PMT was kept at -1.3 kV for all tests. The voltage across the PMT was increased slowly until the light emitted by LED was detected by PMT using scope. The peak amplitude of negative peaks thus obtained were noted for different media and compared.

As can be seen in Figure F2, the peak amplitude was found to be highest in air and lowest in synthetic ester. This means due to the different chemical composition of surrounding media, the light detected by PMT would vary.

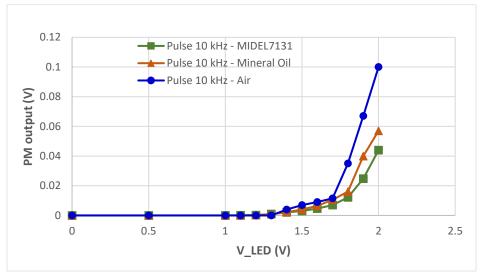


Figure F2: Response of PMT using LED in different dielectric media

Another test is performed by varying the distance between LED and PMT lens to find an optimized distance where PDs in future tests could be detected easily. It is thus found that, for the lowest gap tested, the PMT output is highest. However, for the future PD tests, considering the short cable wires used for high voltage connections, a gap of about 20 cm was used.

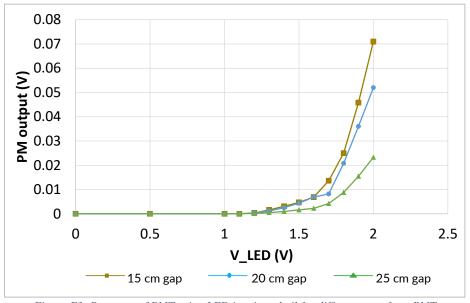


Figure F3: Response of PMT using LED in mineral oil for different gaps from PMT

F2. Confirmation of PD occurrence (Continuation from section 5.3.5)

The occurrence of PD events with Omicron is confirmed in two steps. In the first step, the DC supply of PMT is turned off to prevent any detection of PDs. As can be seen in Figure F4 (a), no

discharges can be seen even after 30 s of acquisition. Only a small peak of less than 0.4 pa.u. as marked in the figure can be detected near the ascending part of control voltage.

In the second step, the needle is removed from the DUT and voltage across the DUT is increased again up to 20 kV with PMT bias at -2 kV. As expected, in the absence of needle, no PD is detected as shown in Figure F4 (b).

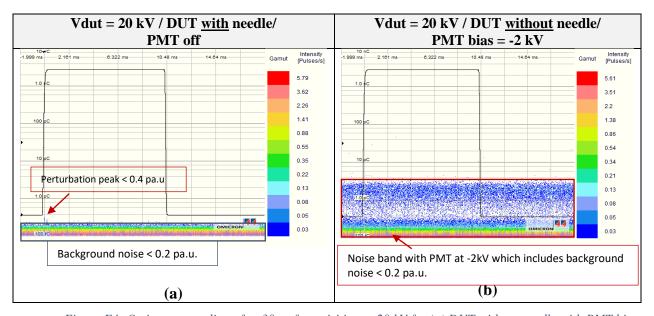


Figure F4: Omicron recording after 30 s of acquisition at 20 kV for (a) DUT without needle with PMT bias at -2 kV and (b) DUT with needle with PMT bias turned off

Appendix G: S-parameters used for modeling of HFCT

S-parameters or scattering parameters is used to describe the electrical behavior of electrical networks in radio (around 20 kHz to 300 GHz) or microwave (around 300 MHz – 300 GHz) frequencies. For convenient measurement at high frequencies, the S-parameter are described in terms of waves instead of voltage and currents. It can be readily formulated into a matrix [119]...

In a 2-port network, as shown in figure G1, the waves incident on 2-port network is 'a' and those travelling away from 2-port are 'b'. From the given 2-port network, the waves a and b can be written as in terms of S-parameters as,

$$\begin{bmatrix} b_1 \\ b_2 \end{bmatrix} = \begin{bmatrix} S_{11} & S_{12} \\ S_{21} & S_{22} \end{bmatrix} \begin{bmatrix} a_1 \\ a_2 \end{bmatrix}$$

Where,

- S11: input reflection coefficient when output Z_L is a matched load
- S21: forward transmission coefficient (from port 1 to 2)
- S12: reverse transmission coefficient (from port 2 to 1)
- S22: output reflection coefficient

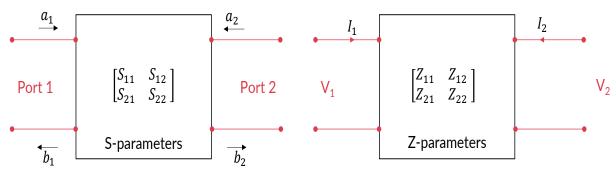


Figure G1: Representation of S-parameters and Z-parameters in a 2-port network

While, using z-parameters, the input voltage V₁ and output voltage V₂ can be expressed in terms of current I₁ and I₂.

$$\begin{bmatrix} V_1 \\ V_2 \end{bmatrix}$$

a) Use of S-parameters for the identification of the HFCT transfer function:

The identification using classical tests for transformers (open-circuit, short-circuit tests, etc.) is not valid at high frequencies because it becomes more complicated to ensure real open-circuit or short-circuit due to parasitic HF phenomena where connection inductances, inter-turn parasitic capacitances and common-mode parasitic capacitances play an important role. The choice was

then made to use a method widely used in the field of HF and RF, the measurement of S-parameters. The S-parameters, which are an equivalent representation of the Z-parameters, allow us to find the transfer impedance Zt.

S-parameter measurements require the equipment under test (EUT) to be connected to the VNA (Vector Network Analyzer) using connectors that induce a difference between the actual characteristics of the EST and the measurement made by the device. A calibration step is therefore necessary to correct this. S-parameter measurements are then made between the frequencies fmin = 300 kHz and fmax = 3 GHz

b) Transformation of S-parameters to Z-parameters

As stated in [93], the S-parameters can be converted to z-parameters using the equations

$$Z_{11} = Z_0 \cdot \frac{(1 + S_{11})(1 - S_{22}) + S_{12}S_{21}}{(1 - S_{11})(1 - S_{22}) - S_{12}S_{21}}$$

$$Z_{12} = Z_0 \cdot \frac{2 \cdot S_{12}}{(1 - S_{11})(1 - S_{22}) - S_{12}S_{21}}$$

$$Z_{21} = Z_0 \cdot \frac{2 \cdot S_{21}}{(1 - S_{11})(1 - S_{22}) - S_{12}S_{21}}$$

$$Z_{22} = Z_0 \cdot \frac{(1 - S_{11})(1 + S_{22}) + S_{12}S_{21}}{(1 - S_{11})(1 - S_{22}) - S_{12}S_{21}}$$

Where, Zo is the characteristics load impedance and usually equal to 50 Ω

c) Determination of transfer impedance Zt

The sensitivity of HFCT is usually referred to as the transfer impedance given by Z_t in $(\Omega) = V_{out}$ / I_{in} , which should be constant within the bandwidth for which the equipment is designed as shown in Figure G2. The impedance curve (Figure G4) as a function of frequency corresponds to what is communicated by the manufacturer (from 1 Ω to 5 Ω above 10 kHz) and has a cut-off frequency of 500 MHz. From the determined transfer impedance, the HFCT does not seem to have the expected characteristic in the bandwidth in which it is intended to be used.

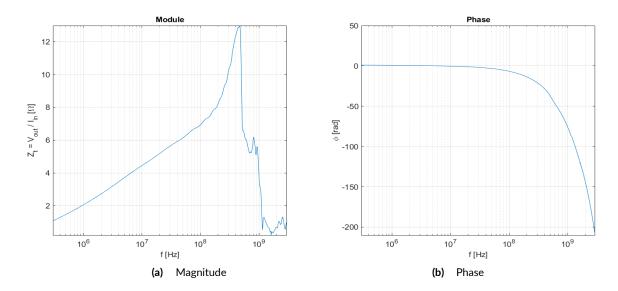


Figure G2: Transfer impedance Zt as a function of frequency

Identification of the transfer function in MATLAB:

The function tfest() takes as argument the data (amplitude, phase and frequency) but we also specify the number of poles 'p' and zeros 'z' desired in the transfer function (always with $p \ge z$). The function uses a non-linear least squares method (Isqnonlin in MATLAB) where the objective function tends to minimize the error between the measurement and the estimate.

d) Validation:

In order to validate the performance of the selected model (15 poles and 12 zeros) with the real equipment (HFCT), a test similar to a calibration was performed (Figure G3). The PD calibrator provides a current with a known load value (10pC, 20pC, 50pC and 100pC). The PD calibrator and the HFCT are connected to inputs of the oscilloscope with impedance Zin = 50Ω .

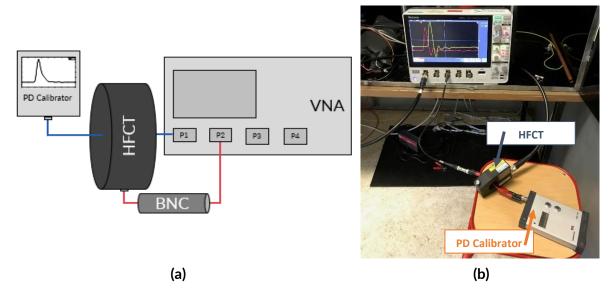


Figure G3 – Set-up for acquiring response from HFCT probe using PD calibrator

Experiments with H-bridge pulse generator

With Nanogen, some initial tests were performed using a DUT cell without needle to check the characteristic of the waveforms. Figure G4 presents the image taken from oscilloscope showing output voltage waveform across the DUT at 3 kV at 10 kHz with 25 % duty cycle. At the same time, the signals from PMT and HFCT (without any PDs) are also captured.

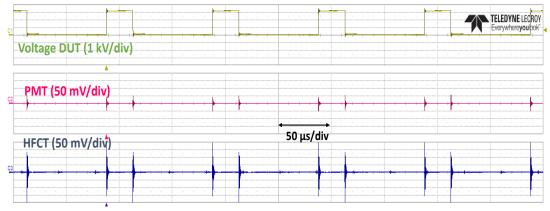


Figure G4: Voltage measured across DUT, signals acquired by PMT and HFCT using oscilloscope

During the test, the rise and fall time across the DUT is measured to be about 71 ns. Both PMT and HFCT signals are found to be impacted by the fast switching action of semiconductor devices in the pulse generator.

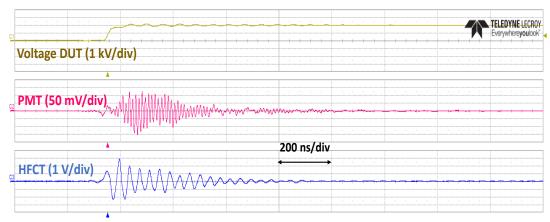


Figure G5: Magnified view of rising front of square voltage waveform and perturbation observed with PMT and HFCT detections

As can be observed in Figure G5, the disturbance due to displacement current in the circuit impacting the HFCT was quite large as compared to radiated EMI impacting the PMT. Due to the short life span of commercially available pulse generator (Nanogen 3) the tests could not be continued.

Abbreviations

BDV : Breakdown voltage DAB : Dual active bridge DC : Direct current DCPR : Direct current polarity reversal div : Division DUT : Device Under Test EMC : Electromagnetic compatibility EMI : Electromagnetic interference FEM : Finite element method GUI : Graphical user interface HVAC : High voltage alternating current HVDC : High voltage direct current IEC : International Electrotechnical Commission IGBT : Insulated gate bipolar transistor LCC : Line commutated converter MFT : Medium frequency transformer MOSFET : Metal oxide semiconductor field effect transistor WVDC : Medium voltage direct current PCB : Printed circuit boards PD : Partial discharges PRPD : Phase resolved partial discharge PDIV : Partial discharge inception voltage PDIF : Partial discharge inception field PMT : Photomultiplier tube Si : Silicon SiC : Silicon carbide WBG : Wide band gap pp : Peak to peak rms : Root mean square vs : versus i.e. : that is	AC	:	Alternating current
DC : Direct current DCPR : Direct current polarity reversal div : Division DUT : Device Under Test EMC : Electromagnetic compatibility EMI : Electromagnetic interference FEM : Finite element method GUI : Graphical user interface HVAC : High voltage alternating current HVDC : High voltage direct current IEC : International Electrotechnical Commission IGBT : Insulated gate bipolar transistor LCC : Line commutated converter MFT : Medium frequency transformer MOSFET : Metal oxide semiconductor field effect transistor WVDC : Medium voltage direct current PCB : Printed circuit boards PD : Partial discharges PRPD : Phase resolved partial discharge PDIV : Partial discharge inception voltage PDIF : Partial discharge inception field PMT : Photomultiplier tube Si : Silicon SiC : Silicon carbide WBG : Wide band gap pp : Peak to peak rms : Root mean square vs : versus	BDV	:	Breakdown voltage
DCPR : Direct current polarity reversal div : Division DUT : Device Under Test EMC : Electromagnetic compatibility EMI : Electromagnetic interference FEM : Finite element method GUI : Graphical user interface HVAC : High voltage alternating current HVDC : High voltage direct current EEC : International Electrotechnical Commission IGBT : Insulated gate bipolar transistor LCC : Line commutated converter MFT : Medium frequency transformer MOSFET : Metal oxide semiconductor field effect transistor MVDC : Medium voltage direct current PCB : Printed circuit boards PD : Partial discharges PRPD : Phase resolved partial discharge PDIV : Partial discharge inception voltage PDIF : Partial discharge inception field PMT : Photomultiplier tube Si : Silicon SiC : Silicon carbide WBG : Wide band gap pp : Peak to peak rms : Root mean square vs : versus	DAB	:	Dual active bridge
div : Division DUT : Device Under Test EMC : Electromagnetic compatibility EMI : Electromagnetic interference FEM : Finite element method GUI : Graphical user interface HVAC : High voltage alternating current HVDC : High voltage direct current IEC : International Electrotechnical Commission IGBT : Insulated gate bipolar transistor LCC : Line commutated converter MFT : Medium frequency transformer MOSFET : Metal oxide semiconductor field effect transistor MVDC : Medium voltage direct current PCB : Printed circuit boards PD : Partial discharges PRPD : Phase resolved partial discharge PDIV : Partial discharge inception voltage PDIF : Partial discharge inception field PMT : Photomultiplier tube Si : Silicon SiC : Silicon carbide WBG : Wide band gap pp : Peak to peak rms : Root mean square vs : versus	DC	:	Direct current
DUT : Device Under Test EMC : Electromagnetic compatibility EMI : Electromagnetic interference FEM : Finite element method GUI : Graphical user interface HVAC : High voltage alternating current HVDC : High voltage direct current IEC : International Electrotechnical Commission IGBT : Insulated gate bipolar transistor LCC : Line commutated converter MFT : Medium frequency transformer MOSFET : Metal oxide semiconductor field effect transistor MVDC : Medium voltage direct current PCB : Printed circuit boards PD : Partial discharges PRPD : Phase resolved partial discharge PDIF : Partial discharge inception voltage PDIF : Partial discharge inception field PMT : Photomultiplier tube Si : Silicon SiC : Silicon carbide WBG : Wide band gap pp : Peak to peak rms : Root mean square vs : versus	DCPR	:	Direct current polarity reversal
EMC : Electromagnetic compatibility EMI : Electromagnetic interference FEM : Finite element method GUI : Graphical user interface HVAC : High voltage alternating current HVDC : High voltage direct current IEC : International Electrotechnical Commission IGBT : Insulated gate bipolar transistor LCC : Line commutated converter MFT : Medium frequency transformer MOSFET : Metal oxide semiconductor field effect transistor MVDC : Medium voltage direct current PCB : Printed circuit boards PD : Partial discharges PRPD : Phase resolved partial discharge PDIV : Partial discharge inception voltage PDIF : Partial discharge inception field PMT : Photomultiplier tube Si : Silicon SiC : Silicon carbide WBG : Wide band gap pp : Peak to peak rms : Root mean square vs : versus	div	:	Division
EMI : Electromagnetic interference FEM : Finite element method GUI : Graphical user interface HVAC : High voltage alternating current HVDC : High voltage direct current IEC : International Electrotechnical Commission IGBT : Insulated gate bipolar transistor LCC : Line commutated converter MFT : Medium frequency transformer MOSFET : Metal oxide semiconductor field effect transistor MVDC : Medium voltage direct current PCB : Printed circuit boards PD : Partial discharges PRPD : Phase resolved partial discharge PDIV : Partial discharge inception voltage PDIF : Partial discharge inception field PMT : Photomultiplier tube Si : Silicon SiC : Silicon carbide WBG : Wide band gap pp : Peak to peak rms : Root mean square vs : versus	DUT	:	Device Under Test
FEM : Finite element method GUI : Graphical user interface HVAC : High voltage alternating current HVDC : High voltage direct current IEC : International Electrotechnical Commission IGBT : Insulated gate bipolar transistor LCC : Line commutated converter MFT : Medium frequency transformer MOSFET : Metal oxide semiconductor field effect transistor MVDC : Medium voltage direct current PCB : Printed circuit boards PD : Partial discharges PRPD : Phase resolved partial discharge PDIV : Partial discharge inception voltage PDIF : Partial discharge inception field PMT : Photomultiplier tube Si : Silicon SiC : Silicon carbide WBG : Wide band gap pp : Peak to peak rms : Root mean square vs : versus	EMC	:	Electromagnetic compatibility
GUI : Graphical user interface HVAC : High voltage alternating current HVDC : High voltage direct current IEC : International Electrotechnical Commission IGBT : Insulated gate bipolar transistor LCC : Line commutated converter MFT : Medium frequency transformer MOSFET : Metal oxide semiconductor field effect transistor MVDC : Medium voltage direct current PCB : Printed circuit boards PD : Partial discharges PRPD : Phase resolved partial discharge PDIV : Partial discharge inception voltage PDIF : Partial discharge inception field PMT : Photomultiplier tube Si : Silicon SiC : Silicon carbide WBG : Wide band gap pp : Peak to peak rms : Root mean square vs : versus	EMI	:	Electromagnetic interference
HVAC : High voltage alternating current HVDC : High voltage direct current IEC : International Electrotechnical Commission IGBT : Insulated gate bipolar transistor LCC : Line commutated converter MFT : Medium frequency transformer MOSFET : Metal oxide semiconductor field effect transistor MVDC : Medium voltage direct current PCB : Printed circuit boards PD : Partial discharges PRPD : Phase resolved partial discharge PDIV : Partial discharge inception voltage PDIF : Partial discharge inception field PMT : Photomultiplier tube Si : Silicon SiC : Silicon carbide WBG : Wide band gap pp : Peak to peak rms : Root mean square vs : versus	FEM	:	Finite element method
HVDC : High voltage direct current IEC : International Electrotechnical Commission IGBT : Insulated gate bipolar transistor LCC : Line commutated converter MFT : Medium frequency transformer MOSFET : Metal oxide semiconductor field effect transistor MVDC : Medium voltage direct current PCB : Printed circuit boards PD : Partial discharges PRPD : Phase resolved partial discharge PDIV : Partial discharge inception voltage PDIF : Partial discharge inception field PMT : Photomultiplier tube Si : Silicon SiC : Silicon carbide WBG : Wide band gap pp : Peak to peak rms : Root mean square vs : versus	GUI	:	Graphical user interface
IEC : International Electrotechnical Commission IGBT : Insulated gate bipolar transistor LCC : Line commutated converter MFT : Medium frequency transformer MOSFET : Metal oxide semiconductor field effect transistor MVDC : Medium voltage direct current PCB : Printed circuit boards PD : Partial discharges PRPD : Phase resolved partial discharge PDIV : Partial discharge inception voltage PDIF : Partial discharge inception field PMT : Photomultiplier tube Si : Silicon SiC : Silicon carbide WBG : Wide band gap pp : Peak to peak rms : Root mean square vs : versus	HVAC	:	High voltage alternating current
IGBT : Insulated gate bipolar transistor LCC : Line commutated converter MFT : Medium frequency transformer MOSFET : Metal oxide semiconductor field effect transistor MVDC : Medium voltage direct current PCB : Printed circuit boards PD : Partial discharges PRPD : Phase resolved partial discharge PDIV : Partial discharge inception voltage PDIF : Partial discharge inception field PMT : Photomultiplier tube Si : Silicon SiC : Silicon carbide WBG : Wide band gap pp : Peak to peak rms : Root mean square vs : versus	HVDC	:	High voltage direct current
LCC : Line commutated converter MFT : Medium frequency transformer MOSFET : Metal oxide semiconductor field effect transistor MVDC : Medium voltage direct current PCB : Printed circuit boards PD : Partial discharges PRPD : Phase resolved partial discharge PDIV : Partial discharge inception voltage PDIF : Partial discharge inception field PMT : Photomultiplier tube Si : Silicon SiC : Silicon carbide WBG : Wide band gap pp : Peak to peak rms : Root mean square vs : versus	IEC	:	International Electrotechnical Commission
MFT : Medium frequency transformer MOSFET : Metal oxide semiconductor field effect transistor MVDC : Medium voltage direct current PCB : Printed circuit boards PD : Partial discharges PRPD : Phase resolved partial discharge PDIV : Partial discharge inception voltage PDIF : Partial discharge inception field PMT : Photomultiplier tube Si : Silicon SiC : Silicon carbide WBG : Wide band gap pp : Peak to peak rms : Root mean square vs : versus	IGBT	:	Insulated gate bipolar transistor
MOSFET: Metal oxide semiconductor field effect transistor MVDC: Medium voltage direct current PCB: Printed circuit boards PD: Partial discharges PRPD: Phase resolved partial discharge PDIV: Partial discharge inception voltage PDIF: Partial discharge inception field PMT: Photomultiplier tube Si: Silicon SiC: Silicon carbide WBG: Wide band gap pp: Peak to peak rms: Root mean square vs: versus	LCC	:	Line commutated converter
MVDC : Medium voltage direct current PCB : Printed circuit boards PD : Partial discharges PRPD : Phase resolved partial discharge PDIV : Partial discharge inception voltage PDIF : Partial discharge inception field PMT : Photomultiplier tube Si : Silicon SiC : Silicon carbide WBG : Wide band gap pp : Peak to peak rms : Root mean square vs : versus	MFT	:	<u> </u>
PCB : Printed circuit boards PD : Partial discharges PRPD : Phase resolved partial discharge PDIV : Partial discharge inception voltage PDIF : Partial discharge inception field PMT : Photomultiplier tube Si : Silicon SiC : Silicon carbide WBG : Wide band gap pp : Peak to peak rms : Root mean square vs : versus	MOSFET	:	Metal oxide semiconductor field effect transistor
PD : Partial discharges PRPD : Phase resolved partial discharge PDIV : Partial discharge inception voltage PDIF : Partial discharge inception field PMT : Photomultiplier tube Si : Silicon SiC : Silicon carbide WBG : Wide band gap pp : Peak to peak rms : Root mean square vs : versus	MVDC	:	Medium voltage direct current
PRPD : Phase resolved partial discharge PDIV : Partial discharge inception voltage PDIF : Partial discharge inception field PMT : Photomultiplier tube Si : Silicon SiC : Silicon carbide WBG : Wide band gap pp : Peak to peak rms : Root mean square vs : versus	PCB	:	Printed circuit boards
PDIV : Partial discharge inception voltage PDIF : Partial discharge inception field PMT : Photomultiplier tube Si : Silicon SiC : Silicon carbide WBG : Wide band gap pp : Peak to peak rms : Root mean square vs : versus	PD	:	
PDIF : Partial discharge inception field PMT : Photomultiplier tube Si : Silicon SiC : Silicon carbide WBG : Wide band gap pp : Peak to peak rms : Root mean square vs : versus	PRPD	:	Phase resolved partial discharge
PMT : Photomultiplier tube Si : Silicon SiC : Silicon carbide WBG : Wide band gap pp : Peak to peak rms : Root mean square vs : versus	PDIV	:	Partial discharge inception voltage
Si : Silicon SiC : Silicon carbide WBG : Wide band gap pp : Peak to peak rms : Root mean square vs : versus	PDIF	:	Partial discharge inception field
SiC : Silicon carbide WBG : Wide band gap pp : Peak to peak rms : Root mean square vs : versus	PMT	:	Photomultiplier tube
WBG : Wide band gap pp : Peak to peak rms : Root mean square vs : versus	Si	:	Silicon
pp : Peak to peak rms : Root mean square vs : versus	SiC	:	Silicon carbide
rms : Root mean square vs : versus	WBG	:	Wide band gap
vs : versus	pp	:	Peak to peak
	rms	:	Root mean square
i.e. : that is	vs	:	versus
	i.e.	:	that is

Units and symbols

Symbol		Unit name	Quantity name
°C	:	Celsius	Temperature
a.u.	:	Arbitrary unit	
fa.u.	:	Femto arbitrary unit	Optical signals (from PDs)
pa.u.	:	Pico arbitrary unit	_
Hz	:	Hertz	
kHz	:	kilo hertz	- Era guan av
MHz	:	Mega hertz	- Frequency
GHz	:	Giga hertz	_
V	:	Volt	
kV	:	kilo volts	Voltage
mV	:	milli volts	_
A	:	Ampere	Current
С	:	Coulomb	
fC	:	Femto coulomb	Charac
pC	:	Pico coulomb	- Charge
nC	:	Nano coulomb	_
S	:	Seconds	
ms	:	Milli seconds	_
μs	:	microseconds	Time
ns	:	nano seconds	_
ps	:	Picoseconds	-
μF	:	Micro farad	
pF	:	Pico-farad	Capacitance
nF	:	Nano farad	-
μН	:	Micro henry	Inductance
nm	:	Nanometer	
μm	:	Micrometer	Length
mm	:	Millimeter	
km	:	kilometer	_
ppm	:	Part per million	
rpm	:	rotation per minute	
Ω	:	ohm	Resistance
Ω.m	:	Ohmmeter	Resistivity
TWh	:	Terawatt hour	Energy
ε (F/m)	:	Farad/meter	Permittivity constant
$\epsilon_{ m r}$:	-	relative permittivity

σ (S/m)	:	Siemens/meter	Conductivity
ρ (C/m ³)	:	Coulomb per cubic meter	Volume charge density
∇	:	-	Divergence operator



FOLIO ADMINISTRATIF

THESE DE L'UNIVERSITE DE LYON OPEREE AU SEIN DE L'INSA LYON

NOM: M. ANAND DATE de SOUTENANCE: 13/01/2022

(avec précision du nom de jeune fille, le cas échéant)

Prénoms: Somya

TITRE : Étude et caractérisation des matériaux isolants à l'aide de mesures de décharges partielles pour l'application de l'électronique de puissance (Study and characterization of insulating material using partial discharge measurements for power electronics application in HVDC and MVDC)

NATURE : Doctorat Numéro d'ordre : 2022LYSEI0001

Ecole doctorale: N° ED160 Electronique, Electrotechnique, automatique (EEA)

Spécialité : Génie Electrique

RESUME : Pour les futures infrastructures de réseaux intelligents, le réseau MVDC peut servir d'épine dorsale en intégrant les sources renouvelables distribuées, en connectant les charges à distance, en interconnectant les sous-stations existantes et en convertissant les sous-stations CA en CC pour limiter les impacts environnementaux. L'utilisation des capacités des dispositifs WBG peut réduire considérablement le poids, le volume et le coût de maturation des applications de puissance. Cependant, la présence de ces dispositifs dans le réseau électrique introduit une contrainte électrique différente sous la forme de formes d'ondes de tension carrées répétitives à montée rapide.

Dans ces circonstances, il devient nécessaire d'étudier la fiabilité des équipements de conversion de puissance du futur réseau de transmission, tels que les transformateurs à moyenne fréquence (MFT). Pour les applications à haute puissance, le système d'isolation du MFT sera principalement incorporent un liquide diélectrique comme milieu d'isolation primaire. Cependant, le mécanisme de décharge du liquide diélectrique sous une tension carrée répétitive rapide n'est pas très clair aujourd'hui.

Par conséquent, cette thèse vise à étudier le système d'isolation en utilisant des mesures de décharge partielle pour les applications électroniques de puissance telles que le MFT sous forme d'onde de tension carrée. Pour ce faire, les spécifications d'un banc d'essai ont été définies puis développées au cours de cette thèse afin de reproduire les contraintes électriques sous forme d'onde carrée et de fréquences de commutation supérieures à 50 Hz. En raison des résidus sous forme d'onde carrée, la mesure de DP par détection optique a été choisie. Dans un premier temps, la technique de détection optique a été validée sous AC 50 Hz en la comparant à la mesure électrique standard telle que définie par IEC 60270 avec une isolation huile/barrière qui représente le système d'isolation du transformateur. Ensuite, des mesures de DP ont été effectuées sous des formes d'onde de tension carrée et les résultats ont été comparés à ceux de la forme d'onde sinusoïdale CA pour comprendre l'impact de la contrainte non sinusoïdale. Par conséquent, la tension d'initiation d DP dans tension carrée unipolaire s'est avérée plus faible que celle du courant alternatif 50 Hz.



MOTS-CLÉS: Décharge partielles, liquide diélectrique, isolation huile/barrière, détection optique, tension carrée,

TMF

Laboratoire (s) de recherche : Ampère

Directeur de thèse: M. BUTTAY Cyril

Président de jury : M. PECASTAING Laurent

Composition du jury : M. LESAINT Olivier, M. CAVALLINI Andrea, Mme LOCATELLI Marie-Laure, Mme AIT AMAR

Sonia, M. JOUBERT Charles, M. VAGNON Eric, M. BUTTAY Cyril